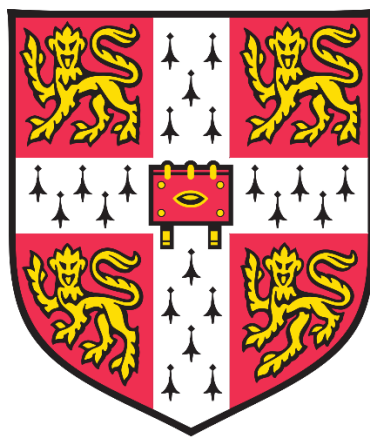


Monitoring apoptosis in intact cells by high-resolution magic angle spinning ^1H NMR spectroscopy



A dissertation submitted for the degree of Doctor of Philosophy at the University of Cambridge.

Submitted January 2021

Marta Wylot



Darwin College

Declaration

This dissertation is the result of my own work and includes nothing which is the outcome of work done in collaboration except as declared in the Preface and specified in the text. It is not substantially the same as any that I have submitted, or, is being concurrently submitted for a degree or diploma or other qualification at the University of Cambridge or any other University or similar institution except as declared in the Preface and specified in the text. I further state that no substantial part of my dissertation has already been submitted, or, is being concurrently submitted for any such degree, diploma or other qualification at the University of Cambridge or any other University or similar institution except as declared in the Preface and specified in the text. It does not exceed the prescribed word limit for the relevant Degree Committee.

Monitoring apoptosis in intact cells by high-resolution magic angle spinning ^1H NMR spectroscopy

By Marta Wylot

Abstract

Apoptosis is a cellular process that maintains an equilibrium between cell proliferation and cell death. Induction of apoptosis is a well-known strategy in developing cancer treatments, therefore non-invasive monitoring of apoptosis in intact cells could contribute towards the characterisation of drug efficacy and hence drug discovery. A known metabolic marker of apoptosis is a notable increase in proton NMR resonances associated with lipids stored in lipid droplets (LDs). MRI-based studies of lipid accumulation have been used to monitor apoptosis-based cancer treatments. However, the cellular processes which lead to the accumulation of lipid droplets remain poorly understood, causing a bottleneck for targeting lipid metabolism in cancer cells.

This thesis investigates the application of High-Resolution Magic Angle Spinning (HRMAS) ^1H NMR spectroscopy in monitoring metabolic changes in intact cells during apoptosis. The technique is used to analyse metabolic profiles of cells treated with cisplatin and etoposide after 3, 8, 24 and 48 h. The results are compared to the analysis of organic cell extracts by solution-state ^1H NMR spectroscopy to demonstrate lipid compartmentalisation and highlight the advantages of HRMAS ^1H NMR spectroscopy in monitoring lipid metabolism during apoptosis. The lipid compartmentalisation is also confirmed by differential centrifugation and mass spectrometry-based lipidomics further validating the importance of LDs.

Previous work linked NMR-visible lipid resonances to increased LD size. In this thesis, an NMR-based diffusion method is described for differentiating between control, apoptotic and necrotic cells. I demonstrate that as apoptosis-induced LDs become larger, the diffusion coefficient of NMR-visible lipids decreases. Therefore, diffusion measurements in conjunction with HRMAS ^1H NMR-derived lipid signals provide a novel means of following apoptosis in intact cells. Mass spectrometry and transcriptomic analysis was used to elucidate the origin of LD during cisplatin and etoposide treatments. This work identifies two treatment-dependent mechanisms of lipid particle organisation, contributing to our understanding of LD formation during apoptosis. It may help validate magnetic resonance spectroscopy as a non-invasive tool for following the efficacy of apoptosis-inducing drugs.

Publications and conference presentations

Metabolomics, Seattle, USA, 2018

Poster: 'Monitoring Lipid Droplet Formation Induced by Apoptosis and Necrosis by HRMAS ^1H NMR Spectroscopy'

NMR in Biology, Paris, France, 2019

Poster: 'High -Resolution Magic Angle Spinning NMR allows monitoring apoptosis in intact cells'

Young Lipid Scientist Award, London, UK, 2019

Talk: 'Lipid droplets and apoptosis'

SymBLS (Symposium of Biological Life Sciences) 2019, Cambridge 2019

Talk: 'When the magic happens in a tiny rotor: monitoring biological events by High-Resolution Magic Angle Spinning NMR Spectroscopy'

M. Wylot; D. Whittaker; S.A.C. Wren; J.H. Bothwell; L. Hughes; and J.L. Griffin, 2020. Monitoring apoptosis in intact cells by high-resolution magic angle spinning ^1H NMR spectroscopy. *NMR in Biomedicine*; awaiting publication.

Acknowledgment

Firstly and foremostly, thank you to Jules, my wonderful supervisor, who a) gave me an opportunity to work on this project, b) gave me ample suggestions what to do with myself in the lab; and c) let me learn from my mistakes and hoped for the best that I would not quench the magnet.

I am equally grateful to my industrial supervisors, Les, Stephen and Dave, for reading my scientific gibberish and helping me convert it into a story.

The following people helped me throughout my PhD:

- James, Antonio, Ben and Fynn for tips on MS
- Zoe for teaching me how to analyse MS data
- Antonio for helping me with MS-based choline assay
- Dean for showing me how to do PCR
- Tom and Ben for showing me how to culture cells
- John Bothwell for teaching me all I needed to know about microscopy
- Fynn for help with RNA-Seq data processing
- Jules for teaching me how to change the probe
- Cecilia for fixing NMR when I accidentally broke it
- Les for sending me to an NMR training course
- Clark for showing me how to use a plate reader
- Steve for helping me find whatever I needed for my experiments and harassing me when I did not read H&S. Because of you, I am still alive!

In addition, big thank you to anyone who crossed my path in Biochemistry Department for making my days fun. Thank you to people who accepted my posters and talks for conferences; and to EPSRC and AstraZeneca who funded my experiments and conference trips.

Thank you to my friends and family, especially the ones who had no clue what I was doing but still supported me.

I would be lost without you!

Table of Contents

Declaration.....	2
Abstract.....	3
Publications and conference presentations	4
Acknowledgement	5
Table of contents	6
List of figures.....	12
List of tables	20
Abbreviations.....	23
Chapter 1. Introduction	27
1.1. System biology and omics	27
1.2. Metabolomics.....	27
1.3. Approaches in metabolomics.....	29
1.4. Analytical methods in metabolomics	30
1.4.1. Nuclear magnetic resonance spectroscopy	30
1.4.2. NMR-based metabolomics.....	32
1.4.3. High-resolution magic angle spinning NMR spectroscopy	33
1.4.4. <i>In vivo</i> NMR spectroscopy.....	37
1.4.5. Combining NMR techniques in metabolomics	37
1.4.6. Mass spectrometry	38
1.4.7. Combining NMR spectroscopy and mass spectrometry.....	41
1.5. Data analysis in metabolomics.....	44
1.6. Apoptosis: definition, importance, and detection methods	47
1.7. Application of metabolomics in studying apoptosis	52
1.8. NMR-visible lipids	56
1.9. Scope and aims.....	59
Chapter 2. Materials and methods.....	61
2.1. Materials and reagents.....	61
2.2. Cell culture.....	61
2.3. Induction of apoptosis.....	62
2.4. Induction of necrosis	62

2.5. Growth medium sample preparation.....	63
2.6. Cell viability.....	63
2.7. Caspase 3-activity assay	63
2.8. Metabolite extraction (Bligh and Dyer).....	64
2.9. Lipid droplet isolation.....	64
2.10. HRMAS ¹ H NMR spectroscopy	65
2.10.1. Sample preparation.....	65
2.10.2. Data acquisition.....	65
2.10.3. Data processing	67
2.11. Solution-state NMR spectroscopy	67
2.11.1. Sample preparation.....	67
2.11.2. Data acquisition.....	68
2.11.3. Data processing	69
2.12. High gradient diffusion NMR spectroscopy.....	69
2.12.1. Sample preparation.....	69
2.12.2. Data acquisition.....	69
2.12.3. Data processing	70
2.13. Untargeted mass spectrometry analysis of lipids.....	70
2.13.1. Sample preparation.....	70
2.13.2. Data acquisition.....	70
2.13.3. Data processing	71
2.14. Targeted mass spectrometry analysis of choline compounds.....	71
2.14.1. Sample preparation.....	71
2.14.2. Data acquisition.....	71
2.14.3. Data processing	72
2.15. Reverse transcription quantitative polymerase chain reaction (qPCR).....	72
2.15.1. Sample preparation.....	72
2.15.2. Data acquisition.....	73
2.15.3. Data processing	73
2.16. The Next Generation Sequencing	74
2.16.1. Sample preparation.....	74
2.16.2. Data acquisition.....	75
2.16.3. Data processing	75
2.17. Lipid droplet visualization	75

2.17.1. Sample preparation.....	75
2.17.2. Data acquisition.....	75
2.17.3. Data processing.....	76
2.18. Data analysis and statistics	76
Chapter 3. Method optimization for HRMAS ¹H NMR spectroscopy	77
3.1. Introduction.....	77
3.2. Aims	80
3.3. Results and discussion.....	81
3.3.1. The effect of sample packing on spectra quality.....	81
3.3.2. The effect of different spinning rates on cell samples	82
3.3.3. Impact of the NMR experiment duration and cell integrity.....	84
3.3.3.1. Cell viability assessed by the Trypan blue assay	84
3.3.3.2. Cell viability by HRMAS ¹ H NMR spectroscopy	85
3.3.3.3. Cell sample recovery after HRMAS NMR experiments	89
3.3.4. Comparison of 1D ¹ H NMR pulse sequences.....	89
3.3.5. Comparison of solution-state and HRMAS ¹ H NMR spectra of intact cells.....	92
3.3.6. Comparison of HRMAS ¹ H NMR spectra of intact cells and solution-state ¹ H NMR spectra of cell extracts.....	93
3.3.7. HRMAS ¹ H NMR spectra of different cell lines	101
3.4. Conclusions.....	102
Chapter 4. HRMAS ¹H NMR spectroscopy for monitoring metabolites in intact cells during apoptosis	103
4.1. Introduction.....	103
4.2. Aims	105
4.3. Methods	107
4.4. Results	107
4.4.1. Establishing dose and incubation time for inducing apoptosis.....	107
4.4.2. ¹ H NMR-based metabolic profiling of apoptotic cells	109
4.4.2.1. Establishing apoptosis in cell samples for HRMAS NMR analysis	109
4.4.2.2. HRMAS ¹ H NMR analysis of intact cells.....	110
4.4.2.3. ¹ H NMR analysis of growth media.....	115
4.4.3. ¹ H NMR-based metabolic profiling of apoptotic cells – time course	117

4.4.3.1. Caspase-3 activity assay and cell viability	117
4.4.3.2. HRMAS ¹ H NMR analysis of intact cells	118
4.4.4. Combined NMR-based metabolomics of intact cell, cell extract, and media	123
4.5. Discussion	126
4.5.1. Metabolic profiling of intact cells	126
4.5.2. Cellular disintegration by ¹ H NMR spectroscopy	127
4.5.3. Lactate co-resonates with -CH ₂ - lipid	128
4.5.4. HRMAS ¹ H NMR spectroscopy of choline compounds in intact cells	130
4.5.5. HRMAS vs solution-state ¹ H NMR spectroscopy	132
4.5.6. Metabolic pathways	133
4.6. Conclusions	136
Chapter 5. The study of apoptosis in intact cells by HRMAS ¹H NMR-based diffusion and T₂-relaxation measurements	137
5.1. Introduction	137
5.1.1. Introduction to the property of relaxation in NMR spectroscopy	137
5.1.2. Introduction to NMR-based diffusion	140
5.2. Aims	144
5.3. Methods	144
5.4. Results	145
5.4.1. T ₂ relaxation time measurements of metabolites and water in intact cells	145
5.4.1.1. Apoptotic cells	145
5.4.1.2. Necrotic cells	146
5.4.2. NMR-based diffusion measurements of metabolites and water in intact cells	147
5.4.2.1. Suitability of NMR-based diffusion methods for analysing biological samples. Model system: full fat and semi-skimmed milk	147
5.4.2.2. Apoptotic cells	148
5.4.2.3. Necrotic cells	151
5.4.2.4. Apoptotic vs necrotic cells	152
5.4.2.5. High gradient diffusion	153
5.4.3. Microscopy compared with HRMAS ¹ H NMR spectroscopy of mobile lipids	154
5.4.4. Viscosity of cytoplasm	155
5.4.5. Determination of mean displacement	156
5.5. Discussion	157

5.5.1. T ₂ relaxation times of metabolites in intact cells	157
5.5.2. Diffusion of metabolites in intact cells	160
5.5.2.1. Choline compounds.....	161
5.5.2.2. Mobile lipids	162
5.5.3. Validating NMR-based diffusion measurements of metabolites in intact cells	163
5.5.3.1. Viscosity.....	163
5.5.3.2. Mean squared displacement.....	164
5.6. Conclusions.....	164
Chapter 6. Study of lipid remodelling by mass spectrometry-based lipidomics and transcriptomic.	167
6.1. Introduction.....	167
6.1.1. Lipidomics of apoptosis.....	167
6.1.2. Lipid-related transcriptomics apoptosis.....	168
6.2. Aims	170
6.3. Methods	170
6.4. Results	170
6.4.1. MS-based lipidomics	170
6.4.2. Transcriptomics	174
6.4.2.1. Pathways enrichment analysis.....	177
6.5. Discussion	185
6.5.1. Composition of apoptosis-induced LDs.....	185
6.5.2. Mechanism of lipid accumulation is treatment specific	186
6.5.3. Peroxisomes also accumulate lipids.....	188
6.6. Conclusions.....	189
Chapter 7. Conclusions and future perspective	191
References	195
Appendix 1 Supporting information for Chapter 4	225
S1.1. Supporting information for cellular disintegration of necrotic cells by ¹ H NMR spectroscopy.	225
S1.2. Supporting information for data reported in Table 4.1 in Chapter 4	227
S1.2.1. Growth media.....	227
S1.2.2. Cell extracts - organic fraction.....	229
S1.2.3. Cell extract - aqueous fraction	232

Appendix 2. Supporting information for Chapter 5	235
S2.1. T ₂ bi-exponential fits	235
S2.2. Fitting errors for T ₂ bi-exponential model	236
S2.3. Diffusion bi-exponential fits	238
S2.4. Fitting errors for diffusion bi-exponential model	239
S2.5. Signal to noise calculated for key resonances at the highest b-value for HRMAS NMR and high-gradient solution-state NMR spectroscopy	240
S2.6. Contribution of non-lipid metabolites to apparent diffusion coefficients of mobile lipids	241
S2.7. Determination of cytoplasmic viscosity for data presented in Table 5.6	242
Appendix 3. Supporting information for Chapter 6	243
Appendix 4. Supporting information for Chapter 3	282

List of Figures	Page
Figure 1.1. Growth in human metabolomics. The number of human metabolites curated by HMDB in 2006-2020 (https://hmdb.ca , March 2020).	27
Figure 1.2. Two approaches for performing metabolomics: targeted and untargeted.	28
Figure 1.3. Splitting of nuclei spin energies in an external magnetic field.	30
Figure 1.4. Schematic of basic mass spectrometer.	38
Figure 1.5. A typical data analysis workflow in metabolomics studies. The schematic shows the steps of the metabolomic data analysis including raw data processing, statistical analysis, and biological interpretation.	44
Figure 1.6. An example of the PCA score plot and its corresponding loading plot for metabolomics data. The score plot shows the separation of four different sample classes and the loading plot shows which variables are most responsible for differences between the groups.	45
Figure 1.7. Molecular mechanism of apoptosis. Apoptosis can proceed via multiple cascades and is balanced by pro- and antiapoptotic mechanisms. I-VI indicate checkpoints used for detection of apoptosis (BOX 1.2).	48
Figure 1.8. Lipid microdomains in a mammalian cell. Lipid rafts are contained within the plasma membrane while lipid droplets originate from the endoplasmic reticulum (ER) and are located in the cytoplasm.	56
Figure 2.1. Cycling method for qPCR analysis. ① 10-minute incubation at 95°C activated the HotStart DNA Taq polymerase; ② 15-second incubation at 95°C denatured the cDNA; ③ 1-minute incubation at 60°C, in which primers annealed to the template and were elongated by the polymerase. Steps ② and ③ were repeated 40 times. Fluorescence measurements were taken at the end of each cycle: excitation and emission maxima for SYBR Green dye are at 494 and 521 nm, respectively.	73
Figure 3.1. HRMAS rotor systems with different sample chamber geometries.	78
Figure 3.2. Light microscopy images of C6 glioma cells (A) and C2C12 myotubes (B). The length of glioma cells is 12-14 μm, while the length of myotubes is 130-520 μm.	79
Figure 3.3. The effect of sample packing on spectra quality. Representative 500 MHz HRMAS ¹ H NMR solvent suppressed spectra of intact cell samples (spinning at 5 kHz) packed in: 80 μL rotor + disposable 30 μL insert (A), 50 μL rotor + 50 μL insert (B), and 12 μL rotor + 12 μL insert (C). TSP was added as a reference compound and its resonance shape compared across the spectra. The images of inserts were taken from www.bruker.com .	81
Figure 3.4. 500 MHz HRMAS ¹ H NMR solvent suppressed CPMG spectra of intact cells at six different spinning rates. The chemical shift scale is presented in Hz to highlight the interaction between the spinning sideband chemical shift and the spinning rate. A) Assignment of selected resonances used for measuring changes in line broadening at different spinning rates. B) Expanded NMR region showing the spinning sidebands. The spinning sidebands of water are visible at low spinning rates. The sidebands of lactate and TSP are visible at 5 kHz.	83

Figure 3.5. The effect of the duration of HRMAS NMR experiments on cell viability. The viability of cells incubated with PBS, DMF, or DMSO was measured before (□) and after the HRMAS ¹H NMR experiments (■ 0.5 h, ■ 3.5 h, 5 kHz spinning). The columns represent the percentage of Trypan blue negative cells (viable cells), error bars represent SEM, n = 3, ANOVA: * p > 0.05, ** p > 0.01 (FDR-adjusted values), post hoc test: before NMR vs 3.5 h after NMR.

84

Figure 3.6. Superimposed 500 MHz HRMAS ¹H NMR spectra recorded immediately after the intact cells were sealed in the rotor (light blue, n = 4) and after 3.5 h of spinning at 5 kHz in the NMR instrument (dark blue, n = 4). Quantitative changes in metabolite resonances are reported in **Table 3.2**.

85

Figure 3.7. Two-dimensional PCA score plot derived from the HRMAS ¹H NMR spectra of control (green triangles), cisplatin- (red squares), and etoposide- (blue circles) treated intact cells recorded at time 0 h (empty shapes) and 3.5 h (filled shapes). One data point represents one sample, n = 4. The numbers in brackets represent the percentage of variability explained by each PC.

87

Figure 3.8. Images of C2C12 cells taken with an Evosfl digital inverted microscope: fresh cells before NMR experiment (A), 12 h of growth after the NMR experiment (B), and 48 h of growth after the NMR experiment (C). Red arrows indicate representative dead cells, blue arrows indicate representative live cells.

88

Figure 3.9. Superimposed 500 MHz HRMAS ¹H NMR spectra of intact cells recorded using different pulses sequences: 1D NOESY (blue) and a T₂-edited CPMG (black). The spectra were normalized to the TSP reference peak. The water region (4.5 – 5.0 ppm) was removed.

89

Figure 3.10. 500 MHz HRMAS ¹H NMR spectra of intact cells showing the effect of NMR-editing techniques. A) A series of superimposed T₂-edited CPMG spectra editing out lipids. The spectrum in black contains mainly the resonances from small metabolites. The arrow indicates the direction of increasing spin-echo number. Empty triangles indicate the decaying lipid resonances. B) A series of superimposed diffusion-edited DOSY spectra editing out small metabolites. The spectrum in black contains mainly the resonances from lipids. The arrow indicates the direction of increasing gradient. Full triangles show the decaying resonances of small metabolites.

90

Figure 3.11. Comparison of the solution-state and HRMAS ¹H NMR spectra of intact cells. A. 500 MHz HRMAS ¹H NMR solvent suppressed spectra of 10⁶ intact cells (4 mm rotor, 50 μL insert, 10⁶ cells per sample, 64 scans). B. 400 MHz solution-state ¹H NMR solvent suppressed spectra of intact cells (5 mm tube, 400 μL insert, 2 × 10⁶ cells per sample, 64 scans). The spectra were normalized to noise levels. Intensified spectra are shown in the insert.

92

Figure 3.12. NMR-based metabolic profiling of cells: 500 MHz ¹H NMR water-suppressed spectra of aqueous fraction of cell extract in D₂O; 500 MHz ¹H NMR of organic fraction of cell extract in chloroform-d; and 500 MHz HRMAS ¹H NMR water-suppressed of intact cells in D₂O. The chemical shift range is split into two parts for clarity: A) 0.6 – 5.4 ppm and B) 5.7 – 9.3 ppm. Metabolite annotation is listed in **Table 3.3**.

93

Figure 3.13. 500 MHz COSY NMR water-suppressed spectra of aqueous fraction of cell extract in D₂O. The chemical shift range is split into two parts for clarity: A) 0.6 – 5.4 ppm and B) 5.7 – 9.3 ppm. Metabolite annotation is listed in **Table 3.3**.

97

Figure 3.14. 500 MHz COSY NMR spectrum of the organic fraction of the cell extract in deuterated chloroform. Metabolite annotation is listed in **Table 3.3**.

98

Figure 3.15. 500 MHz HRMAS COSY NMR water-suppressed spectra of intact cells in D ₂ O. The chemical shift range is split into two parts for clarity: A) 0.6 – 5.4 ppm and B) 5.7 – 9.3 ppm. Metabolite annotation is listed in Table 3.3 .	99
Figure 3.16. Comparison of HRMAS ¹ H NMR spectra from different cell lines: adipose, liver, muscle, and glioma cells. Metabolite annotation is listed in Table 3.3 .	100
Figure 4.1. Chemical structure of cisplatin (A) and etoposide (B).	103
Figure 4.2. NMR methods to study apoptosis induced by cisplatin and etoposide. After incubation, media samples were collected for solution-state ¹ H NMR analysis, intact cells (C2C12 myotubes) were harvested for HRMAS ¹ H NMR analysis, or Bligh and Dyer extraction and solution-state NMR analysis.	105
Figure 4.3. Dose-incubation time response for cisplatin- and etoposide-treated C2C12 myotubes. Apoptosis was normalized to the control group at each time point. SEM represent biological variance (n = 4). ANOVA was used to assess significance and Fisher's least significant difference (LSD) was used for post hoc pairwise comparisons of the treatment groups; p-values are FDR-adjusted; significances (p < 0.05) are reported relative to the control group.	107
Figure 4.4. Cell viability (membrane integrity) and apoptosis (caspase 3 activity) measured in C2C12 myotubes treated with cisplatin 60 μM (red), etoposide 50 μM (blue) and heat (grey) for 48 h. The change in apoptosis was reported relative to the control group (green); n = 4; ANOVA with post hoc Fisher's test: ** p < 0.01, *** p < 0.001.	109
Figure 4.5. Superimposed 500 MHz HRMAS ¹ H NMR spectra of intact C2C12 myotubes treated with cisplatin (red), etoposide (blue), and heat (grey) for 48h. The control spectrum of untreated cells shown in green. All spectra were normalised to the total integral. Partially suppressed water peak at 4.6 ppm was removed. T – tyrosine, H – histidine, G – guanosine, Me – methylhistidine, Pha – phenylalanine.	110
Figure 4.6. Two-dimensional PCA score plot (A) and corresponding loading plot (B) derived from the ¹ H HRMAS NMR spectra of control (green triangles), cisplatin- (red squares), etoposide- (blue circles), and heat- (black asterisks) treated intact C2C12 myotubes. C , D show the same dataset excluding the heat-treated group. The most significant metabolites are highlighted in the loading plots. Other lipids: =CHCH ₂ CH=, -CH ₂ CH ₂ CO, =CHCH ₂ -, -CH ₂ CO; n = 4 for etoposide and heat, n = 8 for control and cisplatin. The numbers in brackets represent the percentage of variability explained by each PC. Spectra were pre-processed with total integral normalization and Pareto scaling.	111
Figure 4.7. Comparison of lipids in C2C12 myotubes: control (green), cisplatin (red), etoposide (blue), and heat (grey), 48 h incubation. ANOVA with post hoc Fisher's test: * p < 0.05, ** p < 0.01, *** p < 0.001, FDR-adjusted; n = 4 for etoposide and heat, n = 8 for control and cisplatin.	112
Figure 4.8. Comparison of metabolites in C2C12 myotubes: control (green), cisplatin (red), etoposide (blue), and heat (grey), 48 h incubation. ANOVA with post hoc Fisher's test: * p < 0.05, ** p < 0.01, *** p < 0.001, FDR-adjusted; n = 4 for etoposide and heat, n = 8 for control and cisplatin.	113
Figure 4.9. 500 MHz ¹ H NMR spectra of growth media collected after 48 h treatments: media from C2C12 myotubes treated with - control (green), cisplatin (red), etoposide (blue), and heat	

(grey). Pink spectra represent media-only samples before adding to the cells. All spectra were normalized to the total integral. Partially suppressed water peak was removed.	115
Figure 4.10. Comparison of metabolites found in growth media of C2C12 myotubes: control (green), cisplatin (red), etoposide (blue), heat (grey), and media-only (pink). ANOVA with post hoc Fisher's test: * $p < 0.05$, ** $p < 0.01$, *** $p < 0.001$ for all treatments vs control group, # $p < 0.05$ for heat vs media-only group, & $p < 0.05$ for cisplatin vs etoposide group, all p -values are FDR-adjusted.	116
Figure 4.11. Cell viability (lines) and apoptosis (bars) of C2C12 myotubes treated with cisplatin 60 μM (red) and etoposide 120 μM (blue). The change in apoptosis is reported relatively to the control group (green); $n = 4$; ANOVA with post hoc Fisher's test: * $p < 0.05$, ** $p < 0.01$, *** $p < 0.001$.	118
Figure 4.12. A) Superimposed 500 MHz HRMAS ^1H NMR spectra of control intact C2C12 myotubes (green), cisplatin- (red), and etoposide-treated (blue). All spectra were normalized to the total integral. The partially suppressed water peak at 4.6 ppm was removed. B) Lactate and lipid signal at ~ 1.3 ppm.	119
Figure 4.13. Comparison of metabolites in C2C12 myotubes: control (green), cisplatin (red), and etoposide (blue). Fold change integral reported relative to control at each time point. ANOVA with post hoc Fisher's test: *(red) $p < 0.05$ for cisplatin vs control group, *(blue) $p < 0.05$ for etoposide vs control group, # $p < 0.05$ for cisplatin vs etoposide group, all p -values are FDR-adjusted.	120-121
Figure 4.14. Comparison of lipids in C2C12 myotubes: control (green), cisplatin (red), and etoposide (blue). Fold change integral reported relative to control at each time point. ANOVA: *(red) $p < 0.05$ for cisplatin vs control group, *(blue) $p < 0.05$ for etoposide vs control group, # $p < 0.05$ for cisplatin vs etoposide group, all p -values are FDR-adjusted.	122
Figure 4.15. Comparison of choline-containing compounds in C2C12 myotubes as measured by HRMAS ^1H NMR spectroscopy: control (green), cisplatin (red), and etoposide (blue). Fold change integral reported relative to control at each time point. PC – phosphocholine, GPC – glycerophosphocholine, PTC – phosphatidylcholine. ANOVA with post hoc Fisher's test: *(red) $p < 0.05$ for cisplatin vs control group, *(blue) $p < 0.05$ for etoposide vs control group, # $p < 0.05$ for cisplatin vs etoposide group, all p -values are FDR-adjusted.	122
Figure 4.16. Comparison of lipid resonances of intact C2C12 myotubes (HRMAS ^1H NMR spectroscopy) and C2C12 myotubes extracts (solution-state ^1H NMR spectroscopy): control (green), cisplatin (red), and etoposide (blue) after 48 h incubation. ANOVA with post hoc Fisher's test: * $p < 0.05$, ** $p < 0.01$, *** $p < 0.001$.	125
Figure 4.17. A) Superimposed 500 MHz HRMAS ^1H NMR T_2 -edited spectra of control (green), cisplatin- (red), and etoposide-treated (blue) C2C12 myotubes (24 h) showing the lactate region only. All spectra were normalized to the total integral. B) Fold change integral of lactate ($-\text{CH}_3$) as compared to the control group; $n = 16$; ANOVA with post hoc Fisher's test: * $p < 0.001$ for control vs treatments, # $p < 0.001$ for cisplatin vs etoposide.	129
Figure 4.18. Comparison of choline containing compounds in C2C12 myotubes as measured by mass spectrometry: control (green), cisplatin (red), and etoposide (blue) after 48 h incubation. Fold change in ion count reported relative to control. ANOVA with post hoc Fisher's test: * $p < 0.05$, ** $p < 0.01$, *** $p < 0.001$.	131

Figure 4.19. CDP-choline pathway for PTC biosynthesis. Cytosolic choline is firstly phosphorylated and then converted to CDP-choline, which is a rate-limiting step regulated by signals from the membrane. CDP-choline is translocated to the membrane and converted to PTC. Red and blue arrows indicate a significant ($p < 0.05$) increase or decrease in choline-containing metabolites in cisplatin- or etoposide-treated cells, respectively.

131

Figure 5.1. Relaxation of magnetization vectors after a 90° radiofrequency pulse (rf). For T_1 relaxation, the z component of the net magnetization (M_z) is reduced to zero and then it recovers to its equilibrium value. For T_2 relaxation, the xy component of the net magnetization (M_{xy}) reaches maximum after the rf pulse and then it decreases to its equilibrium condition of $M_{xy} = 0$. The recovery of magnetization is an exponential process with a time constant T_1 or T_2 .

138

Figure 5.2. Spin echo pulse sequence for measuring T_2 . The 90° pulse flips the spins into the transverse plane followed by a delay (τ) and the 180° pulse, which refocuses spins in the transverse plane. The sequence is incremented n times.

139

Figure 5.3. A basic form of the DOSY pulse sequence with a gradient spin echo (SE). The 90° pulse flips the spins into the transverse plane followed by the gradient pulse for position encoding. The 180° pulse reverses the sign of the phase changes from the first gradient pulse, and the second gradient refocuses the signal unless the spins have diffused over the diffusion time Δ . The loss of the signal intensity as a function of diffusion time was measured.

141

Figure 5.4. Example of a diffusion decay curve with varying gradient strength.

142

Figure 5.5. Modes of diffusion in biological samples: free diffusion and restricted diffusion. The orange circle represents a diffusing molecule, the black line corresponds to its diffusion pathway, the blue circle represents confinement.

143

Figure 5.6. Metabolite T_2 relaxation times in intact cells as measured by HRMAS ^1H NMR spectroscopy: control (green), cisplatin (red), and etoposide (blue) at different incubation times (8, 24 and 48 h). Error bars representing SEM (biological replicates, $n = 4$) not visible if $\text{SEM} < 0.01$, ANOVA with post hoc Fisher's test: $*p < 0.05$, FDR-adjusted.

146

Figure 5.7. Apparent diffusion coefficients of metabolites and water in intact cells measured by HRMAS ^1H NMR spectroscopy: control (green), cisplatin (red), and etoposide (blue) at different incubation times (3, 8, 24, and 48 h). Error bars representing SEM (biological variation, $n \geq 6$ for control and cisplatin, $n \geq 3$ for etoposide).

149

Figure 5.8. Statistical analysis of NMR-based diffusion data of intact cells after (A, B) 24- and (C, D) 48-hour treatments: control (\blacklozenge green), cisplatin (\blacksquare red), and etoposide (\bullet blue). A&C Two-dimensional PCA score plot derived from the diffusion data of selected metabolites. B&D Box-whisker plots comparing apparent diffusion coefficients (ADC) for each metabolite signal across control, cisplatin, and etoposide.

150

Figure 5.9. Apparent diffusion coefficients of metabolites and water in intact cells measured by HRMAS ^1H NMR spectroscopy: control (green) and heat-treated cells (grey). Error bars represent SEM (biological replicates, $n > 3$), Student t-test: $*p < 0.05$, $**p < 0.01$, $***p < 0.001$.

152

Figure 5.10. A tri-exponential diffusion fit for the $-\text{CH}_2-$ signal displayed as a Stejskal-Tanner plot. Diffusion data collected for untreated cells packed in 3 mm tubes using a high gradient 5 mm probe (diff50). Error bars correspond to the line fitting errors.

154

Figure 5.11. Correlation of microscopy-based LD size estimates and HRMAS ¹H NMR-based mean diffusion coefficients. Representative images of fluorescence-labeled LDs in a single cell: **A)** control, **B)** cisplatin treatment, **C)** etoposide treatment. Arrows indicate neutral lipids in LD stained with BODIPY dye. Images were taken after 48 h incubation. **D)** Regression analysis for mean LD size and NMR-based diffusion rates for control (● green), cisplatin (● red), and etoposide (● blue) samples at ● 24 h and ▲ 48 h incubation times. Four dots aligned vertically represent four chemical groups. The graph represents the collective diffusion coefficient from each chemical group.

155

Figure 5.12. **A)** Mean and SEM values of LD displacement calculated from HRMAS ¹H NMR diffusion data and confocal fluorescence microscopy. **B)** Diffusion coefficients of LDs in intact cells as a function of diffusion time. Data correspond to the control (◆ green) and cisplatin (■ red) treated cells at 24 h. Error bars correspond to standard errors; asterisks represent statistical significance (Student t-test): * p<0.05, *** p<0.001.

157

Figure 6.1. RNA-Seq workflow overview. First, RNA is extracted from cells; second, mRNA molecules are isolated, randomly fragmented and converted to complementary DNA (cDNA) by reverse transcription; next, sequencing adaptors (which contain functional elements permitting sequencing) are ligated to the ends of the cDNA fragments. Following amplification by PCR, NGS of the cDNA library produces sequencing reads, which are aligned to a genome of reference and assembled to produce an RNA sequence map.

169

Figure 6.2. PLS-DA analysis of TAG and DAG species extracted from **A)** isolated LDs and **B)** organic fraction of cell extracts for control (◆ green), cisplatin (■ red), and etoposide (● blue) samples. The tables below contain quality metrics for each model: R² – goodness of fit, Q² – goodness of prediction. The analysis was performed after total sum normalization and Pareto scaling; n = 5 for isolated LD samples and n = 4 for cell extracts.

171

Figure 6.3. Unsaturation analysis of TAGs and DAGs extracted from **A)** isolated LD and **B)** whole cells after apoptotic treatment: cisplatin (● red) and etoposide (● blue). Fold changes for each lipid in apoptotic cells was calculated relative to the control group (● green): Abundance_{treatment}/Abundance_{control} or Abundance_{control}/Abundance_{control}. Abundance is the total ion count for a given ion. Each ion corresponds to a mass-to-charge ratio (m/z), which is used to assign the lipid species. SFA – saturated fatty acids, MUFA – monounsaturated fatty acids, PUFA – polyunsaturated fatty acids; n = 5 for isolated LD samples and n = 4 for cell extracts.

172

Figure 6.4. The top 20 lipid species ranked by VIP scores for **A)** isolated LDs and **B)** organic fraction of cell extracts. Species highlighted in bold are the same in isolated LD and cell extract samples. Squares represent the comparison of relative lipid abundance between control, cisplatin, and etoposide groups. TG - triacylglycerol, DG - diacylglycerol.

173

Figure 6.5. Comparison of selected lipid species extracted from isolated LDs and whole cells; control (green), cisplatin (red) and etoposide (blue). TG – triacylglycerol. ANOVA with post hoc Fisher's test: * p < 0.1, ** p < 0.01, *** p < 0.001, FDR-adjusted; n = 5 for isolated LD samples and n = 4 for cell extracts.

174

Figure 6.6. Gene expression profiles of apoptotic cells characterized by RNA-Seq. Only genes related to lipid metabolism and apoptosis are included in the analysis. **A)** Heat map comparing control (cr, green), cisplatin (cis, red), and etoposide (eto, blue) samples. Each coloured cell on the map corresponds to a normalized expression value, with samples in columns and genes in rows. **B)** PCA analysis of selected transcriptomic data.

175

Figure 6.7. <i>A) RNA-Seq results compared to qRT-PCR results for six genes involved in lipid metabolism. Mean fold changes in gene expressions for cisplatin (red) and etoposide (blue) were calculated relative to the respective control group (green); error bars represent SEM of 4 independent cell samples. B) Correlation analysis between RNA-Seq and qRT-PCR, R^2 assesses goodness-of-fit for an idealized model ($y = x$).</i>	176
Figure 6.8. <i>Regulation of lipid particle organization during A) cisplatin and B) etoposide treatments.</i>	181
Figure 6.9. <i>Lipid transporter expressions in C2C12 myotubes treated with cisplatin (red) or etoposide (blue). Mean fold changes in gene expressions were calculated relative to the control group (green); error bars represent SEM of four independent cell samples. All changes are statistically significant (FDR-adjusted $p < 0.05$).</i>	182
Figure 6.10. <i>Differentially expressed genes related to A) lipid droplets, and B) peroxisomes in C2C12 myotubes treated with cisplatin (red) and etoposide (blue). Mean fold changes in gene expressions were calculated relative to the control group (green); error bars represent SEM of four independent cell samples. * indicates statistically significant changes as compared to the controls (ANOVA: FDR-adjusted P-value < 0.05, see Appendix 3, Table S3.7).</i>	183
Figure 6.11. <i>Regulation of very long chain fatty acid (VLCFA) catabolism in peroxisomes during A) cisplatin and B) etoposide treatments.</i>	189
Figure 7.1. <i>Schematic representation of monitoring metabolic reaction rates in intact cells by HRMAS ^1H NMR spectroscopy.</i>	193
Figure 7.2. <i>^{13}C glucose consumption (A) and ^{13}C lactate accumulation (B) rates in intact cells treated with curcumin 50 μM (orange) and 200 μM (red) in DMSO or PEG as measured by HRMAS ^1H NMR spectroscopy. Student t-test: *$p < 0.05$, **$p < 0.01$, $n = 3$. The fold change in reaction rates were calculated from the slope of the curve of the normalised NMR intensity versus time, relative to the control (blue).</i>	194
Figure S1.1. <i>500 MHz ^1H NMR spectra of control (green) and heat-treated (black) cell extracts (aqueous fraction). All spectra were normalised to the total integral.</i>	226
Figure S1.2. <i>500 MHz ^1H NMR spectra of culture media collected after 48 h treatments: control (green), cisplatin (red) and etoposide (blue). All spectra were normalised to the total integral. Partially suppressed water peak was removed.</i>	227
Figure S1.3. <i>Two-dimensional PCA score plot derived from the ^1H NMR spectra of growth media samples: control (green triangles), cisplatin (red squares), etoposide (blue circles); $n = 3$ for etoposide, $n = 5$ for control and cisplatin. The numbers in brackets represent the percentage of variability explain by each principal component (PC).</i>	228
Figure S1.4. <i>500 MHz ^1H NMR spectra of cell extract (organic fraction) collected after 48 h of the following treatments: control (green), cisplatin (red) and etoposide (blue). All spectra were normalised to the total integral.</i>	229
Figure S1.5. <i>Two-dimensional PCA score plot derived from the ^1H NMR spectra of organic fraction of cell extract samples: control (green triangles), cisplatin (red squares), etoposide (blue circles); $n = 4$ for etoposide, $n = 5$ for control and cisplatin. The numbers in brackets represent the percentage of variability explain by each principal component (PC).</i>	230

Figure S1.6. Comparison of fold change integral for selected lipids in organic fraction of cell extracts: control (green), cisplatin (red) and etoposide (blue). * $p < 0.05$, ** $p < 0.01$, *** $p < 0.001$ for control vs treatment; # $p < 0.05$ for cisplatin vs etoposide, FDR adjusted.	231
Figure S1.7. 500 MHz ^1H NMR spectra of cell extract (aqueous fraction) collected after 48 h of the following treatments: control (green), cisplatin (red) and etoposide (blue). All spectra were normalised to the total integral.	232
Figure S1.8. Two-dimensional PCA score plot derived from the ^1H NMR spectra of aqueous fraction of cell extract samples: control (green triangles), cisplatin (red squares), etoposide (blue circles); $n = 4$ for etoposide, $n = 5$ for control and cisplatin. The numbers in brackets represent the percentage of variability explain by each principal component (PC).	233
Figure S2.1. Representative examples of bi-exponential T_2 fits of signal intensity for selected metabolites versus echo time for control (A), cisplatin (B), etoposide (C) and heat (D) treated cells.	235
Figure S2.2. Representative examples of bi-exponential T_2 fits of signal intensity for water versus echo time for control (A), cisplatin (B), etoposide (C) and heat (D) treated cells.	236
Figure S2.3. Representative examples of bi-exponential diffusion fits of signal intensity for selected metabolites versus b-value for control (A), cisplatin (B), etoposide (C) and heat (D) treated cells.	238
Figure S2.4. Representative examples of bi-exponential diffusion fits of signal intensity for water versus b-value for control (A), cisplatin (B), etoposide (C) and heat (D) treated cell	239
Figure S2.5. A biexponential diffusion fit for the $-\text{CH}_2$ signal at 1.3 ppm. The faster apparent diffusion component ($1.37 \cdot 10^{-8} \text{ m}^2/\text{s}$, corresponding to lactate and excluded from ADC calculations) ($b > 124 \text{ s} \cdot \text{mm}^{-2}$).	241
Figure S2.6. Correlation of LD size measured by fluorescence microscopy with diffusion coefficients measured by HRMAS ^1H NMR. ● 24 h and ▲ 48 h for four lipid signals.	242
Figure S3.1. PCA analysis of TAG and DAG species extracted from A) isolated LDs and B) organic fraction of cell extracts for control (green), cisplatin (red), and etoposide (blue) samples. The analysis was performed after total sum normalization and Pareto scaling; $n = 5$ for isolated LD samples and $n = 4$ for cell extracts.	243
Figure S3.2. Differentially expressed genes linked to lipid desaturases in control (green), cisplatin- (red) and etoposide-treated (blue) C2C12 myotubes. <i>Degs1-2</i> – sphingolipid desaturases, <i>Fads1-3</i> and <i>Scd1-2</i> – biosynthesis of unsaturated fatty acids. Mean fold changes in gene expressions were calculated relatively to the control group; error bars represent SEM of four independent cell samples. All changes are statistically significant (ANOVA: FDR-adjusted P-value < 0.05), except for <i>Degs1</i> control vs cisplatin.	281

List of Tables	Page
Table 1.1. A list of NMR spectral parameters most commonly used for interpreting NMR data.	32
Table 1.2. Common NMR experiments used in metabolomics.	34
Table 1.3. Example applications of MS-based metabolomics.	41
Table 1.4. Comparison of NMR spectroscopy and mass spectrometry.	42
Table 1.5. Selected online tools and databases facilitating metabolomic studies.	47
Table 1.6. Morphological and biochemical changes in cells during apoptosis.	47
Table 1.7. Potential metabolic biomarkers and metabolic mechanisms associated with apoptosis.	54
Table 1.8. Comparison of diffusion and T_2 relaxation times for cellular lipid microdomains.	59
Table 2.1. Fragmentation parameter for mass spectrometry analysis of choline compounds.	72
Table 3.1. Peak widths of TSP, lactate, and creatine at different spinning rates. The peak width values do not change significantly with spinning rates.	83
Table 3.2. Percentage change in metabolite signal intensities induced by a 3.5 h HRMAS 1H NMR experiment as compared with reference intensities recorded right after the intact cells were sealed in the rotor. The percentage was calculated for control, cisplatin-, and etoposide treated cells. The reference spectra and the 3.5 h spectra are significantly different in each group; the change is consistent for all groups.	88
Table 3.3. 1H chemical shifts and multiplet patterns of assigned metabolites from the C2C12 cell line based on solution-state and HRMAS 1H NMR spectroscopy. The annotation number corresponds to those shown in Figure 6. Multiplet patterns: s – singlet, bs – broad singlet, d – doublet, t – triplet.	95-96
Table 4.1. Metabolite profiling of apoptotic cells by solution-state (growth media and cell extract) and HRMAS (intact cells) 1H NMR spectroscopy. Two independent experiments for intact cells and growth media were performed (different doses of etoposide: 60 and 120 μM). Supporting data can be found in Appendix I . \uparrow and \downarrow indicate a significant increase or decrease in a fold change integral for cisplatin (red) and etoposide (blue) groups as compared to control; \leftrightarrow indicates non-significant changes, n/a – signal not present or could not be accurately measured.	123-124
Table 5.1. Comparison of T_2 relaxation times of selected metabolites and water for control and necrotic muscle cells. Student t-test: * $p < 0.05$.	147
Table 5.2. Apparent diffusion coefficients [$\mu m^2/s$] for full fat and semi-skimmed milk. Student t-test comparison between respective resonances of full fat and semi-skimmed milk within one method, * $p < 0.05$.	148
Table 5.3. Fold change apparent diffusion coefficient as compared to respective controls ($ADC_{treatment}/ADC_{control}$) for selected metabolites, ANOVA with post hoc Fisher's test: * FDR-adjusted $p < 0.05$. intra. – intracellular.	153

Table 5.4. The viscosity (ν) of cytoplasm calculated from HRMAS ^1H NMR-based diffusion data and fluorescence microscopy for cells at 24 h and 48 h incubation time points. For comparison, literature values are included, measured using T_1 relaxation times of ^{19}F -labelled proteins in cells by ^{19}F NMR spectroscopy.	156
Table 5.5. Comparison of T_2 relaxation times of selected metabolites and water for mouse muscle cells reported in this study, for endometrial cells reported by Griffin et al, and for skeletal muscle tissue reported by Kasturi et al; n/r – not reported.	158
Table 5.6. Mean ADCs of selected lipid signals for untreated muscle cells and endometrial cells and rat glioma tissue, \pm values refer to standard error, * value corresponds to restricted diffusion.	160
Table 6.1. List of pathways linked to lipid metabolism regulated by cisplatin or etoposide in C2C12 cells. Legend: $\uparrow\uparrow$ - significantly upregulated, \uparrow - non-significantly upregulated, \downarrow - non-significantly downregulated, $\downarrow\downarrow$ - significantly downregulated. Pathways ID corresponds to Reactome pathway database.	178-180
Table 6.2. List of lipid transporters differentially expressed in apoptotic cells (Figure 6.9). Upregulated transporters after cisplatin and etoposide treatment are shown in red and blue, respectively. Cr – control, cis – cisplatin, eto – etoposide. Source: GeneCards (www.genecards.org).	184
Table S1.1. Fold change integral for selected metabolites in aqueous fraction of cell extracts: control and heat-treated cells. * $p < 0.05$, ** $p < 0.01$, *** $p < 0.001$ for control vs treatment, FDR adjusted.	225
Table S1.2. Fold change integral for selected metabolites in growth media. * $p < 0.05$, ** $p < 0.01$, *** $p < 0.001$ for control vs treatment; # $p < 0.05$, for cisplatin vs etoposide, FDR adjusted.	228
Table S1.3. Fold change integral for selected metabolites in aqueous fraction of cell extracts. * $p < 0.05$, ** $p < 0.01$, *** $p < 0.001$ for control vs treatment; # $p < 0.05$, for cisplatin vs etoposide, FDR adjusted.	234
Table S3.1. TAG and DAGs species annotated from cell extracts treated with cisplatin and etoposide for 48h. Fold changes are reported relative to the control untreated samples. Included only lipid species with even number of carbon that formed NH_4 adducts. ANOVA: FRD-adjusted p -values, $n \geq 3$. Fisher's least significant difference (LSD) was used for ad hoc pairwise comparisons of the treatment groups. N/S – not significant; Lipid class (number of double bonds/number of carbons)molecular weight_retention time [s]; cr – control, cis – cisplatin, eto – etoposide.	244-246
Table S3.2. TAG and DAG species annotated from isolated lipid droplet from cells treated with cisplatin and etoposide for 48 h. Fold changes are reported relative to the control untreated samples. Included only lipid species with even number of carbon that formed NH_4 adducts. ANOVA: FRD-adjusted p -values, $n \geq 3$. Fisher's least significant difference (LSD) was used for ad hoc pairwise comparisons of the treatment groups. N/S – not significant; Lipid class (Number of carbons:number of double bonds)molecular weight_retention time [s]; cr – control, cis – cisplatin, eto- etoposide.	247-250
Table S3.3. Normalised read count for differentially expressed genes related to programmed cell death in the cells treated with cisplatin or etoposide versus controls. SEM represent biological variance ($n = 4$). ANOVA: FRD-adjusted p -values; Fisher's least significant difference (LSD)	

<p>was used for ad hoc pairwise comparisons of the treatment groups. Green and orange backgrounds indicate upregulation and downregulation, respectively, compared to the controls; cr – control, cis – cisplatin, eto- etoposide.</p>	250-256
<p>Table S3.4. Normalised read count for differentially expressed genes related to lipid metabolism in the cells treated with cisplatin or etoposide versus controls. SEM represent biological variance ($n = 4$). ANOVA: FDR-adjusted p-values; Fisher's least significant difference (LSD) was used for ad hoc pairwise comparisons of the treatment groups. Green and orange backgrounds indicate upregulation and downregulation, respectively, compared to the controls; cr – control, cis – cisplatin, eto- etoposide.</p>	257-271
<p>Table S3.5. List of cell death and cell cycle pathways significantly regulated by cisplatin treatment in C2C12. Legend: ↑ - significantly upregulated, ↓ - significantly downregulated; entities FDR – probability that the overlap between the query and the pathway has occurred by chance corrected for multiple comparison. Pathways ID corresponds to Reactome pathway database.</p>	272-274
<p>Table S3.6. List of cell death and cell cycle pathways significantly regulated by etoposide treatment in C2C12. Legend: ↑ - significantly upregulated, ↓ - significantly downregulated; entities FDR – probability that the overlap between the query and the pathway has occurred by chance corrected for multiple comparison. Pathways ID corresponds to Reactome pathway database.</p>	274-278
<p>Table S3.7. Differentially expressed genes linked to lipid droplets, endosomes, lysosomes, and peroxisomes. ANOVA: FDR-adjusted p-values, post hoc Fisher's test: cr – control, cis – cisplatin, eto- etoposide, Source: GeneCards (www.genecards.org).</p>	279-280

Abbreviations

ABC – ATP binding cassette

ADC – apparent diffusion coefficients

ADP – adenosine diphosphate

ANOVA – one-way analysis of variance

ATP – adenosine triphosphate

BMRB – Biological Magnetic Resonance Data Bank

BODIPY – boron-dipyrromethene

cDNA – complementary DNA

CDP-choline – cytidine diphosphate-choline

COSY – correlation spectroscopy

CPMG – Carr–Purcell– Meiboom–Gill

CVD – cardiovascular diseases

DAG – diacylglycerol

DESI – desorption electrospray ionisation

DG – diacylglycerol

DI – direct infusion

DIMS - direct infusion mass spectrometry

DMA – dimethylamine

DMEM – Dulbecco's modified Eagle's medium

DMF – N,N-dimethylformamide

DMSO – dimethylsulfoxide

DOSY – diffusion ordered spectroscopy

DOU – degree of unsaturation

EI – electron impact ionisation

ER – endoplasmic reticulum

ESI – electrospray ionisation

EX – eoxins

FA – fatty acids

FBS – fetal bovine serum

FDR – false discovery rate

FID – free induction decay

FPKM – fragments per kilobase of exon model per million mapped reads

FTICR – Fourier transform ion cyclotron resonance

FTMS – Fourier transform mass spectrometer
GC – gas chromatography
GPC – glycerophosphocholine
HDL – high-density lipoprotein
HMBC – heteronuclear multiple bond correlation
HMDB – Human Metabolome Database
HR – high-resolution
HRMAS – high-resolution magic angle spinning
HSQC – heteronuclear single quantum coherence
IBD – inflammatory bowel disease
IM – ion mobility
JRES – J-resolved spectroscopy
LC – liquid chromatography
LD – lipid droplet
LESA-MS – liquid extraction surface analysis mass spectrometry
LR – lipid raft
LT – leukotrienes
MA – major ampullate
MALDI MS – matrix-assisted laser desorption ionization mass spectrometry
MPT – mitochondrial permeability transition
MRI – magnetic resonance imaging
mRNA – messenger RNA
MRS – magnetic resonance spectroscopy
MS – mass spectrometry
MS/MS – tandem mass spectrometry
MTT – 3-(4,5-dimethylthiazol-2-yl)-2,5-diphenyl-2H-tetrazolium bromide
MUFA – monounsaturated fatty acids
MWA – microwave ablation
NCI –negative chemical ionisation,
NF – necrosis factor
NGS – Next Generation Sequencing
NMR – nuclear magnetic resonance
NOESY – nuclear Overhauser effect spectroscopy
NSCLC – non-small cell lung cancer patients
PA – Pseudomonas aeruginosa
PBS – phosphate buffered saline
PC – principal components

PCA – principal component analysis
PCD – programmed cell death
Pcholine – phosphocholine
PCI – positive chemical ionisation
PCR – polymerase chain reaction
PIP – phosphatidylinositol phosphate
PL – phospholipids
PLS-DA – partial least squares-discriminant analysis
PTC – phosphatidylcholine
PUFA – polyunsaturated fatty acids.
QqQ – triple quadrupole
qRT-PCR – Quantitative reverse transcription-polymerase chain reaction
QTOF – quadrupole time-of-flight
RNA-Seq – RNA Sequencing
S/N – signal-to-noise ratio
SB – spinning sideband
SE – Salmonella enterica
SEM – standard error of the mean
SFA – saturated fatty acids
SL – sphingolipids
SPM – specialized pro-resolving mediators
TAG – triacylglycerol
TEM – transmission electron microscopic
TG - triacylglycerol
TMS – tetramethylsilane
TOCSY – total correlated spectroscopy
TOF – time-of-flight
TSP – trimethylsilylpropanoic acid
TUNEL – terminal dUTP nick end-labeling
VIP – Variable's Importance in the Projection
VLCFA – Very long chain fatty acids

Chapter 1. Introduction

1.1. System biology and omics

A living organism is a complex system comprised of interconnected networks of genes, proteins, and metabolites. Life depends on impeccable operation and integration of these networks. In a disease state, one or more processes in networks fail to deliver an expected biological outcome. Understanding what part of the system does not function correctly is the first step to developing suitable pharmaceutical solutions and preventative interventions to address modern diseases.

One major aspect of systems biology is a systematic study of interactions between genome, transcriptome, proteome, and metabolome. The phrase “omics” is a collective term for areas of studies in biology ending with ‘-omics’ including genomics, transcriptomics, proteomics, metabolomics. Each omic discipline on its own provides valuable information on the regulation of life. However, the need for a more comprehensive understanding of the cellular processes and their regulation in health and disease drives a multi-omic approach.¹

Genetic changes predispose the biological system to specific behaviour and pass the information via mRNA to proteins for execution. The metabolome is a chemical signature of the current biological status. It can represent immediate perturbations of metabolic reactions or longer time-scale perturbation driven by changes in proteome, transcriptome, and genome. Even though metabolomics is a younger discipline than genomics and proteomics, it holds great promise to become a dominant approach in system biology, linking the gap between genotype and phenotype.²⁻⁴

1.2. Metabolomics

The term metabolome was first introduced by Oliver and colleagues and was used to describe a method that allows ‘the measurement of the change in the relative concentrations of

metabolites as the result of the deletion or overexpression of a gene'.⁵ Following on from that publication, Fiehn defined metabolomics as 'a comprehensive and quantitative analysis of all metabolites'.⁶ Nicholson and colleagues introduced a related term, metabonomics, defined as 'the quantitative measurement of the time-related multi-parametric metabolic response of living systems to pathophysiological stimuli or genetic modification'.⁷

The two terms may seem interchangeable, with some groups favouring one over the other. However, they represent different approaches to metabolic profiling – metabolomics is the systematic study of metabolites in a living system and their interactions, whereas metabonomics is the quantitative measurement of changes across the metabolome, with respect to time, due to an intervention. Both approaches aim to facilitate understanding of metabolic pathways and their perturbations induced by genetic and environmental factors. Throughout this thesis, I have used metabolomics to describe changes in metabolite concentrations induced by drug treatments.

The metabolome comprises structurally and functionally diverse chemical species such as sugars, lipids, nucleotides, and amino acids. The total number of metabolites is regularly revised and validated (**Figure 1.1**). The Human Metabolome Database (HMDB) Version 4.0 published in 2018 contained 114,100 metabolite entries, including 81,396 expected metabolites and 9,917 predicted metabolites.⁸ Since the launch of HMDB 4.0 in 2018, 84 new metabolites have been added to the database (<https://hmdb.ca>, March 2020). Metabolite concentrations within a biological sample have a dynamic nature. Abundant metabolites dominate the metabolome with molar concentration above 1 μM , whereas the concentration of relatively rare metabolites lies below 1 nM.

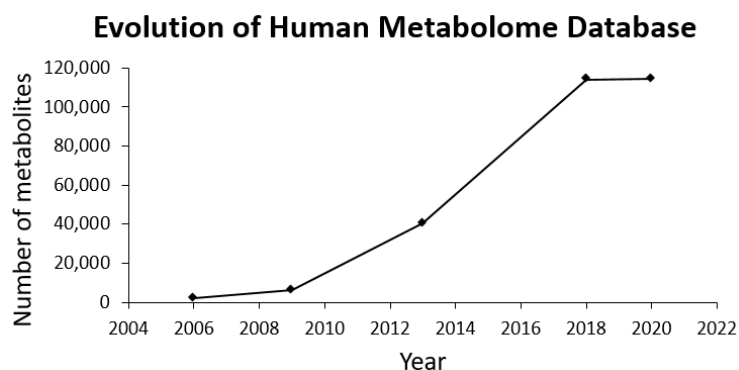


Figure 1.1. Growth in human metabolomics. The number of human metabolites curated by HMDB in 2006-2020 (<https://hmdb.ca>, March 2020).

1.3. Approaches in metabolomics

There are two main approaches for performing metabolomics: targeted and untargeted (**Figure 1.2**). The choice of the metabolic approach depends on the study objectives. Untargeted global metabolomics captures and quantifies all detectable metabolites in a sample, including unknown/novel metabolites. It provides broad coverage of the metabolome; allows pattern identification and classification of phenotypes; and generates a hypothesis. Examples of untargeted approaches include metabolic profiling (putative metabolite identification and semi quantification), fingerprinting (snapshot of the endometabolome), and footprinting (snapshot of the exometabolome).⁹⁻¹¹

In contrast, targeted metabolomics measures specific metabolites. It aims to test and validate the hypothesis from an untargeted analysis. It has a greater quantitative power but requires internal standards, specific experimental procedures, and analytical parameters for sample preparation and analysis.

In some cases, initial untargeted metabolic screening is followed by targeted metabolomics for systematic and comprehensive characterisation of biomarkers. The combined approach increases reliability in the identified biomarkers, which is vital for clinical diagnostics.¹²

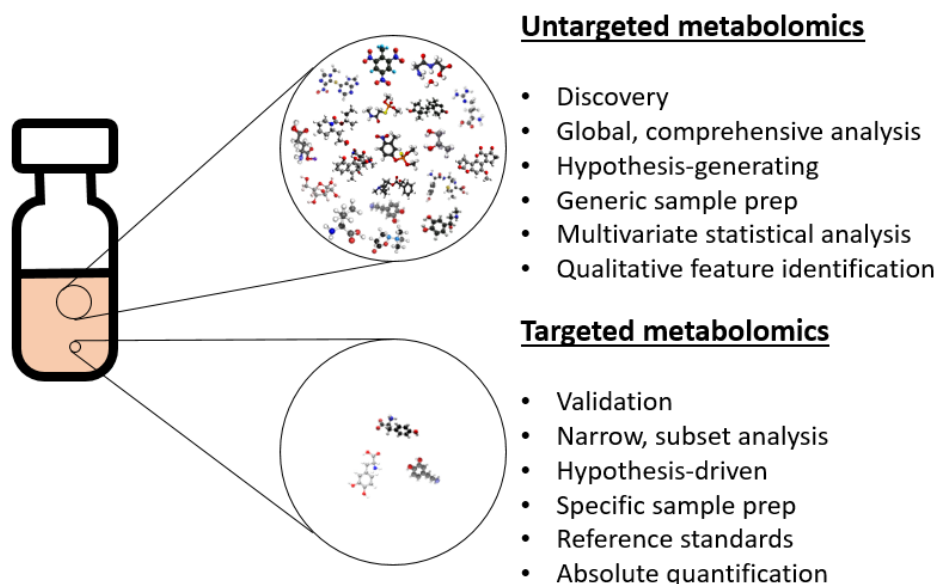


Figure 1.2. Two approaches for performing metabolomics: targeted and untargeted.

1.4. Analytical methods in metabolomics

It is not a trivial task to collect and analyse complex metabolomic data; it requires sophisticated analytical and statistical techniques to measure a fraction of the metabolome. Several excellent books and scientific reviews are available describing the methodology, challenges, and applications of metabolomics in biological research.¹³⁻¹⁷

There are broadly speaking two main analytical techniques used in metabolomics: mass spectrometry (MS) and nuclear magnetic resonance (NMR) spectroscopy. They both have advantages and limitations and the choice of technique depends on the nature of the biological question one is trying to answer.¹⁸⁻²⁰ In some cases, the two techniques are used as complementary methods.^{21,22}

1.4.1. Nuclear magnetic resonance spectroscopy

NMR spectroscopy is an analytical technique based on measuring the nuclear magnetic moment of certain nuclei first described by Rabi.²³ All nuclei with an odd number of protons and neutrons have a characteristic spin, which is associated with a magnetic moment. For spin one-half particles, a spin can exist in two states: parallel or anti-parallel. In the presence of an external magnetic field (B_0), the two spin states have different energy and hence they are unequally populated by spins.²⁴ The lower energy state aligned with B_0 has greater population of spins than the higher energy state opposed to B_0 . In the absence of B_0 the two states have the same energy (**Figure 1.3**). The energy difference ΔE between the two spin states depends on B_0 and the type of nucleus and is very small. Consequently, only a small difference in spin populations exist which hinders NMR sensitivity.

During a ^1H NMR experiment, a sample is placed in the constant magnetic field and excited with radiofrequency energy corresponding to ΔE of a specific set of nuclei. The irradiation leads to an increase in the population of higher-energy-state protons. The protons return to their ground state in precessional motion at a characteristic frequency known as the Larmor frequency.²³ The Larmor frequency is unique to each nucleus as it depends on the magnetic field that the nucleus experiences and the gyromagnetic ratio (ratio of the magnetic momentum of a particle to its angular momentum). The NMR signal is recorded as a free induction decay (FID) and Fourier-transformed into a spectrum, which is a plot of the radio frequency (usually represented as a relative chemical shift scale) against resonance intensity.

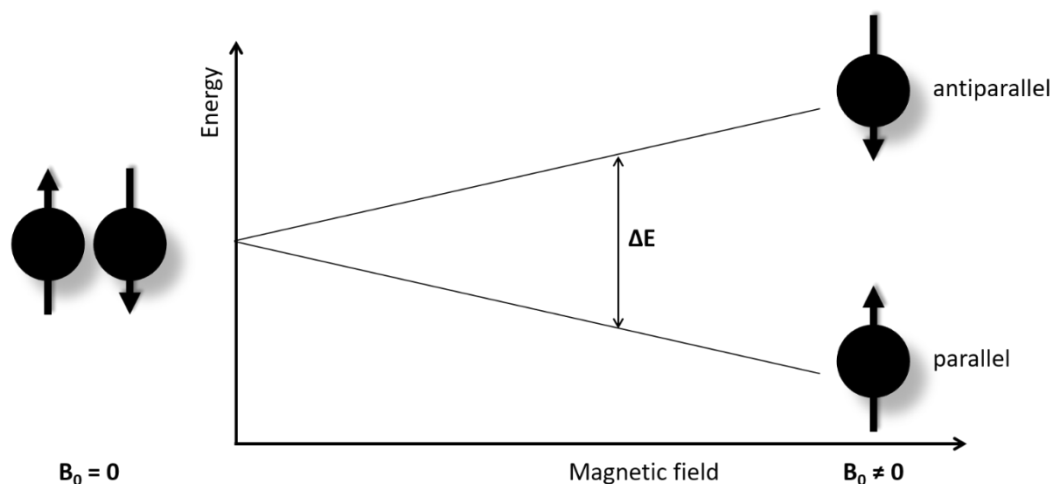


Figure 1.3. Splitting of nuclei spin energies in an external magnetic field.

In ^1H NMR spectroscopy, the integral area of a resonance is proportional to the number of protons which that resonance represents. Chemical shift, which is reported relative to a standard, describes the dependence of the resonance frequency on the environment of a nucleus i.e., local electron distribution and atom electronegativity. Nuclei experiencing the same magnetic environment (i. e. have the same NMR properties) are called magnetically equivalent. Magnetic interactions between magnetically non-equivalent nuclei which are connected via three or less bonds are called J-couplings. For first order spectra, multiplicity is the consequence of J-coupling.^a For example, in $\text{H}_a\text{C}-\text{CH}_b$ fragment, the coupling between H_a and H_b leads to split resonances of the protons into two equivalent components separated by J-constant. This is because H_a aligns with the magnetic field in slightly more than half of the molecules, while remaining molecules have H_a aligned against the magnetic field. Hence, in half of the molecules, H_b is slightly shielded and in the other half, it is slightly deshielded. This effect is reciprocal and the multiplicity depends on number of neighbouring protons. **Table 1.1** summarises the four basic NMR spectral features and provides metabolomics-specific examples of how they are interpreted.

The principles behind time domain NMR spectroscopy for measuring diffusion and T_2 relaxation are described in **Chapter 5**.

^aThe "first order" approximation assumes that, for simple coupled systems, the difference between the Larmor frequencies of the coupled nuclei is large compared to the coupling constant between them ($\Delta\nu \gg J$). When the frequency difference approaches the coupling constant, the spectra are said to be "second order" ($\Delta\nu \sim J$), and the simple rules presented for first order spectra do not necessarily apply to second order spectra.

Table 1.1. A list of NMR spectral parameters most commonly used for interpreting NMR data.

Parameter	Definition	Example
Chemical shift	<ul style="list-style-type: none">- position on the ppm scale where the peak occurs;- depends on a type of nuclei and its chemical environment	Phosphocreatine, inorganic phosphate and ATP show different chemical shifts on ^{31}P NMR spectra ²⁵
Integral	<ul style="list-style-type: none">- area of the peak;- proportional to the number of nuclei that the peak represents	^1H NMR measurements of glucose, triglycerides and HDL in plasma correlate with clinical chemistry measurements of these species ²⁶
Multiplicity	<ul style="list-style-type: none">- a splitting pattern of the peak- the signal is split into lines depending on the number of equivalent nuclei in the proximity	Multiplicity analysis by spin-echo ^1H NMR spectroscopy identifies penicillin metabolites ²⁷
J-couplings	<ul style="list-style-type: none">- the spacing between the lines in the coupling patterns- depends on conformation of protons	J-coupling database for semi-automated metabolite identification ²⁸

1.4.2. NMR-based metabolomics

The versatile nature of NMR spectroscopy makes it a useful tool in metabolomics; it can be used for metabolite identification and quantification, studies of molecular motion, and the study of compartmentation. An NMR spectrum provides information on chemical shifts, multiplicities, J-couplings, and integrals that translate into information about neighbouring atoms, connectivity, relative orientation, and intra- and intermolecular interactions. The NMR integrals are proportional to the number of protons in each magnetic environment in the molecule thus allowing accurate quantification of relative metabolite concentrations. Absolute concentrations can also be measured with the use of an internal standard of known concentration or standard addition of the chemical species of interest.

NMR analysis has been done on a variety of biological samples including body fluids²⁹, cell and tissue extracts^{30,31}, intact cells³² and whole tissue³³, plants³⁴ and food³⁵, providing useful and often unique information about the biological system. It is a non-destructive, highly reproducible, and highly quantitative method that can be adapted to high throughput analysis (>100 samples/day) by using a robotic sampler and automatic data acquisition.

The main limitation of NMR spectroscopy is its sensitivity (nmol - μ mol). The analysis of low signal-to-noise ratio (S/N) samples may need a significantly higher number of scans and can take a long time. The amount of sample required for an NMR analysis depends on the type of NMR experiment needed, the equipment available, and sample packing methods. For example, a simple 1D ^1H NMR experiment is more sensitive than ^{13}C or ^{15}N NMR experiments because of the high natural abundance of protons and their larger gyromagnetic ratio. A modern high-field spectrometer with a cryoprobe, which reduces thermal noise in electronic components, produces higher quality spectra than a low-field spectrometer with a standard probe.³⁶ Sample packing can be optimised for precious low-volume samples, i.e. the use of 3 mm tubes or capillary inserts allows the preparation of more concentrated samples. Advances in pulse sequences, detectors, data processing and higher static magnetic field strengths also contribute to improving NMR sensitivity.^{37,38}

Biological samples are a complex mixture of compounds that generate NMR spectra with overlapping signals, making it difficult to unambiguously annotate and quantitate metabolites. Two-dimensional NMR spectra can increase signal dispersion and help extract additional information. Similarly, diffusion- and T_2 -edited experiments can reduce the NMR-visibility of unwanted signals, simplifying the data. The number of metabolites that can be unambiguously detected and identified depends on spectral resolution and metabolite concentration and is usually less than 200 metabolites.³⁹⁻⁴¹ By contrast, mass spectrometry techniques can detect thousands of different metabolites and identify a few hundred.⁴¹⁻⁴³ The most common NMR techniques used in metabolomics research and diagnostics are highlighted in **Table 1.2**. NMR techniques that make use of less abundant nuclei, such as ^{15}N , ^{31}P , ^{19}F also exist.⁴⁴⁻⁴⁶ Several comprehensive reviews on NMR methods in metabolomics have been published, including 3D NMR experiments.^{31,40,47-60}

1.4.3. High-resolution magic angle spinning NMR spectroscopy

High-resolution magic angle spinning (HRMAS) is a technique used for analysing intact biological tissues or cell samples. Spectra of gel-like heterogeneous samples suffer from line broadening due to dipolar interactions (two dipolar molecules interacting with each other through space create dipolar field) and magnetic susceptibility differences (differences in

Table 1.2. Common NMR experiments used in metabolomics.

NMR experiment	Description	Example application
1D proton (^1H)	Most widely used in metabolomics. The spectrum represents a unique metabolic fingerprint which can be subjected to multivariate analysis. ^1H resonances can also be matched to expected patterns of known metabolites. Complex and many overlapping peaks.	^1H NMR spectra of serum samples revealed the differences between non-small cell lung cancer patients (NSCLC), microwave ablation (MWA) treated patients, and healthy controls. Several potential serum biomarkers of NSCLC were identified. ⁶¹
1D carbon (^{13}C)	Unique metabolic fingerprints for carbon. ^{13}C spectra are better resolved than ^1H spectra but not very sensitive (low natural abundance).	^{13}C NMR used to investigate the role of the ethylmalonyl-CoA pathway in glyoxylate generation in bacteria during growth on methanol. ⁶²
^1H - ^1H 2D J-Resolved Spectroscopy (JRES)	Helps assign all coupling constants and identify the coupled spin systems. The spectrum shows the chemical shift along one axis and the J-constant of each signal along the other axis.	The incorporation of multiplicity information can be used for metabolite identification in biofluids. JRES experiments increased spectral dispersion of glucose resonances. ⁶³
^1H - ^1H Correlation Spectroscopy (COSY)	Shows the correlation between protons which are coupled to each other through 2 or 3 bonds (long-range coupling can also be observed). Disperses complex signals and helps assign metabolites. It can be used for quantitation.	COSY was used to study metabolic changes in dystrophic cardiac tissue. It identified the contribution of lactate to the increased CH_2 -lipid signal at 1.3 ppm. ⁶⁴
^1H - ^1H Total Correlated Spectroscopy (TOCSY)	Records through-bond correlations between all protons in an unbroken chain of coupled spins in the same molecules the same spin system. It can be used for quantitation. Selective TOCSY experiments enable spectra elucidation of complex metabolic mixtures.	TOCSY facilitated the identification of metabolites in cell lysate from <i>E. coli</i> . This approach identified a greater number of compounds as compared with 1D ^1H NMR experiments. ⁶⁵
^1H - ^{13}C Heteronuclear Single Quantum Coherence (HSQC)	Determines proton-carbon single bond correlations. Disperses complex signals and helps assign metabolites. ^1H - ^{15}N HSQC experiments are also used in metabolomics.	^1H - ^{13}C HSQC was used for identifying 23 metabolites in post-prostatic palpation urine samples. ⁶⁶ ^1H - ^{13}C HMQC of blood plasma allowed direct detection of cholesterol and choline species bound in high-density lipoprotein. ⁶⁷
^1H - ^{13}C Heteronuclear Multiple Bond Correlation (HMBC)	Gives correlations between proton and carbon separated by 2,3 or sometimes 4 bonds. Disperse complex signals and helps assign metabolise. ^1H - ^{15}N HMBC experiments are also used in metabolomics.	^1H - ^{13}C HMBC spectra of urine samples from cattle treated with anabolic steroids had greater discriminatory power than 1D ^1H NMR experiments. ⁶⁸
Relaxation-edited spectra	Simplify spectra and reduce unwanted signals from bigger molecules that obstruct signals from small metabolites. It is based on different spin-spin relaxation times (T_2) which depend on molecular characteristics (see Chapter 5). It can be used for molecular dynamics studies.	T_2 -edited spectra of human plasma allowed for attenuation of the broad resonances from proteins and lipoproteins. Several peaks, which were obscured in the standard ^1H spectrum, became visible following relaxation editing. This method can be also applied to 2D experiments. ⁶⁹
Diffusion ordered spectroscopy (DOSY)	Measures diffusion of metabolites in cells or tissue. It can give information about the surrounding microenvironment (see Chapter 5). It is also used for diffusion-edited spectra.	Two distinct environments of water were identified in endometrial cells: slow-diffusing intracellular water and fast-diffusing extracellular water. ⁷⁰

magnetic properties) within the sample. These interactions have some dependence on the orientation of the molecules (anisotropy). Normally, in solution-state NMR, they are averaged out by rapid tumbling and translational diffusion of compounds. Analytes in non-liquid samples have restricted molecular motion and consequently, instead of sharp and well-defined NMR resonances, they give rise to broader resonances and a higher degree of signal overlap. Andrew and Lowe first showed that spinning the samples at 57.4° (magic angle) to the magnetic field reduces line broadening caused by dipolar interaction and anisotropic effects in solid samples.^{71,72} Three decades later, Forbes and colleagues applied the principle of magic-angle spinning to improve the spectral resolution of liquid crystalline lipid bilayers.⁷³ Since then, it has been broadly used for metabolic studies of tissue and cells.^{64,74–76}

The sample preparation for HRMAS NMR experiments is quick and straightforward. There is no need for tedious extraction procedures. A piece of tissue (20 mg) or a small volume cell pellet (10^5 - 10^6 cells per sample) can be directly placed in a rotor and analysed instantly. The sample temperature can be adjusted according to experimental needs, providing that the probe is equipped with a heater and/or a chilling unit.

The pulse sequences used for HRMAS NMR experiments are the same as for solution-state NMR experiments, except the sample is spun at the magic angle. They include gradient-enhanced experiments, variable-temperature experiments, experiments with different solvent suppression methods, and 2D homo- and hetero-nuclear experiments.^{77,78} HRMAS NMR spectroscopy is a versatile technique that has been used for structural and dynamic studies as well as metabolic profiling. Selected examples of HRMAS NMR applications are highlighted in **Box 1.1**.

BOX 1.1. Selected examples of HRMAS NMR applications

Application 1. Structural analysis of protein secondary conformation.

Jenkins and colleagues used HRMAS ^1H NMR spectroscopy to investigate how spiders store and convert the protein-rich fluid stored in the major ampullate (MA) gland to an insoluble silk fibre at the spinneret.⁷⁹ They used 1D and 2D HRMAS ^1H NMR experiments to characterise the secondary structure of proteins in the MA gland and compared it with the secondary structure of the silk fibre obtained from solid-state MAS ^1H NMR spectroscopy. The results showed that the proteins in the gland were in a random coil state whereas the silk fibre showed strong evidence for β -sheet conformation. The finding suggested that there is no protein folding occurring within the MA gland prior to silk fibre formation.

Application 2. Metabolic profiling of intact cells.

Griffin and colleagues compared HRMAS ^1H NMR spectral profiles of different brain cell lines to understand the metabolic contribution of individual cell type to brain tissue.⁸⁰ Pattern recognition analysis readily distinguished the NMR spectra of the three cell types and identified metabolites with significant discriminatory power, namely lipid resonances, choline-containing compounds, and glycine. Furthermore, they reported that the discriminatory metabolites detected by HRMAS ^1H NMR are not the same as the ones detected in the brain by MRS spectroscopy *in vivo*. In the MRS experiments, the information about lipid changes was lost. They proposed to use HRMAS ^1H NMR spectroscopy as a bridging tool between the non-invasive low-resolution MRS spectroscopy *in vivo*, and solution-state ^1H NMR spectroscopy of tissue extracts.

Application 3. Structural study of membrane association.

Huster and colleagues used HRMAS ^1H NMR to study the location of a lipid-modified, membrane-bound peptide that mimicked the human N-Ras protein (a key oncogene).⁸¹ From 2D NOESY spectra, they identified the contact points of peptide residues with the lipid bilayer. Moreover, all of the amide protons were able to undergo exchange with the solvent, suggesting the location of the peptide backbone in the water-accessible part of the membrane. Based on HRMAS ^1H NMR data, they proposed a Ras–membrane binding mechanism.

Application 4. Metabolic identification, metabolite mobility and intermolecular interactions.

Garrod and colleagues compared metabolic profiles of intact tissue samples obtained from different regions of normal rat kidney: outer cortex, inner cortex, and papilla.⁷⁵ They used a combination of 1D and 2D HRMAS ^1H NMR experiments to identify 26 metabolites, and discriminate between cortex and papilla. The comparison of the HRMAS and solution-state ^1H NMR spectra of tissue extract suggested that lactate and citrate were partially bound to macromolecules in the whole tissue since they were not visible in the HRMAS ^1H NMR spectra. Moreover, increased spinning speed influenced lipid resonances. In spectra acquired at 4.2 kHz, the lipid signal intensities were very low, and they significantly increased for the spectra acquired at 12 kHz. They proposed two explanations: 1) at the higher spinning speed, lipid signals were enriched with membrane-bound lipids that were not visible at the lower spinning speed; or 2) the higher spinning rate induced frictional heating and higher temperature contributed to lipid signal peak sharpening.

Application 5. Compartmentation and local environment

Bollard and colleagues studied subcellular compartmentation of metabolites in cardiac tissue.⁸² They compared HRMAS ^1H NMR spectral profiles of intact cardiac tissue and intact mitochondria with solution-state ^1H NMR spectral profiles of cardiac tissue extracts and mitochondrial extracts. The results showed that most of the aqueous metabolites from cardiac tissue extracts were also visible in intact tissue. However, several metabolites were visible in the mitochondria extract but not in the intact mitochondria. They proposed that some metabolites within mitochondria were present in a highly restricted environment and became NMR-visible only after extraction.

1.4.4. *In vivo* NMR spectroscopy

The principles of NMR can also be applied for *in vivo* studies. Magnetic resonance imaging (MRI) and magnetic resonance spectroscopy (MRS) are non-invasive techniques for medical diagnosis of internal tissues and organs. They can detect disorders such as stroke, tumours, kidney injuries, pulmonary fibrosis, spinal cord injuries and multiple sclerosis.^{83–89} Correlating MRI data with NMR-based metabolomics has contributed to our understanding of disease pathogenesis and therapeutic efficacy.^{76,90–93}

In vivo MRS is particularly useful for metabolomic studies as it allows the identification and quantification of metabolites.^{94–96} The most studied metabolites are creatine, choline, N-acetyl aspartate, myo-inositol, glutamine and glutamate, and lactate, particularly in the brain.^{97,98} The concentration of these metabolites can be calculated as a ratio (usually metabolite/creatine ratio) or an absolute value based on an internal or external standard.

MRI and MRS techniques have been used for *ex vivo* studies.⁹⁹ *Ex vivo* experiments on fixed samples permit motion-free long acquisition times that reduce artefacts and increase sensitivity. Since NMR is a non-destructive technique, the samples can be subsequently used for conventional histology, biochemical assays, or metabolic profiling of tissue extracts.^{94,100}

1.4.5. *Combining NMR techniques in metabolomics*

Work done by Lehtimäki and colleagues is a good example of how combining different NMR techniques can be used for probing biological processes.¹⁰⁰ They studied the metabolic effects of ganciclovir-thymidine kinase gene therapy (a therapy that induces a programmed cell death - PCD) in BT4C rat gliomas. They performed comprehensive metabolic profiling using MRI and MRS for *in vivo* samples, HRMAS ¹H NMR spectroscopy for *ex vivo* sample analysis and solution-state ¹H NMR spectroscopy for tumour tissue extracts.

Firstly, they confirmed that the gene therapy induced programmed cell death by showing tumour shrinkage by MRI, MRS and histology images. They then reported a significant decrease in small metabolites such as myo-inositol/glycine, taurine, and creatine; an increase in unsaturated and saturated lipids; and no change in choline-containing compounds on *in vivo* MRS spectra following the treatment.

Ex vivo HRMAS ¹H NMR did not detect any changes in aqueous metabolites with the treatment. However, the technique was able to distinguish between control and tumour samples. The decrease in the concentration of small metabolites was associated with a decrease in tumour cell count. Thus, they concluded these metabolites are poor indicators of the progression of PCD.

Finally, solution-state ¹H NMR spectroscopy showed a decrease in glycine, creatine, and alanine with the treatment, and increased in myo-inositol, and no change in choline-containing compounds. The comparison of *in vivo* NMR with NMR on tumour extract showed that there were some discrepancies in the changes of metabolic profiles during the gene therapy. For example, myo-inositol and glutamate/glutamine showed different trends against tumour cell count for *in vivo* NMR and tumour extracts NMR. It was attributed to different sample preparation and NMR experimental parameters.

By using different NMR approaches, Lehtimäki and colleagues validated saturated and unsaturated lipids as biomarkers of PCD and demonstrated that non-lipid metabolites could not reliably predict the progression of PCD.

1.4.6. Mass spectrometry

Mass spectrometry is a powerful analytical technique that provides qualitative and quantitative data on nanomolar to attomolar amounts of analyte.¹⁰¹ It has become invaluable across a broad range of fields and applications because of its high sensitivity, high mass accuracy, and to some degree, structural information.

Identification of metabolites by MS can be performed on many biological samples including plasma, serum, tissue, saliva, urine, cell pellets, and cell media.^{102–105} Most cases require extraction of metabolites from a complex biological matrix. Different extraction protocols exist depending on the sample type, physicochemical properties of metabolites, metabolomics approach, and MS technique;^{106–109} i.e. the protocol for extracting tissue lipids¹¹⁰ is different from the protocol for extracting cellular thiols.¹¹¹ Volatile compound extraction is challenging and often includes derivatization steps.^{112–114} Samples of intact tissue or cells can be analysed without prior extraction but they require specialised MS instrumentation such as matrix-assisted laser desorption ionization mass spectrometry (MALDI MS),¹¹⁵ liquid extraction surface analysis mass spectrometry (LESA-MS)¹⁰¹ or secondary ion mass spectrometry

(SIMS).¹¹⁶ Special care needs to be taken during any kind of sample handling as it may cause metabolite degradation, loss, or contamination.

The main processes that take place in a mass spectrometer are ion generation (ionisation), separation according to mass-to-charge ratio and detection (**Figure 1.4**).

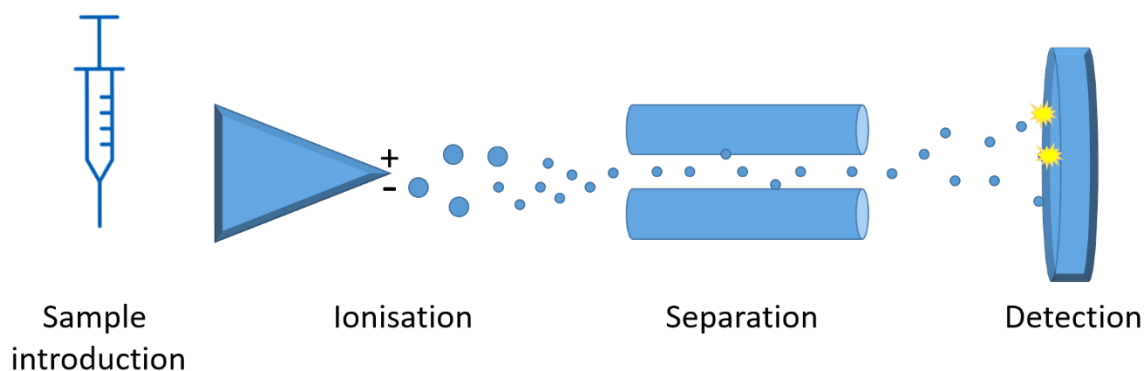


Figure 1.4. Schematic of basic mass spectrometer.

Liquid or gaseous samples which are introduced to the mass spectrometer are vaporized and ionized by the ion source (e.g., electrospray ionization, atmospheric pressure chemical ionization).^{104,117,118} In positive ion mode, ionisation occurs mainly via protonation, and in the negative ion mode, it occurs via deprotonation. Ions are then directed to a mass analyser (e.g., orbitrap, quadrupoles, time-of-flight) that separates individual ions based on their mass-to-charge ratio (m/z).^{42,103,117,119} Separated ions arrive at the detector where the signal is multiplied and recorded.

A mixture of metabolites can be separated by chromatography. Two separation methods are commonly employed in metabolomics: liquid chromatography (LC) and gas chromatography (GC). Reversed-phase liquid chromatography on C-18 (octadecylsilane stationary phase) columns with particle sizes of 3–5 μm is used for the separation of medium polar and non-polar metabolites.¹²⁰ Gas chromatography is used for analysing volatile metabolites such as short-chain alcohols, acids, esters, and hydrocarbons.¹²⁰ These compounds are not inherently volatile and need to undergo derivatization to reduce their polarity and increase their volatility and thermal stability. This analytical step is often lengthy, tedious, and may lead to loss of metabolites. However, GC has many advantages including fast separation, high peak capacity, high selectivity and sensitivity, very good reproducibility of retention times, and robust quantitation.⁴³

Coupling chromatography to MS is attractive because chromatography can separate complex mixtures, which chemical composition needs to be well established. It also provides additional information about metabolites – retention times – that is useful in differentiating isobaric compounds according to their polarities.¹²¹ Even though retention time depends on a separation method, equipment used and matrix effects, and thus cannot be directly compared with other databases, it is still a useful parameter to identify different compound classes provided that standardised chromatographic methods are in place. Another advantage of interfacing chromatography with MS is reduced background noise, which results in improved detection limits and data quality.¹²²

For structural elucidation of metabolites or filtering specific compound classes, tandem mass spectrometry (MS/MS) can be used. This technique employs two or more mass analysers coupled together to obtain fragmentation patterns and/or second level ion separation. Selected ions derived from the first MS stage are fragmented and/or analysed by the second MS stage. Advanced mass spectrometers are capable of high-resolution and accurate mass measurements, which largely improve metabolite identification and give a high degree of structural confirmation. The two most common high-resolution (HR) MS techniques used in metabolomics are Fourier transform ion cyclotron resonance (FTICR) and Orbitrap MS¹²³. HRMS is an attractive method for targeted and quantitative analysis and for simultaneous quantitative and qualitative untargeted assays.¹²⁴

Relative and absolute quantification by MS techniques can be achieved with the use of internal or external standards. Those standards are isotope-labelled metabolites that are chemically similar to the analyte(s) of interest. They are used not only for absolute or relative quantitation but also for data normalization to account for sample processing errors, recovery efficiency, ion suppression effects, matrix effects, and batch effects. Moreover, unambiguous identification of unknown metabolites often includes the comparison of its retention time, mass, and fragmentation patterns with authentic standards. For relative quantitation, a mix of relevant standards is used, while for absolute quantitation, a single standard is needed to establish a calibration curve.

High-throughput and quantitative MS-based metabolomics has enabled significant advances in our knowledge of metabolites, their functions, and dynamics in complex biochemical pathways.^{20,42,43,117–119,122} **Table 1.3** highlights selected examples of MS-based metabolomics.

Table 1.3. Example applications of MS-based metabolomics.

Method	Description
GC – Electron ionisation /Chemical ionisation – Orbitrap	Misra and Olivier evaluated three ionisation modes: positive chemical ionisation (PCI), negative chemical ionisation (NCI), and electron impact ionisation (EI) for GC-MS-based metabolomics analysis using reference human plasma samples. The total number of metabolites detected with all three ionisation modes was 330 out of the expected 635. Only 58 metabolites were common to all three modes and each ionisation mode captured several unique metabolites: 81 (EI), 39 (PCI), 28 (NCI). Comparing the GC-MS results with the existing LC-MS metabolite libraries for the standard, human plasma showed 306 and 450 unique metabolites, respectively, and only a 10% overlap of the total expected metabolites. This demonstrated that different MS platforms capture different subsets of metabolites from the same samples, therefore these technologies were highly complementary for metabolomics studies. ²⁰
LC – Electrospray ionisation (ESI)– Quadrupole Time-of-flight (QTOF)	Benito and colleagues used reversed-phase LC QTOF MS to identify plasma biomarkers for chronic kidney disease in paediatric patients. The result showed a significant increase in glycine, citrulline, creatinine, asymmetric dimethylarginine, and symmetric dimethylarginine as compared to the healthy cohort. They confirmed the hypothesis of the arginine-creatine metabolic pathway being affected in patients with renal impairment. ¹²⁵
LC – ESI – Triple quadrupole (QQQ)	Magnusson and colleagues followed the Malmö Diet and Cancer cohort for 12 years to identify novel markers predicting cardiovascular disease (CVD) development. At the beginning of the study, there were no cases of CVD; by the end of the study, 253 individuals developed CVD. The results showed that elevated fasting plasma levels of isoleucine, tyrosine and phenylalanine could predict CVD events. ¹²⁶
LC – Ion mobility (IM) – Time-of-flight (TOF)	Murgia and colleagues investigated potential discriminatory lipids in patients with inflammatory bowel disease (IBD). By comparing the lipid profiles of IBD patients with healthy controls, they identified potential biomarkers of IBD, namely phosphatidylcholines, lysophosphatidylcholines, fatty acids, cholesteryl esters, and glycerophospholipids. In addition, they found a unique lipid profile for the two main forms of IBD: Crohn’s disease and ulcerative colitis. ¹²⁷
Direct infusion (DI) – ESI – Fourier-transform ion cyclotron resonance (FTICR)	Witting and colleagues used DI FTICR MS to investigate the <i>C. elegans</i> infection model. The metabolic signature of worms infected by <i>Pseudomonas aeruginosa</i> (PA) strain and <i>Salmonella enterica</i> (SE) strain were significantly different as compared to control. The PA infection caused a decrease in amino-acid metabolism and the SE infection caused an increase in sugar metabolism. They also discriminated between infection with the virulent wild-type pathogen and its mutant. ¹²⁸

1.4.7. Combining NMR spectroscopy and mass spectrometry

NMR spectroscopy and mass spectrometry come with their advantages and limitations for metabolomic studies (**Table 1.4**). The choice of the analytical method is an important consideration to obtain reliable metabolomic data. For example, MS techniques are best suited for experiments that require high sensitivity while NMR is better fitted for structural elucidation.

Table 1.4. Comparison of NMR spectroscopy and mass spectrometry.

NMR spectroscopy	Mass spectrometry
<ul style="list-style-type: none"> • Fast • Cost-effective (no need for internal standards, easy sample preparation, no need for derivatisation) • Simple instrument care and maintenance • Non-destructive • Very good reproducibility (no batch effect) • Data can be compared across different NMR instruments • Relatively low sensitivity • Bigger sample volume • Small number of metabolites detected • Challenging deconvolution of overlapping signals • Versatile: metabolite identification, quantitation, structure elucidation of unknown metabolites, dynamic study capabilities (e.g. metabolite-protein interaction, metabolite compartmentalisation, cellular environment characterisation) 	<ul style="list-style-type: none"> • Relatively slow (lengthy separation methods) • Expensive (reagents for sample prep, standards and solvents, instrument parts, e.g. columns) • High-maintenance instruments, easy to damage during analytical runs, need frequent calibrations • Destructive • Moderate reproducibility (depends on instrument set-up, prone to batch effects, column and detector performance changes with history) • Difficult to standardise methods, data cannot be compared across different MS methods • Highly sensitive, low detection limit • Small sample volume • Large number of metabolites detected but difficult to identify • Complex data processing workflows • Fairly versatile: metabolite identification, quantitation, limited structure elucidation capabilities) • Some metabolites cannot be ionized, ion suppression effects due to co-elution • Limited commercial availability of analytical standards

NMR spectroscopy and mass spectrometry have substantial synergies.¹²⁹ The integration of the two technologies by unifying sample preparation protocols and data mining workflows suitable for both techniques would be the most powerful approach for the complete molecular characterisation of metabolites. Although coupling NMR with MS into one system is not a common practice, combining the data has proved to be the most comprehensive approach for solving structural ambiguities in metabolomics.^{20,130–132}

Shockcor and colleagues proposed coupling LC with NMR spectroscopy and mass spectrometry for analysing urine samples.¹³³ It was particularly useful for identity confirmation

of acetaminophen glucuronide and sulphate metabolites. They obtained unequivocal identification of phenylacetylglutamine by combining mass and fragmentation patterns from MS with ^1H NMR structural data, which was not available without prior chromatographic separation due to the high level of overlap.

Another study combined desorption electrospray ionisation (DESI) MS and NMR spectroscopy to study metabolic profiles of urine samples from healthy and diseased mice.¹³⁴ The authors reported a decrease in levels of acetic acid, lactic acid, creatinine, succinic acid, citric acid, and creatine by MS. The same changes were observed on the NMR spectra. Multivariate-based analysis obtained from the NMR or DESI subset of the spectral features common for both techniques, showed similar results. Moreover, since NMR spectroscopy and MS are orthogonal techniques, PCA scores could be combined into a 3D score plot. The approach could have a potential application for large population studies where 2D score plots are insufficient to differentiate between sample classes.

Lanza and colleagues also demonstrated the impact of combining quantitative NMR spectroscopy with highly sensitive LCMS.¹³⁵ They compared the metabolic profiles of plasma samples in insulin-treated (I+) and insulin-deprived (I-) patients with type 1 diabetes. ^1H NMR-based quantitative approach showed elevated levels of lactate, allantoin, and ketones in I- samples, whereas MS showed significant perturbations in plasma amino acid levels. Correlation matrices of NMR and MS data integrated complementary information from the two analytical methods. For example, ketones were positively correlated with tyrosine, valine, and leucine in the I- samples and the correlation was reversed in the I+ samples. The combined NMR and MS data highlighted several known metabolic pathways that are affected by insulin deficiency, such as gluconeogenesis, ketogenesis, amino acid oxidation, and protein synthesis/breakdown.

Bingol and Brüsweiler have developed a novel strategy based on the combined NMR/MS analysis, that helps identify metabolites in complex mixtures.¹³⁶ The approach first uses 2D ^1H - ^{13}C HSQC NMR data from the COLMAR metabolomics database to identify metabolites. It then calculates m/z ratios for most probable ions observed by MS, including adducts, fragments, and isotope patterns. Finally, it matches the predicted MS spectral features with the experimental MS spectrum. The method was successfully applied to human urine samples from healthy individuals. It allowed fast and accurate detection of known metabolites. Moreover, the approach detected metabolites that had not been reported previously. The results demonstrated

that an NMR/MS synergistic approach significantly enhanced the accuracy and efficiency of metabolites identification.

Hao and colleagues described how the statistical correlation between NMR spectroscopy and DIMS data could aid metabolite identification.¹³⁷ They used tissue extracts from earthworms to demonstrate that 15 out of 26 NMR-visible metabolites had the highest-ranking correlation to their corresponding mass spectral ion. For example, lysine-betaine is difficult to assign based on NMR data as it gives only one resonance in a complex spectrum with very little structural information. Supporting evidence was provided by DIMS spectral peaks: $[M+H]^+$ and $[M+Na]^+$ that corresponded to lysine-betaine and correlated highly to the relevant NMR resonance. Even though this approach came with challenges such as NMR signal overlap, it could improve the confidence of compound identification.

1.5. Data analysis in metabolomics

Data analysis workflows in metabolomics encompass the following steps: processing raw data, statistical analysis, and biological interpretation (**Figure 1.5**). The design of processing workflows for metabolomic studies depends on analytical technique, whereas the analysis workflows depend on the study design and often more than one statistical approach are run in parallel.^{19,138–140}

Generating reliable metabolic information relies on uniformly processed spectral data. This step is necessary to ensure that each measurement refers to the same metabolomic feature in all samples. It also includes data normalization, elimination of spectral noise/artefacts, and quality control measures. Processing data generates a data matrix including characteristic metabolic features, intensities/concentrations and sample metadata, which are subsequently used for statistical analysis: multivariate or univariate analysis.

Multivariate statistics is well suited for metabolomics since many variables can be analysed at once.¹⁴¹ This approach reduces the number of variables of a data set by defining new set of uncorrelated variables called principal components (PC). PCs are constructed from linear combination of initial variables and should contain most of the information from the large set.

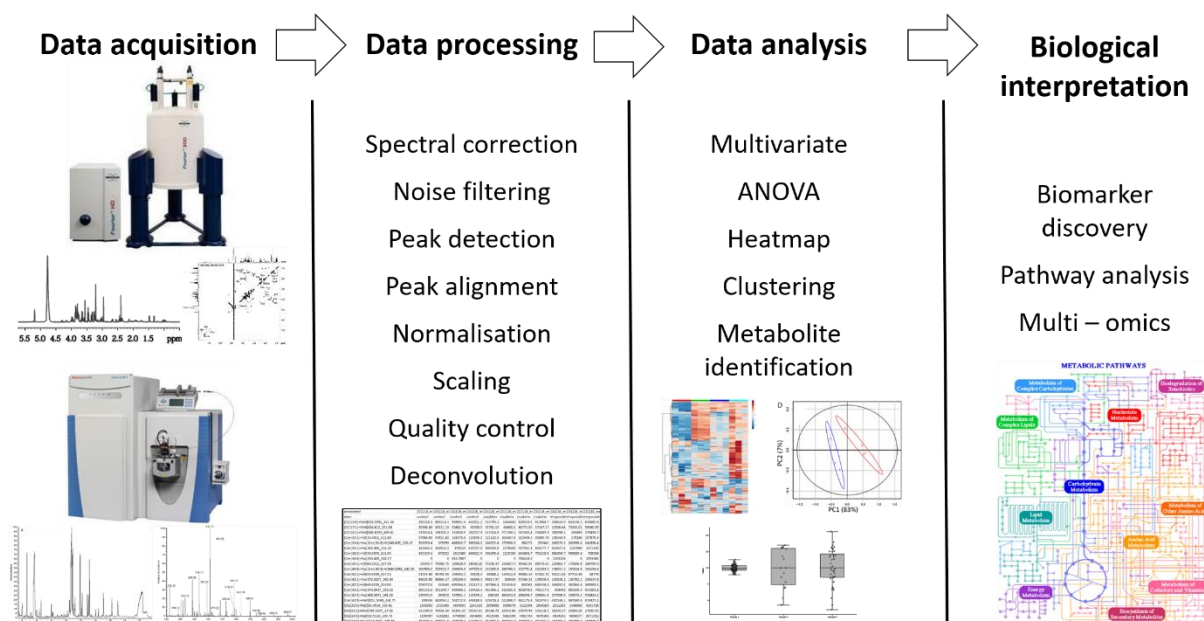


Figure 1.5. A typical data analysis workflow in metabolomics studies. The schematic shows the steps of the metabolomic data analysis including raw data processing, statistical analysis, and biological interpretation.

Multivariate results are visualised with a score plot and a loading plot (**Figure 1.6**). Scores represent the original data in a new PC coordinate system while loadings correspond to the contribution of each original variable to selected PCs. A score plot provides information about patterns in the samples and is used for analysing separation between groups and detecting outliers generated by instrumental variabilities or experimental errors. The loading plot shows how strongly each variable influences the PCs. The variables that are furthest away from the loading plot centre are most accountable for differences between the samples.

There are two types of pattern recognition algorithms in multivariate statistical analyses: unsupervised and supervised. Principal Component Analysis (PCA), an example of an unsupervised method, transforms all variables into a smaller number of principal components (typically two or three) that emphasize the greatest variances in the data set. A supervised approach (e.g., Partial Least Squares - Discriminant Analysis, PLS-DA) incorporates label information into a PCA algorithm.

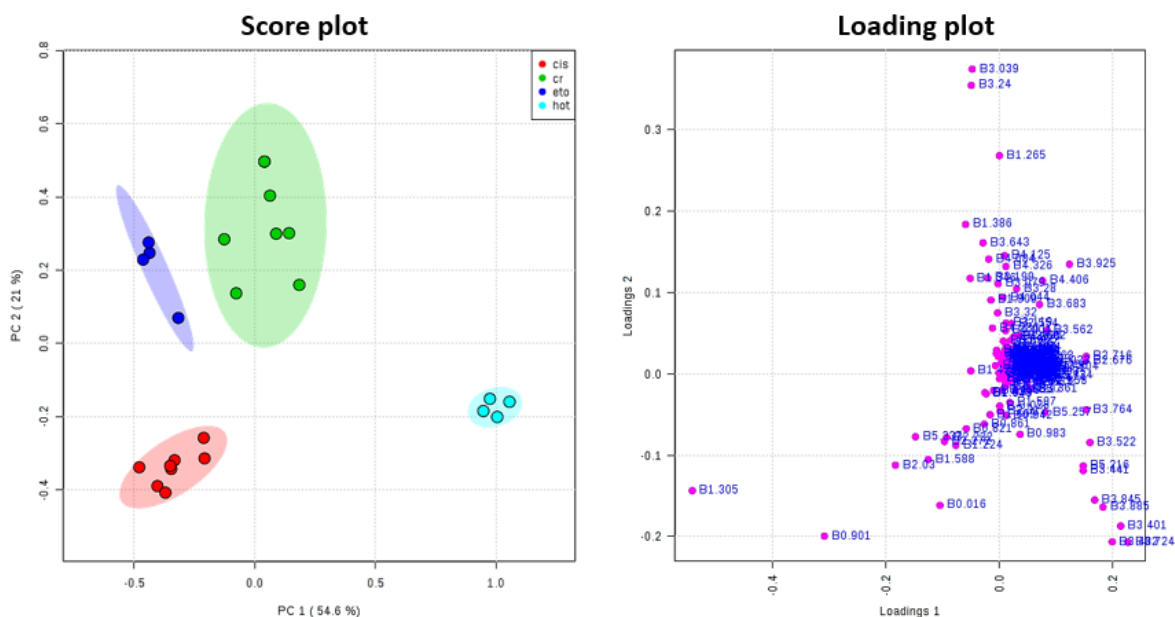


Figure 1.6. An example of the PCA score plot and its corresponding loading plot for metabolomics data. The score plot shows the separation of four different sample classes and the loading plot shows which variables are most responsible for differences between the groups.

Univariate statistical methods analyse one variable at a time. It provides an overview of the metabolomic features that are potentially significant in discriminating between two or more sets of samples.¹⁴² Examples of univariate statistical tests are:

- Student's *t*-test for two groups; and
- one-way analysis of variance (ANOVA) for more than two groups.

Univariate methods in metabolomics are prone to false-positive results due to an increased probability that the observed positive results are owed to chance.¹³⁸ Overinterpretation of the data can be avoided by applying a multiple testing correction technique such as the Benjamini–Hochberg correction. The correction is applied to *p*-values to limit the false discovery rate (FDR).

Metabolomic data analysis and interpretation are facilitated by open access resources including databases, online tools, and tutorials.^{143–145} **Table 1.5** summarises databases and online tools that I found most useful during my Ph.D. The list is not exhaustive and other resources are reviewed in detail elsewhere.^{140,143,145–147}

Table 1.5. Selected online tools and databases facilitating metabolomic studies.

Name	Description	Link
HMDB	Online database of small molecule metabolites found in the human body	www.hmdb.ca
KEGG	Online databases curating information about genomes, biological pathways, diseases, and drugs	www.genome.jp/kegg
MetaCyc	Online metabolic database that contains metabolic pathways, enzymes, metabolites, and reactions from various organisms.	www.metacyc.org
Chenomx	Software for identifying and quantifying metabolites in NMR spectra	www.chenomx.com
NMRshiftDB	NMR shift database for compound identification and structure elucidation	www.nmrshiftdb.nmr.uni-koeln.de
MetaboAnalyst	Online tools for metabolomic data analysis and interpretation	www.metaboanalyst.ca
W4M	Online tools for metabolomic data processing and analysis	www.galaxy.workflow4metabolomics.org

1.6. Apoptosis: definition, mechanism, and detection methods

Apoptosis is a mode of programmed cell death that maintains the balance of healthy cells in a living organism.¹⁴⁸ It eliminates redundant cells via a highly coordinated cascade of biochemical and morphological events that requires cellular energy (**Table 1.6**).

Table 1.6. Morphological and biochemical changes in cells during apoptosis.

Morphological stages of apoptosis	<ul style="list-style-type: none"> • Cell shrinks • Chromatin condensation • Cell shrinks • Chromatin condensation • Cytoplasm becomes denser, organelles are more crowded • Plasma membrane blebbing • Fragmentation of the nucleus • Separation of cell fragments into apoptotic bodies (budding)
Biochemical stages of apoptosis	<ul style="list-style-type: none"> • Endonuclease cascade (DNA cleavage) • Protease cascade (protein cleavage) • Extensive protein cross-linking • DNA breakdown • Externalization of phosphatidylserine on the surface of apoptotic cells/bodies • Phagocytic recognition and degradation by macrophages

Apoptosis is a part of normal physiology during development or aging when it removes the excess of healthy cells or deteriorating cells that can no longer perform their designated functions efficiently.¹⁴⁸ Apoptosis is an essential mechanism in spermatogenesis,¹⁴⁹ the formation of blood cells,¹⁵⁰ and foetal development.¹⁴⁹ During wound healing, apoptosis removes inflammatory cells and facilitates the evolution of granulation tissue into scar tissue.^{151,152} In addition, apoptosis maintains proper housekeeping functions by eliminating pathogens and pathogen-invaded host cells.¹⁵³

Apoptosis plays an important role in the defence and repair mechanisms of cells damaged by disease or noxious agents. Excessive or reduced apoptosis is linked to many diseases.¹⁵⁴ Lymphocytes from HIV-1 infected patients have an increased propensity to undergo apoptosis, which causes deterioration of immunological functions.¹⁵⁵ Contrarily, reduced lymphocyte apoptosis leads to the accumulation of T-cells that escalate the immune response. The inability to switch off the immune system is a fundamental feature of common autoimmune diseases such as multiple sclerosis and Crohn.^{155,156}

Failure of apoptosis is one of the key mechanisms behind cancer.¹⁵⁷⁻¹⁵⁹ A cell that becomes mutated or damaged first attempts to repair the damage. If that is not possible, the cell begins a signalling process to undergo apoptosis. Cells which lose this critical ability are more likely to be cancerous and continue to divide and accumulate, harbouring the mutations. Many anticancer treatments are based on activation or re-activation of apoptotic pathways.¹⁶⁰⁻¹⁶⁵ Radiotherapy and chemotherapy directly or indirectly induce DNA damage in cancer cells, which leads to apoptotic death.^{166,167} Other apoptotic-based treatments involve suppressing anti-apoptotic factors and restoring or enhancing pro-apoptotic factors.¹⁵⁷

Apoptosis is triggered by a variety of stimuli. These could be toxic agents, hypoxia, radiation, or cellular messengers such as hormones or death ligands. Depending on the type of stimulus, exposure time and intensity, other cell deaths can be activated in parallel or subsequently. Currently, there are over 15 distinct cell death types that are morphologically and biochemically distinct from apoptosis - necrosis, pyroptosis, and autophagy being most common.¹⁶⁸⁻¹⁷⁰ The understanding of different cell death mechanisms and discriminating between them is important for discovering new drug targets and developing therapies.¹⁶²

Apoptosis occurs via two main pathways: extrinsic and intrinsic.¹⁷¹ They both activate a group of cysteine proteases called caspases. The extrinsic pathway is mediated by the death receptor and recruits a series of downstream proteins to activate caspase-8. The intrinsic pathway is

initiated by radiation, toxic agents, and other factors that cause DNA damage and/or oxidative stress. The signalling cascade involves changes in the mitochondrial membrane and release of cytochrome c that eventually activates caspase-9.¹⁷² An additional apoptotic pathway involving cytotoxic T-cells of the immune system has also been described.¹⁷³ All pathways converge on the same execution pathway resulting in cell apoptosis (**Figure 1.7**). The initiator caspases-8/9/10 activate the executioner caspases-3/6/7 which in turn initiate the apoptotic events described in **Table 1.6**.

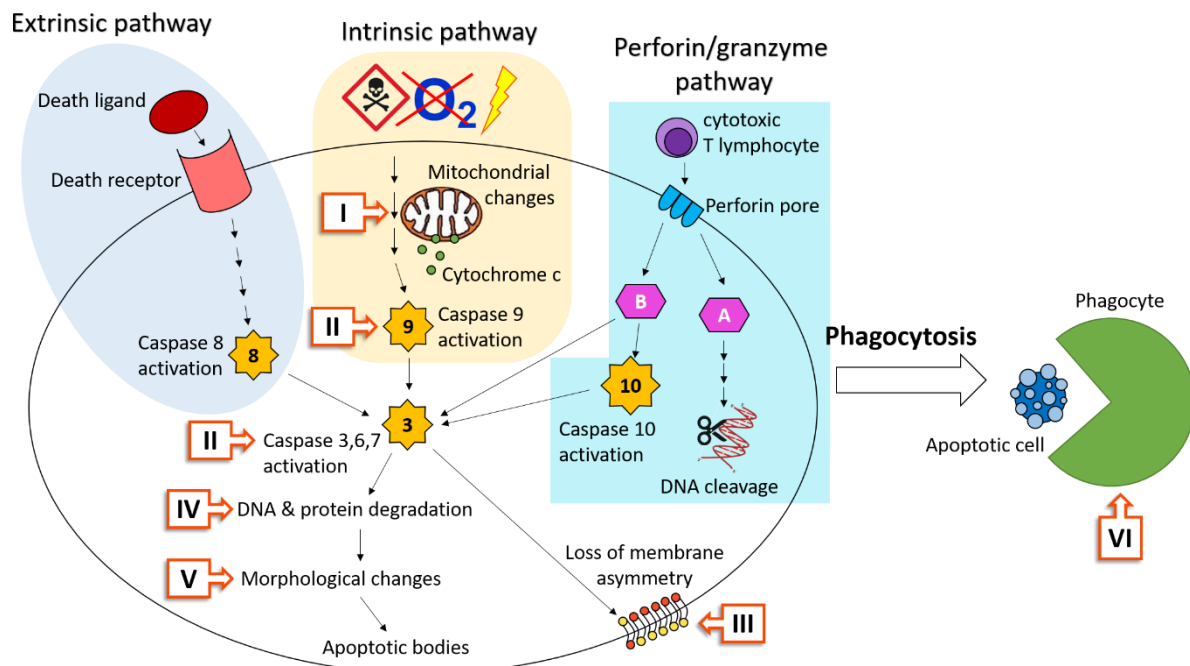


Figure 1.7. Molecular mechanism of apoptosis. Apoptosis can proceed via multiple cascades and is balanced by pro- and antiapoptotic mechanisms. I-VI indicate checkpoints used for detection of apoptosis (**BOX 1.2**)

This cascade of tightly coordinated events has many checkpoints that can be used for detecting apoptosis. Detection of the early stages of apoptosis relies on mitochondrial changes and the presence of activated initiator-caspases. The activated executioner-caspases and changes in DNA, cytoskeletal structure, and membrane asymmetry indicate mid-stages of apoptosis, whereas apoptotic bodies, phagocytic activities, and secondary necrosis are characteristic to late stages of apoptosis. Thus, the time point is an important factor determining the choice of the assay. Due to the invasive nature of biochemical assays, they have a low temporal resolution, meaning that it is difficult to study the progression of apoptosis in the same samples.

Common apoptosis assays can be classified into six different categories (**BOX 1.2**). As any detection technique, they exhibit advantages and limitations, and often more than one technique

is needed to confirm apoptosis.^{148,173} Of particular importance is to distinguish between apoptosis and necrosis. The two processes can occur simultaneously or sequentially but follow different biochemical pathways and produce different biological outcomes.¹⁷⁴

In contrast to apoptosis, necrosis is a type of cell death defined as unregulated (although regulated necrosis has also been researched).¹⁷⁵⁻¹⁷⁷ Necrosis is mainly triggered by extreme conditions, such as mechanical trauma, high or low temperatures or toxic agents and leads to rapid and irreversible cell and tissue damage. Necrosis is morphologically and biochemically very different to apoptosis.¹⁷⁸ It is described as a passive process, which does not require cellular energy¹⁷⁹ and has deleterious effects on the neighboring cells. Thus, necrosis in human body always required medical intervention to avoid further damage of adjacent areas.

In cell culture, secondary necrosis follows apoptosis because of a lack of phagocytic activity.¹⁸⁰ Necrosis can replace an ongoing apoptotic process if intracellular ATP is depleted. Thus, necrosis can be an indication of the late-stage apoptosis *in vitro*. Moreover, cultured cells may undergo a higher degree of necrosis caused by sample mishandling or faulty laboratory equipment. Thus, it can be difficult to interpret the outcome of these assays.

The most common viability assay, the dye exclusion assay, stains necrotic cells that exhibit impaired membrane integrity.¹⁸¹ Apoptosis does not lead to loss of membrane integrity and the dye penetrates only dead cells. The assay is quick, easy, and cost-effective but the dyes are toxic for the cells and with time, will enter live cells. Furthermore, while the assay discriminates between live and dead cells, it does not give information about how the cell dies. The use of alternative assays such as a colorimetric assay for assessing cell metabolic activity (MTT) and transmission electron microscopy (TEM) for detecting distinct morphological features is recommended for more comprehensive studies.¹⁸²

Monitoring the progression of apoptosis has two main benefits. Firstly, apoptotic biomarkers can be used for monitoring apoptotic-based treatment or the diagnosis of diseases driven by impaired apoptosis. Secondly, it contributes to the elucidation of molecular processes and a better understanding of the pathways associated with programmed cell death. That, in turn, leads to the discovery of novel drug targets and treatments.

Most biochemical assays give only a snapshot of one or two apoptotic events and can often result in ambiguous conclusions. Performing many independent apoptotic assays is costly and time-consuming. Comprehensive and robust methods for monitoring apoptosis could greatly facilitate research in diagnostics and drug discovery.

BOX 1.2. Common apoptosis assays.^{148,183,184}

Mitochondrial assays (I)

Mitochondrial changes such as mitochondrial permeability transition (MPT), cytochrome c release, membrane potential depolarization, Ca²⁺ fluxes, changes in redox potential, and reactive oxygen species are characteristic features of the early phase of the intrinsic apoptotic pathway. They can be monitored by laser scanning confocal microscopy (LSCM), western blotting, or dye-based assay (e.g. rhodamine) in intact or fixed cells and tissue. Mitochondrial dye-based assays do not provide information about cell death mechanisms at later stages. Some mitochondrial events can occur during necrosis and the initiation of apoptosis does not guarantee the execution of apoptosis thus an additional assay is needed (e.g. caspase assay). It is important to consider the stability of dyed proteins, and alterations in mitochondrial metabolism induced by dyes.

Detection of caspases, cleaved substrates, regulators, and inhibitors (II)

Western blot, immunoprecipitation, and immunohistochemistry can detect activated caspases, intermediate substrates (PARP), regulator proteins (Bax, Bid, and Bcl-2) or modifications associated with apoptosis (phosphorylated histones). A large number of apoptosis biomarkers and versatile probes allow for studying many apoptotic events. They provide high information content including the earliest stages of apoptosis and allow for rapid and consistent quantification of apoptotic cells. The assays are usually destructive and hence not suitable for following the progression of apoptosis. Many of them cannot be used on intact cells. In addition, caspase assays tend to have poor specificity for different caspases.

Polymerase chain reaction (PCR) microarrays allow for apoptosis-related gene expression profiling. It can provide comprehensive information for over 100 genes that regulate apoptosis.

Membrane alterations (III)

The annexin V assay detects externalization of phosphatidylserine residues on the outer plasma membrane during mid- to late-stages of apoptosis. Tissues, embryos, or cultured cells can be analysed by fluorescent microscopy or flow cytometry. It has good sensitivity but depends on the cell line and the elapsed time after induction. Not suitable for differentiating apoptosis from necrosis as membranes of necrotic cells are labelled as well. It is often combined with a membrane integrity assay.

DNA fragmentation (IV)

The DNA laddering technique detects the DNA fragments after endonuclease cleavage. Uniform DNA degradation is characteristic of programmed cell death. It can be performed on tissue and cell samples; careful sample preparation is important to avoid non-apoptotic DNA fragmentation. This technique has low sensitivity – DNA fragments cannot be detected until the later stages meaning that the absence of a DNA ladder does not definitely exclude apoptosis. It is not suitable for samples with low numbers of apoptotic cells. Necrosis leads to a rapid non-specific cleavage of DNA and therefore do not produce the ladder pattern.

The Comet assay, based on gel electrophoresis, can detect various forms of DNA cleavage. It has higher sensitivity and gives more information about DNA fragments.

Terminal dUTP Nick End-Labeling (TUNEL) enzymatically labels the DNA fragments with UTP and is a suitable probe for detection by light microscopy, fluorescence microscopy or flow cytometry. It is a fast and sensitive method but expensive and prone to false positive from necrotic cells and cells in the process of DNA repair. It has also been reported that the TUNEL assay could also give positive signals in necrosis and therefore should not be used explicitly for discriminating between apoptosis and necrosis.

BOX 1.2. Continued.

Morphological alterations by electron microscopy (V)

The high spatial resolution of electron microscopy allows the visualisation of nuclear fragmentation, intact or ruptured cell membrane, disintegration of cytoplasmic organelles, vacuole formation, blebs at the cell surface, loss of cell-to-cell adhesions, apoptotic bodies, and phagocytosis of apoptotic bodies. This is useful for distinguishing between apoptosis and necrosis. It can be coupled with immunochemical staining for biochemical information (e.g. localisation of cytochrome c). Tissue sections and intact cells can be analysed but, due to the invasive nature of the method, samples cannot be used for subsequent tests. The technique can only analyse small areas of samples at once and gives limited information about the early stages of apoptosis. The equipment is expensive, requires a highly skilled operator and sample preparation and analysis are lengthy. It is prone to false-positives, and hence confirmation with other methods may be necessary.

Detection of phagocytic activity (VI)

Dye-based assays are used to detect high lysosomal and phagocytic activity associated with late-stage apoptosis. It is usually used as a complementary assay since lysosomes degrading is not highly specific to apoptosis. Like for any dye-based assay, it is important to use a fluorescent tag, which does not interfere with native cell behaviour.

1.7. Application of metabolomics in studying apoptosis

In recent years, metabolomics has played an important role in studying apoptosis. Metabolomic approaches provide valuable information about the underlying mechanisms of an apoptotic agent that may be difficult to predict based on biochemical apoptosis assays listed in **BOX 1.2**. Although metabolomics approaches have been used for studying apoptosis in tissue, cells and *in vivo*,⁹⁶ the focus of this section is on describing selected examples of MS- and NMR-based metabolomic studies on cell culture systems. The summary of potential metabolic biomarkers of apoptosis discussed below is presented in **Table 1.7**.

The high sensitivity of MS techniques allows for routine and sophisticated analysis of ultra-small volumes of samples. Dong and colleagues proposed a novel detection method of apoptosis in cultured mammalian cells based on MALDI-TOF-MS.¹⁸⁵ They reported several MS spectral features that could distinguish apoptotic cells from control and necrotic cells independently of the cell lines investigated. They also found a good correlation between the relative peak intensities and the percentage of apoptotic cells in the sample showing potential for this method to become a quantitative assay of apoptosis. Halama and colleagues studied MS-based metabolic profiles of two cell lines treated with pro-apoptotic agents: etoposide or 5-fluorouracil, and heat treatment for the induction of necrosis.¹⁸⁶ Eleven of the 42 assayed metabolites showed significant changes when compared with the control cells. However, only three metabolites, namely alanine, glutamate, and acetylcarnitine, showed a consistent trend

regardless of the apoptotic agent or cell line. In their previous study,¹⁸⁷ they showed that staurosporine treatment increased levels of aspartate, methionine, glutamate, and alanine. They concluded that only alanine and glutamate could be considered as promising metabolic biomarkers of apoptosis. However, their specificity in detecting apoptosis is yet to be demonstrated.

MS-based metabolomics approaches can help elucidate molecular mechanisms of apoptosis. Pradelli and colleagues combined biochemical assays and MS-based metabolomics to investigate glucose metabolism in apoptotic cells.¹⁸⁸ They reported a caspase-dependent decrease in ATP and ADP and phosphoenolpyruvate levels. The key glycolysis-related metabolites including glucose-6-phosphate, fructose-6-phosphate, alpha-ketoglutarate, and nucleotides were not significantly altered, suggesting that regulation of glycolysis was likely to occur downstream of phosphofructokinase-1, and that the Krebs cycle and the pentose phosphate pathway were not modulated by caspases. They also observed a significant decrease in the levels of phosphoserine indicating an impairment in the serine pathway and, consequently, the reduction of pyruvate kinase activity. Lu and colleagues conducted an MS-based metabolomics study focusing on lipid perturbations caused by natrin-induced apoptosis in human hepatocellular carcinoma cells.¹⁸⁹ They found 13 potential biomarkers associated with lipid metabolism. They proposed a putative mechanism of natrin-induced apoptosis involving dysfunction of sphingolipid metabolism, fatty acid biosynthesis, fatty acid metabolism, glycerophospholipid metabolism, and glycosphingolipid biosynthesis.

NMR-based metabolomics has also contributed to the investigation of apoptosis. The main advantage of NMR spectroscopy over MS is its quantitative power and non-destructive nature. Previous reports show that NMR spectroscopy can detect apoptosis-induced alternations in glucose and lipid metabolism.^{190,191} It can identify cell lines that are resistant to specific pro-apoptotic agents and discriminate apoptosis from other forms of cell death.¹⁹²⁻¹⁹⁵ Furthermore, the metabolic profiling of intact cells by NMR spectroscopy can contribute to elucidating the mechanisms of drug action.¹⁹⁶

Table 1.7. Potential metabolic biomarkers and metabolic mechanisms associated with apoptosis.

Study	Cell line	Apoptotic agent	Metabolic change
MS-based ¹⁸⁷ (cell extracts)	hepatocellular carcinoma, human embryonic kidney	Etoposide 5-fluorouracil	Alanine, glutamate ↑
MS-based ¹⁸⁸ (cell extracts)	HeLa	Actinomycin D	ATP, ADP, phosphoenolpyruvate, phosphoserine ↓
MS-based ¹⁸⁹ (cell extracts)	hepatocellular carcinoma	Natrin	Caprylic acid, caproic acid, sphinganine, lauric acid, palmitic acid, phytosphingosine, phosphatidylethanolamine, tricaprylic glyceride, ganglioside ↑ Phosphatidylcholine ↓
NMR-based ¹⁹⁷ (cell extracts)	Leukaemia	Bezafibrate + Medroxyprogesterone acetat	Acetate, isoleucine, leucine, asparagine, phenylalanine, glutamine, glutamate, glycine, succinate, asparagine, valine ↑ Citrate, α-ketoglutarate, glutathione ↓
NMR-based ¹⁹⁸ (cell lysates)	Glioma	Glabrescione B	Pyruvate, lactate, succinate ↑ Glucose, citrate, malate ↓
HRMAS NMR-based ⁷⁰ (intact cells)	Endometrial	Tamoxifen	Nucleotides, ethanolamine, glucose, glutamate ↑ Myo-Inositol ↓
NMR-based ¹⁹⁴ (intact cells)	Leukaemia	Doxorubicin Radiation	CH ₂ , CH ₃ lipids ↑ Glutamine, glutamate, taurine, glutathione, choline-metabolites ↓
NMR-based ¹⁹⁵ (intact cells)	Cervical carcinoma	Etoposide	CH ₂ , CH ₃ lipids ↑ Choline-metabolites ↓
NMR-based ¹⁹⁹ (cell extracts)	Jurkat T-cells	Fas mAb	CH ₂ , CH ₃ lipids ↔ TAGs ↑ Phosphatidylcholine ↓
HRMAS NMR-based (intact cells)	Medulloblastoma	Cisplatin	CH ₂ , CH ₃ , unsaturated lipids ↑
NMR-based ²⁰⁰ (intact cells)	T-lymphoblastoid	Doxorubicin Dexamethasone	Unsaturated lipids ↔ CH ₂ , CH ₃ lipids ↑

Cell extracts of acute myeloid leukaemia were studied by Tiziani and colleagues.¹⁹⁸ They investigated the changes in NMR metabolic profiles induced by bezafibrate and medroxyprogesterone acetate. The metabolites involved in the Krebs cycle were the main discriminatory factors between treated and untreated cells, which confirmed the role of reactive

oxygen species in the antileukaemic activity of the drugs. Leukaemia cell lines with different mutations gave distinct NMR spectra after the same treatment. The findings demonstrated that NMR-based metabolic profiling could contribute to the development of personalised medicines. Similarly, D'Alessandro and colleagues studied glioma cell lysates (*endo*-metabolites) and cell growth media (*exo*-metabolites) after Glabrescione B treatment.¹⁹⁸ NMR-based metabolomics discriminated between control and treated samples harvested at different time points. Both *endo*- and *exo*-metabolites were significantly altered. Metabolic data suggested that the treatment enhanced the aerobic glycolysis and anabolic-to-catabolic transition.

Griffin and colleagues studied the metabolic impact of tamoxifen (a pro-apoptotic agent) on intact endometrial cells by HRMAS ¹H NMR spectroscopy.⁷⁰ They identified changes in several metabolites that could play a role in the mechanism of apoptosis. For example, an increase in nucleotide levels might be linked to alteration in RNA transcription, and a decrease in *myo*-inositol levels provided clues about the changes in cell membrane characteristics during apoptosis.

Rainaldi and colleagues examined ¹H NMR metabolic profiles of intact leukaemia cells after pro-necrotic and pro-apoptotic treatments.¹⁹⁴ Necrotic cells showed a significant increase in resonances assigned to $-\text{CH}_3$ lipids, glutamine/glutamate, taurine, and choline-metabolites and no change in $-\text{CH}_2-$ lipids. Conversely, the spectra of apoptotic cells were characterised with a significant increase in the resonances of $-\text{CH}_2-$ and $-\text{CH}_3$ lipids and a decrease in glutamine/glutamate, taurine, glutathione, and choline-metabolites. In addition, ¹H NMR spectroscopy discriminated between two apoptotic treatments: doxorubicin and radiation. Bezabeh and colleagues, also reported elevated levels of $-\text{CH}_3$ and $-\text{CH}_2-$ lipids in intact apoptotic cells but no change in $-\text{CH}_2-$ lipids in necrotic cells as measured by ¹H NMR spectroscopy.¹⁹⁵ However, they observed a decrease in choline-metabolite resonances for both necrotic and apoptotic cells. The increase in $-\text{CH}_2-$ and $-\text{CH}_3$ NMR-visible lipid resonances during apoptosis is consistent with several other studies and, unlike small metabolites, seems to be independent of pro-apoptotic agents or cell lines.^{199–207} Another NMR study in intact cells not only confirmed the abnormal accumulation of lipids during apoptosis but also showed that treatment with Triacsin C (a specific inhibitor of long-chain acyl-CoA synthetase that blocks *de novo* lipid synthesis) abolished the increase in the intensities of the lipid resonances in apoptotic cells.²⁰⁸

The increased ratio of CH_2/CH_3 lipid resonances can also be used as an estimation of the extent of apoptosis as it correlates well with apoptotic assays such as Annexin V, TUNEL and fluorescence microscopy.^{193,195,209} Other studies found no significant changes in the ratio, suggesting that this may be cell line-specific.^{210,211} One also needs to be cautious about the contribution of other metabolites such as lactate and amino acids to the resonances at 0.9 and 1.3 ppm which would confound the use of these regions as potential markers of apoptosis. This contribution may be different for different cell lines. Furthermore, the observation may not be valid for lipid cell extracts as non-mobile lipids from membranes will contribute to the NMR signal. Indeed, Al-Saffar and colleagues reported no significant change in the $-\text{CH}_2-$ and $-\text{CH}_3$ lipid resonances or in the CH_2/CH_3 ratio of the lipid extracts from apoptotic cells relative to control.¹⁹⁹

Other lipid units can also be studied by NMR spectroscopy. Monitoring the resonances that correspond to $-\text{CH}=\text{CH}-$ (5.2 ppm), $=\text{CH}-\text{CH}_2-\text{CH}_2-$ (2.1 ppm) and $=\text{CH}-\text{CH}_2-\text{CH}=\text{CH}-$ (2.8 ppm) lipid protons provides information about the average degree of unsaturation of cellular lipids.^{30,200} Several NMR studies *in vivo* and *ex vivo* on tumour tissue samples reported an increase in unsaturated lipids induced by apoptosis-based treatments.^{96,207,212} A similar observation was detected in medulloblastoma cancer cells in response to cisplatin (pro-apoptotic) treatment.²⁰⁴ By contrast, Vito and colleagues reported no significant increase in unsaturated lipids in apoptotic T-lymphoblastoid cells with respect to untreated control.²⁰⁰ The reason for contradicting results may be twofold:

- Unsaturated lipid accumulation during apoptosis may vary according to cell type (different biological functions) and apoptotic treatment;
- Overlapping NMR resonances and the contribution of small metabolites to lipid signals may hinder accurate interpretation of spectra.

Nevertheless, NMR experiments suggest that the accumulation of lipids plays an important role in programmed cell death and monitoring changes in lipid behaviour during apoptosis could provide valuable insights to molecular events *in vitro* and *in vivo*.

1.8. NMR-visible lipids

The size and mobility of molecules are important factors rendering NMR relaxation times, and hence their spectral visibility.²¹³ Inside cells, some molecules such as proteins or membrane

lipids are integrated into semi-rigid intracellular structures. Their tumbling motions are very slow, their relaxation rates are very rapid and consequently, their NMR signals are difficult or impossible to detect by solution-state NMR spectroscopy because the resonances associated with the molecule are very broad. While cell membrane lipids are poorly detectable by conventional solution-state NMR spectroscopy, cellular lipid microstructures with sufficient tumbling rates needed for NMR detection include lipid rafts and lipid droplets (**Figure 1.8**).

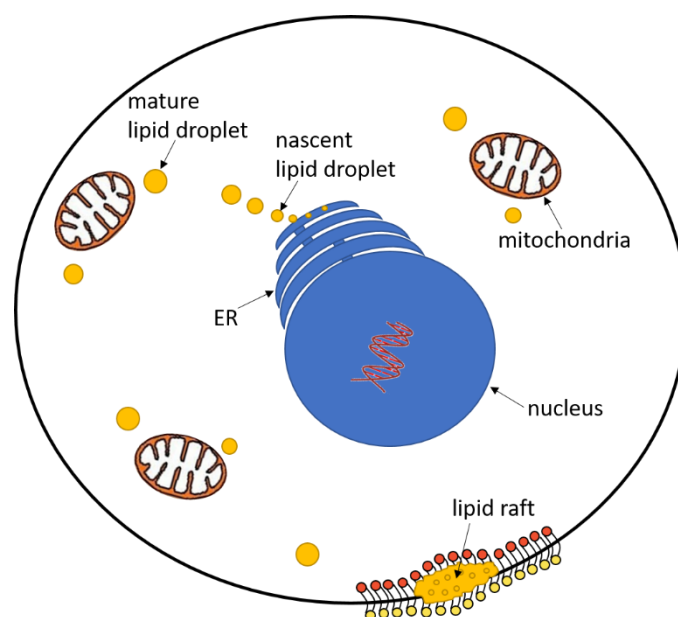


Figure 1.8. Lipid microdomains in a mammalian cell. Lipid rafts are contained within the plasma membrane while lipid droplets originate from the endoplasmic reticulum (ER) and are located in the cytoplasm.

Lipid rafts (LRs) are signalling microdomains within membrane lipid bilayers comprising cholesterol, glycosphingolipids, and membrane proteins. They play an important role in regulating the curvature and rigidity of membranes.²¹⁴ They are involved in the regulation of membrane permeability and the formation of trafficking vesicles such as endosomes and lysosomes.²¹⁵ It has been shown that the formation of LR is vital for lipid signalling functions.²¹⁶ Methods for the detection of membrane lipid domains in model- and bio-membranes include microscopy, X-Ray diffraction, solid-state ^2H NMR, ^1H MAS NMR, and other spectroscopic methods.²¹⁷ NMR-based lateral diffusion measurements of lipids in simple membrane models suggest that these domains are mobile. Gaede and Gawrisch reported the lateral diffusion coefficient of a phosphocholine compound in multilamellar liposomes at 322 K was $\sim 8.5 \times 10^{-12} \text{ m}^2 \text{ s}^{-1}$.²¹⁸ Filippov and colleagues studied the formation of LR by NMR spectroscopy.²¹⁹ They found that the lateral diffusion of lipids in model bilayers could be described by two diffusion coefficients, 5.0 and $1.0 \times 10^{-12} \text{ m}^2 \text{ s}^{-1}$, corresponding to liquid-

disordered and liquid-ordered phases of LRs, respectively. Ferretti and colleagues demonstrated the contribution of LRs to NMR-visible lipid resonances by separating cellular lipids into Triton-soluble (mainly cytoplasmic lipid droplets) and Triton-insoluble (LRs) mobile lipids.²²⁰ They also demonstrated the temperature dependence of the NMR lipid resonances which was consistent with the transformation between liquid-ordered and liquid-disordered phases characteristic for LRs. Recently, Ceñido and colleagues showed that HRMAS ¹H NMR spectroscopy can characterize membrane lipid microdomains isolated from human platelets.²²¹

Lipid droplets (LDs) are cytosolic organelles composed of neutral lipids (triglycerides and cholesterol esters) enclosed within a phospholipid monolayer. In healthy cells, they are a source of energy, hormones, and secondary messengers, and they protect cells from lipotoxicity.²²² Abnormal formation of LDs has been associated with pathologies such as infection, inflammation, and cancer.^{223–225} Numerous studies suggest that NMR-visible lipids represent LDs rather than LRs.^{226–229} Pan and colleagues reported a very good correlation between the HRMAS ¹H NMR lipid resonances and the size of LDs measured by fluorescence microscopy.²³⁰ In another study, they compared the HRMAS ¹H NMR spectra of intact cells and of isolated LDs.²³¹ Both spectra showed marked similarities suggesting that NMR-visible lipid resonances of intact cells originated primarily from LDs. Vito and colleagues also found a close correlation between ¹H NMR-visible lipids and the volume of cytoplasmic lipid bodies detected by fluorescence microscopy.²³¹

Griffin and colleagues studied lipid droplet dynamics in intact cells by HRMAS ¹H NMR spectroscopy.⁷⁰ They reported diffusion coefficients of lipid droplets in intact cells in the range of $0.2 - 0.5 \times 10^{-9} \text{ m}^2 \text{ s}^{-1}$. The LD diffusion values are 1000 times higher than the diffusion values for LRs, meaning that LDs are more mobile and likely to have a higher contribution to the NMR signals.

Relaxation of an NMR signal is determined by the transverse (T_2) relaxation time of the resonance and will determine the visibility of lipids on an NMR spectrum. The T_2 relaxation times for LDs in intact cells measured by HRMAS ¹H NMR spectroscopy are in the range of $0.15 - 0.3 \text{ s}$.⁷⁰ The T_2 relaxation times for sphingomyelin (a component of lipid rafts) in a model membrane system measured by ²H solid-state NMR spectroscopy at a spinning rate of 2 kHz are in the range of $0.0025 - 0.01 \text{ s}$.²³² LR relax 6 – 15 times faster than LDs thus it is

expected that LRs will contribute less to NMR resonances than LDs. **Table 1.8** compares T_2 relaxation times and diffusion coefficients of LDs and LRs.

Table 1.8. Comparison of diffusion and T_2 relaxation times for cellular lipid microdomains

NMR measurement	Lipid droplets	Lipid rafts
Diffusion [$\text{m}^2 \text{s}^{-1}$]/ 10^{-9}	0.2 – 0.5	0.0010 – 0.0085
T_2 relaxation time [s]	0.15 – 0.30	0.0025 – 0.0100

1.9. Scope and aims

This PhD focuses on establishing NMR-based methods for monitoring apoptosis-based cancer treatments and validating them with existing biochemical and microscopy methods. In order to do that I characterise metabolic profiles of cells treated with two commonly used cancer treatments: cisplatin and etoposide, and investigate potential biomarkers linked to the treatments.

The main aims are:

- 1) To characterise intact cells undergoing apoptosis by means of HRMAS ^1H NMR-based metabolomics.
- 2) To develop a HRMAS ^1H NMR-based diffusion method for differentiating between apoptotic and control cells and validate it with the common fluorescence microscopy methods.
- 3) To validate HRMAS ^1H NMR-based metabolomics data by comparing with solution-state NMR, MS and transcriptomic data.

In **Chapter 3**, I describe HRMAS NMR spectroscopy method optimisation for analysing intact cells. This includes investigating an optimum spin rate, the sample packing process, pulse sequences and experimental time. Cell viability in a MAS rotor is also investigated.

In **Chapter 4**, I investigate potential biomarkers of apoptosis in intact cells detected by HRMAS ^1H NMR spectroscopy, and whether the biomarkers are different for different apoptosis-based treatments. I compare data obtained from solution-state ^1H NMR spectroscopy of cell extracts and discuss the advantages and limitations of both techniques for studying

apoptosis *in vitro*. I also assess the usefulness of information that we can obtain from studying endogenous metabolites from culture media.

In **Chapter 5**, I describe changes in the physical properties of LDs using time domain NMR experiments such as transverse relaxation rate and diffusion coefficient measurements. I also propose an NMR-diffusion based method for studying LD formation during apoptosis, which I validate with a common fluorescence microscopy method.

In this introduction, I have highlighted the benefits of combining NMR- and MS-based metabolomic data and the growing trend of integrating omic data. In **Chapter 6**, I combine NMR- and MS-based metabolomic data with transcriptomic data to map apoptosis-induced changes in cellular metabolism and to understand the processes behind the accumulation of lipids during apoptosis. I analyse transcripts involved in *de novo* lipid synthesis, lipid desaturation and lipid particle organisation to understand their contribution to the apoptotic events.

Finally, I discuss the advantages and limitations of HRMAS NMR spectroscopy and propose future directions based on the results obtained during my PhD.

Chapter 2. Materials and methods

2.1. Materials and reagents

All materials and reagents were obtained from Sigma-Aldrich (Merck) (St. Louis, MO, USA) unless otherwise specified.

2.2. Cell culture

C2C12 cell line sub-cloned from a myoblast line established from normal adult C3H mouse leg muscle (ATCC, Manassas, Virginia, US) was cultured in Dulbecco's modified Eagle's medium (DMEM- D6429) containing 10% Fetal Bovine Serum (FBS) and 1% PenStrep (100 U/mL Penicillin + 100 µg/mL Streptomycin) in a humidified 5% carbon dioxide atmosphere at 37°C. Cells were grown in T-75 Greiner cell culture flasks (Merck, St. Louis, MO, USA) (for metabolomics) or T-175 Nunc cell culture flasks (Thermo Fisher Scientific, Waltham, MA, USA) (for lipid droplet isolation) with filter-vented caps, seeded at approx. 1.5×10^6 or 3.0×10^6 cells per flask, respectively. The passage number was limited to four and kept constant for all experiments. Cells Myogenic differentiation was initiated upon reaching 60% confluence, by switching the cells to medium containing 2% horse serum supplemented with 1 µM insulin. After 5 days of differentiation, the cells were treated as described in **Section 2.3**. After the incubation, the cells were trypsinized and washed twice with phosphate buffered saline (PBS). The harvested cells were either used fresh (for viability and caspase 3-activity assays, lipid droplet isolation, metabolite extraction) or were frozen immediately in growth media + 5% Dimethylsulfoxide (DMSO) and stored at -80°C until use (for HRMAS NMR spectroscopy)^b. Cell freezing and thawing were performed according to the manufacturer recommendations (ACTT).

^b Limited HRMAS NMR sample throughput (3-4 samples per day) means that samples have to be kept frozen before running HRMAS NMR experiments to prevent cell death.

2.3. Induction of apoptosis

The cells were treated with apoptotic agents: cisplatin or etoposide, purchased from Cambridge Bioscience Ltd (Munro House, Cambridge, UK) in powder form. DMSO was used as a vehicle for drugs and the equivalent volume was added to control cells (<1% v/v). Fresh stocks of cisplatin and etoposide were prepared on the day of experiments by suspending in DMSO and vortexing (Cole-Parmer Vortex Mixer, Cole-Parmer Instrument Company Ltd, Colmworth Business Park, St. Neots, UK) until completely dissolved.

The dose and incubation time varied depending on the experiment, and were as follows:

Dose and incubation time by caspase 3-activity assay (**Chapter 4, Section 4.3.1**)

Cisplatin: 20, 40, 60 μ M

Etoposide: 48, 60, 84, 120 μ M

Incubation time: 2, 8, 24, 48, 72 h

NMR experiment (**Chapters 4, Section 4.3.2**)

Cisplatin: 60 μ M

Etoposide: 50 μ M

Incubation time: 48 h

Time course NMR experiment (**Chapters 4, Section 4.3.3 and Chapter 5**)

Cisplatin: 60 μ M

Etoposide: 120 μ M

Incubation time: 8, 24, 48 h

Confocal microscopy (**Chapters 5**)

Cisplatin: 60 μ M

Etoposide: 120 μ M

Incubation time: 24, 48 h

MS and RNA-Seq experiments (**Chapters 6**)

Cisplatin: 60 μ M

Etoposide: 120 μ M

Incubation time: 48 h

2.4. Induction of necrosis

The cells were incubated at 60°C in a water bath for 15 minutes. Then they were incubated at 37°C in a 95% air/5% CO₂ atmosphere and harvested together with other treatments.

2.5. Growth medium sample preparation

Growth medium samples were collected prior to harvesting the cells and pre-processed according to a protocol published by Kostidis and colleagues.²³³ Briefly, 0.5 mL of media was aspirated from each flask and transferred to a 2 mL microcentrifuge tube. Ice-cold methanol (1:2 v/v ratio) was added immediately after sample collection and the samples were placed at -20°C overnight to allow the proteins to precipitate. Next day, the samples were centrifuged at 16000 × g at 4°C for 30 minutes (Micro-Centrifuge 5424, Eppendorf Corporate, Hamburg, Germany). The supernatant was then collected, and all solvents were evaporated under a stream of dry nitrogen gas and stored at -80°C for further analysis.

2.6. Cell viability

The Trypan Blue exclusion test was used to determine the number of viable cells present in cell suspensions before and after NMR experiments. The test was performed according to a standard cell counting protocol.²³⁴ Briefly, 25 µL freshly harvested cells were transferred to a plastic vial and diluted with PBS (1:5 dilution). An equal volume of 0.4% trypan blue dye was added to 8 µL cell suspension to obtain a 1:2 dilution and mixed by pipetting. The cell-dye mixture (10 µL) was transferred to Countess™ cell counting chamber slides (Thermo Fisher Scientific, Waltham, MA, USA) by placing the tip of the pipette at the notch. The viability of cell samples was measured with a Countess™ Automated Cell Counter (Thermo Fisher Scientific, Waltham, MA, USA). The total number of cells was used for normalisation of the caspase 3-activity assay. Cell viability was expressed as a percentage of live cells.

After a HRMAS ¹H NMR experiment, the cells were recovered from the MAS rotor and diluted with PBS (1:5 dilution) prior to cell viability assessment.

2.7. Caspase 3-activity assay

Relative apoptosis levels in freshly harvested cell samples were measured using the Caspase-3 Assay Kit (fluorogenic caspase-3 substrate: Ac-DEVD-AMC, BD Pharmingen™, San Jose, CA, USA) following the manufacturer's instructions. Briefly, reaction buffer containing Ac-DEVD-AMC was added to each cell lysate (10⁶ cells/ml) and incubated in a black 96-well microplate (Nunc®, Thermo Fisher Scientific, Waltham, MA, USA) for 1 h at 37°C in the dark. The fluorescence intensities were measured with a FLUOstar OPTIMA Microplate Reader (BMG Labtech GmbH, Bucks, UK) at excitation/emission wavelengths of 380/420 nm.

2.8. Metabolite extraction (Bligh and Dyer)

Thawed cells (5×10^6 per sample) were washed with 5 mL PBS at room temperature. The metabolites and lipids were extracted simultaneously using a methanol/chloroform/water extraction method.²³⁵ LCMS-grade methanol (Fisher Scientific, Loughborough, UK) and chloroform in a ratio of 2:1 (v/v; 500 μ L) were added to each sample and the cells were briefly pulverized with a plastic pipette tip, vortexed and sonicated at room temperature for 1.5 h. Subsequently, Milli-Q water and chloroform in a ratio of 1:1 (v/v; 500 μ L) was added, vortexed and sonicated again for 30 minutes. The two layers and cell pellet were separated by centrifuging (7000 rpm, 7 minutes); the upper methanol-water fractions containing the water-soluble cellular metabolites were collected in Eppendorf tubes and the lower chloroform fractions containing the cellular lipids were collected in glass vials. All solvents were then evaporated under a stream of dry nitrogen gas and the residue was stored at -80°C for further analysis.

2.9. Lipid droplet isolation

Lipid droplets were isolated from freshly harvested cells by simple gradient centrifugation using a lipid droplet isolation kit (Cell Biolabs, Inc., San Diego, CA, USA). The isolation was performed according to the manufacturer's instructions. Briefly, 10^7 cells were trypsinized, transferred into 5 ml ice-cold PBS in a 15 ml plastic tube and pelleted by centrifuging for 4 minutes at $1000 \times g$, at 4°C . The cells were transferred to a 2 mL microcentrifuge tube, resuspended thoroughly with 200 μ L of Reagent A and incubated on ice for 10 minutes. Subsequently, 800 μ L of 1X Reagent B was added, mixed, and incubated on ice for 10 minutes. The cell samples were homogenized by passing them five times through a one inch 27-gauge needle attached to a 3 mL syringe and centrifuged at $100 \times g$ for 5 seconds. Additional 600 μ L of 1X Reagent B were carefully layered on top of the homogenate by dropwise addition taking care not to disturb the homogenate. The microcentrifuge tubes were centrifuged for 3 h at $18,000 - 20,000 \times g$ at 4°C . Floating lipid droplets were transferred to a fresh microcentrifuge tube. Lipids from lipid droplets were extracted as described above for metabolite extracts. At least three independent samples were prepared for each isolation.

2.10. HRMAS ¹H NMR spectroscopy

2.10.1. Sample preparation

Thawed cells (5×10^6 per sample) were washed in deuterated PBS. Cell pellets were combined with 10 μ L deuterated PBS with 0.05 mM trimethylsilylpropanoic acid-d₄ (TSP) (Cambridge Isotope Laboratories, Tewksbury, MA, USA) and packed into 4 mm zirconium oxide rotors. The rotors were placed in microcentrifuge tubes and briefly centrifuged ($100 \times g$ for 30 seconds) to remove air bubbles. The rotors were closed with a 50 μ L Kel-F insert and a cap (Bruker Corp., Billerica, MA, USA). At least three independent samples were prepared for each group.

2.10.2. Data acquisition

All measurements were carried out at 300 K and 5 kHz spinning rate on a 500 MHz NMR Bruker AVANCE II+ spectrometer (Bruker Corp., Billerica, MA, USA) equipped with a 4 mm HRMAS probe with a gradient coil allowing gradient pulses up to 34 G.cm⁻¹. Shimming for each sample was optimised using the D₂O resonance in the sample. Tuning and matching was optimized for each sample. The spectrometer was operated using TopSpin v3.2 (Bruker Corp., Billerica, MA, USA).

Solvent suppression using a NOESYPR1D pulse sequence

One-dimensional ¹H NMR spectra were acquired at 300 K using a solvent suppression pulse sequence based on a one-dimensional NOESY (*noesypr1d*) to saturate the residual ¹H water signal. The experiments were run with 4 dummy scans and 64 acquisition scans with an acquisition time of 4.09 s, relaxation delay 2 s and mixing time of 50 ms. 65.5k data points were recorded across a spectral width of 8012.82 Hz. Total acquisition time was 6 minutes 59 s. A line-broadening apodization function of 1.0 Hz was applied to all 1D HRMAS ¹H NMR free induction decays prior to Fourier transformation.

1D Carr–Purcell–Meiboom–Gill (CPMG)

One-dimensional T₂-edited Carr–Purcell–Meiboom–Gill ¹H NMR spectra were acquired using pulse sequences with continuous wave solvent presaturation (*cpmgpr1d*).²³⁶ All experiments were run with 4 dummy scans and 64 acquisition scans

with an acquisition time of 5.45 s and relaxation delay of 4 s. 65.5k data points were recorded across a spectral width of 6009.615 Hz. For the acquisition of CPMG spectra, total spin–spin relaxation delay ($2n\tau$) of 40 ms was used where the spin echo number was $n = 20$ and echo spacing $\tau = 1$ ms. Total acquisition time for this pulse sequence was 10 minutes 48 s. A line-broadening apodization function of 1.0 Hz was applied to all 1D HRMAS ^1H NMR free induction decays prior to Fourier transformation.

Correlation spectroscopy (COSY) ^1H - ^1H

Gradient COSY spectra were acquired using a standard Bruker pulse sequence (*cosygpprqf*).²³⁷ A data matrix of 300×4096 points covering 8012×8012 Hz was recorded with 64 scans for each increment, spectral width of 16 ppm, and a relaxation delay of 2 s. Total acquisition time was 12 h 19 minutes. Data was zero-filled to twice the original length. The FIDs were Fourier transformed with sine-bell functions and 0.3 Hz (F1) and 1 Hz (F2) exponential and 0.1 Hz Gaussian (F1 only) effective line broadening functions applied.

Hetero- nuclear single quantum correlation spectroscopy (HSQC) ^1H - ^{13}C

The spectra were obtained using the standard Bruker pulse sequence (*hsqcetgpsisp.2*).²³⁶ The acquisition parameters were as follows: number of scans 128, dummy scans 16, relaxation delay 4 s, spectral width 10 ppm (F2) and 165 ppm (F1), transmitter offset 4.7 and 75 ppm for the ^1H and ^{13}C dimension, respectively. 1024 points were acquired in F2 for each of 256 increments in F1 domain. Total acquisition time for each experiment was 18 h 23 minutes. Data was zero-filled to twice the original length. The FIDs were Fourier transformed with squared sine-bell functions (sine bell shift, SSB = 2) and 0.3 Hz (F1) and 1 Hz (F2) exponential and 0.1 Hz Gaussian (F1 only) effective line broadening functions applied.

T_2 -CPMG

The T_2 -CPMG experiment employed was a modified version of the standard Bruker 2D ^1H experiment (*cpmg*) with the addition of a presaturation pulse. The total duration of each spin echo was fixed to 1 ms ($\tau = 500$ μs), whereas the number of echoes in the pulse train was varied from 10 to 400. Relaxation delay was 5 s, the number of scans was 16, and total acquisition time was 42 minutes.

2D Diffusion Ordered Spectroscopy (DOSY)

Two-dimensional DOSY spectra were recorded using the longitudinal eddy current delay bipolar gradient pulse sequence (*ledbpgp2s*)²³⁸ with a diffusion delay (Δ) of 0.05 s, a diffusion-encoding pulse width (δ) of 2 ms, and gradient strengths increasing from $b = 124 - 1571 \text{ s}\cdot\text{mm}^{-2}$ in 16 linear steps. At each gradient strength, 32 scans and 65.5k data points were acquired with an acquisition time of 5.45 s, a relaxation delay of 4.0 s, echo time of 2.2 ms and a line broadening of 1 Hz. Total acquisition time was 1 h 23 minutes.

2.10.3. Data processing

All FIDs were pre-processed with TopSpin v3.2 (Bruker Corp., Billerica, MA, USA). Manual phasing and baseline correction were applied in MNOVA software (Mestrelab Research, Santiago de Compostela, Spain). All chemical shifts were referenced with respect to TSP at 0 ppm. Signal integrals were normalised to the total intensity of the spectral region from 0.5 to 8.5 ppm excluding water region (4.5 - 5.0 ppm). Spectral assignments were confirmed using literature values^{70,80}, Chenomx NMR Profiler v8.51 (Chenomx, Edmonton, Canada) and homo and heteronuclear correlation experiments (COSY and HSQC). For general statistical analysis such as by PCA, the normalised spectral regions between 0.5 and 8.5 ppm, with the exclusion of the water region (4.5–5.0 ppm), were binned (0.02 ppm) and Pareto scaled. Metaboanalyst v4.0 (University of Alberta, Canada)²³⁹ was used to identify significant features, which were then manually peak-picked on unbinned spectra and quantified relative to the control group (fold change). T_2 relaxation and diffusion data were analysed in MNOVA software (Mestrelab Research, Santiago de Compostela, Spain) or Dynamics Centre v2.5.1 (Bruker Corp., Billerica, MA, USA). The data was first fitted to a mono-exponential model, and the probability that the fit is not mono-exponential was calculated - for probability values above 0.7, the data was fitted to a bi-exponential model. The relative standard deviations of all diffusion fits to exponential decays were < 5%. Minimum S/N for the highest b-values was 42.9 (**Appendix 2**).

2.11. Solution-state NMR spectroscopy

2.11.1. Sample preparation

The dried organic fractions were dissolved in 500 μL of chloroform-d with 0.05% (v/v) tetramethylsilane-d4 (TMS) (Cambridge Isotope Laboratories, MA, USA). The dried aqueous

fractions were dissolved in 500 μL D_2O (Goss Scientific Instruments Limited, Crewe, UK) with 0.01% (v/v) TSP (Cambridge Isotope Laboratories, MA, USA). The dried media samples were dissolved in 500 μL D_2O (Goss Scientific Instruments Limited, Crewe, UK) with 0.01% (v/v) TSP (Cambridge Isotope Laboratories, MA, USA).

2.11.2. Data acquisition

^1H NMR spectra of cell extracts and growth media were recorded on a Bruker AVANCE II+ spectrometer (Bruker Corp., Billerica, MA, USA) operating at a frequency of 500.13 MHz and fitted with a 5 mm TXI probe.

1D NOESY

One-dimensional ^1H NMR spectra were acquired at 300 K using a solvent suppression pulse sequence based on a one-dimensional NOESY pulse sequence (*noesypr1d*) to saturate the residual ^1H water signal. The experiments were run with 4 dummy scans and 128 acquisition scans with an acquisition time of 4.09 s, relaxation delay 2 s and mixing time of 80 ms. Total acquisition time was 13 minutes 48 s. 65.5k data points were recorded across a spectral width of 8012.82 Hz. A line-broadening apodization function of 0.3 Hz was applied to all 1D ^1H NMR free induction decays.

COSY ^1H - ^1H

For the COSY, a standard Bruker pulse sequence (*cosygpprqf*) was used. A data matrix of 512×4096 points covering 8012×8012 Hz was recorded with 32 scans for each increment and a relaxation delay of 2 s. Total acquisition time was 12 h 19 minutes. Data was zero-filled to twice the original length. Spectra were Fourier transformed with sine-bell functions and 0.3 Hz (F1) and 1 Hz (F2) exponential and 0.1 Hz Gaussian (F1 only) effective line broadening apodization functions applied.

Heteronuclear Single Quantum Coherence Spectroscopy (HSQC) ^1H - ^{13}C

The spectra were obtained using the standard Bruker pulse sequence (*hsqcetgpsi2*)²³⁶. The acquisition parameters were as follows: number of scans 128, dummy scans 16, relaxation delay 1 s, spectral width 10 ppm (F2) and 165 ppm (F1), transmitter offset 4.7 and 75 ppm for the ^1H and ^{13}C dimension, respectively. 1024 points were recorded for each of 256 increments. Total acquisition time for each experiment was 10 h 15

minutes. Data was zero-filled to twice the original length. The FIDs were Fourier transformed with squared sine-bell (sine bell shift, SSB = 2) functions and 0.3 Hz (F1) and 1 Hz (F2) exponential and 0.1 Hz Gaussian (F1 only) effective line broadening apodization functions applied.

2.11.3. Data processing

All FIDs were pre-processed with TopSpin v3.2 (Bruker Corp., Billerica, MA, USA). All spectra were pre-processed in MNOVA software (Mestrelab Research, Santiago de Compostela, Spain): manual batch phasing and baseline correction, chemical shift referencing signal normalization, spectra alignment, peak-picking, and binning in the same way as for HRMAS NMR data. All chemical shifts were referenced with respect to TMS (organic samples) or TSP (aqueous samples) at 0 ppm. Further data processing was performed as described for HRMAS NMR spectroscopy.

2.12. *High gradient diffusion NMR spectroscopy.*

All measurements were carried out at 300 K and on a Bruker AVANCE IIIHD 400 MHz NMR spectrometer fitted with a 5 mm Diff50 z-diffusion probe for a wide bore magnet, comprising an actively shielded Z-gradient with strengths up to $50 \text{ G.cm}^{-1}.\text{A}^{-1}$ (up to 2800 G.cm^{-1}).

2.12.1. Sample preparation

Thawed cells (1×10^7 per sample) were washed in deuterated PBS (PBS powder dissolved in D₂O (Goss Scientific Instruments Limited, Crewe, UK). Cell pellets were resuspended in 100 μL PBS containing D₂O with 0.05 mM TSP (Cambridge Isotope Laboratories, MA, USA) and packed into 3 mm inserts.

2.12.2. Data acquisition

DOSY spectra were recorded using the same pulse sequence and diffusion parameters as for the HRMAS NMR diffusion experiments. The gradient strength was increased from $b = 6\text{-}420951 \text{ s.mm}^{-2}$ in 256 linear steps. For each gradient strength, 32 scans and 50k data points were acquired with an acquisition time of 5.21 s, a relaxation delay of 0.5 ms, and a line broadening of 1 Hz.

2.12.3. Data processing

Manual phasing and baseline correction were applied before peak-picking in Dynamics Centre v2.5.1 (Bruker Corp., Billerica, MA, USA). The data were fitted to a triexponential curve. Minimum S/N for the highest b-values was 21.3 (**Appendix 2**).

2.13. *Untargeted mass spectrometry analysis of lipids*

2.13.1. Sample preparation

The organic fractions were reconstituted in 50 μ L of methanol/chloroform (1:1) and vortexed thoroughly. Ten μ L of the sample was then diluted into 190 μ L of HPLC-grade propan-2-ol (Fisher Scientific, Loughborough, UK), acetonitrile (Honeywell, Charlotte, NC, USA) and water (Honeywell, Charlotte, NC, USA) (IPA:ACN:H₂O; 2:1:1). Samples were briefly vortexed to ensure complete mixing.

2.13.2. Data acquisition

Five μ L of sample was injected onto a C18 CSH column, 2.1 \times 100 mm (1.7 μ m pore size; 186005297, Waters Ltd, Wilmslow), which was held at 55°C using an Ultimate 3000 UHPLC system (Thermo Fisher Scientific, Waltham, MA, USA). The mobile phase comprises solvents A (ACN/H₂O; 60:40) and B (ACN/IPA; 10:90), run through the column in a gradient (40% B, increased to 43% B after 2 minutes, 50% B at 2.1 minutes, 54% B at 12 minutes, 70% B at 12.1 minutes, raised to 99% B at 18 minutes before returning to 40% for 2 minutes). Total run time was 10 minutes, with a flow rate of 0.500 μ L/min. In positive mode, 10 mM ammonium formate (Fisher Scientific, Loughborough, UK) was added to solvents A and B. Solvent additives were chosen based on current literature.²⁴⁰

Mass spectrometry was then carried out using the LTQ Orbitrap Elite Mass Spectrometer (Thermo Fisher Scientific, Waltham, MA, USA) in positive mode. Metabolites were ionised by heated electrospray before entering the spectrometer. The source temperature was set to 420°C, and the capillary temperature to 380°C. The spray voltage was set to 3.5 kV. Data was collected using the Fourier transform mass spectrometer (FTMS) analyser. The resolution was set to 60,000 and the data was obtained in profile mode. The full scan was performed across an m/z range of 110-2000.

2.13.3. Data processing

For data processing, spectra were converted from Xcalibur .raw files into .mzML files using MS Convert (Proteowizard) for analysis by XCMS within R studio. XCMS software was used to process data and identify peaks. Peaks were identified based on an approximate FWHM (full width at half maximum) of 5 seconds and a signal to noise threshold of 5. To improve peak identification, peaks had to be present in a minimum of 25% of the samples in one group. Peaks were annotated by accurate mass, using an automated R script and comparison to the LipidMaps database.²⁴¹ Intensity was normalised to internal standards, and cell number.

2.14. Targeted mass spectrometry analysis of choline compounds

2.14.1. Sample preparation

The dried aqueous fractions were reconstituted in 0.1 mL of an acetonitrile:10 mM ammonium carbonate water solution (7:3 v/v) containing a mixture of 3 internal standards at the concentration of 10 μ M (U - ^{13}C glutamic acid, 2D_3 -succinic acid and adenosine- $^{13}C_{10}$, $^{15}N_5$ 5' monophosphate).

2.14.2. Data acquisition

A Thermo Scientific UHPLC⁺ series coupled with a TSQ Quantiva mass spectrometer (Thermo Fisher Scientific, Waltham, MA, USA) was used with an ESI source, operated in positive and negative ion mode at the same time. The electrospray voltage was set to 3500 V for the positive ionisation and to 2500 V for the negative ionisation. Nitrogen at 48 mTorr and 420°C was used as a drying gas for solvent evaporation. The organic phases were analysed with a BEHAmide (150 \times 2.1 mm 1.7 μ m; Waters Ltd) column. The column was conditioned at 30°C. The mobile phase consisted of: (A) a 0.1% of ammonium carbonate water solution and (B) an acetonitrile solution. The mobile phase was pumped at a flow rate of 600 μ L/min programmed as follows: initially maintained at 20% of A for 1.50 minutes, then was subjected to a linear increase from 20% to 60% of A in 2.5 minutes and kept at this percentage for one minute and then brought back to the initial condition after 0.1 minutes. The full scan was performed across an m/z range of 10-500. The Xcalibur software (Thermo Fisher Scientific, Waltham, MA, USA) was used for data acquisition.

2.14.3. Data processing

Putative recognition of all detected metabolites was performed using a targeted MS/MS analysis. Calculated masses and mass fragments of the calculated compounds were reported relatively to the control group.

The fragmentation parameters were as follows:

Table 2.1. Fragmentation parameter for mass spectrometry analysis of choline compounds.

Compound	Retention Time [min]	Precursor (m/z)	Product (m/z)	Collision Energy [V]	RF Lens [V]
Choline	0.84	104.1	60.3	19	71
CDP	3.98	404	38	38	89
CDP-choline	3.84	489.1	184.111	15	60

2.15. Reverse transcription quantitative polymerase chain reaction (qPCR)

2.15.1. Sample preparation

RNA was extracted and purified in situ, using an RNeasy mini kit (74104, Qiagen, Hilden, Germany), following the manufacturer's instructions. Briefly, 350 μ L of lysis buffer was added to the cells in situ. Following lysis, 350 μ L of 70% ethanol was added, and the sample was well mixed by pipetting up and down, before transfer to a spin column. Samples were centrifuged ($9500 \times g$, 30 s), and the eluent was discarded. A series of washes with the provided buffers removed contaminants. First, 700 μ L of buffer RW1 was added to the column to remove biomolecules such as carbohydrates and fatty acids that non-specifically bind to the membrane. The samples were centrifuged at $9500 \times g$ for 30 s and the eluent discarded. Two 500 μ L washes with buffer RPE followed to remove traces of salts from the previous buffers. After the first addition, the samples were centrifuged at $9500 \times g$ for 30 s and the eluent discarded. After the second addition samples were centrifuged at $9500 \times g$ for 2 minutes and the eluent discarded. Spin columns were transferred to a fresh collection tube and centrifuged at full speed for one minute to dry the membrane. RNase free water (40 μ L) was then added to the spin column and samples centrifuged at $9500 \times g$ for one minute to elute the RNA.

The concentration and quality of RNA was determined using a NanoDrop-1000 spectrophotometer (NanoDrop Technologies, Wilmington, NC, USA) and then standardized to 50 ng/mL in a volume of 8 μ L for all samples. A two-step synthesis of cDNA was performed using the RT2 First Strand Kit (330404, Qiagen, Hilden, Germany). Genomic DNA was

removed by the addition of 2 μL of genomic elimination buffer followed by incubation at 42°C for 5 minutes in a PrimeG thermal cycler (Techne, Cole-Parmer, Stone, UK). Ten μL of a reverse transcriptase mix (containing the reverse transcription buffer BC3, RNase free water, the reverse transcriptase enzyme mix RE3, and the primer and external control mix P2 in a ratio of 4:3:2:1) was then added to each sample, mixed well, and incubated at 42°C for 15 minutes in the thermal cycler. The reaction was ended by increasing the temperature to 95°C for 5 minutes. Samples were cooled to 4°C. Subsequently samples were diluted with RNase free water to a total volume of 100 μL . For PCR, cDNA (5 μL) was mixed with 10 μL of a SYBR Green PCR mastermix containing ROX (330523, Qiagen, Hilden, Germany), 4.4 μL of RNase-free water and 0.6 μL of a primer mix (Qiagen, Hilden, Germany) for one of the genes in question in each well of a 96-well plate (4346906, Applied Biosystems, Foster City, CA, USA).

2.15.2. Data acquisition

Samples were analysed using a Step One Plus Real Time Cycler (Applied Biosystems, Foster City, CA, USA), quantified using the $-\Delta\Delta C_T$ method²⁴² with expression normalized to the housekeeping gene ACTB (PPH00073G, Qiagen, Hilden, Germany). The method is outlined in **Figure 2.1**.

2.15.3. Data processing

ΔC_T values were calculated by first subtracting the C_T -value for the housekeeping gene from the C_T -value of the gene of interest for each sample. The ΔC_T -value from a treated sample is then subtracted from the ΔC_T -value from a control sample giving the $\Delta\Delta C_T$ value for that sample. The fold-change for each gene is calculated using the equation: $\text{fold change} = 2^{(-\Delta\Delta C_T)}$. The following genes linked to lipid metabolism were assessed: ABHD5 (PPM37242A), LPCAT3 (PPM36695A), FABP5 (PPM24572C), PPARG (PPM05108C), ACOX1 (PPM04407B) and LIPE (PPM03313A), all purchased from Qiagen (Hilden, Germany).

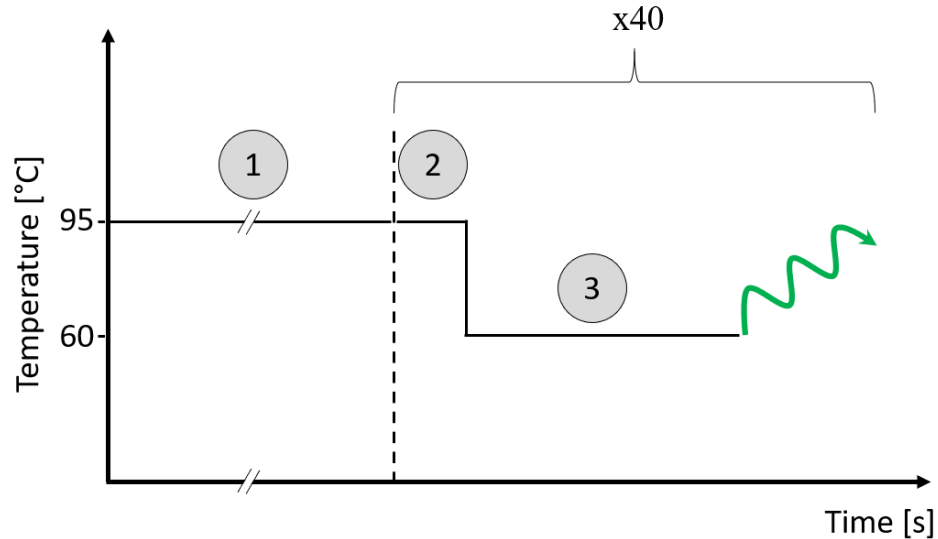


Figure 2.1. Cycling method for qPCR analysis. ① 10-minute incubation at 95°C activated the HotStart DNA Taq polymerase; ② 15-second incubation at 95°C denatured the cDNA; ③ 1-minute incubation at 60°C, in which primers annealed to the template and were elongated by the polymerase. Steps ② and ③ were repeated 40 times. Fluorescence measurements were taken at the end of each cycle: excitation and emission maxima for SYBR Green dye were at 494 and 521 nm, respectively.

2.16. The Next Generation Sequencing

2.16.1. Sample preparation

RNA was extracted and purified in situ, using the RNeasy mini kit (74104, Qiagen, Hilden, Germany), following the manufacturer's instructions. Briefly, 350 μL of lysis buffer was added to the cells in situ. Following lysis, 350 μL of 70% ethanol was added, and the sample was well mixed by pipetting up and down, before transfer to a spin column. Samples were centrifuged ($9500 \times g$, 30 s), and the eluent was discarded. A series of washes with the provided buffers removed contaminants. First, 700 μL of buffer RW1 was added to the column to remove biomolecules such as carbohydrates and fatty acids that non-specifically bind to the membrane. The samples were centrifuged at $9500 \times g$ for 30 s and the eluent discarded. Two 500 μL washes with buffer RPE followed to remove traces of salts from previous buffers. After the first addition, samples were centrifuged at $9500 \times g$ for 30 s and the eluent discarded. After the second addition samples were centrifuged at $9500 \times g$ for 2 minutes and the eluent discarded. Spin columns were transferred to a fresh collection tube and centrifuged at full speed for one minute to dry the membrane. RNase free water (40 μL) was then added to the spin column and samples centrifuged at $9500 \times g$ for one minute to elute the RNA.

2.16.2. Data acquisition

RNA concentration was determined using a NanoDrop-1000 spectrophotometer (NanoDrop Technologies, Wilmington, NC, USA). The RNA integrity check was evaluated using an Agilent 2100 Bioanalyzer (Agilent Technologies, Santa Clara, CA, USA). Transcriptome sequencing was performed by the Sequencing Facility of The Department of Biochemistry, University of Cambridge (Cambridge, UK) on an Illumina NextSeq500 (San Diego, CA, USA) according to the manufacturer's instructions using a 75-cycle paired-end sequencing strategy. Four biological replicates were used for each group.

2.16.3. Data processing

RNA-Seq reads for each sample were first cleaned using Seqtk tool (<https://github.com/lh3/seqtk>) and then aligned to the mouse genome (mm10, Genome Reference Consortium Mouse Build 39) using TopHat 2.1.1 software.²⁴³ Normalization was carried out using TMM (trimmed mean of M values) and FPKM (Fragments Per Kilobase of exon model per Million mapped reads) values were calculated by an in-house R script. Differential expression analysis and pathways enrichment analysis was performed using REACTOME with default settings.²⁴⁴

2.17. Lipid droplet visualisation

2.17.1. Sample preparation

After the apoptotic treatment, differentiated myotubes (5×10^4 cells per mL) were transferred onto 35 mm glass base collagen-coated dishes (Nunc®, Thermo Fisher Scientific, Waltham, MA, USA) and left to attach overnight. The samples were incubated with 1 mL staining solution (50 μ g/mL BODIPY in PBS) for 10 minutes in the dark, washed with PBS twice before being observed under a microscope, and photographed.

2.17.2. Data acquisition

Images were acquired on a Leica TCS SP8 confocal microscope (Leica Biosystems, Wetzlar, Germany) using a 1.3 NA, 63x oil immersion objective lens, a scan speed of 400 Hz and a line averaging of 2. Multichannel imaging was performed on a $100 \mu\text{m} \times 100 \mu\text{m}$ area (sampled at 1024×1024 pixels) using an excitation laser line of 488 nm (emission detection 500-520 nm).

2D time-lapse sequences were taken every 5 seconds resulting in 50-60 images of a 50×50 μm area (2048×2048 pixels).

2.17.3. Data processing

Image analysis and measurements were carried out using ImageJ software package v1.52i (National Institute of Health, Rockville, MD, USA). The results were averaged across 548, 1183 and 560 LDs in control, cisplatin, and etoposide samples, respectively. Time-lapse images were pre-processed to extract object characteristics and trajectories using standard image processing techniques and tracking algorithms from the TrackMate plugin (ImageJ).²⁴⁵

2.18. Data analysis and statistics

Univariate and multivariate statistical analyses was carried out in Metaboanalyst v4.0 (University of Alberta, Canada). One-way ANOVA with the *post hoc* Fisher's least significant difference analysis was used when multiple comparisons were made. Student's unpaired t-test with equal variance was used to compare two groups (Microsoft Excel, Redmond, WA, USA). Unless otherwise stated, data are presented as mean \pm standard error of the mean (SEM) and represent a biological variance of at least 3 repeats. FRD adjusted²⁴⁶ p-values < 0.05 were considered significant.

Mean square displacement analysis was based on NMR diffusion data and calculated from the following equation: $\langle x \rangle^2 = 2D\tau$, where $\langle x \rangle^2$ – mean square displacement, D – diffusion rates measured by NMR, τ – diffusion time (50 ms). For curve and line fitting, partial least-squares regression was used (Microsoft Excel, Redmond, WA, USA).

Chapter 3. Method optimization for HRMAS ^1H NMR spectroscopy.

3.1. Introduction

Metabolic profiling of intact cells by HRMAS ^1H NMR spectroscopy can provide valuable information about biological systems (examples of studies are reviewed in **Chapter 1**). Intact-cell studies using HRMAS ^1H NMR spectroscopy often pose a question about cell viability during the experiments and hence the effect of magic angle spinning on the biological interpretation of data. Cells subjected to high centrifugal forces during these experiments may suffer mechanical stress, structural distortion, or rearrangement of intracellular environment followed by reduced cell integrity. Sample packing procedures and limited oxygen and nutrients in a sealed MAS rotor also may contribute to cellular stress.

Several studies regarding cell viability during HRMAS have been published. Li and colleagues correlated the NMR signal intensities in HSQC spectra with the rotor spinning rates.²⁴⁷ They showed that an increase in a spinning rate (up to 2.5 kHz) resulted in increased NMR signal intensities, which was explained by more efficient averaging of anisotropic interactions. However, cell integrity was compromised due to the higher centrifugal forces. They reported a 7% decrease in bacterial cell viability after a 2-hour HRMAS ^1H NMR experiment at 2.5 kHz. Another study on bacterial cell viability by Zandomeneghi and colleagues reported ‘*roughly the same*’ number of colony-forming units (an estimate for the number of viable bacteria in a sample) before and after a 1-hour HRMAS NMR experiment.²⁴⁸ They demonstrated that bacteria survived despite enduring oxygen depletion and mechanical stress during the measurement period inside the sealed rotor spinning at 8 kHz. Other studies support this finding by reporting an insignificant effect of spinning on viability of intact yeast or bacterial cells.^{249,250}

Mammalian cells were found to be more fragile when subjected to faster HRMAS rates. Aime and colleagues compared cell viability, before and after HRMAS ^1H NMR experiments, across different mammalian cell lines including human lymphoma, rat hepatocyte, and mouse fibroblasts.²⁵¹ They concluded that while spinning at 1.5 kHz for short times did not affect cell integrity, cell death was more pronounced at 4 kHz. Some cell lines were more affected than others, for example, hepatocytes showed very low viability at the end of the NMR experiment whereas mouse fibroblasts preserved over 70% viability. Duarte and colleagues also reported that the behaviour of cells under HRMAS conditions depended on cell type.⁴⁸ They found that between 5 and 25% of cells were compromised during a 2-hour HRMAS NMR experiment at 4 kHz, amniocytes being most affected and osteosarcoma cells being least affected. Similar studies were performed on adipocyte cells (15-19% decrease in cell viability after 2 h HRMAS at 3.5 kHz)²⁵² and for neuronal cells (10% decrease in cell viability after 0.5 h HRMAS at 5 kHz).⁸⁰ This suggests that for some cell lines, a significant loss in viability is likely to hinder HRMAS NMR studies.

The role of spinning the sample is to average-out the residual dipolar interactions and magnetic susceptibility caused by the heterogeneous nature of the intact cells and consequently improve the spectral resolution. As discussed previously, cell viability is a major limiting factor for applying high spinning rates for metabolomics studies. A commonly used range of spinning rates for mammalian cells is 1 – 6 kHz.^{80,196,247,248,253,254} This value depends on cell resistance to mechanical stress and needs to be optimized for each cell line. The minimum spinning rate is governed by the required spectral resolution and the presence of spinning sidebands – signals that result from modulation of the magnetic field at the spinning frequency. The sidebands appear on either side of a large genuine resonance at a separation equal to the spinning rate. Renault and colleagues demonstrated that the number and the magnitude of spinning sidebands could be reduced by modifying sample packing procedures, i.e. volume and shape of the sample in the rotor.²⁵⁵ Optimisation of spinning rate is important for obtaining high-quality NMR spectra, in which the sidebands do not hinder interpretation of the spectrum and integration of the peak at the isotropic chemical shift.

Sample packing affects not only the presence of sidebands but also the S/N, line symmetry, and line broadening. Intact cells are usually packed in a 4 mm Zirconia rotor and the sample volume is adjusted with Teflon® or Kel-F® inserts to 12, 30, or 50 μL .²⁵⁶ Inserts facilitate homogenous sample packing, ensure a tight seal, and prevent solvent evaporation or

contamination of the probe with solvent. In addition, the sample volume and geometry can be adjusted with inserts. The shape of samples inside the rotor can be spherical or cylindrical (**Figure 3.1**). In the 12 μL rotor, the near-spherical small sample volume positioned at the centre of the radiofrequency coil shows less spatial magnetic field variability than the cylindrical geometries of the 30 and 50 μL rotors.²⁵⁷ Small volume helps reduce the effects of differences in magnetic field susceptibility across the sample. In contrast, greater volumes are more prone to spatial variation in the magnetic field i.e., line broadening caused by magnetic susceptibility is more pronounced. The main benefit of using the 30 and 50 μL rotors is improved S/N ratio. In addition, disposable inserts are practical for multiple-sample runs, and allow a straightforward exchange of samples without having to wash and dry the rotor between runs.

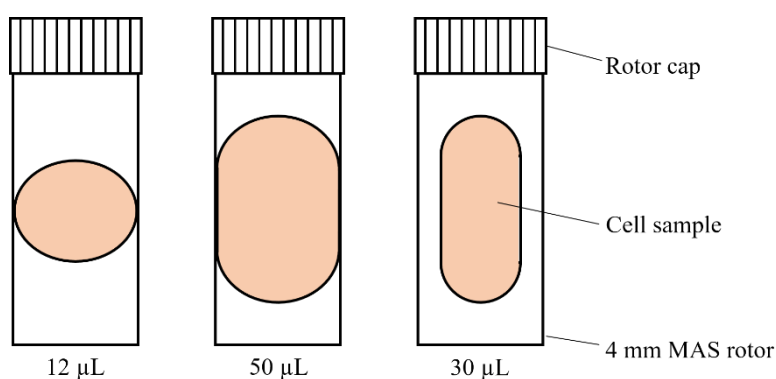


Figure 3.1. HR-MAS rotor systems with different sample chamber geometries: 12 μL insert restricts the sample to a small semi-spherical volume – diameter = ~ 2.84 mm; 50 μL insert restricts the sample to a wide cylindrical volume – length = ~ 7.3 mm; disposable 30 μL insert restricts the sample to a narrow cylindrical volume - length = ~ 7.3 mm.

The number of cells available is an important consideration when choosing the inserts. In previous studies, the authors used $10^5 - 10^7$ cells per sample.^{48,70,194,195,247,258} Small cells such as glioma require a higher number of cells per sample, while differentiated myotubes require a lower number of cells per sample (**Figure 3.2**).

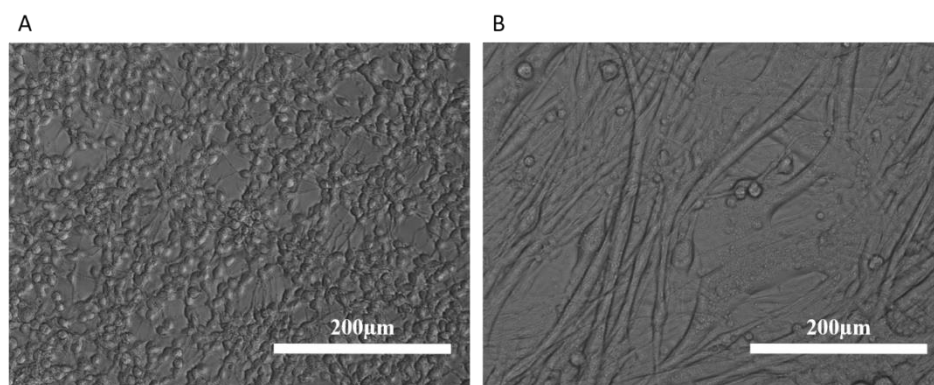


Figure 3.2. Light microscopy images of C6 glioma cells (A) and C2C12 myotubes (B). The length of glioma cells is 12-14 μm , while the length of myotubes is 130-520 μm .

In metabolomics, the most commonly used NMR pulse sequence is the 1D NOESY with water presaturation.³⁹ It is relatively easy to set up, does not require advanced NMR expertise to optimize parameters, and it has good water suppression ability without impacting metabolite resonances or distorting the baseline.²⁵⁹ This pulse sequence is suitable for liquid samples such as blood, urine, or cell extracts. Some samples contain a high concentration of high-molecular-weight species and their resonances mask the signals from metabolites. In this case, broad resonances can be removed by applying a 1D CPMG pulse sequence with a T_2 relaxation filter, a process referred to as spectral editing.^{69,258} When higher-molecular weight species are of interest, a diffusion edited 1D DOSY can be applied to reduce the signal from small metabolites.²⁶⁰

The spectra of biological samples are complex and difficult to analyse without additional 2D NMR experiments for metabolite identification. Homonuclear and heteronuclear 2D experiments such as ^1H - ^1H COSY, J-resolved, ^1H - ^{13}C HSQC, and ^1H - ^{15}N HSQC spectra can greatly enhance metabolite identification by providing additional information about atomic connectivity^{54,66,131} They also improve spectral resolution by dispersing signals into a second dimension, thus they have been used to aid quantification of metabolites.²⁶¹⁻²⁶³

3.2. Aims

All NMR experiments require the adjustment of different parameters to ensure a high S/N and good quality NMR spectrum. In **Chapter 3**, I describe preliminary experiments that aim to optimize experimental procedures and instrumental parameters for obtaining good quality HRMAS ^1H NMR data of intact cells. I report the results from the following experiments:

- Optimization of sample-packing procedures
- Optimization of NMR experimental parameters including:
 - Spinning speed
 - NMR experiment duration and cell viability
 - Optimization of 1D pulse sequences: NOESY, CPMG, DOSY
- Comparison of HRMAS and solution-state NMR spectra of intact cells
- Comparison of HRMAS NMR spectra of intact cells and solution-state NMR spectra of cell extracts.
- Metabolite assignment for myotubes (muscle cells)
- Comparison of HRMAS NMR metabolic profiles of different cell lines: muscles, glioma, adipocyte, liver.

3.3. Results and discussion

3.3.1. The effect of sample packing on spectral quality

Several different rotors and inserts are commercially available for HRMAS NMR experiments (Bruker, Revolution NMR, Doty Scientific). The choice of the rotor/insert is a trade-off between the volume of the sample available and the quality of spectra required. For biological applications, 4 mm rotors with inserts giving an active volume of 12 μL or 50 μL are commonly used.

Three different 4 mm rotors from Bruker BioSpin were investigated: an 80 μL rotor with a 30 μL disposable insert (**Figure 3.3A**), a 50 μL rotor with a 50 μL insert (**Figure 3.3B**), and a 12 μL rotor with a 12 μL insert (**Figure 3.3C**). Three spectra were recorded for each group. The spectra were assessed based on the shape of the reference resonance at 0 ppm (TSP) and S/N. Sharp and symmetric resonances are characteristics of good quality spectra.

A sample that contained only a solution of TSP in the disposable insert gave a sharp resonance with a broad shoulder and the manual shimming was not sufficient to correct it. The metabolites in intact cells also gave rise to asymmetric resonances (indicated by arrows, **Figure 3.3A**). The elongated geometry of cell samples packed in the disposable insert might cause magnetic susceptibility artefacts in the z-direction. The sample packed in the 12- μL insert gave a fairly symmetric but broad TSP resonance, while the sample packed into the 50- μL insert gave a

symmetric and relatively sharp TSP resonance. The metabolite resonances were comparable between the two inserts and the loss of S/N observed for the 12- μ L samples was not significant for metabolomic studies. However, the packing procedure was easier for the 50- μ L insert, making it more reproducible with shorter manual shimming times per sample. Therefore, it was used in subsequent experiments.

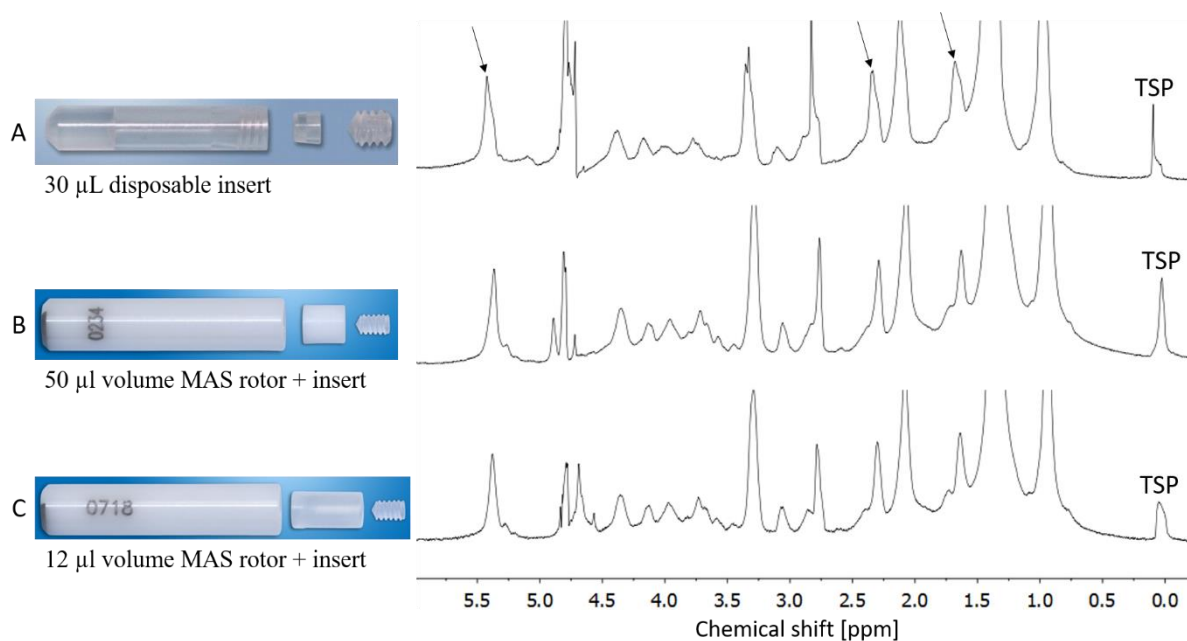


Figure 3.3. The effect of sample packing on spectra quality. Representative 500 MHz HRMAS ^1H NMR solvent suppressed spectra of intact cell samples (spinning at 5 kHz) packed in: 80 μL rotor + disposable 30 μL insert (A), 50 μL rotor + 50 μL insert (B), and 12 μL rotor + 12 μL insert (C). TSP was added as a reference compound and its resonance shape compared across the spectra. The images of inserts were taken from www.bruker.com.

3.3.2. The effect of different spinning rates on cell samples

The optimum spinning rates were investigated to ensure the integrity of biological samples and good quality of HRMAS ^1H NMR spectra. Previously, it was reported that spinning rates up to 6 kHz did not significantly alter the metabolic profiles of intact cells.^{78,80} **Figure 3.4** shows a set of HRMAS ^1H NMR spectra of intact cells recorded at different spinning rates. Peak widths for TSP, lactate, and creatine were measured from the spectra to assess changes in line broadening with spinning rates (**Table 3.1**). The peak widths did not vary significantly with spinning rates, demonstrating that even at a spinning rate of 1 kHz residual anisotropic interactions were removed in this system.

Table 3.1. Peak widths of TSP, lactate, and creatine at different spinning rates. The peak width values do not change significantly with spinning rates.

spinning rate [kHz]	peak width [Hz]		
	TSP	lactate	creatine
1	2.87	4.57	4.36
2	2.75	4.38	4.23
3	2.73	4.48	4.41
4	2.74	4.55	4.55
5	2.67	4.48	4.26
6	2.72	4.58	4.57
Mean	2.75 ± 0.06	4.51 ± 0.07	4.40 ± 0.13

Figure 3.4B shows SBs of TSP, lactate, and partially suppressed water resonances. The chemical shift scale is presented in Hz to highlight the link between the spinning sideband chemical shift and the spinning rate (at 1 kHz, the sidebands of water are present at frequency spacing of 1 kHz). The left spinning sideband of the water resonance was visible in the spectra recorded at 1, 2 and 3 kHz. The right spinning sideband was obscured by overlapping resonances (expected at frequencies of ~1350 Hz and ~350 Hz for the 1 kHz and 2kHz rates, respectively). For the rates above 4 kHz, the spinning sidebands of water were outside of the presented chemical shift range. At 5 kHz, the sidebands from TSP and lactate became visible as they shifted downfield from the crowded area of the spectra (0.5 – 2 kHz). The intensities of the spinning sidebands were low and did not significantly hinder interpretation of the spectra but could potentially cause errors in qualitative analysis of metabolomics data. The spinning rate chosen for all subsequent experiments was 5 kHz, for which the sidebands of the high-intensity resonances were outside of the chemical shift range of interest.

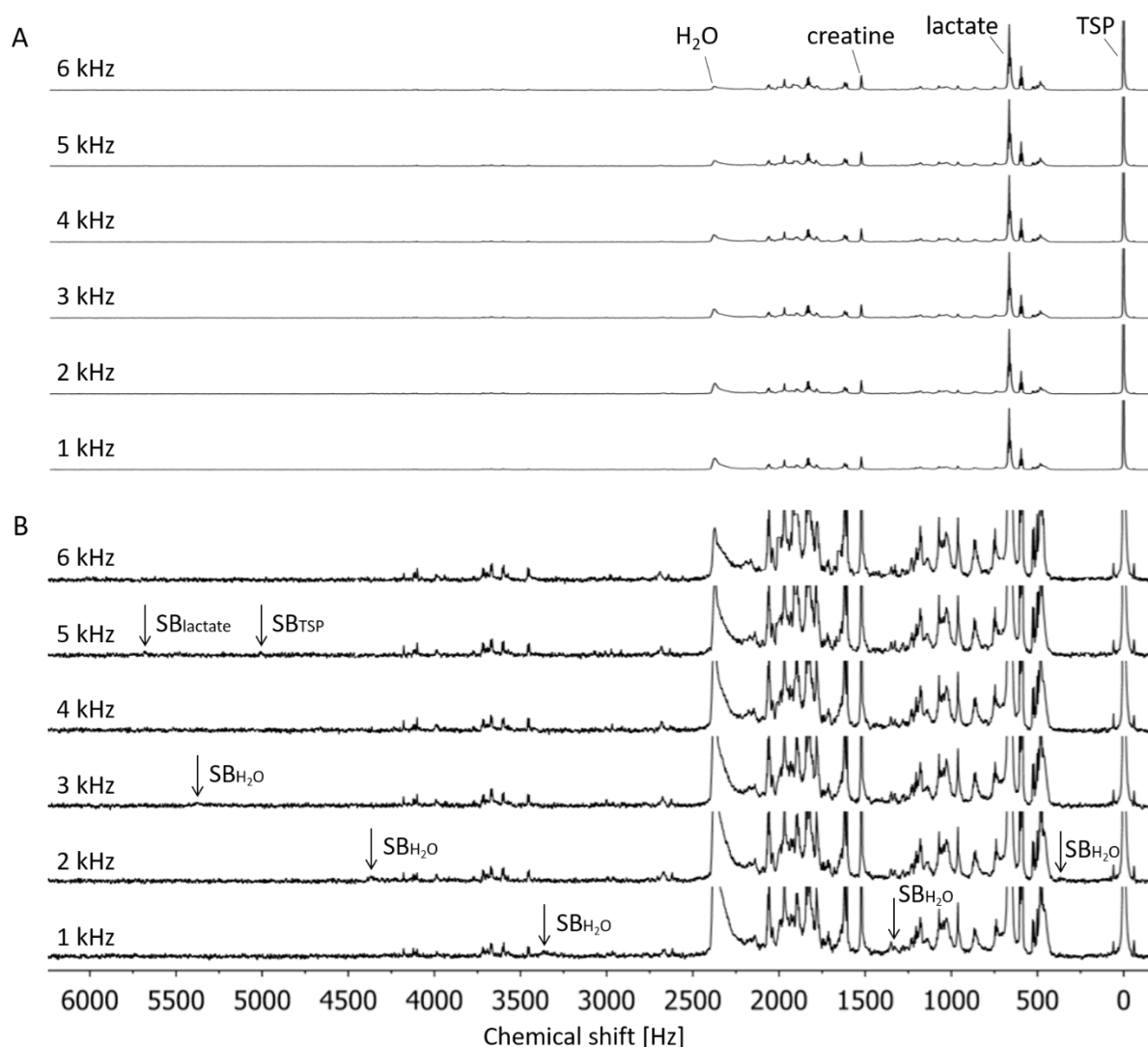


Figure 3.4. 500 MHz HRMAS ¹H NMR solvent suppressed CPMG spectra of intact cells at six different spinning rates. The chemical shift scale is presented in Hz to highlight the interaction between the spinning sideband chemical shift and the spinning rate. **A)** Assignment of selected resonances used for measuring changes in line broadening at different spinning rates (**Table 3.1**). **B)** Expanded NMR region showing the spinning sidebands. The spinning sidebands of water are visible at low spinning rates. The sidebands of lactate and TSP are visible at 5 kHz.

3.3.3. Impact of NMR experiment duration and cell integrity

3.3.3.1. Cell viability assessed by the Trypan blue assay

Cell sample integrity was tested before and after HRMAS ¹H NMR experiments with a Trypan blue exclusion assay. C2C12 differentiated muscle cells were incubated with common drug vehicles: PBS, DMF, or DMSO for 48 h, harvested and packed in a 50- μ L rotor. Cell viability was measured before and after 0.5 h and 3.5 h of spinning at 5 kHz in the NMR spectrometer

(**Figure 3.5**). There was no significant decrease in the cell viability of samples after 0.5 h of spinning, with cell viability being greater than 87% for each group. This indicated that short NMR experiments on intact cells run under biologically meaningful conditions. The cell viability of samples kept in the NMR instrument for 3.5 h decreased by 10 – 12%; the lowest value of viable cells recorded for the DMF group was 76 %.

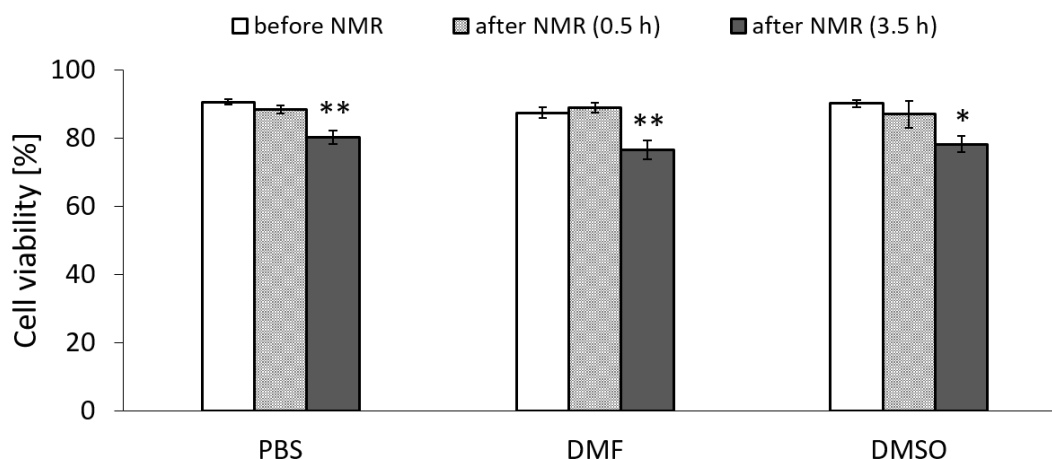


Figure 3.5. The effect of the duration of HRMAS NMR experiments on cell viability. The viability of cells incubated with PBS, DMF, or DMSO was measured before (□) and after the HRMAS ^1H NMR experiments (■ 0.5 h, ■ 3.5 h, 5 kHz spinning). The columns represent the percentage of Trypan blue negative cells (viable cells), error bars represent SEM, $n = 3$, ANOVA: * $p > 0.05$, ** $p > 0.01$ (FDR-adjusted values), post hoc test: before NMR vs 3.5 h after NMR.

3.3.3.2. Cell viability by HRMAS ^1H NMR spectroscopy

NMR spectroscopy can also provide information about decreasing cell viability. By recording a series of 1D ^1H NMR spectra, we can monitor time-dependent metabolic changes induced by HRMAS conditions. Identification of changes in metabolic profiles of intact cells induced by limited oxygen and nutrients, and exposure to mechanical stress could help to establish whether the changes are the same for treated and untreated cells and validate control models for HRMAS ^1H NMR experiments. HRMAS ^1H NMR spectra were recorded immediately after the intact cells were sealed in the rotor (reference spectrum) and after 3.5 h of spinning at 5 kHz in the NMR instrument. The spectrum recorded after 3.5 h (**Figure 3.6**, dark blue) showed an increase in several resonance intensities compared with the reference spectrum (**Figure 3.6**, light blue), including lactate, glutathione, and choline.

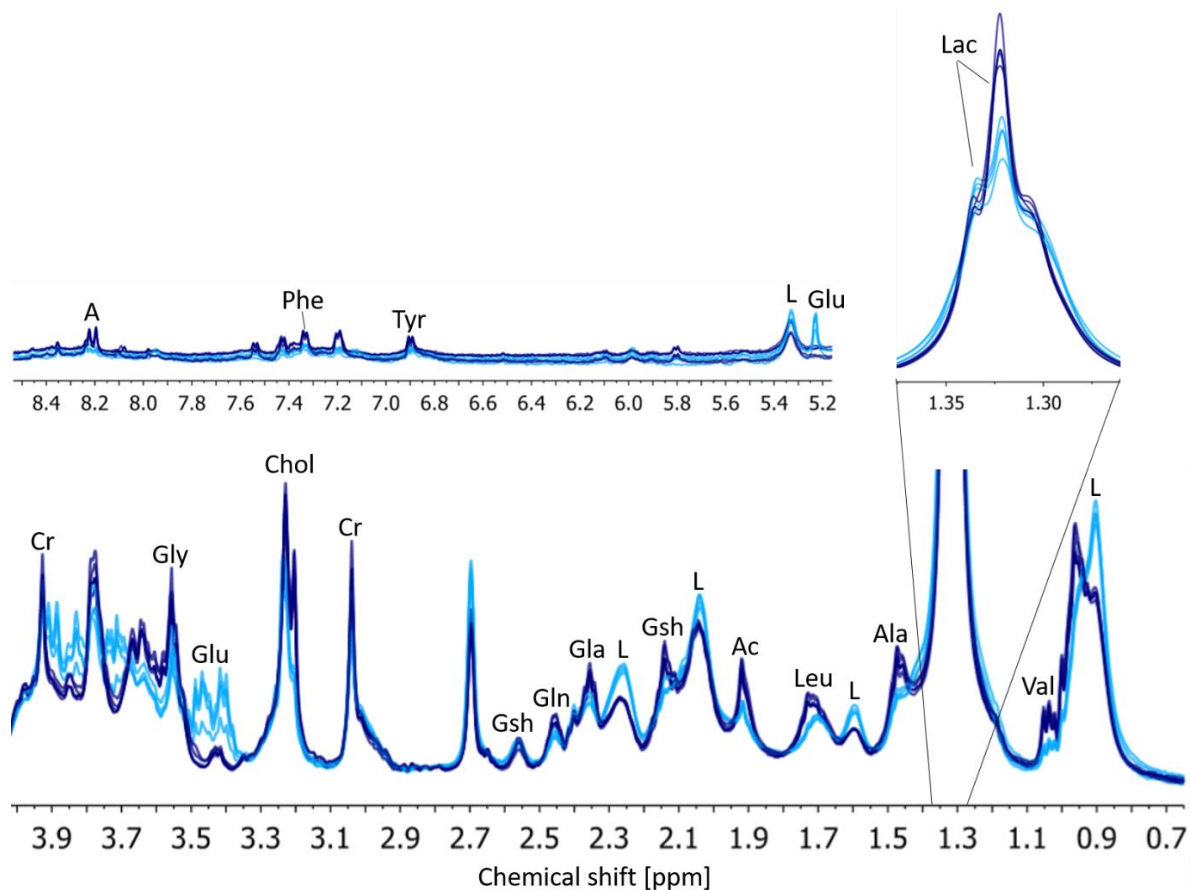


Figure 3.6. Superimposed 500 MHz HRMAS ^1H NMR spectra recorded immediately after the intact cells were sealed in the rotor (light blue, $n = 4$) and after 3.5 h of spinning at 5 kHz in the NMR instrument (dark blue, $n = 4$). Quantitative changes in metabolite resonances are reported in **Table 3.2**. Lac – lactate, Ala – alanine, Glu – glucose, Gla – glutamate, Gln – glutamine, Gly – glycine, Val – valine, Leu – leucine, Gsh – glutathione, Cr – creatine, Chol – choline, L – lipids, A – adenosine, Phe – phenylalanine, Tyr – tyrosine.

The increase in resonance intensities may result from cell disintegration and a partial metabolite release. Extracellular metabolites tumble faster, become more NMR-visible, and give rise to sharper resonances of higher intensities. Another reason for the increased metabolite resonances may lie in cell swelling and remodelling biochemical reactions as a result of suboptimal cell culture conditions in the NMR instrument.

An increase in lactate levels, as measured by increased peak area in the spectra, is a common marker of anaerobic metabolism and occurs when cells become hypoxic.²⁶⁴ This is consistent with NMR experimental conditions where cells endure inadequate oxygenation. Similarly, the concentration of glutathione is known to increase during hypoxic conditions to facilitate glutathionylation. An increase in glutathionylation of the sodium-potassium pump (Na, K-ATPase) results in an increase in cell viability under hypoxic conditions.^{265,266} The increase in

choline compounds may indicate membrane degradation. Choline serves as a precursor for the synthesis of membrane phospholipids: phosphatidylcholine and sphingomyelin. During membrane degradation, phosphatidylcholine and sphingomyelin can be released and hydrolysed to choline.²⁶⁷

In contrast, intracellular glucose levels drastically decreased after the 3.5 h NMR experiment, most likely because it was anaerobically metabolised into lactate and amino acids such as leucine, alanine and valine. Interestingly, a small decrease in the lipid resonances was also observed, indicating that the cells might have used cellular lipids as a secondary energy source. Since cells cannot utilize lipids as a source of energy under hypoxic conditions, the decrease in lipids likely happened before oxygen decreased to a critical level.²⁶⁸ This observation may be important for studying lipid accumulation during apoptosis by HRMAS ¹H NMR spectroscopy studied subsequently in this thesis.

The significant changes in metabolic profiles of intact cells induced by the NMR experimental conditions needed to be accounted for. I tested whether the metabolic profiles of intact cells undergo comparable changes when treated with anticancer agents. I compared the reference spectra of control, cisplatin-, and etoposide-treated cells with their respective 3.5 h spectra. The most significant changes in metabolite concentration induced by the 3.5-hour HRMAS ¹H NMR experiment are presented in **Table 3.2**. The data showed that the metabolic profiles of treated intact cells also changed under the HRMAS conditions and the changes were compared with the untreated intact cells. The statistical analysis confirmed this observation.

Figure 3.7 shows a PCA score plot comparing control, cisplatin, and etoposide samples at time 0 h and 3.5 h. The clustering patterns for the reference spectra and the 3.5 h spectra are similar among the groups – both treated and untreated samples are clustered the left of the PC1 axis. ANOVA analysis showed that the metabolic changes induced by the HRMAS conditions were not significantly different across the groups. This finding demonstrated that the HRMAS experimental conditions affected the treated and untreated cells in a similar manner. This suggests that NMR-induced cellular stress can be corrected for by taking appropriate control measures. The effect of NMR experimental conditions can be reduced to a minimum when reporting data relative to an untreated control group.

Table 3.2. Percentage change in metabolite signal intensities induced by a 3.5 h HRMAS ^1H NMR experiment as compared with reference intensities recorded right after the intact cells were sealed in the rotor. The percentage was calculated for control, cisplatin-, and etoposide treated cells. The reference spectra and the 3.5 h spectra are significantly different in each group; the change is consistent for all groups.

Metabolite	Control	Cisplatin	Etoposide
Valine	89.1 \pm 6.6 \uparrow	92.9 \pm 4.3 \uparrow	91.5 \pm 3.9 \uparrow
Lactate	16.6 \pm 1.7 \uparrow	9.0 \pm 1.4 \uparrow	12.3 \pm 2.8 \uparrow
Alanine	37.9 \pm 4.4 \uparrow	36.4 \pm 2.8 \uparrow	35.8 \pm 1.1 \uparrow
Leucine	46.5 \pm 4.1 \uparrow	49.0 \pm 1.9 \uparrow	45.8 \pm 3.7 \uparrow
Acetate	33.0 \pm 3.5 \uparrow	36.9 \pm 1.5 \uparrow	37.2 \pm 2.1 \uparrow
Glutathione	28.4 \pm 4.2 \uparrow	25.0 \pm 0.7 \uparrow	28.6 \pm 1.9 \uparrow
Glutamate	15.9 \pm 3.1 \uparrow	8.4 \pm 2.2 \uparrow	12.0 \pm 2.2 \uparrow
Glutamine	26.8 \pm 4.4 \uparrow	31.0 \pm 0.8 \uparrow	29.8 \pm 1.5 \uparrow
Creatine	9.4 \pm 3.6 \uparrow	11.5 \pm 4.6 \uparrow	14.0 \pm 5.0 \uparrow
Choline	29.6 \pm 2.0 \uparrow	26.6 \pm 4.5 \uparrow	27.5 \pm 2.4 \uparrow
Glycine	48.8 \pm 4.4 \uparrow	44.1 \pm 2.5 \uparrow	39.5 \pm 2.2 \uparrow
Dimethylamine	27.8 \pm 1.4 \downarrow	23.9 \pm 2.1 \downarrow	24.9 \pm 0.9 \downarrow
Glucose	84.4 \pm 7.2 \downarrow	80.4 \pm 7.6 \downarrow	75.1 \pm 2.3 \downarrow
Lipids 0.9ppm	27.7 \pm 0.8 \downarrow	23.2 \pm 1.7 \downarrow	25.1 \pm 1.9 \downarrow
Lipids 1.59 ppm	25.4 \pm 0.3 \downarrow	22.2 \pm 1.8 \downarrow	24.7 \pm 2.2 \downarrow
Lipids 2.04 ppm	10.8 \pm 0.8 \downarrow	8.7 \pm 1.5 \downarrow	9.3 \pm 0.8 \downarrow
Lipids 2.26 ppm	25.3 \pm 0.4 \downarrow	20.5 \pm 1.3 \downarrow	24.5 \pm 0.6 \downarrow
Lipids 5.33 ppm	29.0 \pm 7.5 \downarrow	30.3 \pm 1.1 \downarrow	30.0 \pm 2.3 \downarrow
Tyrosine	127.4 \pm 13.0 \uparrow	82.0 \pm 10.4 \uparrow	66.5 \pm 4.5 \uparrow
Adenosine	127.5 \pm 14.6 \uparrow	88.9 \pm 13.6 \uparrow	76.3 \pm 4.4 \uparrow
Phenylalanine	122.3 \pm 7.3 \uparrow	92.2 \pm 10.6 \uparrow	81.8 \pm 6.0 \uparrow

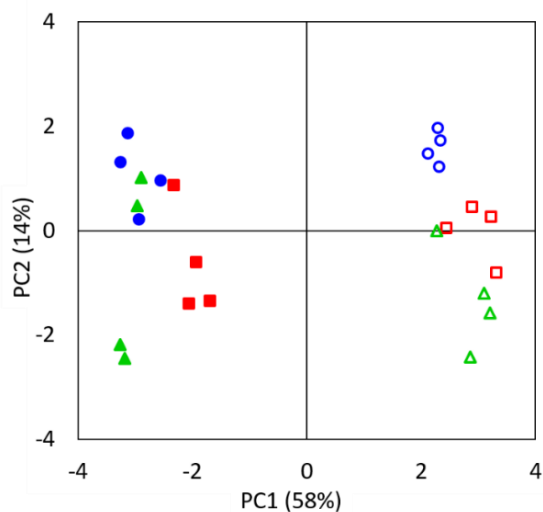


Figure 3.7. Two-dimensional PCA score plot derived from the HRMAS ^1H NMR spectra of control (green triangles), cisplatin- (red squares), and etoposide- (blue circles) treated intact cells recorded at time 0 h (empty shapes) and 3.5 h (filled shapes). One data point represents one sample, $n = 4$. The numbers in brackets represent the percentage of variability explained by each PC.

3.3.3.3. Cell sample recovery after HRMAS NMR experiments

Further investigation proved that cells recovered from the HRMAS NMR experiments can be reseeded. **Figure 3.8** shows images of cells before harvesting for the NMR experiment (**A**), recovered cells from the NMR experiment 12 h after seeding (**B**), and 48 h after seeding (**C**). At first, the recovered cells showed low confluence and there were several dead cells observed (red arrows). After 48 h, the cells looked healthy and were 70% confluent. The cell culture showed no signs of bacterial infection.

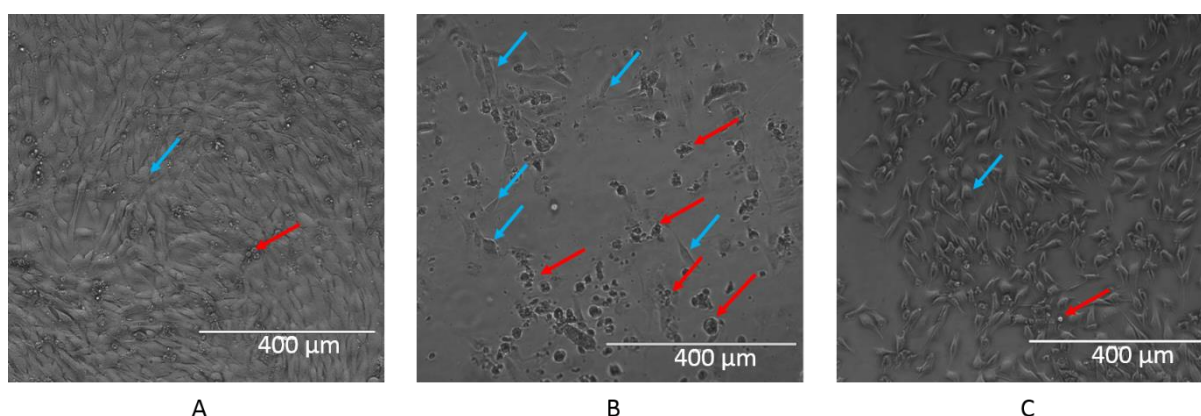


Figure 3.8. Images of C2C12 cells taken with an Evosfl digital inverted microscope: fresh cells before NMR experiment (**A**), 12 h of growth after the NMR experiment (**B**), and 48 h of growth after the NMR experiment (**C**). Red arrows indicate representative dead cells, blue arrows indicate representative live cells.

3.3.4. Comparison of 1D ^1H NMR pulse sequences

The choice of an NMR pulse sequence plays an important role in obtaining high-quality spectra. Different pulse sequences and acquisition parameters were tested to identify the most suitable HRMAS ^1H NMR experiments for intact cells. A standard 1D NOESY experiment with water presaturation was compared with a T_2 -edited CPMG experiment. T_2 -edited NMR experiments greatly reduce signal contributions from macromolecules or mid-molecular-weight compounds such as lipids. NMR-active nuclei in macromolecules tumble slowly and therefore have shorter T_2 relaxation times compared to small metabolites and lipids. Therefore, relatively short spin-spin relaxation delays reduce the intensities of their NMR resonances. In the NOESY spectra (**Figure 3.9**, blue), the contribution of broad signals from macromolecules to the spectrum baseline was significantly reduced by applying a CPMG pulse sequence with an echo delay of 40 ms (**Figure 3.9**, black). Longer echo delays could reduce broad resonances further but this would lead to significant attenuation of resonances of interest such as lipids and

small metabolites (**Figure 3.10**) and could hinder metabolomic data analysis. Therefore, an echo delay of 40 ms was chosen for the effective elimination of baseline effects while still preserving metabolite resonances. The CPMG experiment allowed for a more accurate interpretation of signals arising from small metabolites and lipids.

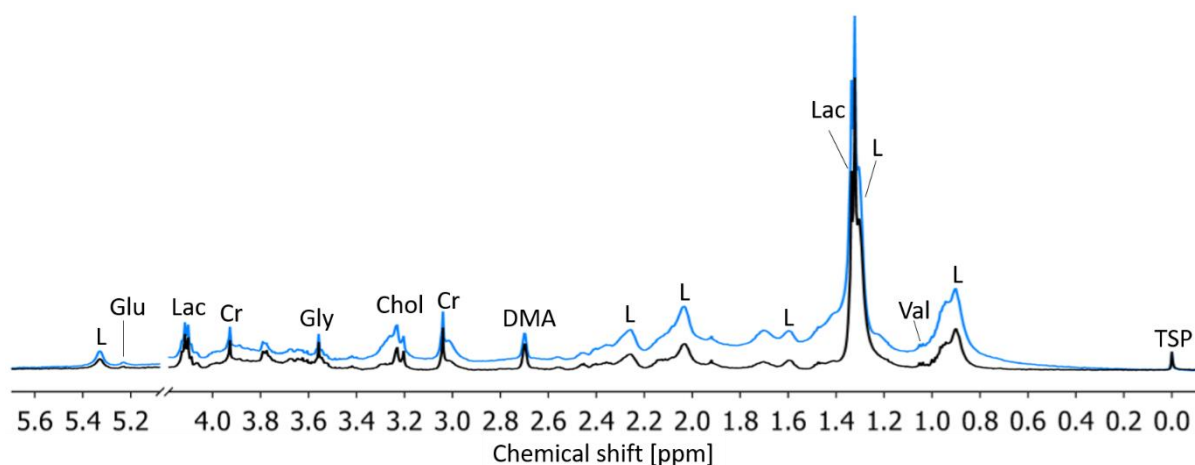


Figure 3.9. Superimposed 500 MHz HRMAS ^1H NMR spectra of intact cells recorded using different pulse sequences: 1D NOESY (blue) and a T_2 -edited CPMG (black). The spectra were normalized to the TSP reference peak; Lac – lactate, Ala – alanine, Glu – glucose, Gla – glutamate, Gln – glutamine, Gly – glycine, Val – valine, Leu – leucine, Gsh – glutathione, Cr – creatine, DMA – dimethylamine, Chol – choline, L – lipids. The water region (4.5 – 5.0 ppm) was removed.

CPMG experiments can also be used to attenuate lipid signals and to help resolve signals from small metabolites in overlapping regions. Applying short spin-spin relaxation delays reduces the signal from macromolecules while applying longer spin-spin relaxation delays reduces the signals from lipid molecules.

Figure 3.10A shows a series of CPMG experiments with varying T_2 relaxation delays from 40 ms to 800 ms. As the T_2 relaxation delay increased, the lipid signals diminished, and the spectrum contained mainly resonances from small molecules. As a result, the spectra exhibited a lower degree of signal overlap, which could facilitate more accurate identification and quantification of small non-lipid metabolites. For example, the reduction of the lipid resonance at 0.9 ppm and 1.3 ppm unveiled multiplets of leucine, isoleucine, and valine. The reduction of the lipid resonances at 1.3, 1.6, 2.1, and 2.3 ppm also uncovered the resonances of lactate, lysine, glutamine, glutamate, and glutathione. In **Chapter 4**, T_2 -editing will be used for probing changes in lactate concentration during apoptosis.

Another useful NMR-editing technique, diffusion-edited 1D DOSY, can be used to resolve the NMR signals of different species based on their diffusion coefficient. The signal from fast-diffusing metabolites is removed by increasing the pulse field gradient strengths while the signals from slower-diffusing lipids are preserved. **Figure 3.10B** shows a series of 1D DOSY experiments with increasing gradient strengths, from 0.681 to 33.375 Gcm⁻¹. At high gradients, most resonances from small metabolites significantly decayed and only the lipid signals were visible in the spectrum. The elimination of small metabolite resonances reduced the spectral complexity making interpretation of the lipid signals more robust.

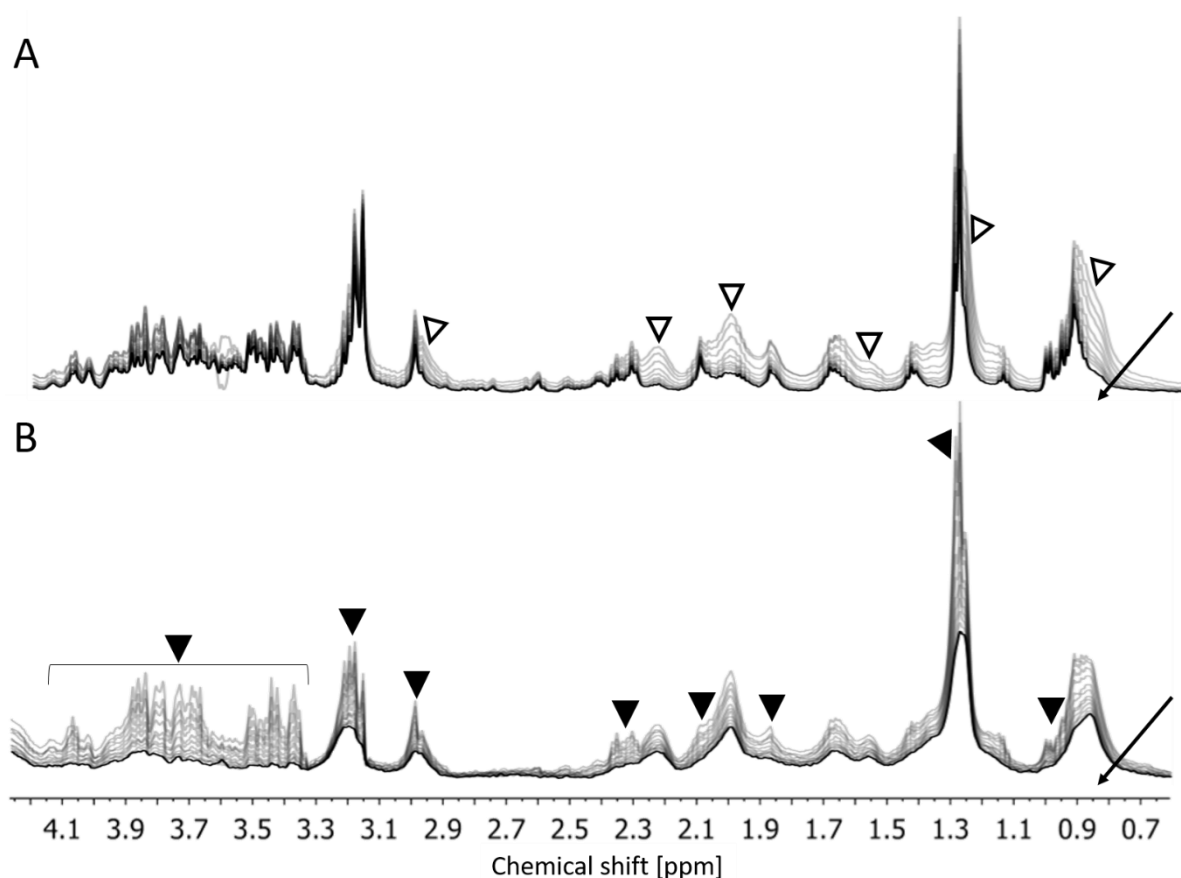


Figure 3.10. 500 MHz HRMAS ¹H NMR spectra of intact cells showing the effect of NMR-editing techniques. **A**) A series of superimposed T₂-edited CPMG spectra editing out lipids. The spectrum in black contains mainly the resonances from small metabolites. The arrow indicates the direction of increasing spin-echo number (10, 20, 40, 80, 120, 180, 220, 260, 300, 400). Empty triangles indicate the decaying lipid resonances. **B**) A series of superimposed diffusion-edited DOSY spectra editing out small metabolites. The spectrum in black contains mainly the resonances from lipids. The arrow indicates the direction of increasing gradient (0.681, 3.653, 6.626, 9.598, 12.570, 15.542, 18.514, 21.486, 24.459, 27.431, 30.403, 33.375 Gcm⁻¹). Full triangles show the decaying resonances of small metabolites.

By adjusting the NMR experimental parameters and pulse sequence, we can probe different classes of metabolites and simplify complex spectra. The CPMG experiment with low spin-echo numbers reduced baseline noise from macromolecules. The CPMG experiment with higher spin-echo numbers is most suitable for small molecules. The DOSY experiment with high gradient strengths is most suited for studying slowly diffusing molecules. In **Chapter 5**, diffusion-editing will be used for excluding small metabolites (e.g., lactate) from diffusion measurements.

The NMR spectral editing techniques were previously applied to metabolic profiling of tissue and proved to be useful in distinguishing lipid and low-molecular-weight metabolites.²⁶⁰ The application of spectral editing in metabolomics has limitations. First, the resolving power is low, meaning that it is not suitable for separating resonances from metabolites of a similar size/freedom to rotate. Second, with overlapping resonances, it is not easy to assess if the contribution from unwanted resonances is completely removed. Lastly, the relaxation delay or gradient strength needed to significantly reduce unwanted resonances may also reduce resonances of interest. These limitations need to be considered during a quantitation analysis.

3.3.5. Comparison of solution-state and HRMAS ¹H NMR spectra of intact cells.

To demonstrate the advantages of HRMAS ¹H NMR spectroscopy, I compared the HRMAS ¹H NMR spectra of intact cells with the spectra obtained from solution-state 400 MHz ¹H NMR experiments (**Figure 3.11**). The NMR parameters were set to be analogous in both experiments. For the solution-state experiment, 2×10^6 cells suspended in deuterated PBS were placed in a 5 mm tube, while for the HRMAS experiment, 10^6 cells were suspended in deuterated PBS and packed in a 4 mm rotor. The resonances from the solution-state spectra were considerably less intense than those in the HRMAS spectra – only the broad peaks at 0.9, 1.3, 2.0, 2.2 and 2.8 ppm were detected (**Figure 3.11B**). This could be explained by the packing differences: the 5 mm NMR tube contained 5,000 cells/ μ L and substantial dead volume, which is outside of the receiver coil. By contrast, the HRMAS sample was 4 times more concentrated – the 4 mm rotor contained 20,000 cells/ μ L.

It is worth noting that studies on intact cells by solution-state NMR spectroscopy can analyse metabolites such as mobile lipids, lactate, creatinine, and choline compounds.^{199,210,211} The number of cells per sample used in these studies was $2.5 \times 10^7 - 2 \times 10^8$; 25 – 200 times more than for the HRMAS ¹H NMR experiments reported here. In-cell NMR approaches to study

protein structure or protein-ligand interactions in the native environment typically require $2.5 - 8 \times 10^7$ cells per samples.^{269–271}

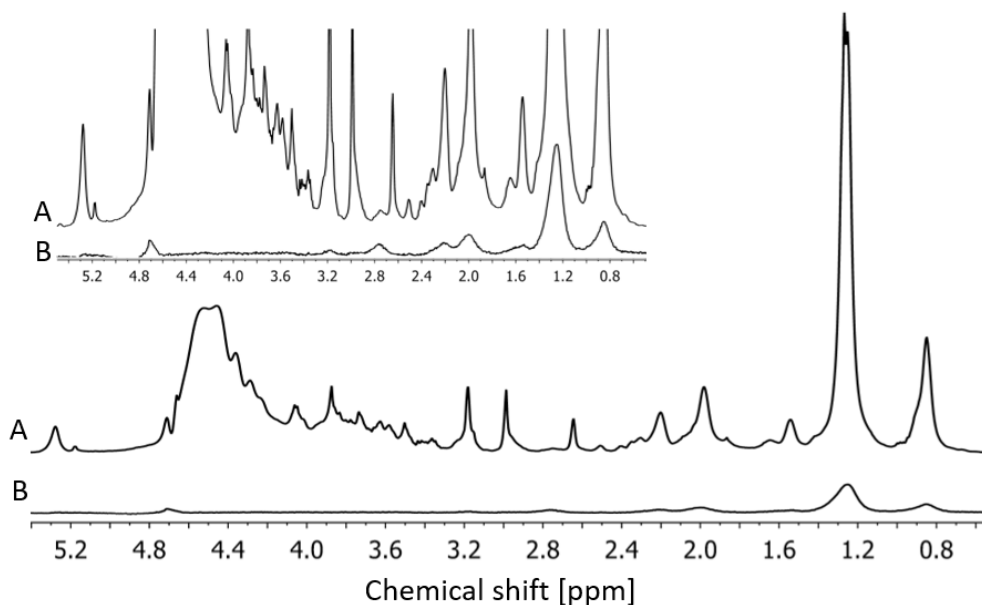


Figure 3.11. Comparison of the solution-state and HRMAS ^1H NMR spectra of intact cells. A. 500 MHz HRMAS ^1H NMR solvent suppressed spectra of 10^6 intact cells (4 mm rotor, 50 μL insert, 10^6 cells per sample, 64 scans). B. 400 MHz solution-state ^1H NMR solvent suppressed spectra of intact cells (5 mm tube, 400 μL insert, 2×10^6 cells per sample, 64 scans). The spectra were normalized to noise levels. The intensity scale is magnified 8-fold in the insert.

3.3.6. Comparison of HRMAS ^1H NMR spectra of intact cells and solution-state ^1H NMR spectra of cell extracts.

Metabolic profiling of cells can be performed on intact cells or cell extracts. Representative spectra of aqueous and organic fractions of cell extracts, and intact cells are shown in **Figure 3.12**. The chemical shifts assignment in ^1H NMR spectra were confirmed with COSY NMR experiments (**Figure 3.13** – **Figure 3.15**) and NMR metabolomics databases (BMRB: www.bmrwisc.edu and HMDB: www.hmdb.ca). In total, 51 metabolites were identified and are summarized in **Table 3.3**.

The extraction of metabolites can be laborious but comes with benefits. First, aqueous and organic fractions are separated and consequently, the spectra are less crowded. Since extracted small metabolites tumble rapidly in solution, they give rise to sharp resonances, reducing signal overlap. Small hydrophobic molecules (e.g., cholesterol, labelled 48 in **Figure 3.12**) also give sharp resonances but larger lipid molecules (e.g., long fatty acyl chains, 42, 50, **Figure 3.12**)

tumble more slowly and give broader resonances. Second, the extraction procedures release bound metabolites from cellular organelles making them “NMR-visible”.

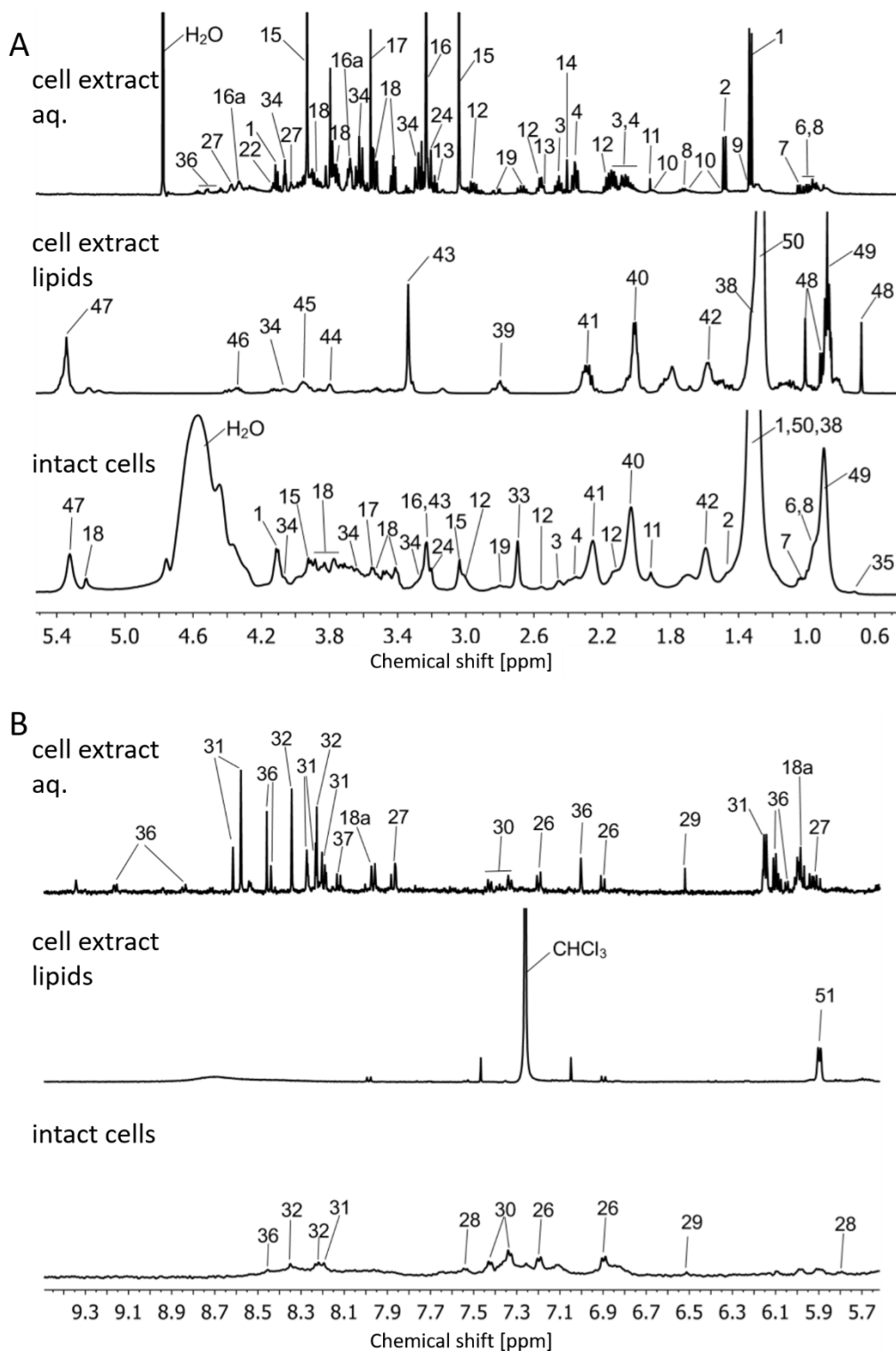


Figure 3.12. NMR-based metabolic profiling of cells: 500 MHz ^1H NMR water-suppressed spectra of aqueous fraction of cell extract in D_2O ; 500 MHz ^1H NMR of organic fraction of cell extract in chloroform- d ; and 500 MHz HRMAS ^1H NMR water-suppressed spectra of intact cells in D_2O . The chemical shift range is split into two parts for clarity: **A**) 0.6 – 5.4 ppm and **B**) 5.7 – 9.3 ppm. Metabolite annotation is listed in **Table 3.3**.

Table 3.3. ^1H chemical shifts and multiplet patterns of assigned metabolites from the C2C12 cell line based on solution-state and HRMAS ^1H NMR spectroscopy. The annotation number corresponds to those shown in **Figure 3.12**. Multiplet patterns: *s* – singlet, *bs* – broad singlet, *d*- doublet, *t* – triplet, *q* - quartet.

Metabolite	Annotation (Fig. 3.13 – 3.15)	Shift range (ppm)
Lactate	1	1.33(d); 4.11(q)
Alanine	2	1.49(d); 3.81(q)
Glutamate	3	2.04(m); 2.10(m); 2.37(m); 3.78(t)
Glutamine	4	2.06(m); 2.14(m); 2.45(m); 3.78(t)
Arginine	5	1.69(m); 1.93(m); 3.24(t)
Isoleucine	6	0.95(t); 1.02(d); 1.29(m); 1.49(m); 1.99(m)
Valine	7	1.00(d); 1.05(d); 2.30(m)
Leucine	8	0.95(d); 0.98(d); 1.74(m)
Threonine	9	1.34(d); 3.59(d); 4.27(m)
Lysine	10	1.52(m); 1.74(m); 1.91(m); 3.04(t); 3.78(t)
Acetate	11	1.92(s)
Glutathione	12	2.17(m); 2.58(m); 2.96(m); 3.79(m)
β -alanine	13	2.56(t); 3.18(t)
Succinate	14	2.40(s)
Creatine	15	3.04(s); 3.90(s)
Choline/phosphocholine	16	3.20(s)
Glycerophosphocholine	16a	3.20(s); 3.68(m); 4.33(m)
Glycine	17	3.56(s)
Glucose	18	3.43(dt); 3.53(t) 3.76(m) 3.88(m)
UDP-glucose	18a	5.99(m); 7.96(d)
Aspartate	19	2.68(m); 2.81(m); 3.92(m)
Asparagine	20	2.83(m); 2.94(m); 4.02(m)
Histidine	21	7.199s); 7.73 (d)
Proline	22	2.03(m); 2.36(m); 3.30(m); 4.13(m)
Malate	23	2.36(m); 2.69(m); 4.30(m)
Carnitine	24	2.42(m); 3.45(m)
Taurine	25	3.26(t); 3.42(m)
Tyrosine	26	3.05(m); 3.22(m); 4.00(m); 6.91(d); 7.21(d)
Uridine	27	4.03(m); 4.40(t); 6.01(m); 5.91(m); 7.91(d)
Uracil	28	5.80(d); 7.53(d)
Fumarate	29	6.5(s)
Phenylalanine	30	3.30(m); 3.97(m); 7.34(m); 7.53(m)
ATP, ADP, AMP	31	6.15(d); 8.19(m); 8.24(s); 8.27(m); 8.58(s); 8.62(s)
Adenosine	32	8.2(s); 8.3(s)
Dimethylamine	33	2.7 (s)
Myo-inositol	34	3.29(t); 3.53(dd); 3.64(t); 4.07(t)
α -Hydroxyisobutyrate	35	1.37(s) 2.35(m); 4.13(m)
NAD ⁺ , NADH	36	6.05(d); 6.11(d); 7.01(s); 8.44(s); 8.46(s); 8.85(m); 9.15(m)
UMP	37	8.12(d); 6.00(m)

Table 3.3. Continued.

Metabolite	Annotation (Fig. 3.13 – 3.15)	Shift range (ppm)
Lipids (=CHCH ₂ CH ₂ -)	38	1.32 (bs)
Lipids (=CHCH ₂ CH=)	39	2.80 (m)
Lipids (=CHCH ₂ -)	40	2.01 (q)
Lipids (-CH ₂ CO)	41	2.29 (m)
Lipids (-CH ₂ CH ₂ CO)	42	1.57 (m)
Choline (-N(CH ₃) ₃)	43	3.34 (s)
Glycerol phospholipids	44	3.80 (bs)
Glycerol (TG)	45	3.95 (bs)
Sphingomyelin (-CH ₂ CH ₂ N)	46	4.34 (bs)
Lipids (-HC=CH-)	47	5.35 (m)
Sterols	48	0.68 (9s), 0.92 (d), 1.02 (s)
Lipids (-CH ₃)	49	0.89 (m)
Lipids (-CH ₂)	50	1.30 (m)
Lipids (HOOCCH=)	51	5.90 (d)

In this comparison it was possible to assign a greater number of metabolites in the ¹H NMR spectra of cell extracts compared to the HRMAS ¹H NMR spectra of intact cells. However, the loss of metabolites is inevitable during extraction and may lead to sample contamination. For example, the aqueous cell extract spectrum in **Figure 3.12** shows very low levels of glucose (5.2 ppm, 18) as compared to the intact cell spectrum. In contrast, HRMAS ¹H NMR spectroscopy measures metabolites in living cells, sample preparation is reduced to harvesting the cell culture, washing with deuterated PBS and packing the cells inside the MAS rotor. There is no need for quenching cellular reactions or cell lysis thus the likelihood of compound loss or contamination is very low.

The resonances in the HRMAS NMR spectrum come from unbound metabolites that tumble relatively fast. For example, lipid resonances in the intact cell spectrum (**Figure 3.12**) come from cytoplasmic mobile lipids rather than membrane phospholipids. In contrast, the lipid resonances in the cell extract spectrum are a collective signal from all extracted lipids. Indeed, HRMAS ¹H NMR spectroscopy is a method of choice for monitoring mobile lipids in cells and tissues^{18,64,78,201,204,230,272,273}

To further assign metabolites in the cell pellet I performed 2D NMR spectroscopy. The COSY spectra acquired for both intact cells and cell extracts added extra metabolomics information (**Figure 3.13** – **Figure 3.15**). The assignment, based only on ^1H NMR spectra, yielded 30 metabolites, whereas the analysis of the COSY spectra expanded the total number by 21 metabolites. In addition, the assignments between solution-state (cell extract) and HRMAS (intact cell) ^1H NMR spectroscopy were consistent and further aided in the identification of metabolites detected by HRMAS ^1H NMR spectroscopy.

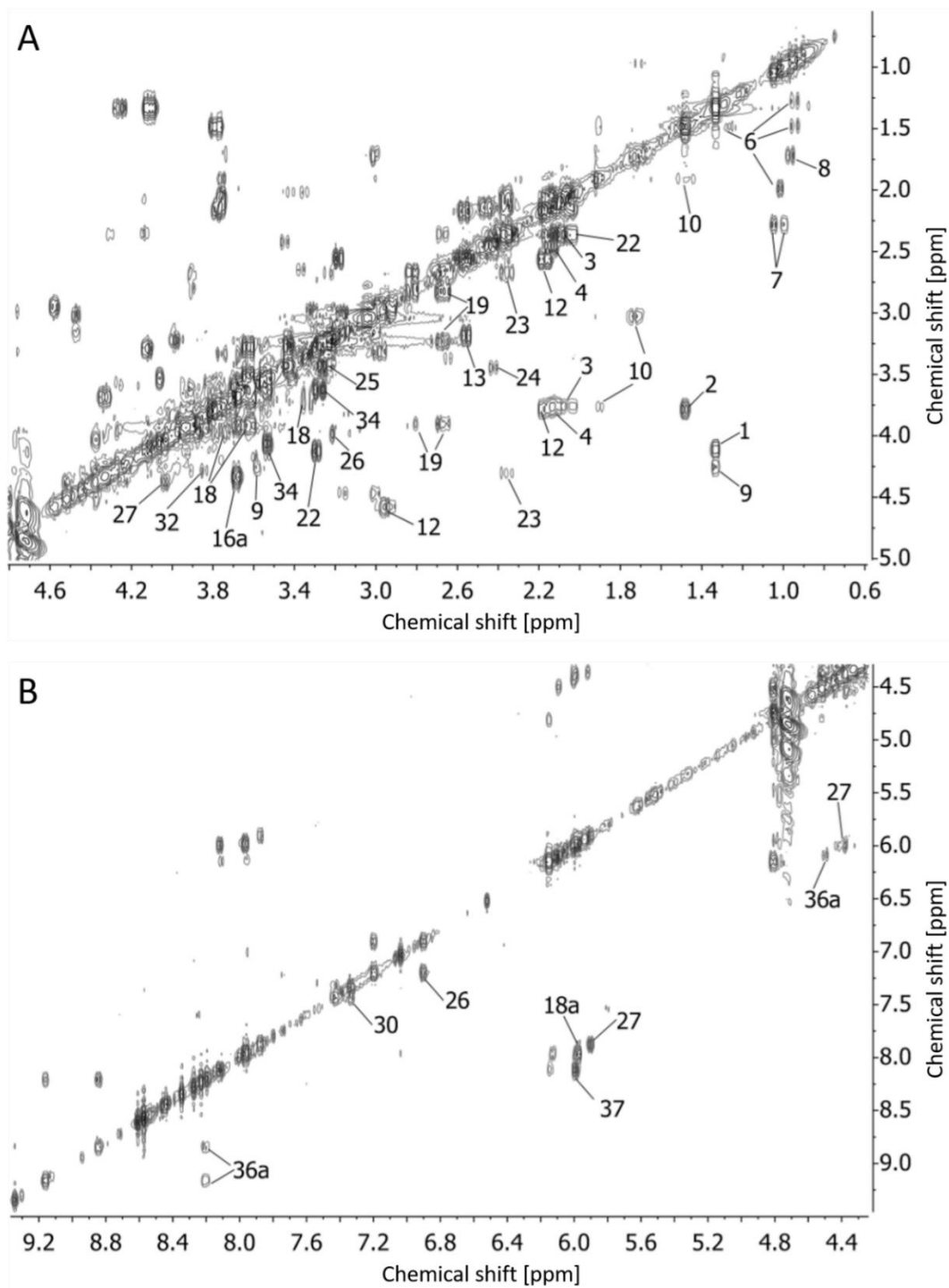


Figure 3.13. 500 MHz COSY NMR water-suppressed spectra of aqueous fraction of cell extract in D_2O . The chemical shift range is split into two parts for clarity: **A)** 0.6 – 5.4 ppm and **B)** 5.7 – 9.3 ppm. Metabolite annotation is listed in **Table 3.3**.

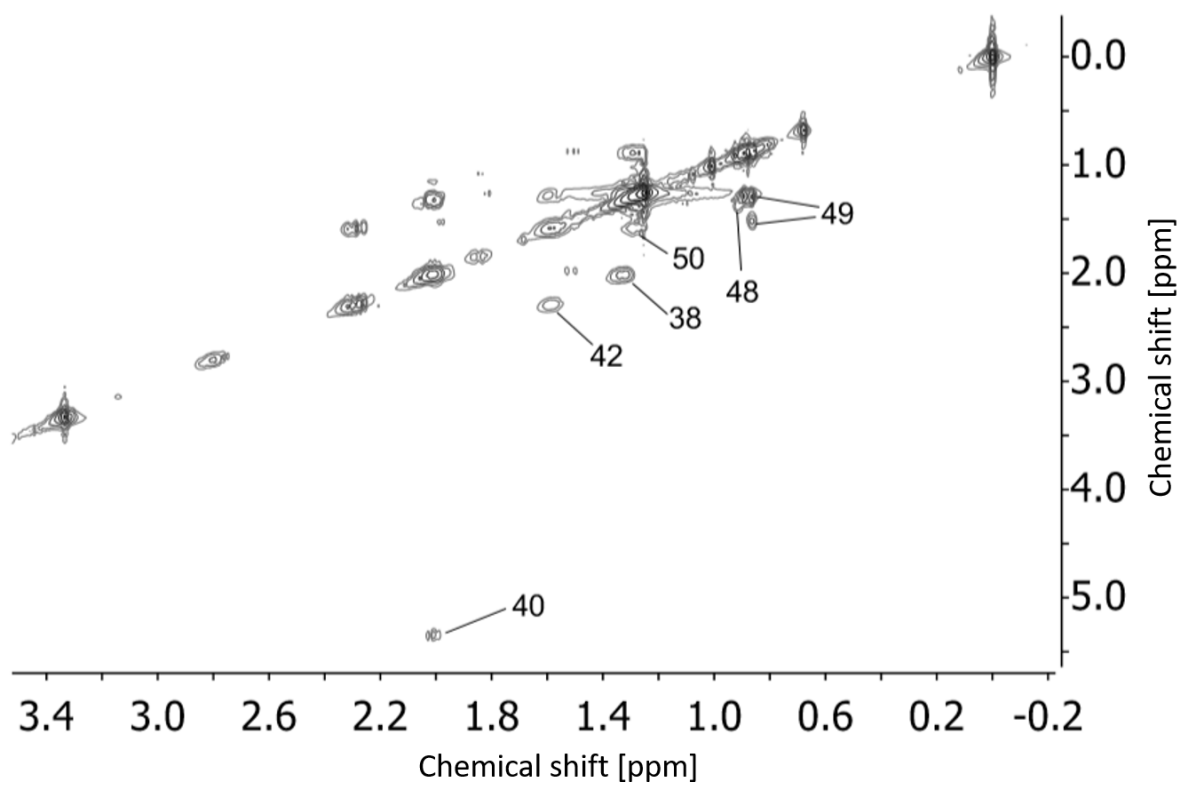


Figure 3.14. 500 MHz COSY NMR spectrum of the organic fraction of the cell extract in deuterated chloroform. Metabolite annotation is listed in **Table 3.3**.

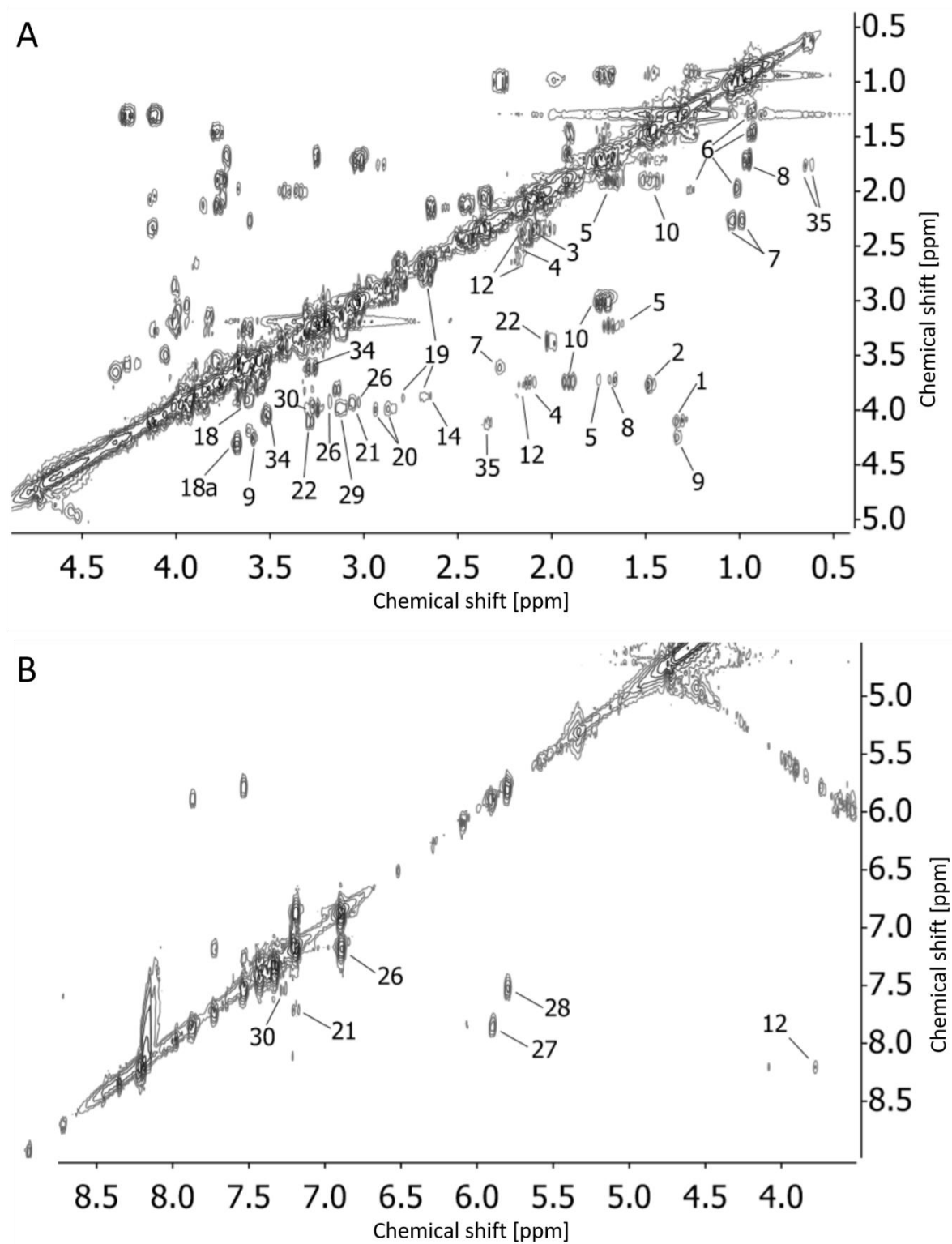


Figure 3.15. 500 MHz HRMAS COSY NMR water-suppressed spectra of intact cells in D_2O . The chemical shift range is split into two parts for clarity: A) 0.6 – 5.4 ppm and B) 5.7 – 9.3 ppm. Metabolite annotation is listed in **Table 3.3**.

3.3.7. HRMAS ^1H NMR spectra of different cell lines

Figure 3.16 compares the spectra obtained from adipocyte, liver, muscle, and glioma cells (cell culture methods described in **Appendix 4**). As expected, adipose and liver cells have high levels of lipids while glioma cells have considerably lower levels of lipids and higher levels of low molecular weight metabolites such as taurine, *myo*-inositol, lysine, glycine, and acetate. The muscle cell spectra showed relatively high levels of lipids, creatine, and lactate.

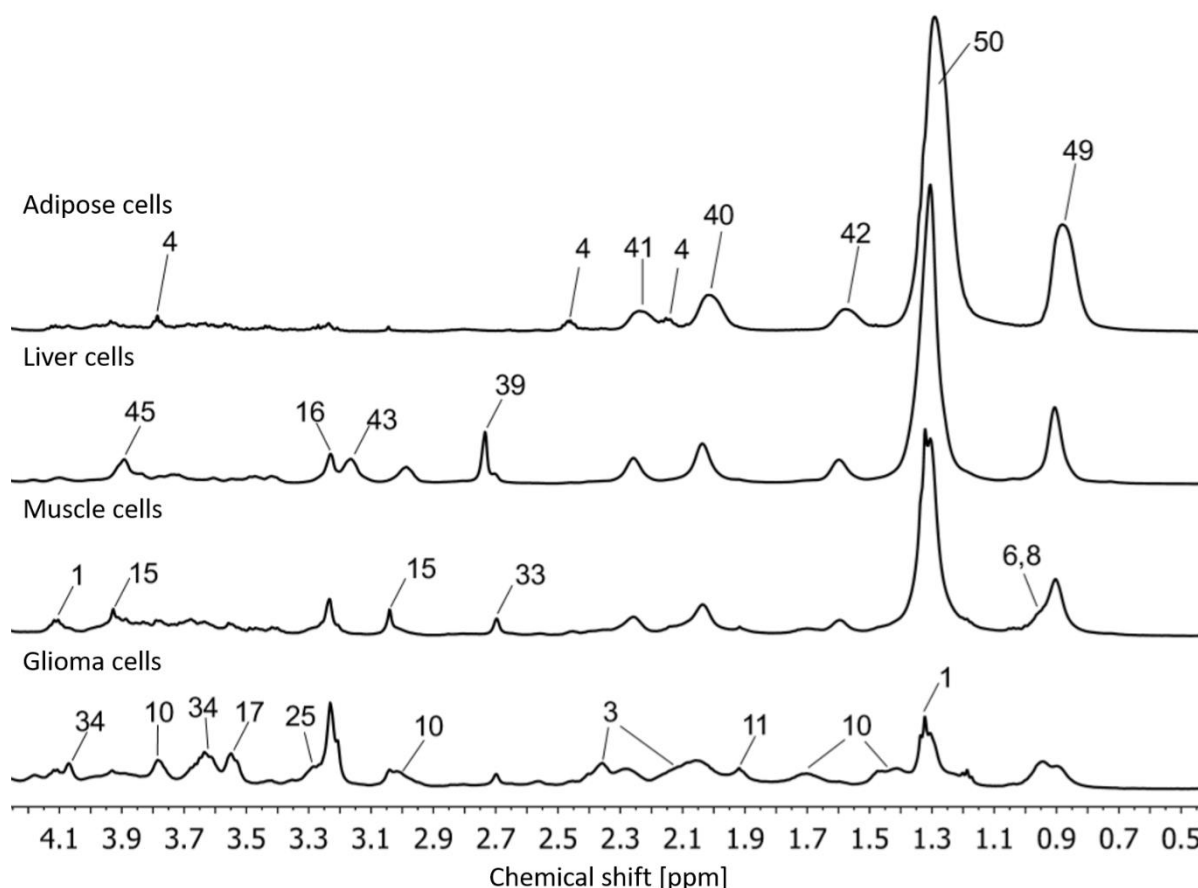


Figure 3.16. Comparison of HRMAS ^1H NMR spectra from different cell lines: adipose, liver, muscle, and glioma cells. Metabolite annotation is listed in **Table 3.3**.

Adipose cells contain big lipid droplets and would be ideal to study their formation. However big lipid droplets are fragile, and they break under the HRMAS conditions. The concentration of lipids in glioma cells is much lower and comparable to non-lipid metabolites such as glutamate, glutamine and lactate, which may affect analysis of lipids due to resonance overlap. For the purpose of this thesis, I focused on muscle cells because they can be grown most readily in culture and exhibit adaptive capacity to mechanical stress.²⁷⁴

3.4. Conclusions

Chapter 3 described method optimization to ensure high-quality HRMAS ^1H NMR data of intact cells in subsequent studies. It also highlighted the advantages and limitations of applying HRMAS ^1H NMR spectroscopy in cell metabolomics.

The volume and geometry of samples in a 50- μL HRMAS rotor gave the most optimum spectra quality and S/N. The spinning rate of 5 kHz was selected for future experiments to avoid interference from spinning sidebands. After 3.5 h under HRMAS conditions, cell viability decreased by 10%. This significant decrease could be corrected using control measures, as the behaviour of both treated and untreated cells in the NMR instrument was comparable. I also demonstrated that cells can be recovered after HRMAS NMR experiments. This observation opens opportunities for investigating changes in metabolic profiles with time and passage number.

The CPMG pulse sequence with short relaxation delays was found to be more suitable for intact cells than the standard NOESY pulse sequence. Moreover, I showed the advantages of using T_2 relaxation and diffusion edited spectra to probe different metabolite species in intact cells. In **Chapter 5**, these experiments will be used to probe changes in the cellular environment and physical properties of metabolites induced by various treatments.

The HRMAS ^1H NMR spectra contained resonances that were not visible in the solution-state ^1H NMR spectra of intact cells. More densely packed cells and minimum dead volume allowed for the analysis of smaller sample sizes without a significant decline in sensitivity and resolution. When HRMAS ^1H NMR spectra of intact cells were compared to solution-state ^1H NMR spectra of cell extracts, it was clear that more metabolites could be identified in the cell extracts. However, minimum sample preparation, low risk of contamination or loss of metabolites, and the ability to monitor metabolites in living cells are attractive features of HRMAS ^1H NMR spectroscopy. Moreover, it is a method of choice for monitoring mobile lipids in intact cells.

In summary, this chapter described an optimized experimental method to ensure efficient implementation of HRMAS ^1H NMR spectroscopy in studying the effect of apoptosis on myotubes.

Chapter 4. HRMAS ^1H NMR spectroscopy for monitoring metabolites in intact cells during apoptosis.

4.1. Introduction

Impaired apoptosis is one of the key mechanisms behind cancer.¹⁵⁷ Apoptosis is a naturally occurring mechanism that prevents the development of cancer via the death of defective cells. A cell that is defective or undergoes DNA damage, first attempts to repair the damage. If that is not possible, the cell receives signals to undergo apoptosis. Cancer cells lose this critical ability and continue to divide and accumulate; thus many anticancer treatments are based on activation of apoptotic pathways.¹⁶⁰ Two well-known apoptosis-based cancer treatments are cisplatin and etoposide.

Cisplatin (**Figure 4.1A**) is a clinically proven chemotherapy treatment for several cancers including ovarian, cervical, breast, testicular, bladder, lung, head, neck, and brain.²⁷⁵ Cisplatin enters the cell via a membrane transporter and is hydrolysed in the cytoplasm. This activated product has a strong affinity for non-hydrogen bonded nitrogen atoms in nucleic acid bases. Once bound, it causes distortion of the DNA, which inhibits replication and transcription. This leads to the activation of p53 (tumour suppressor), cell cycle arrest, and apoptosis.

Etoposide (**Figure 4.1B**) is an antineoplastic agent commonly used in treatments of testicular, bladder, prostate, uterine, stomach, and lung cancers, Hodgkin's and non-Hodgkin's lymphoma, sarcoma, and brain tumors.²⁷⁶ It belongs to the class of topoisomerase II inhibitors - enzymes that cut both strands of the DNA helix and regulate DNA topology. Etoposide acts by inducing high levels of permanent DNA breaks followed by DNA damage response and eventually caspase-dependent apoptosis.²⁷⁷

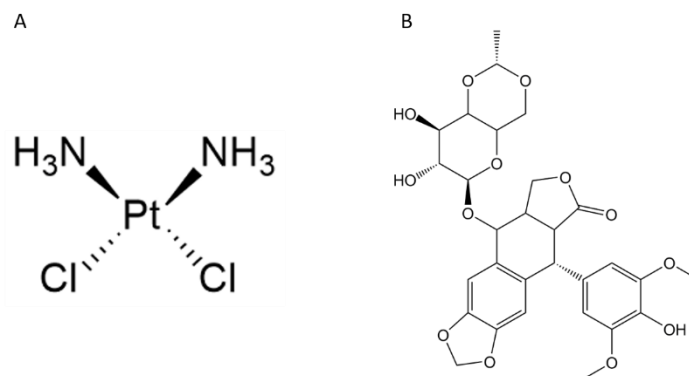


Figure 4.1. Chemical structure of cisplatin (A) and etoposide (B).

The molecular mechanisms of cisplatin and etoposide have been studied for decades, revealing the roles of enzymes, messengers, and transporters in controlling apoptosis.^{275–278} Metabolomic approaches can directly reflect the current biochemical status of cells, thus they contribute additional information on what has exactly happened during treatment with these drugs. They are particularly useful for the discovery of biomarkers that help monitor apoptosis-based cancer treatments and for understanding the mechanism of drug action.^{17,186,191,278}

Several NMR-based metabolomics studies have focused on searching for apoptosis-specific biomarkers in cell extracts or intact cells. In these studies, apoptosis was induced by well-known apoptotic agents such as taxol,²⁰² cisplatin,^{279,280} etoposide,¹⁹⁵ radiation, doxorubicin,¹⁹⁵ tamoxifen,⁷⁰ CdCl₂,¹⁹³ or novel compounds such as hexacationic ruthenium metallaprim.¹⁹⁶ Rainaldi and colleagues reported a decrease in the concentration of lactate, alanine, glutathione, taurine, and choline induced by doxorubicin treatment.¹⁹⁴ In the same study, they reported an increase in lactate and alanine after radiation treatment. Vermathen and colleagues reported a decrease in lactate concentration after hexacationic ruthenium treatment while other metabolite changes (lysine, alanine, glutamine, *myo*-inositol, choline) depended on cell line and incubation time.¹⁹⁶ Griffin and colleagues reported an increase in nucleotides and a decrease in *myo*-inositol after tamoxifen treatment.⁷⁰ These studies suggest that while changes in concentration of small aqueous metabolites can provide clues about biochemical changes in apoptotic cells they seem to be treatment and cell line-specific. The most common metabolic change reported was an increase in NMR-visible lipid resonances during apoptosis, regardless of the apoptotic agent. Thus, NMR-visible lipids may be treated as a reliable biomarker for apoptosis and they are often used to distinguish between apoptosis and necrosis in NMR-based studies.^{193,194}

Metabolomic data obtained from cell extracts and/or intact cells can be complemented by metabolomic data obtained from growth media. Studying growth media is particularly useful for time-course experiments as it is relatively easy to collect and process the samples, which are not fragile like cell samples. This approach can provide information about metabolites secreted into media (exometabolome),²⁸¹ as well as metabolites taken up from media (e.g. glucose, choline, glycerol). Aranibar and colleagues monitored media components and cellular metabolites over time to assess the impact of bioreactor scale and the presence of anti-apoptotic agents in the media.³¹ They demonstrated that cell viability and productivity correlated with many changes in metabolites from the media. Similarly, Feng and colleagues demonstrated how combining NMR-based metabolomics of intact cells and growth media could help understand the biological mechanisms of silica nanoparticles in HeLa cells.²⁸² They followed glucose and amino acid utilization, and lactate and acetate release as markers for glycolytic activities. Moreover, the cellular stress response correlated well with an elevation of formate, histidine, and tryptophan and a decrease in methionine. Thus, NMR spectroscopy of growth media has been shown to be sensitive to a variety of biological processes.

4.2. *Aims*

In **Chapter 4**, I aim to demonstrate the usefulness of NMR-based metabolic profiling for monitoring drug treatments in vitro. In particular, I investigate advantages of metabolic profiling of intact cells by HRMAS ¹H NMR spectroscopy. I compare and combine NMR-based metabolic profiling of intact cells, cell extracts, and growth media to determine the most suitable approach for measuring metabolic alterations induced by apoptotic and necrotic treatments (**Figure 4.2**). I explore additional information obtained from each NMR approach and how it can be used to probe metabolic pathways.

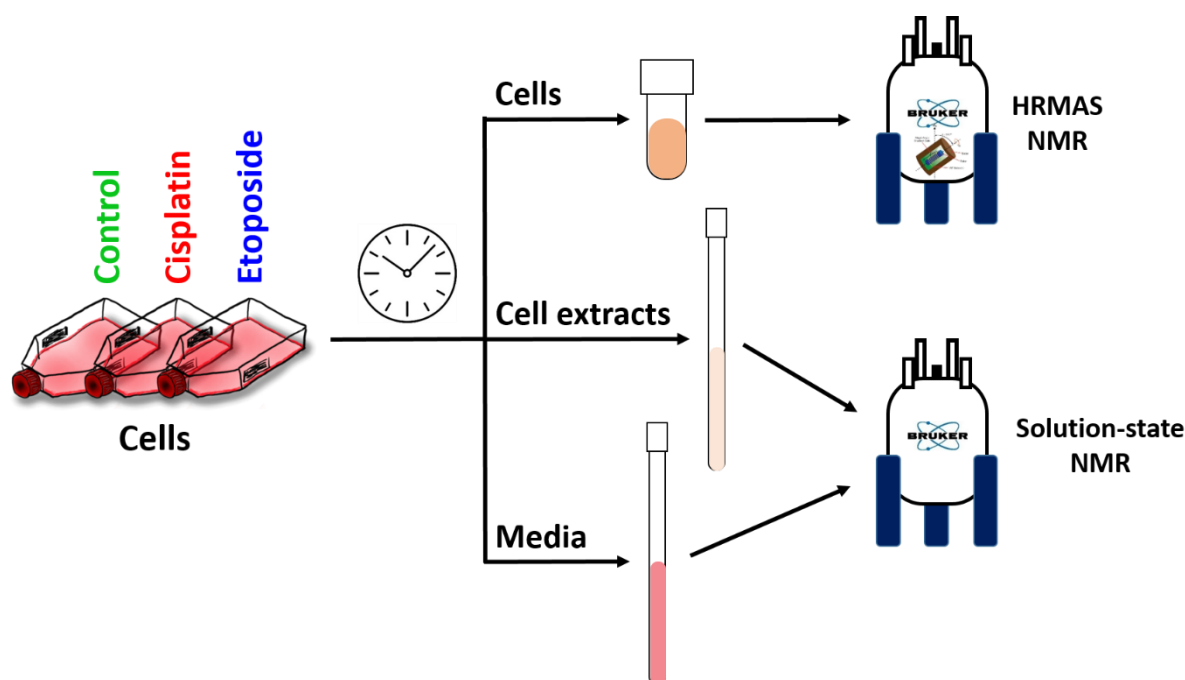


Figure 4.2. NMR methods to study apoptosis induced by cisplatin and etoposide. After incubation, media samples were collected for solution-state ^1H NMR analysis, intact cells (C2C12 myotubes) were harvested for HRMAS ^1H NMR analysis, or Blish and Dyer extraction and solution-state NMR analysis.

In order to achieve that, I describe the following experiments:

- developing a robust model of apoptosis in C2C12 myotubes. I report results from conventional measures of cell viability such as caspase-3 activity and trypan blue assay, which identify an effective dosage and incubation time for cisplatin and etoposide treatments;
- untargeted NMR-based metabolic profiling of intact C2C12 myotubes for the selected treatment conditions and identify potential biomarker;
- analysing changes in the metabolic profiles with apoptosis progression for selected biomarkers including small metabolites (energy metabolism and signalling), mobile lipids (neutral lipid metabolism) and choline containing compounds (membrane metabolism);
- integrating NMR metabolomics data of intact cells, cell extracts, and growth media samples.

4.3. Methods

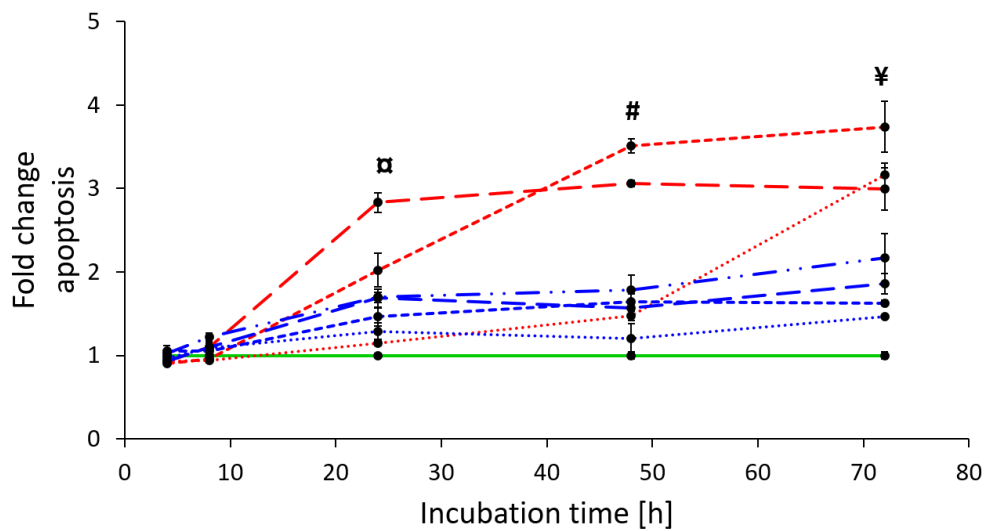
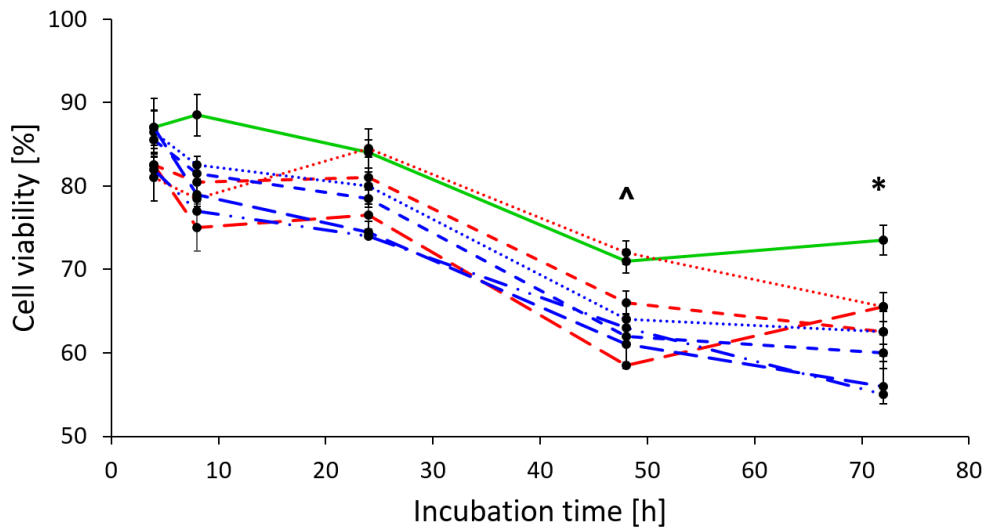
All experimental methods used for collecting, processing and analysing data are defined in **Chapter 2**.

4.4. Results

4.4.1. Establishing dose and incubation time for inducing apoptosis

The effects of cisplatin and etoposide doses and incubation times on C2C12 myotube cells were investigated with the trypan blue exclusion assay and the caspase-3 activity assay (**Figure 4.3**). The changes in cell viability (live cells divided by total cells expressed in %) and fold change apoptosis (caspase-3 activity in treated cells divided by caspase-3 activity in control cells) were monitored with time (3 – 72 h) and drug dose (20 – 40 μM for cisplatin; 50 – 120 μM for etoposide). The cell viability decreased steadily with incubation time and was lower for the higher doses. After 48 h, the decrease in cell viability became significant (ANOVA: $p < 0.05$) for cisplatin dosed at 60 μM ; after 72 h, it was significant for cisplatin dosed at both 40 μM and 60 μM , and etoposide dosed at 84 μM and 120 μM . The highest doses of cisplatin and etoposide induced significant levels of apoptosis after 24 h, whereas after 72 h, apoptosis was present in all treatment groups. However, the 72-h data was less reliable for comparing treatments due to secondary necrosis (30-45% dead cells).

The groups with high levels of apoptosis (i.e., cisplatin 60 μM , 48 h) and low levels of apoptosis (i.e., etoposide, 50 μM , 48 h) were selected for preliminary HRMAS ^1H NMR experiments on intact cells (**Section 4.4.2**). The experimental design aimed to answer two questions: 1) can HRMAS ^1H NMR spectroscopy discriminate between caspase-dependent apoptosis and control; 2) can HRMAS ^1H NMR spectroscopy detect significant metabolic changes in the group for which caspase-3 assay did not show a significant level of apoptosis. Since several other pathways are activated, preceding the caspase cascade, it was interesting to establish whether NMR spectroscopy can distinguish between the control group and the insignificant apoptosis group. Subsequent NMR-based experiments investigated the impact of incubation times on metabolic profiles (**Section 4.4.3**).



* $p < 0.05$ for cisplatin 40, 60 μM , etoposide 84, 120 μM

^ $p < 0.05$ for cisplatin 60 μM

□ $p < 0.05$ for cisplatin 60 μM , etoposide 84, 120 μM

$p < 0.05$ for cisplatin 20, 40, 60 μM , etoposide 84, 120 μM

¥ $p < 0.05$ for all treatments

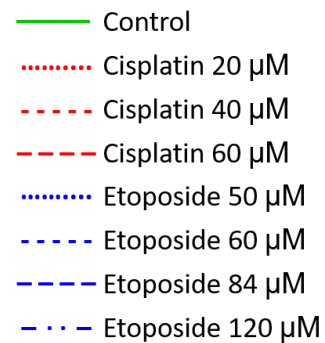


Figure 4.3. Dose-incubation time response for cisplatin- and etoposide-treated C2C12 myotubes. Apoptosis was normalized to the control group at each time point. SEM represent biological variance ($n = 4$). ANOVA was used to assess significance and Fisher's least significant difference (LSD) was used for post hoc pairwise comparisons of the treatment groups; p -values are FRD-adjusted; significances ($p < 0.05$) are reported relative to the control group.

4.4.2. ¹H NMR-based metabolic profiling of apoptotic cells

This section describes metabolic profiles of C2C12 myotubes treated with either cisplatin 60 μ M or etoposide 50 μ M for 48 h. In addition, heat-treated cells were analysed to investigate the metabolic changes associated with necrosis. The cells were divided into two samples: approximately 10^5 cells for cell viability and caspase-3 activity assays to test the presence of apoptosis and cell death; the remaining cells (approximate 10^6) were set aside for HRMAS ¹H NMR analysis. First, I investigate the levels of apoptosis in the NMR samples using caspase-3 activity assay and trypan blue exclusion assay. Then, I examine HRMAS ¹H NMR-based metabolic profiles of intact apoptotic cells to establish metabolic differences between control, apoptotic and necrotic cells. Finally, I analyse ¹H NMR-based metabolic profiles of culture media from apoptotic cells to investigate whether this method can also be used for differentiating between the treatments and control.

4.4.2.1. Establishing apoptosis in cell samples for HRMAS NMR analysis

Figure 4.4 shows the levels of apoptosis and cell viability in the treated cells. Samples treated with cisplatin showed at least a 5-fold increase in apoptosis compared with the control group while samples treated with etoposide showed no significant apoptosis according to caspase-3 activity assay. Interestingly, the etoposide samples showed lower cell viability, but no change in caspase-3 activity as compared to the controls. This suggests the absence of caspase-dependent cell death. The heat-treated samples showed significantly lower cell viability and caspase-3 activation as compared to the control cells. The decrease in caspase-3 activity after heat treatment implies that there was detectable caspase-3 activity already present in the control cells. Indeed, activation of caspase-3 is a normal biological process during myoblast differentiation.²⁸³ Cellular differentiation was stopped during the heat treatment and therefore the level of caspase-3 activity was lower when compared to the differentiating control cells. The results from the biochemical assays confirmed apoptosis in the cisplatin-treated samples and caspase-independent cell death in the etoposide- and heat-treated samples.

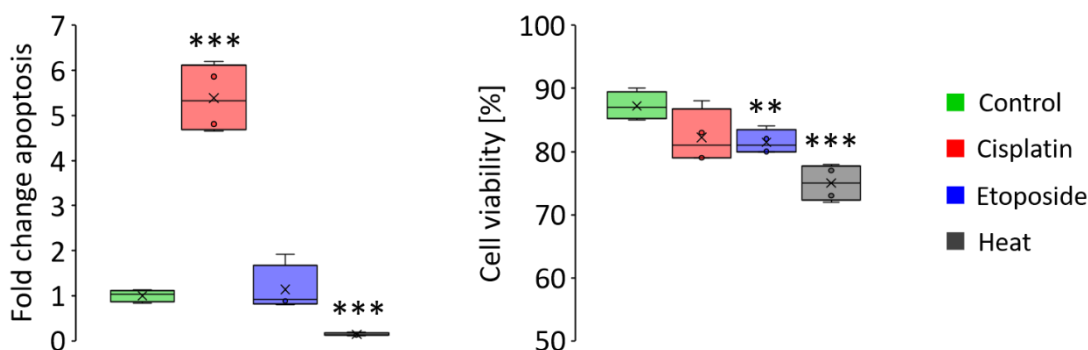


Figure 4.4. Cell viability (membrane integrity) and apoptosis (caspase 3 activity) measured in C2C12 myotubes treated with cisplatin 60 μM (red), etoposide 50 μM (blue) and heat (grey) for 48 h. The change in apoptosis was reported relative to the control group (green); $n = 4$; ANOVA with post hoc Fisher's test: ** $p < 0.01$, *** $p < 0.001$.

4.4.2.2. HRMAS ^1H NMR analysis of intact cells

The NMR spectra (**Figure 4.5**) of intact cell samples were subjected to chemometric and multivariate analysis. Visual inspection of the spectra pointed to several metabolite alterations. For apoptotic cells (**Figure 4.5**, red and blue), the most obvious increase in resonance intensities was observed in spectral regions which corresponded to lipids (~ 0.9 ppm, 1.3 ppm, 1.6 ppm, 2.0 ppm, 2.2 ppm and 5.3 ppm). In contrast, these resonances decreased in necrotic cells (**Figure 4.5**, black), while the resonance intensities of choline, glucose and DMA increased as compared to the control (**Figure 4.5**, green).

For quantitative assessment of the spectral data, PCA was performed on binned spectra as described in **Chapter 2, Section 2.10.3** and shown in **Figure 4.6**. The multivariate analysis showed a significant difference in the distribution of PCA scores between the control, cisplatin, etoposide, and heat-treated groups (**Figure 4.6A**). The scores of the heat-treated group concentrated in the second quadrant, while those of the cisplatin, etoposide, and control groups were concentrated in the third, fourth, and first quadrants, respectively. All groups showed good clustering with no clear outliers. The most significant spectral features driving the separation, as outlined in the loading plot (**Figure 4.6B**), corresponded to the following metabolites: lactate, creatine, glucose, glutamine, choline compounds, and mobile lipids (mainly $-\text{CH}_3$ and $-\text{CH}_2-$).

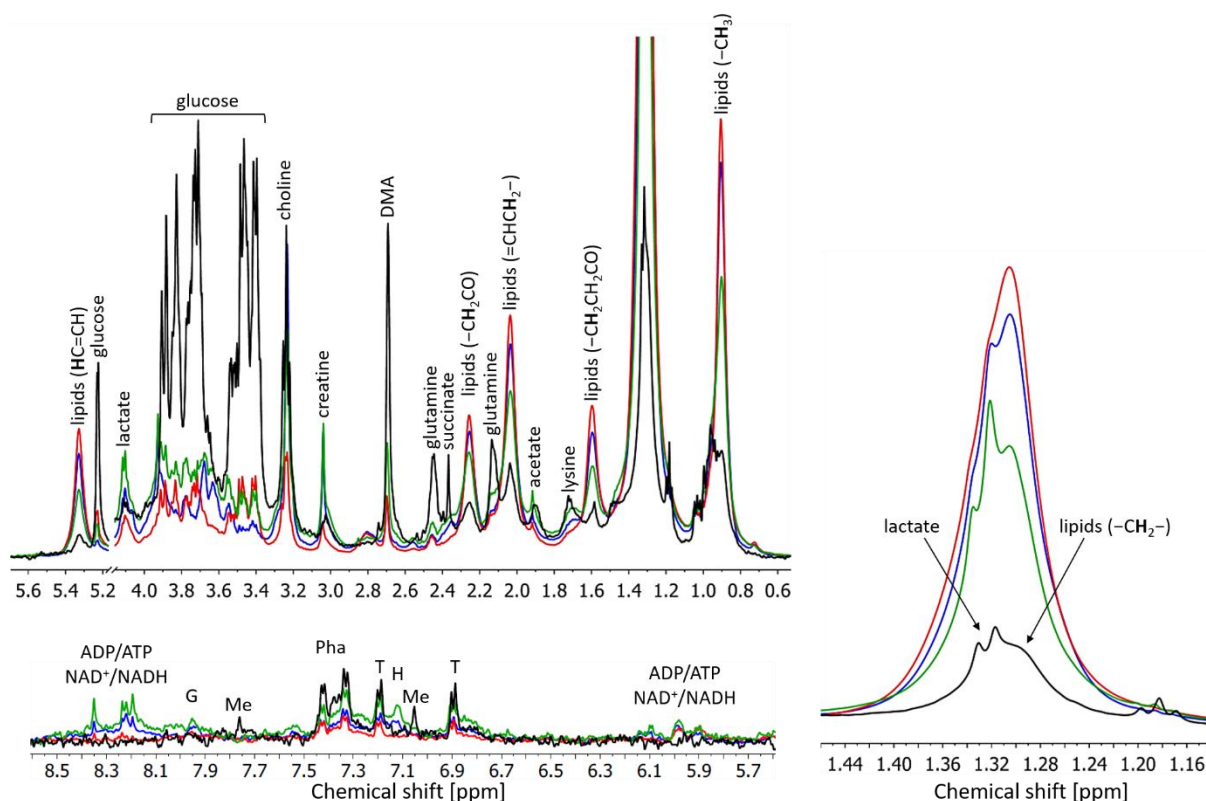


Figure 4.5. Superimposed 500 MHz HRMAS ^1H NMR spectra of intact C2C12 myotubes treated with cisplatin (red), etoposide (blue), and heat (grey) for 48h. The control spectrum of untreated cells shown in green. All spectra were normalised to the total integral. Partially suppressed water peak at 4.6 ppm was removed. T – tyrosine, H – histidine, G – guanosine, Me – methylhistidine, Pha – phenylalanine.

The heat-treated group comprising necrotic cells was strikingly different compared to the other groups and dominated the results. To better identify significant metabolites that were responsible for the separation of the control and apoptotic cells, PCA was performed on the same dataset excluding the heat-treated group. The score plot in **Figure 4.6C** shows a clear clustering of control, cisplatin, and etoposide groups. In this case, the most significant spectral features corresponded to lipids (mainly $-\text{CH}_3$ and $-\text{CH}_2-$), choline compounds, *myo*-inositol, creatine, lactate, and glucose.

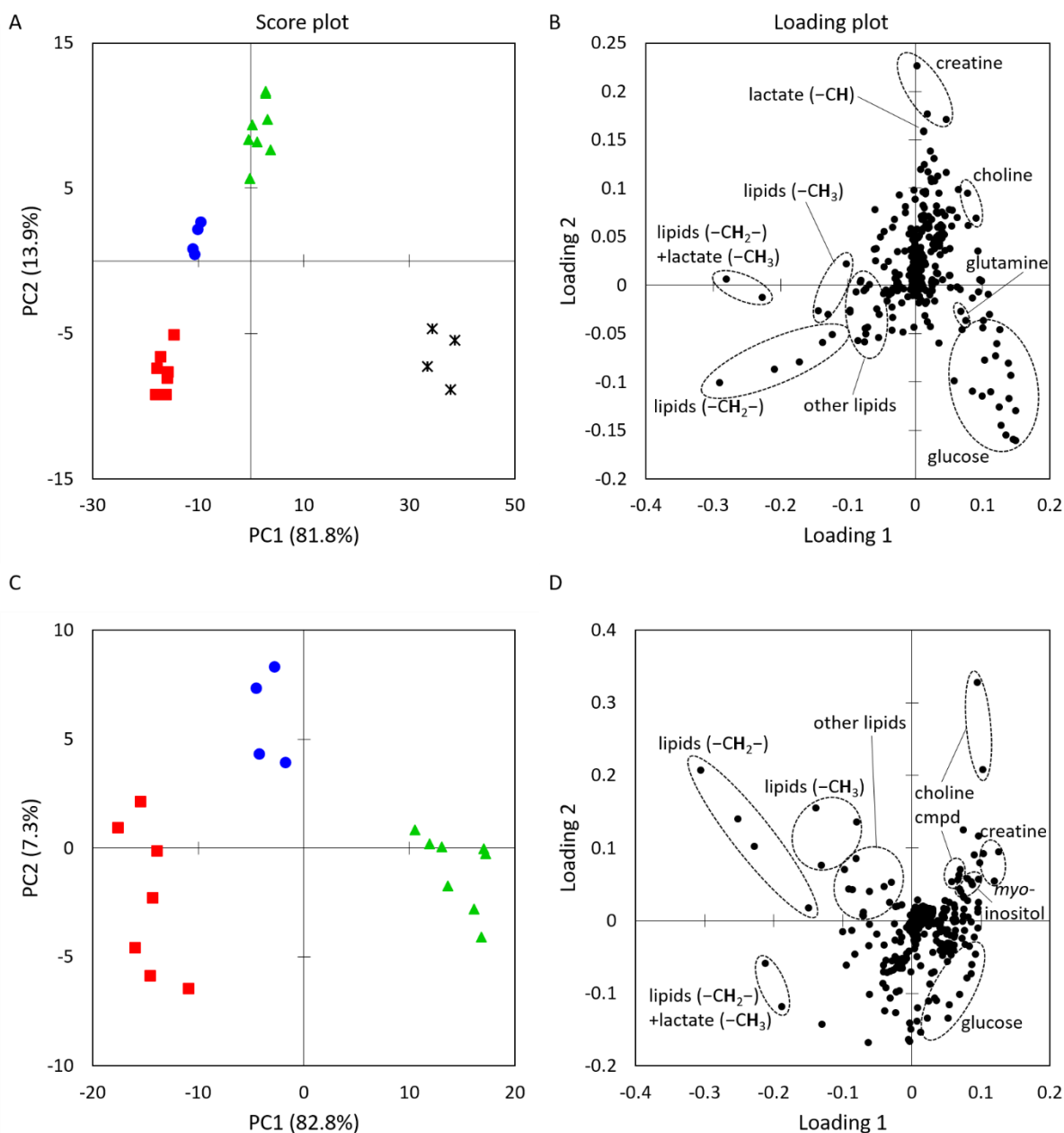


Figure 4.6. Two-dimensional PCA score plot (A) and corresponding loading plot (B) derived from the ¹H HRMAS NMR spectra of control (green triangles), cisplatin- (red squares), etoposide- (blue circles), and heat- (black asterisks) treated intact C2C12 myotubes. C, D show the same dataset excluding the heat-treated group. The most significant metabolites are highlighted in the loading plots. Other lipids: =CHCH₂CH=, -CH₂CH₂CO, =CHCH₂-, -CH₂CO; n = 4 for etoposide and heat, n = 8 for control and cisplatin. The numbers in brackets represent the percentage of variability explained by each PC. Spectra were pre-processed with total integral normalization and Pareto scaling.

A detailed analysis of significant features was performed for NMR-visible lipids (**Figure 4.7**) and small metabolites (**Figure 4.8**). Both necrotic and apoptotic cells showed distinct metabolomic variations as compared to the control group. The NMR-visible lipid signals increased for both cisplatin and etoposide groups by 20-85% as compared to the control group. Contrary to this, during heat treatment NMR-visible lipid signals were 50-70% lower compared to the control group. Several small metabolites such as creatine, glutathione, *myo*-inositol, acetate, lactate, ATP/ADP, and NAD⁺/NADH decreased for both apoptotic and necrotic cells. Other metabolites, including glutamine, glutamate, DMA, glycine, succinate, lysine, tyrosine, and phenylalanine decreased during apoptosis but increased during necrosis.

Cisplatin and etoposide-induced cell death was distinct by HRMAS ¹H NMR spectroscopy. The most significant difference was observed for choline compounds, creatine, and lactate. For the etoposide group, the levels of *myo*-inositol, glutathione were comparable with the levels in necrotic cells. For the cisplatin group, the levels of ATP, NADH and guanosine closely match the characteristics of necrosis. The different metabolic profiles were expected as the two apoptotic agents have different modes of action.

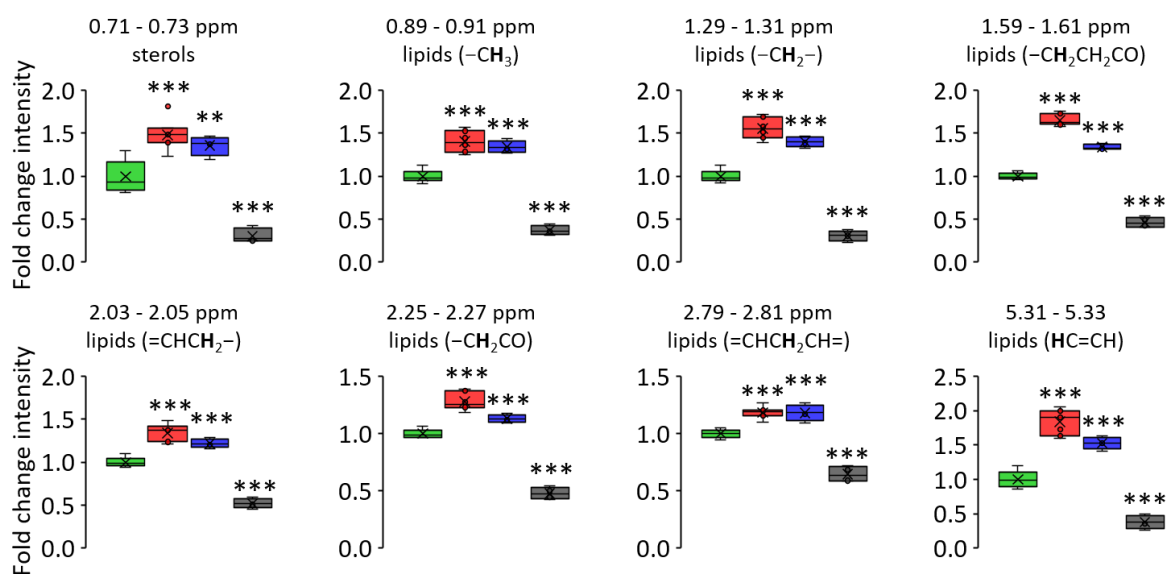


Figure 4.7. Comparison of lipids in C2C12 myotubes: control (green), cisplatin (red), etoposide (blue), and heat (grey), 48 h incubation. ANOVA with post hoc Fisher's test: * $p < 0.05$, ** $p < 0.01$, *** $p < 0.001$, FDR-adjusted; $n = 4$ for etoposide and heat, $n = 8$ for control and cisplatin.

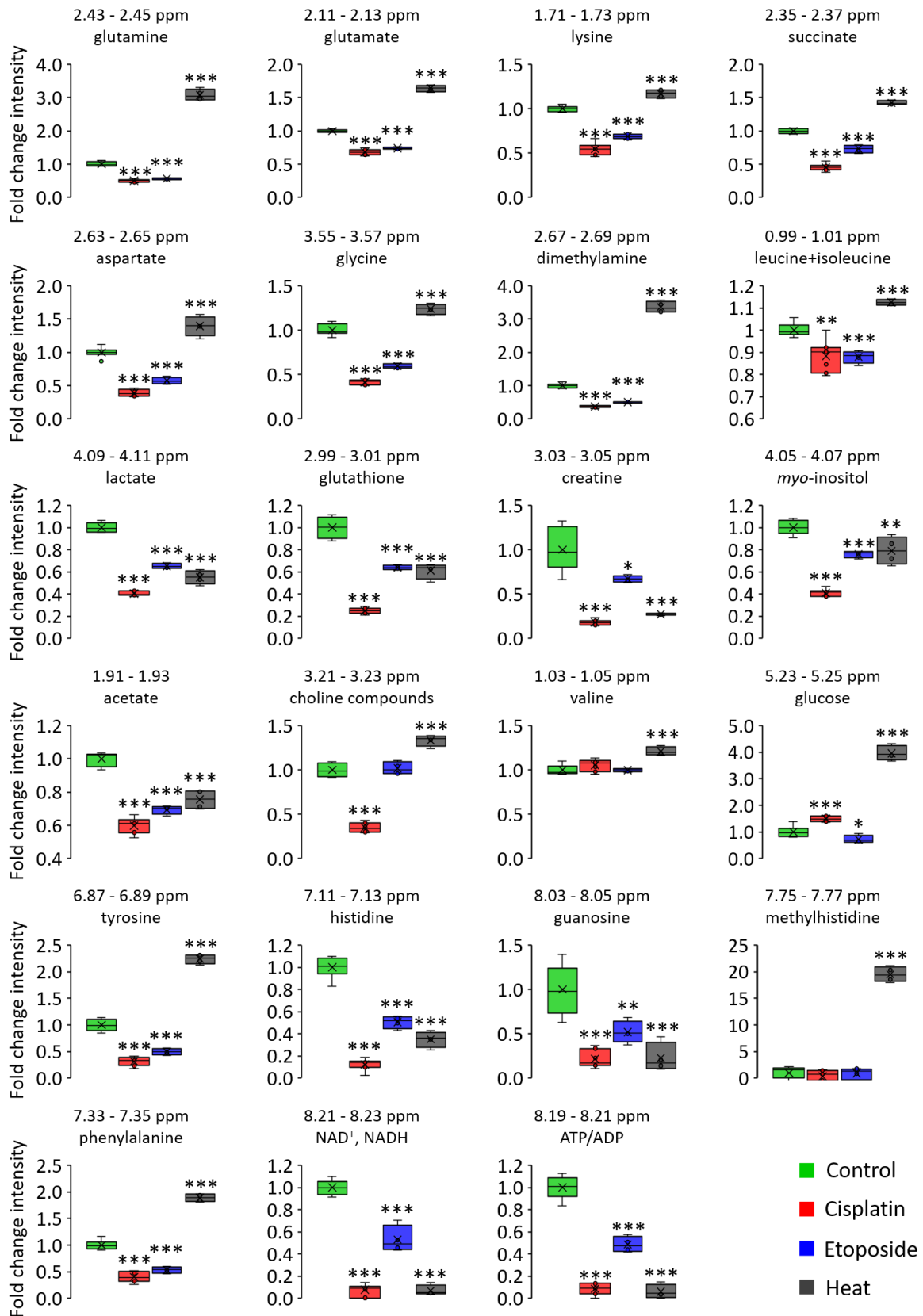


Figure 4.8. Comparison of metabolites in C2C12 myotubes: control (green), cisplatin (red), etoposide (blue), and heat (grey), 48 h incubation. ANOVA with post hoc Fisher's test: * $p < 0.05$, ** $p < 0.01$, *** $p < 0.001$, FDR-adjusted; $n = 4$ for etoposide and heat, $n = 8$ for control and cisplatin.

4.4.2.3. ^1H NMR analysis of growth media

The increase in metabolite resonance intensities in the HRMAS ^1H NMR spectra could correspond to increased tumbling of extracellular metabolites, which leaked out through the compromised cellular membranes. I tested if evidence of cellular disintegration could be detected in the growth media by solution-state ^1H NMR spectroscopy. The media samples were collected after 48 h of each treatment before harvesting the cells for HRMAS ^1H NMR experiments. To establish media baseline components and nutrients, non-incubated growth media was also collected as a media-only control group. **Figure 4.9** shows representative ^1H NMR spectra from each group and **Figure 4.10** shows the fold change of key metabolites relative to the media-only group. The significant changes between all 5 groups were determined by ANOVA with a *post hoc* test.

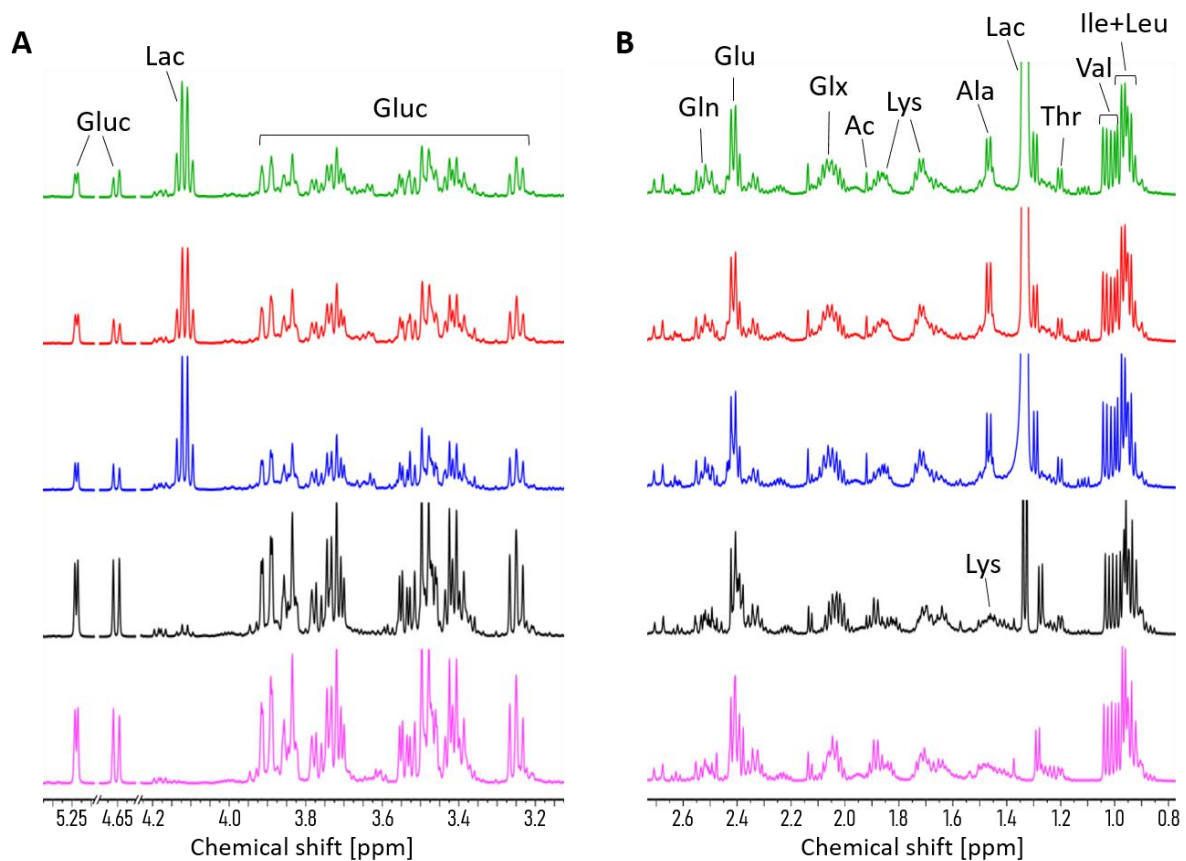


Figure 4.9. 500 MHz ^1H NMR spectra of growth media collected after 48 h treatments: media from C2C12 myotubes treated with - control (green), cisplatin (red), etoposide (blue), and heat (grey). Pink spectra represent media-only samples before adding to the cells. All spectra were normalized to the total integral. Partially suppressed water peak was removed. Ile – isoleucine, leu – leucine, val – valine, thr – threonine, lac – lactate, ala – alanine, lys – lysine, ac – acetate, glx – glutamine+ glutamate, glu – glutamate, gln – glutamine, gluc – glucose.

The spectra of media from heat-treated cells were very similar to non-incubated control media. Quantitative analysis of the spectra (**Figure 4.10**) revealed that four metabolites in heat-treated cells, namely lactate, glutamine, acetate, and threonine, increased significantly compared to the media-only group but their levels were lower compared to the control cell group.

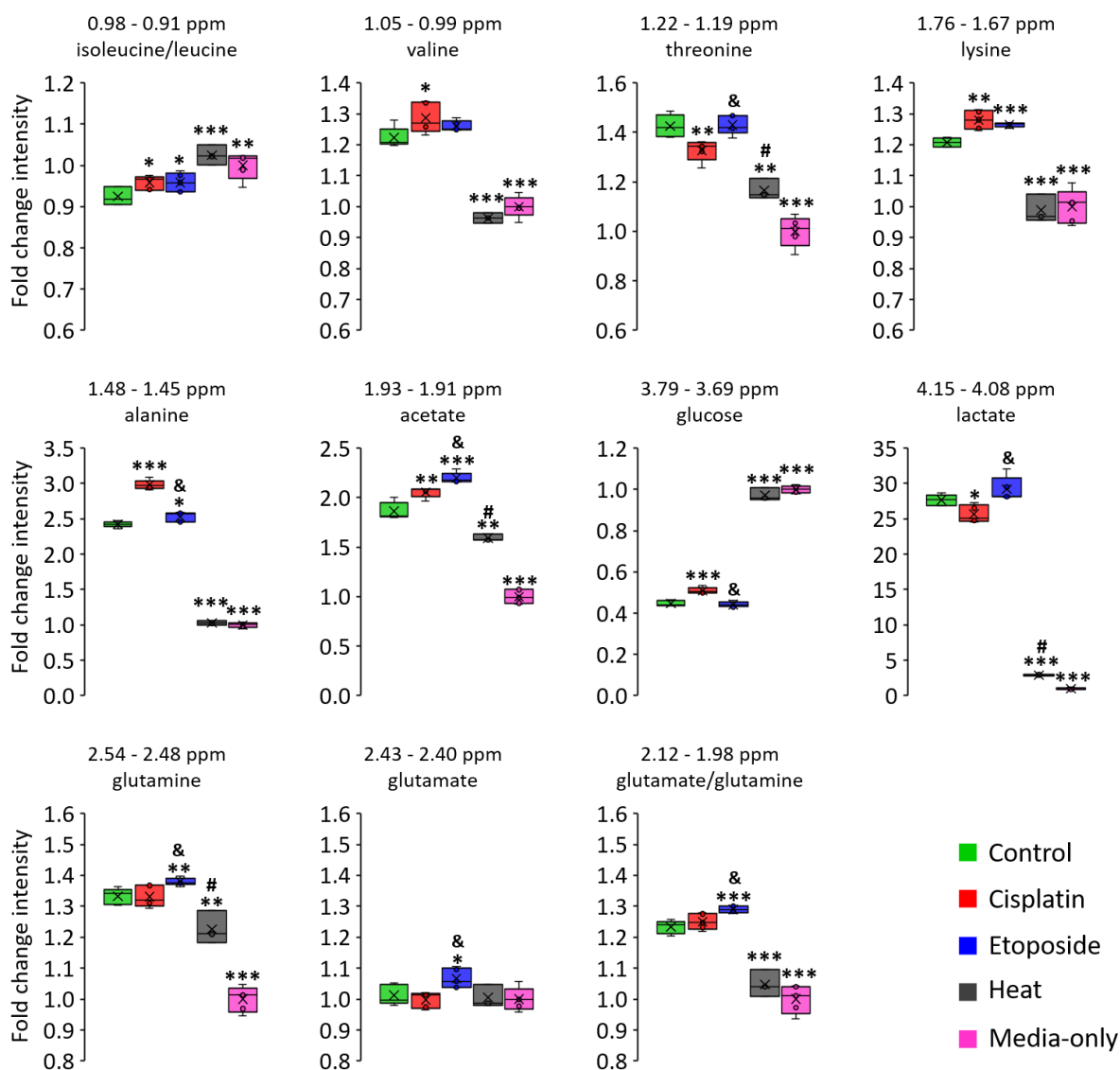


Figure 4.10. Comparison of metabolites found in growth media of C2C12 myotubes: control (green), cisplatin (red), etoposide (blue), heat (grey), and media-only (pink). ANOVA with post hoc Fisher's test: * $p < 0.05$, ** $p < 0.01$, *** $p < 0.001$ for all treatments vs control group, # $p < 0.05$ for heat vs media-only group, & $p < 0.05$ for cisplatin vs etoposide group, all p -values are FDR-adjusted.

Chemometrics and multivariate analysis of media spectra revealed several significant changes in the “secretome” (compounds released by cells) of the two apoptotic groups (**Figure 4.10**). The levels of isoleucine/leucine, lysine, alanine, acetate in the growth media were significantly

higher for both cisplatin- and etoposide-treated cells as compared to the control cell group, while the levels of threonine and lactate were lower for the cisplatin group. All of these metabolites must have been secreted by the cells, as their levels were higher than in the media-only samples. Moreover, analysis of PCA loadings identified that the most significant spectral features driving the discrimination between the cisplatin and etoposide treatments were threonine, alanine, lactate, glutamine, and glutamate.

4.4.3. ¹H NMR-based metabolic profiling of apoptotic cells – time course

This section describes a time-course experiment, in which I monitored changes of NMR-detectable metabolites during apoptosis progression. C2C12 myotubes were incubated with 60 μ M cisplatin or 120 μ M etoposide for 8, 24, and 48 h. To ensure adequate levels of apoptosis, the etoposide dose was doubled compared to the previous experiment (**Figure 4.4**). Cells cultured in T-75 flasks were divided into two samples: cells (approximately 10^5) for cell viability and caspase-3 assays to test the presence of cell death and apoptosis, respectively, and the remaining cells (approximately 10^6) were set aside for HRMAS ¹H NMR analysis. First, I investigated the levels of apoptosis in the NMR samples using caspase-3 activity and trypan blue exclusion assays. Subsequently, I analysed HRMAS ¹H NMR-based metabolic profiles of treated intact cells to investigate metabolite dynamics during apoptosis.

4.4.3.1. Caspase-3 activity assay and cell viability

According to the caspase assay (**Figure 4.11**), a significant level of apoptosis was induced in cisplatin- and etoposide-treated cells after 24 h. Apoptosis levels did not differ significantly between the cisplatin- and the etoposide-treated groups. Cell viability was significantly lower for the cisplatin group after 48 h, suggesting higher levels of secondary necrosis.

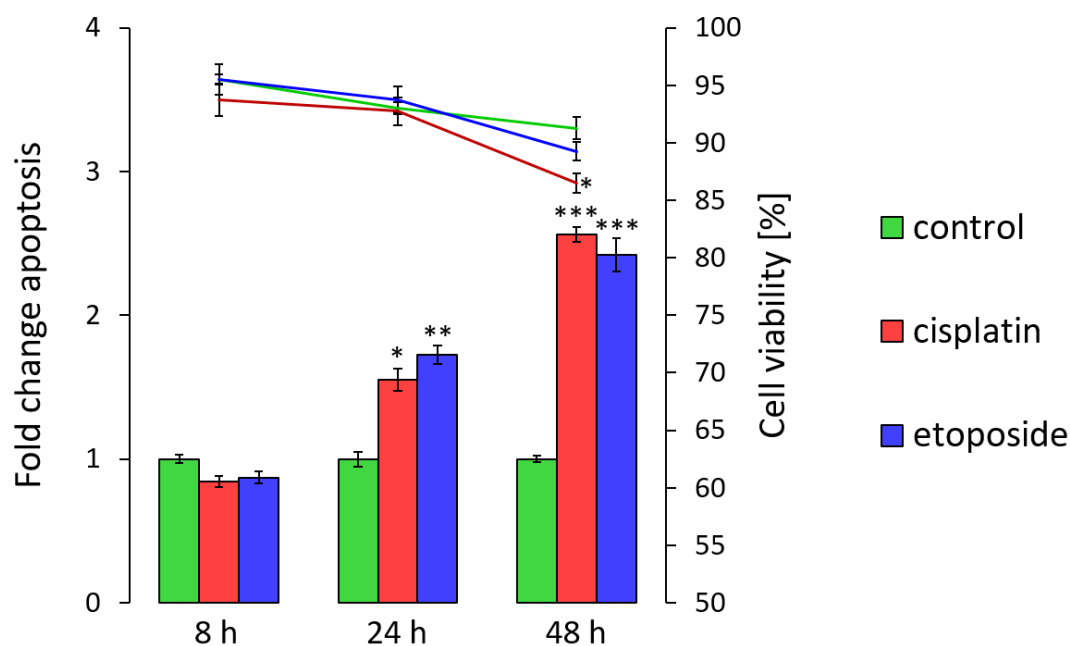


Figure 4.11. Cell viability (lines) and apoptosis (bars) of C2C12 myotubes treated with cisplatin 60 μ M (red) and etoposide 120 μ M (blue). The change in apoptosis is reported relatively to the control group (green); $n = 4$; ANOVA with post hoc Fisher's test: * $p < 0.05$, ** $p < 0.01$, *** $p < 0.001$.

4.4.3.2. HRMAS ^1H NMR analysis of intact cells

Figure 4.12 shows representative HRMAS ^1H NMR spectra of intact cells for each treatment and time point. The integrals of significant NMR bins (areas of the spectra that were significantly different from the control), which could be unambiguously annotated, were analysed as a function of time. The key metabolites were divided into two groups: small metabolites shown in **Figure 4.13** and lipids shown in **Figure 4.14**. When possible, multiple spectral bins corresponding to the same metabolite were analysed to assess consistency and exclude any effects from overlapping signals. In general, the levels of small metabolites decreased while the levels of lipids increased in apoptotic cells.

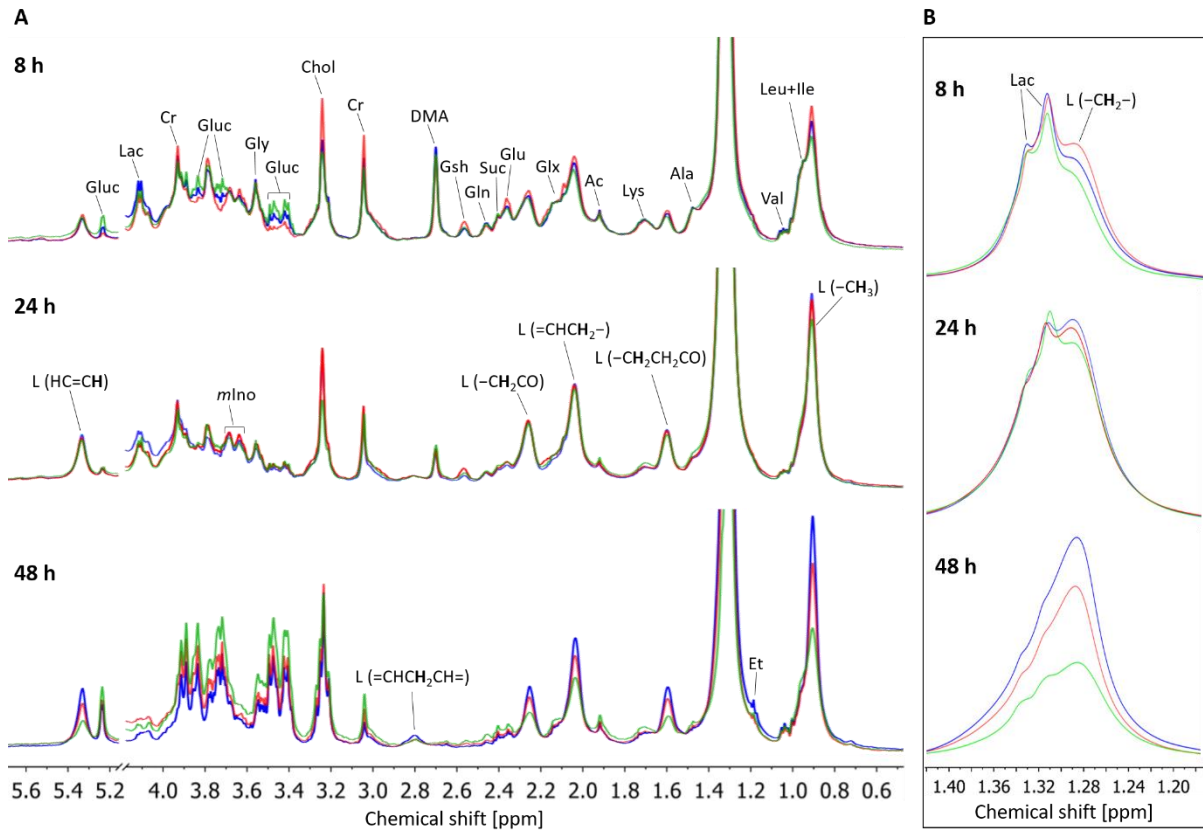


Figure 4.12. *A*) Superimposed 500 MHz HRMAS ^1H NMR spectra of control intact C2C12 myotubes (green), cisplatin- (red), and etoposide-treated (blue). All spectra were normalized to the total integral. The partially suppressed water peak at 4.6 ppm was removed. Gluc – glucose, lac – lactate, cr – creatine, gly – glycine, chol – choline compounds, DMA – dimethylamine, gsh – glutathione, suc – succinate, gln – glutamine, glu – glutamate, glx – glutamine+ glutamate, ac – acetate, lys – lysine, ala – alanine, val – valine, ile – isoleucine, leu – leucine, et – ethanol, L – lipids. *B*) Lactate and lipid signal at ~1.3 ppm.

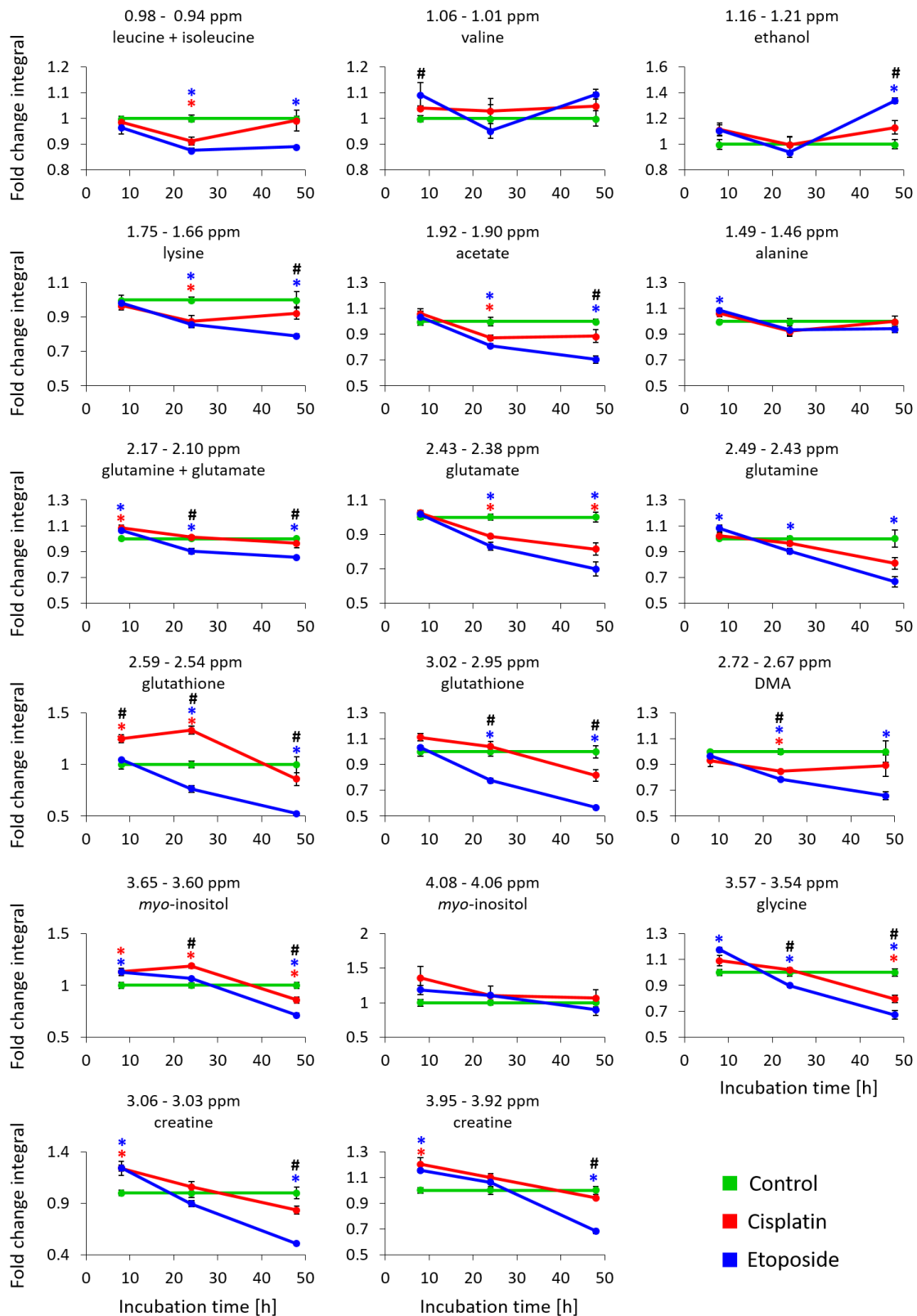


Figure 4.13. Comparison of metabolites in C2C12 myotubes: control (green), cisplatin (red), and etoposide (blue). Fold change integral reported relative to control at each time point. ANOVA with post hoc Fisher's test: *(red) $p < 0.05$ for cisplatin vs control group, *(blue) $p < 0.05$ for etoposide vs control group, # $p < 0.05$ for cisplatin vs etoposide group, all p -values are FDR-adjusted.

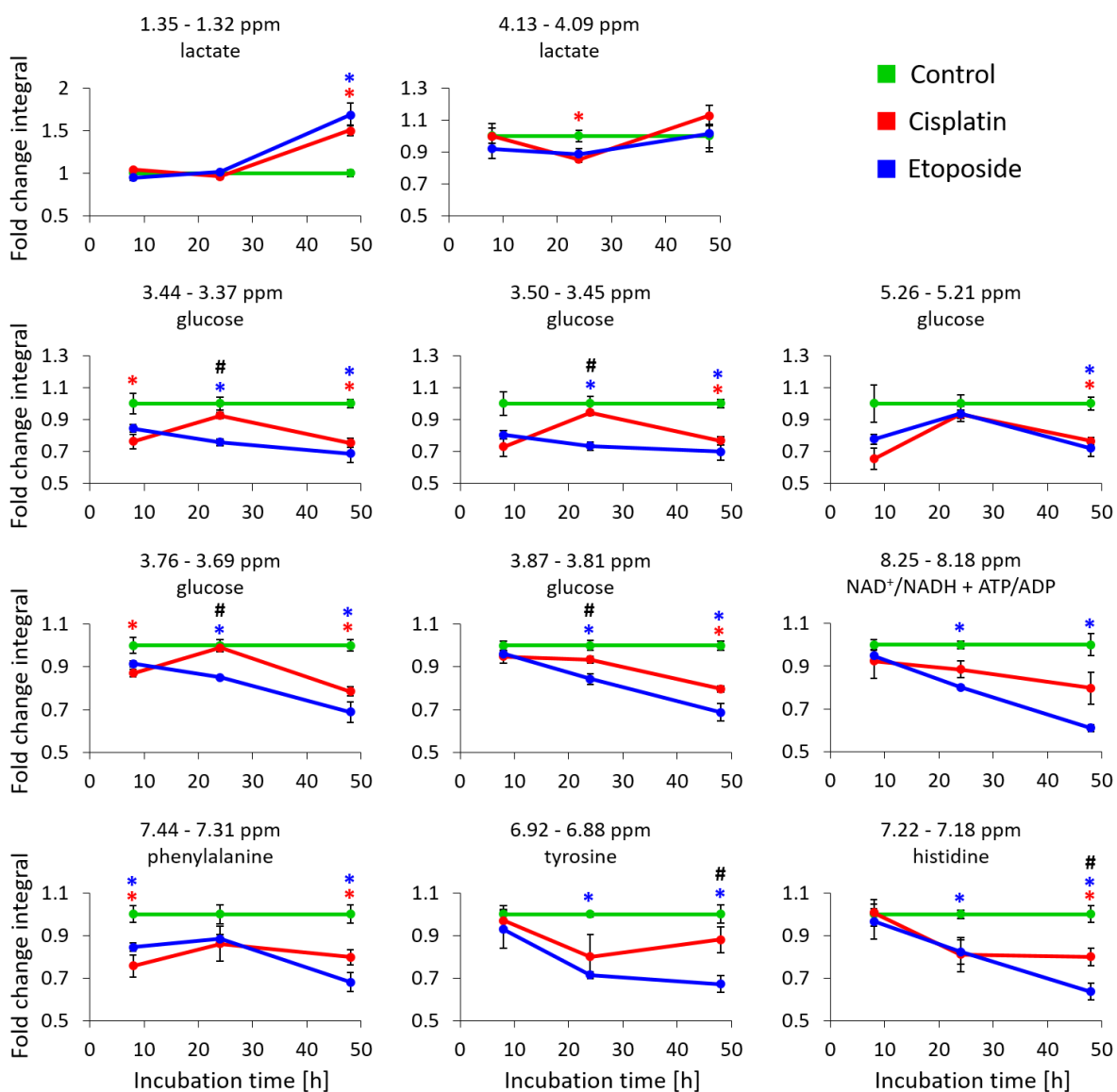


Figure 4.13. *Continued.*

Monitoring metabolic changes with time revealed that some metabolites, such as DMA, tyrosine and ATP/ADP decreased consistently throughout the treatment (8 – 48 h), while other metabolites such as creatine, glycine, and *myo*-inositol increased during early apoptosis (8 h) and decreased during late apoptosis (48 h).

Figure 4.15 shows the changes in choline compounds with apoptosis progression. The levels of choline compounds in intact cells monitored by HRMAS ¹H NMR spectroscopy increased in the early stage of apoptosis (8 – 24 h) and decreased in the late stage of apoptosis (48 h).

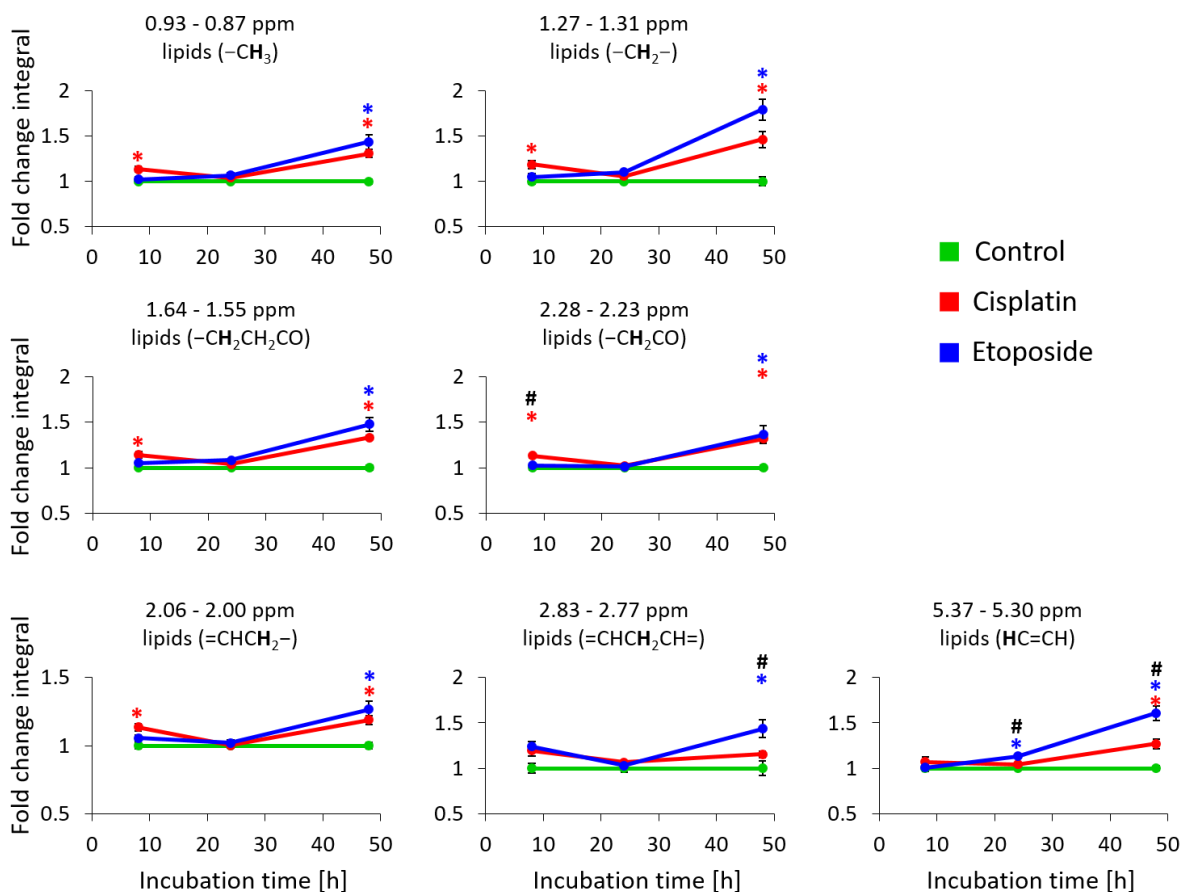


Figure 4.14. Comparison of lipids in C2C12 myotubes: control (green), cisplatin (red), and etoposide (blue). Fold change integral reported relative to control at each time point. ANOVA: *(red) $p < 0.05$ for cisplatin vs control group, *(blue) $p < 0.05$ for etoposide vs control group, # $p < 0.05$ for cisplatin vs etoposide group, all p -values are FDR-adjusted.

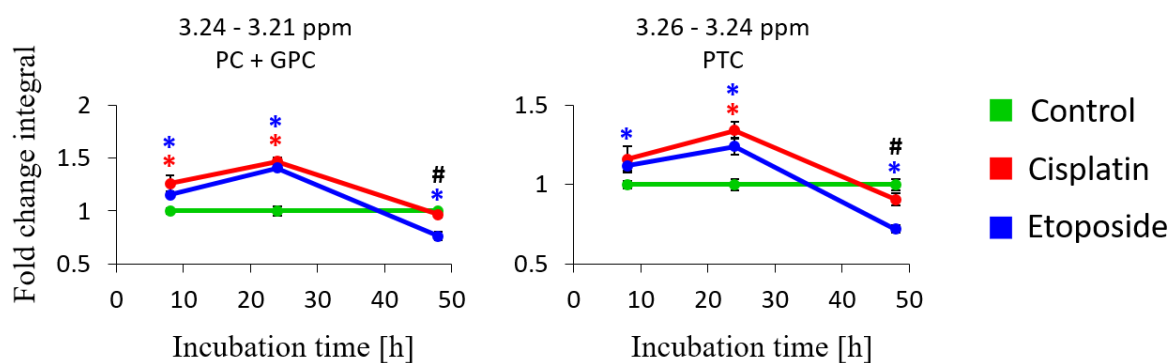


Figure 4.15. Comparison of choline-containing compounds in C2C12 myotubes as measured by HRMAS ¹H NMR spectroscopy: control (green), cisplatin (red), and etoposide (blue). Fold change integral reported relative to control at each time point. PC – phosphocholine, GPC – glycerophosphocholine, PTC – phosphatidylcholine. ANOVA with post hoc Fisher's test: *(red) $p < 0.05$ for cisplatin vs control group, *(blue) $p < 0.05$ for etoposide vs control group, # $p < 0.05$ for cisplatin vs etoposide group, all p -values are FDR-adjusted.

4.4.4. Combined NMR-based metabolomics of intact cell, cell extract, and media

In addition to the above results, I conducted a solution-state NMR analysis of cell extract samples collected after 48 h incubation with the apoptotic agents. For comprehensive NMR-based metabolic profiling of apoptotic cells, **Table 4.1** combines the results from HRMAS ^1H NMR-based metabolic profiles of intact cells (**Section 4.4.2.2** and **4.4.3.2**), solution-state ^1H NMR-based metabolic profiles of intact cells (**Section 4.4.2.2** and **4.4.3.2**), solution-state ^1H NMR-based metabolic profiles of cell extracts (**Section 4.4.4**) and the solution-state ^1H NMR-based metabolic profiles of culture media (**Section 4.4.2.3**). Two independent experiments on intact cells and growth media samples treated with 60 μM cisplatin were performed and the results were compared to evaluate the reproducibility of the experiment (etoposide doses were different: 50 μM for experiment 1 – low levels of apoptosis, 120 μM for experiment 2 – high levels of apoptosis).

Table 4.1. Metabolite profiling of apoptotic C2C12 myotubes by solution-state (growth media and cell extract) and HRMAS (intact cells) ^1H NMR spectroscopy. Two independent experiments for intact cells and growth media were performed (Intact cell 1 and Media 1: cisplatin 60 μM etoposide 50 μM ; Intact cells 2, Cell extract 2, Media 2: cisplatin 60 μM , etoposide 120 μM). Supporting data can be found in **Appendix 1**. \uparrow and \downarrow indicate an increase or decrease in a fold change integral for cisplatin (red) and etoposide (blue) groups as compared to control; \leftrightarrow indicates non-significant changes, n/a – signal not present or could not be accurately measured.

Metabolite	Intact cells 1	Intact cells 2	Cell extract 2	Media 1	Media 2
Sterols 0.71 – 0.73 ppm	$\uparrow\uparrow$	n/a	$\uparrow\uparrow$	n/a	n/a
Lipids ($-\text{CH}_3$) 0.89 – 0.91 ppm	$\uparrow\uparrow$	$\uparrow\uparrow$	$\uparrow\uparrow$	n/a	n/a
Lipids ($-\text{CH}_2-$) 1.29 -1.31 ppm	$\uparrow\uparrow$	$\uparrow\uparrow$	$\uparrow\uparrow$	n/a	n/a
Lipids ($-\text{CH}_2\text{CH}_2\text{CO}$) 1.59 – 1.61 ppm	$\uparrow\uparrow$	$\uparrow\uparrow$	$\downarrow\downarrow$	n/a	n/a
Lipids ($=\text{CHCH}_2-$) 2.03 – 2.05 ppm	$\uparrow\uparrow$	$\uparrow\uparrow$	$\leftrightarrow\downarrow$	n/a	n/a
Lipids ($-\text{CH}_2\text{CO}$) 2.25 – 2.27 ppm	$\uparrow\uparrow$	$\uparrow\uparrow$	$\downarrow\downarrow$	n/a	n/a
Lipids ($=\text{CHCH}_2\text{CH}=\text{}$) 2.79 – 2.81 ppm	$\uparrow\uparrow$	$\uparrow\uparrow$	$\uparrow\uparrow$	n/a	n/a
Lipids ($-\text{HC}=\text{CH}-$) 5.31 – 5.33 ppm	$\uparrow\uparrow$	$\uparrow\uparrow$	$\leftrightarrow\uparrow$	n/a	n/a
PC lipids 3.28 – 3.26 or 3.37 – 3.35 ppm	$\downarrow\downarrow$	$\downarrow\downarrow$	$\leftrightarrow\uparrow$	n/a	n/a

Table 4.1. Continued.

Metabolite	Intact cells 1	Intact cells 2	Cell extract 2	Media 1	Media 2
Glutamine 2.43 – 2.45 ppm	↓↓	↓↓	↓↔	↔↑	↔↔
Glutamate 2.35 – 2.28 ppm	↓↓	↓↓	↓↓	↔↑	↑↔
Lysine 1.71 – 1.73 ppm	↓↓	↔↓	↓↔	↑↑	↓↔
Succinate 2.35 – 2.37 ppm	↓↓	n/a	↓↓	n/a	n/a
Glycine 3.55 – 3.57 ppm	↓↓	↓↓	↓↓	n/a	n/a
DMA 2.67 – 2.69 ppm	↓↓	↔↓	↔↓	n/a	n/a
Leucine + isoleucine 0.99 – 1.01 ppm	↓↓	↔↓	↔↔	↑↑	↑↔
Lactate 4.09 – 4.11 ppm	↓↓	↔↔	↓↑	↓↔	↓↓
Glutathione 2.99 – 3.01 ppm	↓↓	↔↓	↔↓	n/a	↓↓
Creatine 3.03 – 3.05 ppm	↓↓	↔↓	↑↓	n/a	n/a
Myo-inositol 4.05 – 4.07 ppm	↓↓	↓↓	↑↑	n/a	n/a
Acetate 1.91 – 1.93 ppm	↓↓	↔↓	↓↓	↑↑	↔↓
Valine 1.03 – 1.05 ppm	↔↔	↔↔	↔↔	↑↔	↓↓
Glucose 5.23 – 5.25 ppm	↑↓	↓↓	↑↑	↑↔	↑↑
Tyrosine 6.87 – 6.89 ppm	↓↓	↔↓	↑↑	↓↔	↔↔
Histidine 7.11 – 7.13 ppm	↓↓	↓↓	n/a	n/a	n/a
Phenylalanine 7.33 – 7.35 ppm	↓↓	↓↓	↔↔	↔↔	↔↔
ATP/ADP 8.23 – 8.19 ppm	↓↓	↔↓	↓↓	n/a	n/a
Choline compounds 3.21 – 3.23 ppm	↓↓	↔↓	↑↑	n/a	n/a
Alanine 1.48 – 1.45 ppm	↔↔	↔↔	↓↔	↑↑	↑↑

The increase in lipid resonances was consistent across the two experimental batches of intact cells. However, not all lipid resonances in the cell extract samples increased after apoptotic treatment. Both NMR methods showed a significant increase in the intensities of lipid $-\text{CH}_3$,

$-\text{CH}_2-$, and $=\text{CHCH}_2\text{CH}=\text{}$ resonances. The HRMAS ^1H NMR spectra showed a greater increase in the intensity of the lipid signals (30 – 70%, **Figure 4.16**, intact cells), whereas solution-state ^1H NMR showed a much smaller increase (5 – 20%, **Figure 4.16**, cell extracts; more detailed analysis in **Appendix 1**). Some lipid resonances decreased or did not change significantly in the cell extract samples, namely $-\text{CH}_2\text{CH}_2\text{CO}$, $=\text{CHCH}_2-$, $-\text{CH}_2\text{CO}$.

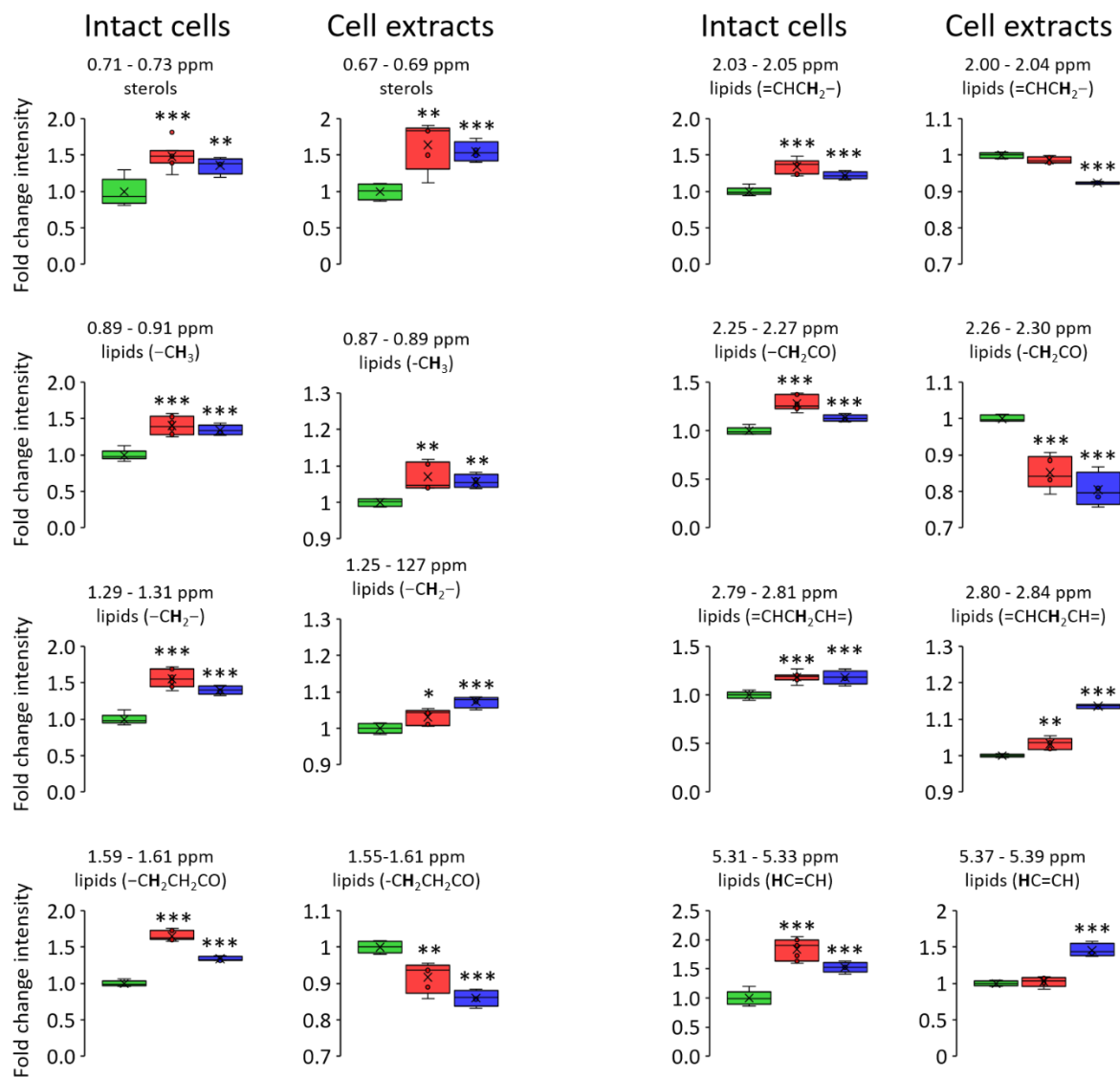


Figure 4.16. Comparison of lipid resonances of intact C2C12 myotubes (HRMAS ^1H NMR spectroscopy) and C2C12 myotubes extracts (solution-state ^1H NMR spectroscopy): control (green), cisplatin (red), and etoposide (blue) after 48 h incubation. ANOVA with post hoc Fisher's test: * $p < 0.05$, ** $p < 0.01$, *** $p < 0.001$.

4.5. Discussion

In **Chapter 4**, I investigated the metabolic profiles of control and treated cells by ^1H NMR spectroscopy to identify metabolites that can be used for differentiating between control and apoptotic/necrotic treatments. The levels of apoptosis and necrosis induced by cisplatin, etoposide or heat treatments were assessed with conventional biochemical assays. Changes in the metabolic profiles of intact cells were measured by HRMAS ^1H NMR spectroscopy, whereas changes in the metabolic profiles of growth media and cell extracts were measured by solution-state ^1H NMR spectroscopy. All applied NMR methods showed distinct metabolic profiles discriminating between the treatment groups and control cells.

4.5.1. Metabolic profiling of intact cells

HRMAS ^1H NMR-based profiling of intact cells showed an increase in lipid resonances for apoptotic samples as compared to the controls (**Figure 4.7**). This finding supports previous reports that linked apoptosis with increased intensities for resonances of NMR-visible lipids. Pan and colleagues reported an increase in the concentration of unsaturated fatty acids in cells undergoing cisplatin-induced cell death.²⁰⁴ Duarte and colleagues also reported an increase in the lipid profile of cells treated with cisplatin.²⁷⁹ Schmitz and colleagues reported increased mobile lipids after etoposide treatment.²¹¹ NMR-visible lipids have been linked to the formation of cellular lipid droplets and are a recognised biomarker of apoptosis.^{205,208,284}

According to the biochemical assays, etoposide-treated cells showed no caspase-3 activation, but significant cell death as compared to the control group (**Figure 4.4**). However, the NMR-based lipid profile suggested more similarities to the cisplatin (apoptosis) group than the heat (necrosis) group (**Figure 4.7**). Similarly, the changes in aqueous metabolites (e.g., glutamine, glutamate, lysine, aspartate, and dimethylamine) were consistent with apoptosis rather than necrosis (**Figure 4.8**). This may suggest that low doses of etoposide trigger a caspase-independent pathway that leads to apoptosis. Indeed, Bruni and colleagues showed that at high dose, etoposide promoted caspase-3 mediated apoptosis, while at low dose, it induced caspase-3 independent cell death, displaying features similar to apoptosis.²⁸⁵

The levels of several small metabolites changed significantly during apoptosis and necrosis and could be used to discriminate between the groups (**Figure 4.8**). These results are consistent with a HRMAS ^1H NMR study by Duarte and colleagues who reported a decrease in glutamate,

glycine, and *myo*-inositol in MG-63 osteosarcoma cells after cisplatin treatment (30 μ M and 50 μ M).²⁷⁹ The results are also consistent with the findings reported by Rainaldi and colleagues.¹⁹⁴ They subjected leukaemia cells to a heat treatment (57°C) and observed an increase in glutamate, glutamine and choline, and a decrease in glutathione in intact cells as measured by ¹H NMR spectroscopy. Relevant literature on etoposide metabolic signatures in intact cells was not found. However, Gey and colleagues reported NMR-detectable metabolic changes in cell extracts of lung fibroblasts induced by etoposide treatment (34 μ M).²⁸⁶ They reported an increase in isoleucine and leucine and a decrease in acetate. Interestingly, they used etoposide for induction of senescence rather than caspase-dependent apoptosis. MS-based results reported by Halamal and colleagues are also in agreement with the HRMAS ¹H NMR results presented in this chapter.¹⁸⁶ In their study, etoposide treatment (100 μ M) induced a decrease in aspartate, glutamate, glutamine, glycine, and leucine among other metabolites.

Agreement with the existing literature on cisplatin validated the experimental methodology in this thesis. Furthermore, it demonstrated that HRMAS ¹H NMR spectroscopy of intact cells can differentiate between different drug-dependent apoptotic mechanisms. This could have a potential application in *in vitro* monitoring of apoptotic-based treatments for drug discovery and may be extended to other non-apoptotic treatments.

4.5.2. Cellular disintegration by ¹H NMR spectroscopy

The increase of metabolites during necrosis, as measured by HRMAS ¹H NMR spectroscopy, can be explained in two ways: 1) disruption of metabolic pathways, which leads to the accumulation of reaction products or substrates, or 2) cellular disintegration, which increases tumbling rates of the metabolites and thus NMR-visibility. In particular during necrosis, severely compromised cellular membranes and damaged organelles may trigger the release of cytoplasmic content into the growth media.²⁸⁷ To test the second hypothesis I looked for evidence of increased concentration of exometabolome components in growth media.

The spectra of growth media (**Figure 4.9**) from heat-treated cells were very similar to these from media-only control group. Four metabolites namely lactate, glutamine, acetate, and threonine increased significantly compared to the media-only group, but their levels were lower compared to the control cell group (**Figure 4.10**). This observation suggests that rapid, heat-induced necrosis halted glucose consumption and the secretion of intracellular metabolites into

the growth media. In addition, no evidence of excessive leakage of metabolites out of necrotic cells was detected by NMR spectroscopy, suggesting that the metabolites were contained inside the necrotic cells. However, the media study cannot exclude that the increased signals of small metabolites in the necrotic HRMAS ^1H NMR spectra occurred due to increased molecular tumbling of metabolites inside necrotic cells. This will be further investigated by measuring ^1H NMR relaxation times and diffusion coefficients of metabolites (**Chapter 5**).

Comparing NMR-based metabolic profiles of intact cells and cell extracts could also help establish the origin of the increased HRMAS ^1H NMR resonances. If the resonances increase in the HRMAS but not on the solution-state ^1H NMR spectra, this would indicate that the metabolites in intact cells become more mobile due to changes in the cellular environment. Necrotic cell extracts showed a decrease in glutamine, glutamate, DMA, glycine, and no significant changes in succinate, lysine, tyrosine, and phenylalanine (data shown in **Appendix 1, Table S1.1, Figure S1.1**). Therefore, the increase in some metabolites in necrotic cells, as measured by HRMAS ^1H NMR spectroscopy, is most likely due to cellular disintegration and changes in the molecular environment.

This study demonstrates that combining NMR-based metabolomics of intact cells, cell extracts and growth media can provide useful structural information to explain metabolic changes induced by heat or drug treatment. This approach could be potentially used to establish an NMR-based assay for cellular disintegration. More experiments are needed to establish if cellular disintegration caused by treatments other than heat could be observed in HRMAS ^1H NMR spectra and what levels of disintegration could be detected.

4.5.3. Lactate co-resonates with $-\text{CH}_2-$ lipid

A significant signal overlap at ~ 1.3 ppm introduces some ambiguity about the changes of lactate and lipid ($-\text{CH}_2-$) during apoptosis. The lactate $-\text{CH}_3$ and $-\text{CH}$ resonances at 1.3 and 4.1 ppm, respectively, did not show consistent results (**Figure 4.13**). This discrepancy may be explained by overlap with the lipid $-\text{CH}_2-$ resonance at 1.3 ppm. To test this hypothesis, I conducted T_2 -edited CPMG experiments, which largely reduced the lipid resonances (spin-spin relaxation delay of 1.2 s). **Figure 4.17A** shows the T_2 -edited spectra (lactate region only: 1.20 – 1.45 ppm) of treated and control cells harvested after 24 h, and **Figure 4.17B** shows a comparison of lactate integrals between the treated and control groups. The lipid $-\text{CH}_2-$ (1.3

ppm) resonance is still visible in the spectra, but its intensity is greatly reduced and thus its contribution to the lactate $-\text{CH}_3$ (1.3 ppm) resonance. The lactate $-\text{CH}_3$ (1.3 ppm) integral analysis showed a decrease in lactate levels during apoptosis, which is consistent with the data reported for the lactate ($-\text{CH}$, 4.1 ppm) resonance at 4.1 ppm in the experiment without a T_2 -filter (**Figure 4.13**, 24 h).

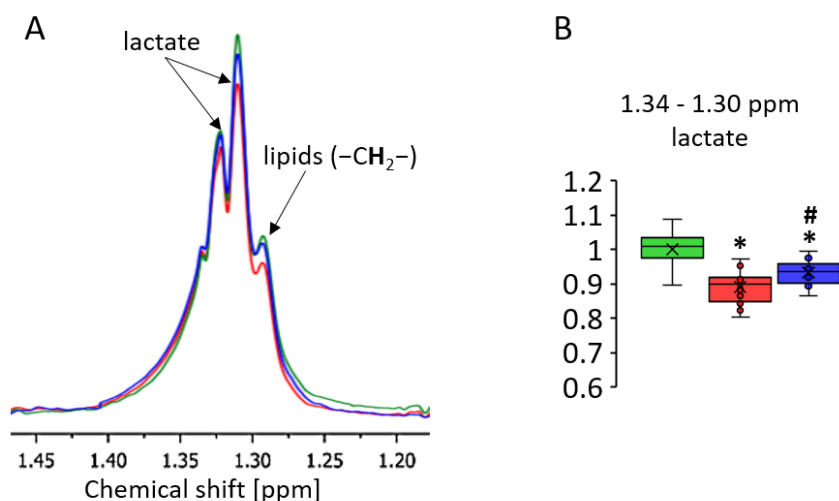


Figure 4.17. **A)** Superimposed 500 MHz HRMAS ^1H NMR T_2 -edited spectra of control (green), cisplatin- (red), and etoposide-treated (blue) C2C12 myotubes (24 h) showing the lactate region only. All spectra were normalized to the total integral. **B)** Fold change integral of lactate ($-\text{CH}_3$) as compared to the control group; $n = 16$; ANOVA with post hoc Fisher's test: * $p < 0.001$ for control vs treatments, # $p < 0.001$ for cisplatin vs etoposide.

An analysis of the lactate and lipid $-\text{CH}_2-$ co-resonance at 1.3 ppm revealed that while the $-\text{CH}_2-$ lipid levels increase with apoptosis, the lactate levels decrease. These counteracting effects could lead to misleading interpretations of lactate metabolism. I demonstrated that the lactate ($-\text{CH}$, 4.1 ppm) resonance may be more suitable for monitoring changes in lactate concentration. However, one should be cautious about the effect of water suppression on the lactate ($-\text{CH}$, 4.1 ppm) resonance. In some cases, insufficient water suppression could artificially increase the signal while excessive water suppression could decrease the signal. This effect is visible in **Figure 4.12** especially in the 24 and 48 h spectra. For the calculation in **Figure 4.13**, this was corrected by empirical adjustment of the baseline in this region.

Moreover, the decrease in lactate levels for cisplatin and etoposide treatments at 24 h could contribute to a small decrease in the lipid ($-\text{CH}_2-$) resonances (**Figure 4.14**). It is noticeable that for many lipid resonances cisplatin treatment caused an increase in signal intensity at 8 h

and 48 h, but a decrease at 24 h. This may be caused by co-resonant aqueous metabolites associated with lactate, glutamate, leucine, and isoleucine - metabolites that decreased in concentration at 24 h. This observation was not seen for the lipid resonance at 5.3 ppm which is not co-resonant with other metabolites, with the resonance being significantly higher for the etoposide group at 24 h.

4.5.4. HRMAS ^1H NMR spectroscopy of choline compounds in intact cells

Choline compounds are important building blocks of cellular membranes. Large molecules containing choline that are incorporated in the membrane are not NMR-visible as their tumbling is restricted. However, small, unbound choline-containing compounds, such as phosphocholine (Pcholine), phosphatidylcholine (PTC) and glycerophosphocholine (GPC), can be detected in intact cells. These are important molecules for cancer biology because of their link to membrane changes during apoptosis and their role as secondary messengers.

The changes in choline compounds monitored by HRMAS ^1H NMR spectroscopy reported here (**Figure 4.15**) are consistent with the results reported by Duarte and colleagues.²⁷⁹ The initial increase in the concentration of choline-containing compounds as observed by HRMAS ^1H NMR spectroscopy can be explained by membrane breakdown and the release of phospholipids, while the decreased levels at late stages of apoptosis reflect the depletion of choline in the cell. It was also demonstrated that the formation of small endosomes during apoptosis can contribute to the resonances of NMR-visible choline compounds.²⁸⁸

PTC is an important building block of plasma membranes and the cytidine diphosphate-choline (CDP-choline) pathway (**Figure 4.19**) is the predominant mechanism by which it is biosynthesized for incorporation into membranes. Alterations in this pathway are well-studied in the context of apoptosis.^{289–291} I therefore tested if the decrease in PTC measured by HRMAS ^1H NMR spectroscopy (**Figure 4.15**) can be explained by downregulation of the CDP-choline pathway.

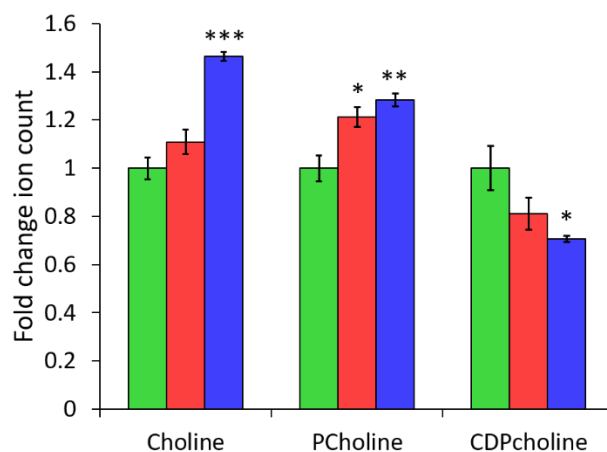


Figure 4.18. Comparison of choline containing compounds in C2C12 myotubes as measured by mass spectrometry: control (green), cisplatin (red), and etoposide (blue) after 48 h incubation. Fold change in ion count reported relative to control. Pcholine – phosphocholine, CDP-choline – cytidine 5'-diphosphocholine. ANOVA with post hoc Fisher's test: * $p < 0.05$, ** $p < 0.01$, *** $p < 0.001$.

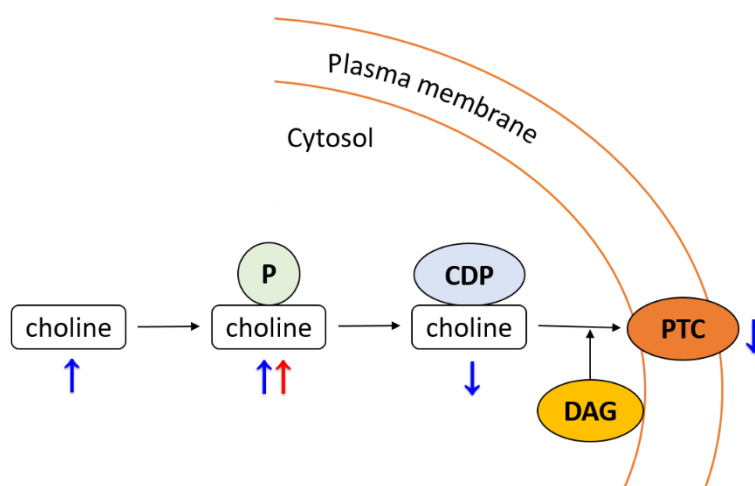


Figure 4.19. CDP-choline pathway for PTC biosynthesis. Cytosolic choline is firstly phosphorylated and then converted to CDP-choline, which is a rate-limiting step regulated by signals from the membrane. CDP-choline is translocated to the membrane and converted to PTC. Red and blue arrows indicate a significant ($p < 0.05$) increase or decrease in choline-containing metabolites in cisplatin- or etoposide-treated cells, respectively. Choline, Pcholine and CDP-choline were measured by MS (**Figure 4.18**) and PTC was measured by HRMAS ^1H NMR spectroscopy (**Figure 4.15**).

The three precursors of PTC: choline, Pcholine and CDP-choline were investigated by quantitative mass spectrometry (same treatments, 48 h) (**Figure 4.18**) (for detailed experimental description see **Chapter 2, Section 2.14**). The concentrations of choline and Pcholine increased significantly for etoposide-treated cells while the concentration of cytidine

5'-diphosphocholine (CDP-choline) significantly decreased. Combined MS and NMR measurements of the choline-containing compounds are mapped in **Figure 4.19**. Firstly, both analytical techniques detected significant changes in etoposide-treated cells but not in cisplatin-treated cells. In addition, the decrease in the formation of CDP-choline as measured by MS could explain the decrease in the PTC levels as measured by HRMAS ^1H NMR spectroscopy. Therefore, it was proposed that the CDP-choline pathway is disrupted by etoposide but not cisplatin. These results demonstrated that MS and HRMAS NMR can be used as complimentary methods to confirmed proposed alterations in metabolic pathways.

4.5.5. HRMAS vs solution-state ^1H NMR spectroscopy

The data showed that the increase in NMR-visible lipids during apoptosis is larger as detected by HRMAS ^1H NMR spectroscopy in intact cells and smaller as detected by solution-state ^1H NMR spectroscopy of cell extracts (**Figure 4.16**). This discrepancy between cell extract and intact cell samples may be explained in two ways: 1) the changes in total lipid content as measured by solution-state ^1H NMR spectroscopy can be different to the changes in lipid droplet content as measured by HRMAS ^1H NMR spectroscopy; and/or 2) the increase in lipid resonances in the HRMAS ^1H NMR spectra may be driven by structural changes of lipids and the cellular environment, which increase tumbling rates of the lipids and thus NMR-visibility.

Solution-state ^1H NMR spectra of the lipid fraction from cell extracts represent the collective signal from cytosolic LDs, membrane lipids, and lipids contained within cell organelles. The change in lipid concentration within LDs was 'masked' due to opposing changes in phospholipids during apoptosis. Cells undergoing apoptosis are characterized not only by increased mobile lipid profiles, but also by decreased concentrations of phosphatidylcholines and total phospholipids as reported by Gibbons and colleagues.^{292,293} In order to characterize lipids in LDs using a solution-state NMR approach, LDs need to be isolated first. This is a time- and labour-expensive process and not all lipids may be extracted. The data presented in this chapter suggest that HRMAS ^1H NMR offers an improved way to monitor changes in the concentrations of mobile lipids in intact cells as it is more selective.

Cellular and biochemical changes during apoptosis could also contribute to increases in NMR-visible lipids in intact cells, for example, the formation of small endosomes. Martin-Sitjar and colleagues reported that increasing the MAS spinning rate resulted in a reversible increase in NMR-visible lipid resonances and attributed this to the fatty acyl chains of phospholipids in intracellular endosomes.²⁹⁴ Indeed, I also detected an increase in choline-containing

compounds but only at the early stage of apoptosis (3.21 – 3.28 ppm, **Figure 4.15**). Quintero and colleagues reported an increase in NMR-visible lipids during cell proliferation but no absolute increase in neutral lipids; and proposed an increased transport of triacylglycerols as a possible explanation.²⁸⁸ Cytoskeletal remodelling during apoptosis can also lead to an increase in LD mobility, which then becomes NMR visible.¹⁹²

Changes in aqueous metabolites (non-lipids) were more difficult to analyse as signal overlap had a significant impact on metabolite quantification. The following metabolites had good inter-batch reproducibility: glutamine, glutamate, glycine, *myo*-inositol, valine, histidine, phenylalanine, and alanine (**Table 4.1**). Some metabolites showed the same trends, including ATP/ADP, creatine, glutathione, DMA, acetate, lysine (**Figure 4.13**), but the changes were not statistically significant (these are not shown **Table 4.1**). A similar limitation was observed for the NMR spectra of growth media, where only alanine, lactate, and glucose were reliable indicators of apoptosis.

Moreover, non-lipid metabolism may be more sensitive to the extent of apoptosis. Cisplatin treatment was identical in both experiments, but according to the caspase-3 assay, the levels of apoptosis after 48 h were different: 5-fold for experiment 1 and 2.5-fold for experiment 2 (**Figure 4.4** vs **Figure 4.11**). The HRMAS ¹H NMR data could potentially reflect this biological variation in the level of apoptosis. More batch repeats should be tested to confirm the correlation between non-lipid metabolites and the level of apoptosis. For metabolic pathway analysis, I focused on selected metabolites from experiment 2 (**Table 4.1**).

4.5.6. Metabolic pathways

Glucose

The NMR results showed that glucose decreased in intact cells, while it increased in cell extracts and growth media. The increased glucose level in cell extracts was expected as glycolysis is inhibited by activated caspases.^{188,295} Additionally, inhibition of glucose metabolism has been shown to decrease glucose uptake,¹⁸⁸ which is consistent with the increase in glucose level in growth media as detected by solution-state NMR spectroscopy. The reduced rate of glycolysis results in ATP depletion which was also observed in the NMR spectra. It is worth noting that while the glucose level in cell extracts increases during apoptosis, it decreases in intact cells. This suggests that, during apoptosis, glucose in intact cells may be converted

into an NMR-invisible form, i.e., a higher proportion of glucose is bound to receptors and/or transporters in intact apoptotic cells. Another explanation could be that unused glucose was redirected to a cellular environment that decreases the tumbling rate of glucose (for example glycogen).

Myo-inositol

The NMR results showed that *myo*-inositol levels in intact cells decreased during apoptosis, while they increased in cell extracts, suggesting that different *myo*-inositol pools could be detected. *Myo*-inositol is involved in several cellular functions including signalling, protein phosphorylation, chromatin remodelling and gene expression, and mRNA transport, and is a building block of membrane phospholipids.²⁹⁶ HRMAS ¹H NMR spectroscopy recorded changes in free, fast tumbling *myo*-inositols, whereas solution-state ¹H NMR recorded changes in total extractable *myo*-inositols. This situation is analogous to the changes in lipid droplets and total lipids discussed in **Section 4.4.4**. An apoptosis-induced decrease in *myo*-inositol in intact cells detected by HRMAS ¹H NMR spectroscopy has been previously reported.^{70,279} It is known that increased cellular levels of inositol hexaphosphate protect from apoptosis and decreased levels promote it.²⁹⁷ Additionally, low levels of *myo*-inositol cause abnormal accumulation of triacylglycerols,²⁹⁸ which could translate into an increase in NMR-visible lipids in intact apoptotic cells. Phosphatidylinositol lipids are thought to play an important role in membrane signalling but their role in membrane-associated events during apoptosis is poorly understood.²⁹⁹ In the nucleus, an increase in phosphatidylinositol 5-phosphate promotes acetylation of p53, stabilizing it and thereby increasing apoptosis.²⁹⁷ This change can contribute to the increased levels of *myo*-inositol resonances detected in cell extracts.

Glycine, glutamate, and glutathione

The NMR results showed that the intracellular levels of glycine, glutamate, and glutathione decreased during apoptosis for both intact cells and cell extracts. Glutathione depletion is a common feature of apoptotic cell death because it maintains intracellular redox homeostasis, which is disrupted during oxidative stress.³⁰⁰ Glutathione depletion can be a result of the shift from the reduced to the oxidized form or as a result of increased active efflux of glutathione.³⁰¹ For cisplatin and etoposide, the levels of glutathione in growth media decreased, suggesting that the latter mechanism is unlikely. Moreover, depletion of glycine and glutamate (precursors for *de novo* synthesis of glutathione) can also contribute to the decreased glutathione levels in

intact cells. It has been shown that glutathionylation of proteins, which leads to depletion of glutathione, is a critical regulator of apoptosis.³⁰²

Phenylalanine, tyrosine

The NMR results showed that levels of phenylalanine decreased during apoptosis for intact cells and there was no change for cell extracts or media samples. Tyrosine decreased in intact cells but increased in cell extracts. Perturbations of tyrosine/phenylalanine metabolism during apoptosis vary depending on cell lines and apoptotic agents; therefore, it is difficult to determine their role in apoptosis. Duarte and colleagues reported a decrease in intracellular phenylalanine and tyrosine in osteosarcoma cells,²⁷⁹ while Feng and colleagues reported the opposite change in HeLa cells.²⁸² It has been shown that dietary restriction of tyrosine and phenylalanine suppresses melanoma cell growth and dramatically inhibits metastasis in mice.^{303,304} Ge and colleagues proposed a mechanism whereby tyrosine and phenylalanine deprivation induced cell death by activating caspase-8, which triggered a cascade of events leading to the release of cytochrome c from mitochondria.³⁰⁵ The NMR results reported here support the hypothesis that deprivation of phenylalanine may trigger apoptosis. In particular, the time-course experiment (**Figure 4.13**) showed low levels of phenylalanine in the early stages of apoptosis as compared to the control group. Conversely, tyrosine did not significantly decrease until the later stages of apoptosis. This may suggest that the decrease in tyrosine happens after apoptosis initiation.

Alanine

The NMR results showed that intracellular alanine levels did not change during apoptosis, while it increased in growth media. In addition, the levels of alanine for cell extracts were treatment-dependent: decreased for cisplatin-treated cells and no change for etoposide-treated cells. The HRMAS ¹H NMR data needs special caution as the alanine –CH₃ resonance overlaps with the lactate/lipid –CH₂– resonance (**Figure 4.12**), therefore the results may not accurately reflect changes in the metabolic state of apoptotic cells. Solution-state ¹H NMR data from the aqueous fractions are more reliable as metabolite extraction improves spectral resolution and eliminates the lipid –CH₂– resonance. Decreased alanine has previously been linked to cisplatin and jolkinolide B induced apoptosis.^{279,306} Extracellular alanine (among other metabolites) has previously been associated with apoptosis, and is thought to induce specific gene programs (suppression of inflammation, cell proliferation, and wound healing) in healthy neighbouring cells to reduce the extent of apoptosis.³⁰⁷

4.6. Conclusions

Chapter 4 describes the metabolic profiling of intact apoptotic cells by HRMAS ^1H NMR spectroscopy. It combines HRMAS ^1H NMR data from intact cells with solution-state ^1H NMR data from cell extracts and growth media to identify possible metabolic pathways altered during cisplatin and etoposide treatments.

The HRMAS ^1H NMR metabolic profiles of apoptotic cells were significantly different from control and necrotic cells. The cisplatin group could also be discriminated from the etoposide group. According to the caspase-3 assay, the low dose etoposide-treated cells did not undergo caspase-dependent apoptosis, but the viability test confirmed that cell death had genuinely occurred. However, the HRMAS ^1H NMR metabolic profile of etoposide-treated cells was more similar to that of cisplatin-treated cells rather than necrotic cells. This observation demonstrated that HRMAS ^1H NMR spectroscopy is a useful tool to discriminate not only between apoptotic and control groups but also between apoptotic and necrotic groups or between different apoptotic treatments.

Both NMR-visible lipids and small metabolites contributed to the separation of these groups. Time-course experiments revealed that changes in lipid signal intensities tended to increase gradually with the onset of apoptosis. Changes in small metabolite signal intensities were more dynamic: the early stage of apoptosis was characterized by an increase in certain metabolites, which then decreased at a later stage of apoptosis.

Combining HRMAS NMR data of intact cells with solution-state NMR data of cell extracts helped to identify the compartmentalisation of lipid metabolism. Signals from lipid in intact apoptotic cells increased during apoptosis but in cell extracts, they either decreased or increased depending on the lipid resonance. In necrotic cells, the combined approach confirmed cellular disintegration.

Overall, ^1H NMR-based cell metabolomics showed that apoptotic agents induced variations in the metabolite content of intact cells, cell extracts, and growth media. The results showed that several metabolic pathways were affected, including downregulation of glutathione synthesis, suppression of glycolysis, and abnormal alanine, phenylalanine and *myo*-inositol, and lipid metabolism. In the future, this methodology could be applied as an NMR-based cellular assay to monitor the effectiveness of drug treatment *in vitro*.

Chapter 5. The study of apoptosis in intact cells by HRMAS ^1H NMR-based diffusion and T_2 -relaxation measurements.

5.1. Introduction

The 1D HRMAS ^1H NMR spectra of intact cells provide quantitative and qualitative information about metabolites but are not the only type of data that can be collected owing to the versatility of NMR spectroscopy. Relaxation times and apparent diffusion coefficients (ADC) of metabolites and water are also important parameters, for example used to provide contrast to images in MRI. NMR relaxation times and diffusion coefficients are sensitive to the cellular environment and often reflect pathological states allowing the discrimination of disease.³⁰⁸ These parameters play a pivotal role in understanding the motions, structure, and interactions of molecules in biological systems.

5.1.1. Introduction to the property of relaxation in NMR spectroscopy

The relaxation of the magnetic polarization during the NMR experiment can be described by two relaxation times referred to as T_1 and T_2 .^{309,310} The longitudinal relaxation time T_1 describes the equilibration of the polarization component parallel to the external magnetic field (**Figure 5.1**). T_1 relaxation happens because of energy transfer from spins to the nearby environment through collisions, rotations, and electromagnetic interactions. The transverse relaxation time (T_2) describes the decay of the transverse component (**Figure 5.1**), as a result of spin dephasing by local field disturbance. Longitudinal and transverse relaxation processes are closely linked and T_2 relaxation always occurs at the same time as T_1 relaxation.

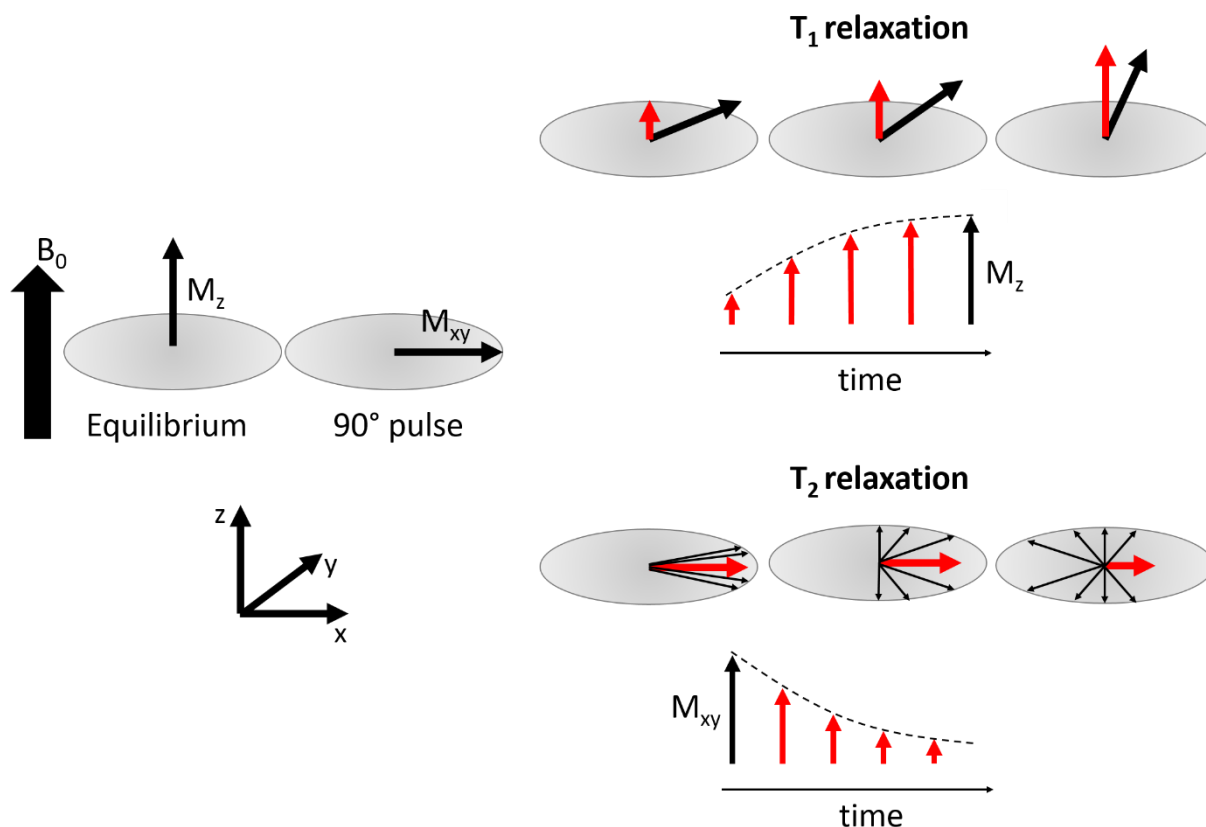


Figure 5.1. Relaxation of magnetization vectors after a 90° radiofrequency pulse (rf). For T_1 relaxation, the z component of the net magnetization (M_z) is reduced to zero and then it recovers to its equilibrium value. For T_2 relaxation, the xy component of the net magnetization (M_{xy}) reaches maximum after the rf pulse and then it decreases to its equilibrium condition of $M_{xy} = 0$. The recovery of magnetization is an exponential process with a time constant T_1 or T_2 .

These relaxation times are related to the Brownian motion of molecules as they tumble (or reorient) around the three principal axes of a molecular structure. Hence, relaxation parameters T_1 and T_2 provide information about molecular dynamics and the surrounding environment. In biological samples, molecular tumbling is restricted, and average local magnetic field variation is high resulting in shortened T_2 relaxation times for macromolecules, lipids, and bound metabolites.

T_2 relaxation times can be measured with Carr-Purcell-Meiboom-Gill (CPMG) pulse sequence. The simplest form of the CPMG experiment is based on the spin-echo pulse sequence and consists of: 1) a 90° pulse, which creates transverse magnetization (M_{xy}); 2) a block of delay– 180° pulse–delay incremented n times, during which the M_{xy} magnetization decays; and 3) acquisition (**Figure 5.2**).

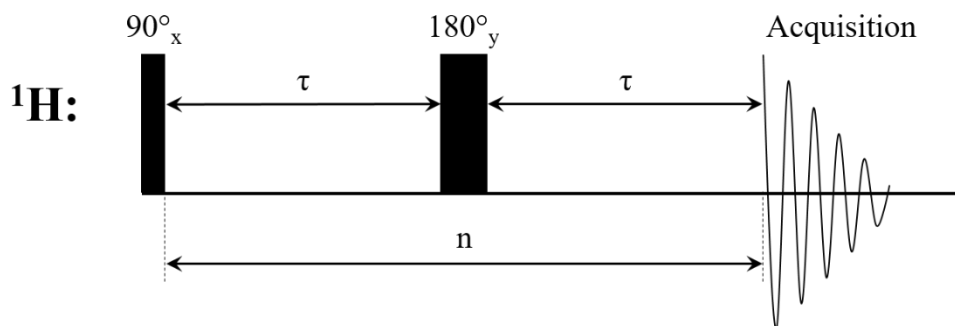


Figure 5.2. Spin echo pulse sequence for measuring T_2 . The 90° pulse flips the spins into the transverse plane followed by a delay (τ) and the 180° pulse, which refocuses spins in the transverse plane. The sequence is incremented n times. Acquisition begins after the second delay (τ).

T_2 values are obtained by acquiring a set of 1D CPMG spectra using different evolution times ($2n\tau$, **Figure 5.2**) and fitting the intensities to the exponential function (**Equation 5.1**):^{310,311}

$$I = I_0 e^{-\frac{t}{T_2}} \quad \text{Equation 5.1}$$

Where

I – observed intensity [arbitrary unit]

I_0 – unattenuated signal intensity [arbitrary unit]

t – evolution time ($2n\tau$) [s]

T_2 – transverse relaxation time [s]

T_2 relaxation can provide information about the microenvironment in which metabolites exist in intact cells. Unbound metabolites with higher tumbling rates in the cytosol have longer T_2 values whereas partially bound metabolites have shorter T_2 values. For example, nonpolar triglycerides stored in lipid droplets exist in semi-liquid states with partially restricted motions of their fatty acid chains and the whole molecule itself. These molecules have relatively short T_1 and T_2 values, but long enough to be visible in the NMR spectrum. Polar lipids such as phosphatidylcholines which are part of the cell membrane bilayer, have highly restricted motions resulting in very short relaxation rates and are not detected in routine NMR spectra.³¹²

Tissue-dependent differences in the T_2 value of water are widely utilized to produce MR signal contrast in clinical diagnostics.³¹³ Liimatainen reported dramatic changes in T_1 and T_2 relaxation times of NMR-visible lipids during apoptotic cell death in rat glioma.³¹⁴ Similarly,

Truskiewicz and colleagues used MRI for the *in vitro* study of breast cell cultures.³¹⁵ They observed that tumour breast cells had a shorter T_1 time compared to normal breast cells, but T_2 measurements were inconclusive. On the other hand, Callahan and colleagues demonstrated that normal and neoplastic fibroblasts, which had similar levels of hydration, could be distinguished based on T_2 but not T_1 values.³¹⁶ It is interesting to test whether T_1 and T_2 measurements would be useful in distinguishing between control, apoptotic and necrotic cells. In this project, I investigated changes in T_2 values since they are considered more sensitive to changes in the microenvironment of intact cells.³¹⁴

5.1.2. Introduction to NMR-based diffusion

Diffusion ordered spectroscopy (DOSY) is another useful method to probe cellular environments as it can distinguish between the restricted movement of intracellular metabolites and the free movement of extracellular metabolites.^{70,317} DOSY measures the translational migration of molecules driven by their random thermal motion. Self-diffusion of molecules depends on the size and shape of the molecule, the viscosity of the medium, and temperature, and is described by the Stokes-Einstein equation given below:

$$D = \frac{kT}{6\nu\pi} \left(\frac{1}{r} \right) \quad \text{Equation 5.2}$$

Where

D – diffusion constant [$\text{m}^2 \cdot \text{s}^{-1}$]

k – Boltzmann's constant [$\text{m}^2 \cdot \text{kg} \cdot \text{s}^{-2} \cdot \text{K}^{-1}$]

T – temperature [K]

ν – viscosity [$\text{kg} \cdot \text{m}^{-1} \cdot \text{s}^{-1}$]

r – radius of diffusing particle [m]

The most basic form of the DOSY experiment was described in 1965 by Stejskal and Tanner.³¹⁸ It combines a spin echo sequence with magnetic field gradients that encode spatial information (**Figure 5.3**). After the diffusion time Δ , a second gradient is applied to refocus the signal. For nuclei, which move during the diffusion time Δ , refocusing cannot be achieved and NMR signal intensity is attenuated. The change in signal intensity depends on the diffusion time Δ and the gradient strength (g) and duration (δ) and is described by the Stejskal-Tanner formula³¹⁸:

$$I = I_0 e^{-D\gamma^2 g^2 \delta^2 (\Delta - \frac{\delta}{3})} \quad \text{Equation 5.3}$$

Where

I – observed intensity [arbitrary unit]

I_0 – unattenuated signal intensity [arbitrary unit]

D – diffusion coefficient [$\text{m}^2 \cdot \text{s}^{-1}$]

γ – gyromagnetic ratio of the observed nucleus [$\text{s}^{-1} \text{G}^{-1}$]

g – gradient strength [G m^{-1}]

δ – duration of the gradient [s]

Δ - diffusion time [s].

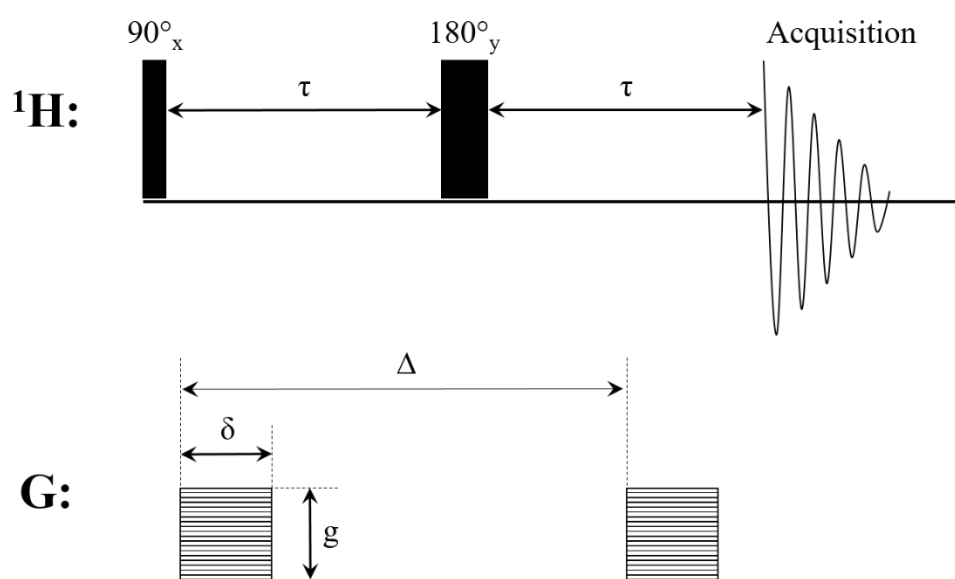


Figure 5.3. A basic form of the DOSY pulse sequence with a gradient spin echo (SE). The 90° pulse flips the spins into the transverse plane followed by the gradient pulse for position encoding. The 180° pulse reverses the sign of the phase changes from the first gradient pulse, and the second gradient refocuses the signal unless the spins have diffused over the diffusion time Δ . The loss of the signal intensity as a function of diffusion time is measured.

The diffusion constant can be extracted from a non-linear curve fit to the resulting Gaussian decay (**Figure 5.4**).

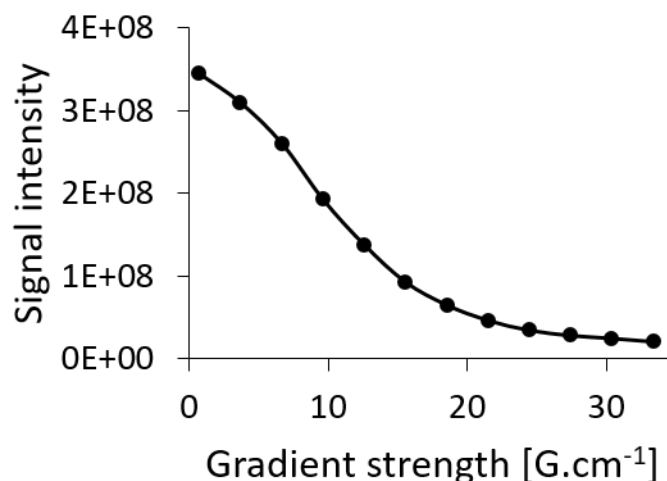


Figure 5.4. Example of a diffusion decay curve with varying gradient strength.

Since 1965, several DOSY sequence modifications have been introduced to improve sensitivity and reduce artifacts arising from transverse relaxation, J-modulation effects, background gradients, and eddy currents.³¹⁹ The sequence of choice for DOSY experiments on intact cells in this project was the BPP-LED sequence, which allowed maximum gradient strengths with small temperature rises.²³⁸

In theory, diffusion coefficients can be measured by recording a series of 1D experiments with varying diffusion time, gradient duration, or gradient strength. In practice, the most common choice of the variable parameter is the gradient strength while other parameters are kept constant. The advantage of this method is the constant timing of the DOSY experiment, resulting in constant relaxation during the diffusion delay period. Therefore, the effect of relaxation on the signal attenuation can be excluded.

Complex biological samples are characterized as undiluted systems, thus other factors such as interactions with macromolecules, cellular organelles, and compartment boundaries contribute to the diffusion coefficient. The term *apparent diffusion coefficient* (ADC) is used to account for deviation from the model self-diffusion.³²⁰

In tissue and cell samples, there are two principal modes of diffusion: 1) free diffusion, for which ADC is a constant function of diffusion time; and 2) restricted diffusion, for which ADC decreases with increasing diffusion time³²¹ (**Figure 5.5**). It is possible to distinguish between free and restricted diffusion by running a combined variable-gradient DOSY experiment with a variable-diffusion-time DOSY experiment. In this case, each variable-gradient-diffusion experiment is recorded over a range of diffusion times. The decreasing ADC corresponds to a

larger proportion of the spins colliding with the plasma membrane or other organelles, which is characteristic of restricted diffusion.³²²

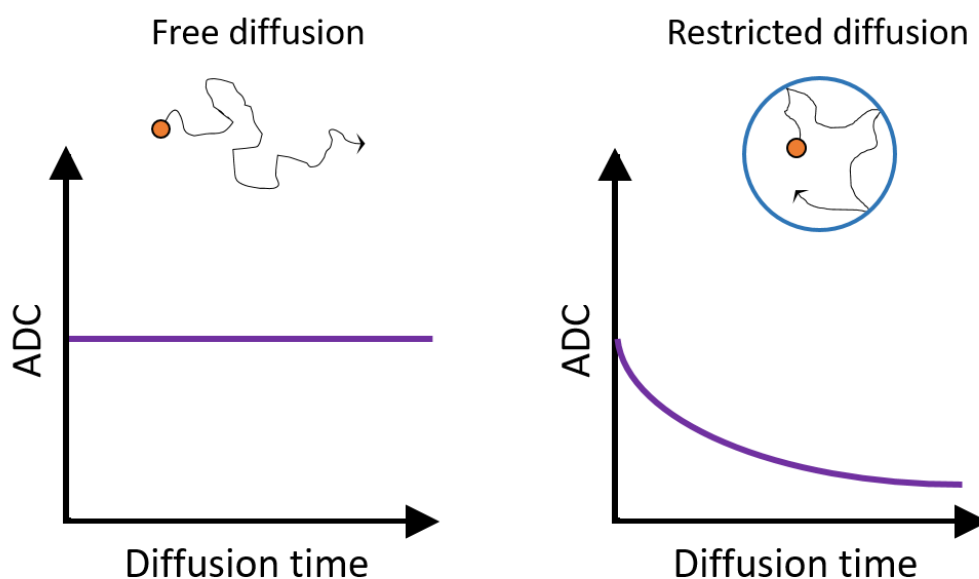


Figure 5.5. Modes of diffusion in biological samples: free diffusion and restricted diffusion. The orange circle represents a diffusing molecule, the black line corresponds to its diffusion pathway, the blue circle represents confinement.

The diffusion properties of biological samples depend on the structural properties of organelles and their interaction with water and small metabolites. In MRI, changes in the diffusion of water can indicate structural abnormalities and it is a common clinical practice to use diffusion-weighted MRS for diagnostic purposes.³²³ For example, in oncology, tumors are characterized by a reduction in the ADC of water, while tumor shrinkage following an anticancer treatment is often associated with increased ADCs.^{91,324,325} However, diffusion imaging of lipids in tissue is relatively understudied.^{326,327}

Restricted diffusion measurements have been used to probe the size of LD in tissue *ex vivo*³²⁸ and *in vivo*.³²⁹ A few studies have focused on NMR-based diffusion of lipids in intact cells.^{70,330} Griffin and colleagues measured ADC and T_2 values for water in endometrial cells by HRMAS ^1H NMR spectroscopy.⁷⁰ They were able to distinguish between two water environments (intracellular and extracellular) based on diffusion but not on T_2 measurements. In another HRMAS ^1H DOSY NMR study, ADCs for water and key metabolites in dystrophic and control tissues were measured but no significant changes were detected.⁶⁴

5.2. Aims

In **Chapter 5**, I investigate whether T_2 relaxation and NMR-based diffusion measurements of metabolites can provide evidence for changes in the cellular environment during apoptosis and necrosis. I explore the application of these methods to distinguish between control cells, and cells undergoing apoptosis or necrosis, and thus their potential application to monitor apoptosis-based treatments in intact cells.

I report the following results:

- T_2 relaxation times for metabolites in intact cells as a comparison between control cells and cells undergoing apoptosis and necrosis.
- Diffusion coefficients for metabolites in intact cells as a comparison between control cells and cells undergoing apoptosis and necrosis.
- Measurements of slowly diffusing lipid species by high gradient DOSY.
- Correlation of NMR-based diffusion coefficients and microscopy-based lipid droplet size measurements.
- Comparison of NMR-based and microscopy-based mean displacement of mobile lipids.

5.3. Methods

All experimental methods for collecting, processing and analysing data are defined in **Chapter 2**.

5.4. Results

5.4.1. T_2 relaxation time measurements of metabolites and water in intact cells

5.4.1.1. Apoptotic cells

To investigate changes in the cellular environment during apoptosis progression, T_2 relaxation times were measured in C2C12 myotubes treated with 60 μM cisplatin or 120 μM etoposide for 8, 24, and 48 h. Cells cultured in T-75 flasks were divided into two samples: 10^5 cells for cell viability and caspase-3 assays to test for the presence of apoptosis and cell death (data reported in **Chapter 4, Figure 4.11**), and the remaining cells (approximately 10^6) were designated for HRMAS ^1H NMR experiments. The transverse relaxation time T_2 was measured by a conventional CPMG sequence with a short echo spacing ($2\pi\tau = 40$ ms, **Chapter 2, Section 2.10.2**) to minimize diffusion effects.³³¹ Representative examples of bi-exponential T_2 fits and fitting errors can be found in **Appendix 2, Figure S2.1** and **Figure S2.2**.

Figure 5.6 shows T_2 relaxation times for control and treated cells as a function of incubation time. Only subtle variations existed between the healthy cells as compared to the cells undergoing apoptosis. Even at the late stage of apoptosis, T_2 measurements did not detect significant changes in the cellular environment of the selected metabolites. The motional freedom of water molecules did not appear to change in intact apoptotic cells except after 8 hours of etoposide treatment. Choline molecules showed a non-significant decrease in T_2 relaxation times at late-stage apoptosis 48 h, which might signal membrane degradation.

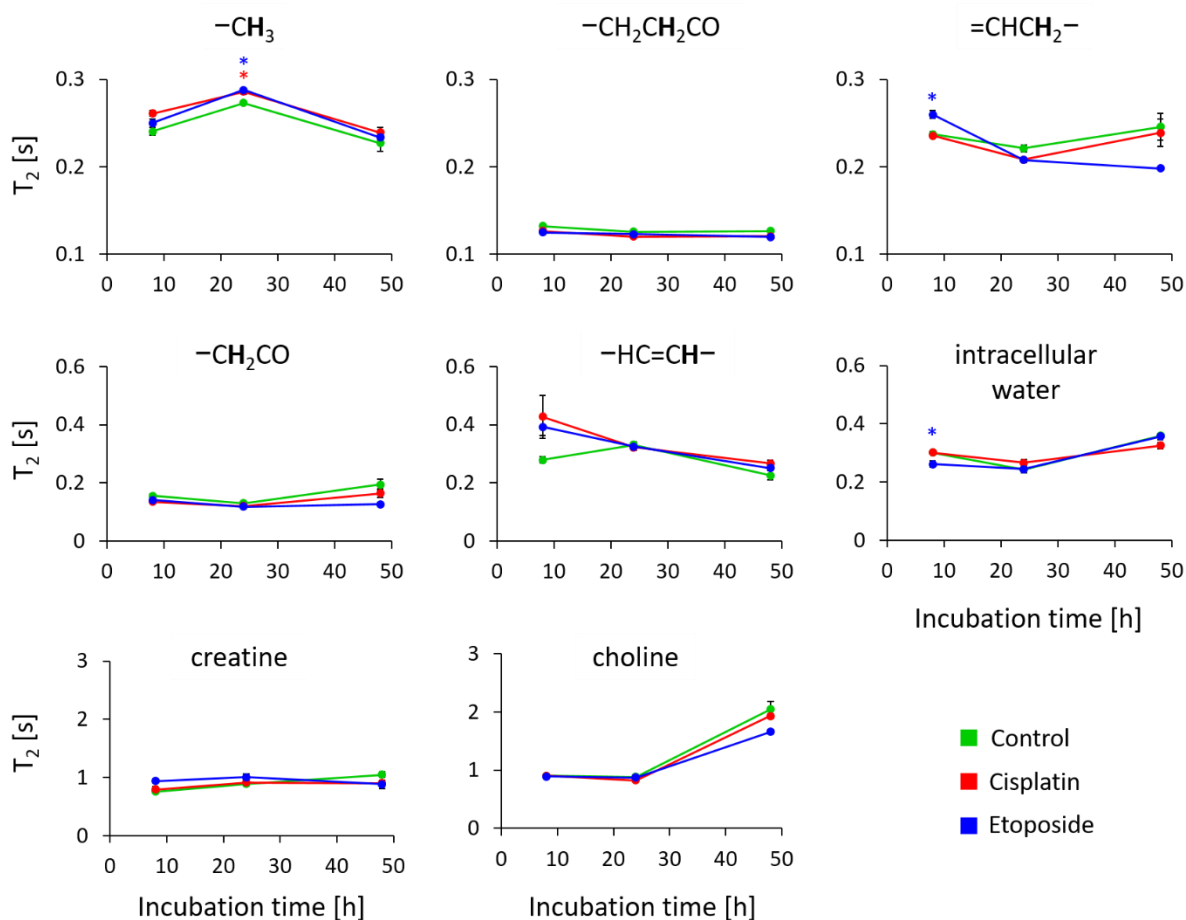


Figure 5.6. Metabolite T_2 relaxation times in intact cells as measured by HRMAS ^1H NMR spectroscopy: control (green), cisplatin (red), and etoposide (blue) at different incubation times (8, 24 and 48 h). Error bars representing SEM (biological replicates, $n = 4$) not visible if $\text{SEM} < 0.01$, ANOVA with post hoc Fisher's test: $*p < 0.05$, FDR-adjusted.

5.4.1.2. Necrotic cells

T_2 relaxation times for the heat-treated cells were recorded to analyse changes in the cellular environment during necrosis (**Table 5.1**). T_2 measurements of lipids in heat-treated cells exhibited 30% variation in these measurements and were excluded from the analysis. However, T_2 values of non-lipid metabolites such as lactate, choline, and intracellular water were notably lower for necrotic cells as compared to control cells.

Table 5.1. Comparison of T_2 relaxation times of selected metabolites and water for control and necrotic muscle cells. Student *t*-test: * $p < 0.05$.

Metabolite	Control		Heat	
	Mean [s]	SEM [s]	Mean [s]	SEM [s]
creatine	1.31	0.05	0.50***	0.11
choline 3.24 ppm	1.06	0.03	0.82***	0.02
lactate 1.3 ppm	0.82	0.03	0.48***	0.01
lactate 4.1 ppm	0.99	0.09	0.35***	0.04
intracellular water	0.30	0.02	0.46***	0.01

5.4.2. NMR-based diffusion measurements of metabolites and water in intact cells

5.4.2.1. Suitability of NMR-based diffusion methods for analysing biological samples. Model system: full fat and semi-skimmed milk.

Milk samples were used to investigate the diffusion of lipid droplets by two NMR-based diffusion methods: 1) variable diffusion time, and 2) variable gradient strength.

Lipid droplets in milk can be classified into two main groups according to their size: droplets below 0.25 μm corresponding to casein micelles and droplets at 1-2 μm corresponding to fat globules.³³² Full-fat milk contains ~4% fat and lipid droplets with a radius of < 1.502 μm , whereas semi-skimmed milk contains ~2% fat and lipid droplets with a radius of <1.103 μm .³³² In addition, the viscosity of the two milk samples and their macromolecular compositions are different.³³³ Therefore, we expect the ADCs of lipids in full-fat milk to be lower than in semi-skimmed milk.

Table 5.2 shows apparent diffusion coefficients of $-\text{CH}_3$ and $-\text{CH}_2-$ lipid resonances in full fat and semi-skimmed milk measured by variable-gradient-strength or variable-diffusion-time DOSY ^1H NMR spectroscopy. The variable-gradient-strength method gave consistent values of apparent diffusion coefficients for both lipid resonances – as expected, the lipids diffused slower in full-fat milk and faster in semi-skimmed milk. The variable-diffusion-time method gave less consistent ADC values and the discrimination between the two milk samples could only be based on the ADC of $-\text{CH}_2-$ lipid. This suggested that other factors contributing to the diffusion mechanism (such as relaxation, collisions with macromolecules, and non-Newtonian

behaviour of milk) became more apparent at longer diffusion times. Interestingly, the range of diffusion times Δ (25 – 800 ms or 25 – 1500 ms), for which NMR spectra were recorded, did not affect ADC values for the milk samples. The variable-gradient-strength method was used for subsequent experiments on intact cells.

Table 5.2. Apparent diffusion coefficients [$\mu\text{m}^2/\text{s}$] for full fat and semi-skimmed milk. Student *t*-test comparison between respective resonances of full fat and semi-skimmed milk within one method, * $p < 0.05$.

Method	Full fat milk		Semi-skimmed milk	
	–CH ₃	–CH ₂ –	–CH ₃	–CH ₂ –
variable diffusion time (25-800 ms) b-value: $3.31 \cdot 10^8 - 1.06 \cdot 10^{10} \text{ s.m}^{-2}$	12.8±1.6	0.14±0.01	15.5±1.3	49.6±4.5*
variable diffusion time (25-1500 ms) b-value: $3.31 \cdot 10^8 - 1.99 \cdot 10^{10} \text{ s.m}^{-2}$	30.0±3.7	0.13±0.01	16.5±0.9*	52.8±4.6*
variable gradient strength constant diffusion time: 100 ms b-value: $6.30 \cdot 10^6 - 1.51 \cdot 10^{10} \text{ s.m}^{-2}$	0.10±0.01	0.26±0.05	43.6±2.2*	33.6±2.8*

5.4.2.2. Apoptotic cells.

To investigate if HRMAS ¹H NMR-based diffusion measurements can discriminate between control and apoptotic cells, I measured ADCs of NMR-visible lipids and selected metabolites in C2C12 myotubes treated with cisplatin 60 μM or etoposide 120 μM for 3, 8, 24, and 48 h. Representative examples of bi-exponential diffusion fits and fitting errors can be found in **Appendix 2, Figure S2.3** and **Figure S2.4**.

Figure 5.7 shows changes in the ADCs of NMR-visible lipids and selected metabolites in intact cells during apoptosis. The ADCs of the lipids decreased during apoptosis; for the –CH₂– and –CH₃ lipid signals, the difference between the control and apoptotic samples was significant after 8 h of the cisplatin treatment. The greatest difference between the control and apoptotic samples was observed at the 24-h time point, after which lipid ADC values for apoptotic samples continued to decrease at slower rates while the ADC values of lipids for the control samples began to decrease. The ADC values for choline compounds decreased at early stages of apoptosis and increased at the late stage of apoptosis as compared to the controls. The ADC

values for intracellular water and creatine did not change significantly during early apoptosis (8 and 24 h).

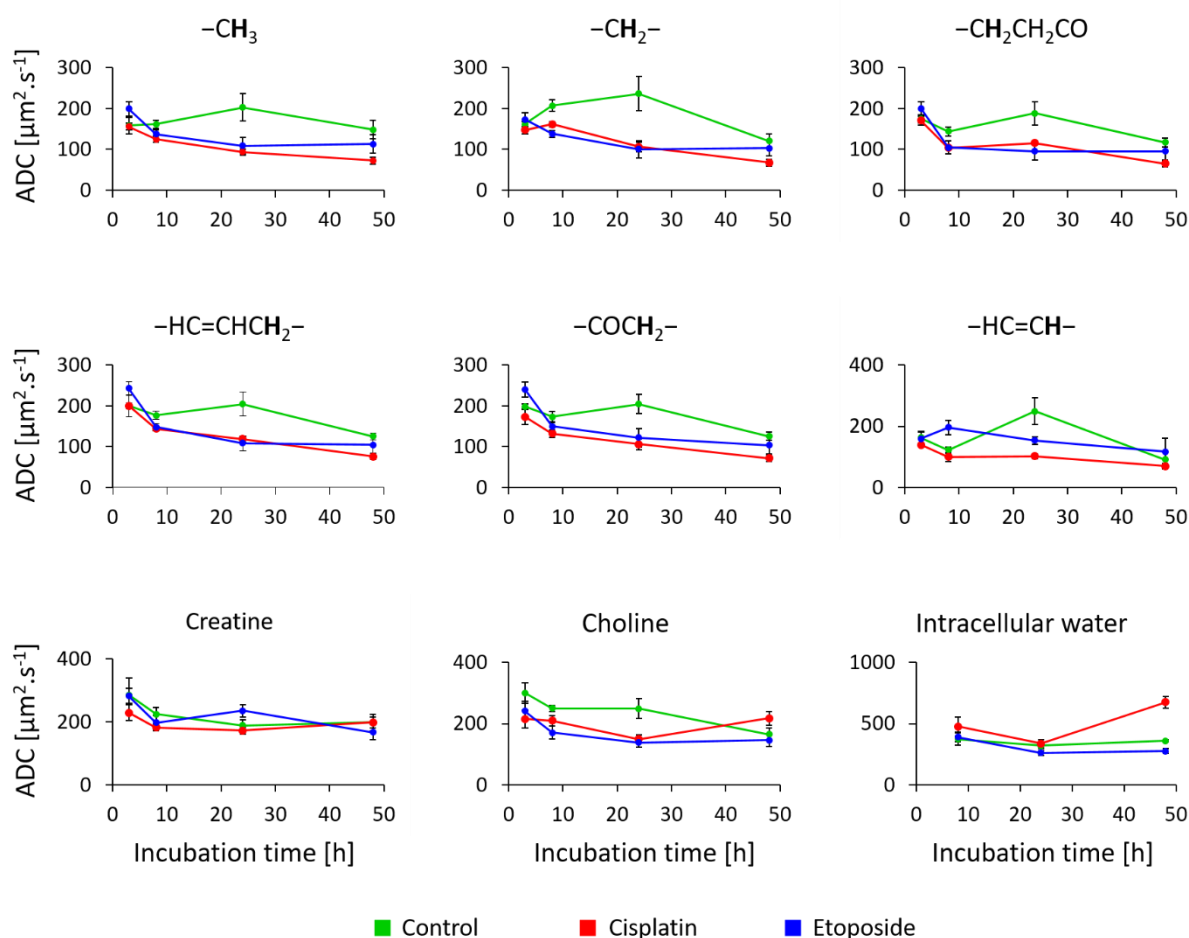


Figure 5.7. Apparent diffusion coefficients of metabolites and water in intact cells measured by HRMAS ^1H NMR spectroscopy: control (green), cisplatin (red), and etoposide (blue) at different incubation times (3, 8, 24, and 48 h). Error bars representing SEM (biological variation, $n \geq 6$ for control and cisplatin, $n \geq 3$ for etoposide).

In order to highlight differences between the control and treated samples, the NMR-based diffusion data of cells collected after 24 and 48 h were subjected to multivariate statistical analysis in MetaboAnalyst. PCA was used to observe inherent clustering and to discriminate the variables that are responsible for variation between the groups. For the 24-hour treatment (**Figure 5.8A**), group separation along PC1 accounted for 75.2% of the total variation and PC2 accounted for 11.6%. Five ADCs showed significant discriminative power between the control and cisplatin samples ($-\text{CH}_3$, $-\text{CH}_2-$, $-\text{CHCH}_2-$, $-\text{CH}_2\text{CO}$, and $-\text{HC}=\text{CH}-$), while only two ADCs ($-\text{CH}_2-$ and choline) were able to discriminate between the control and etoposide

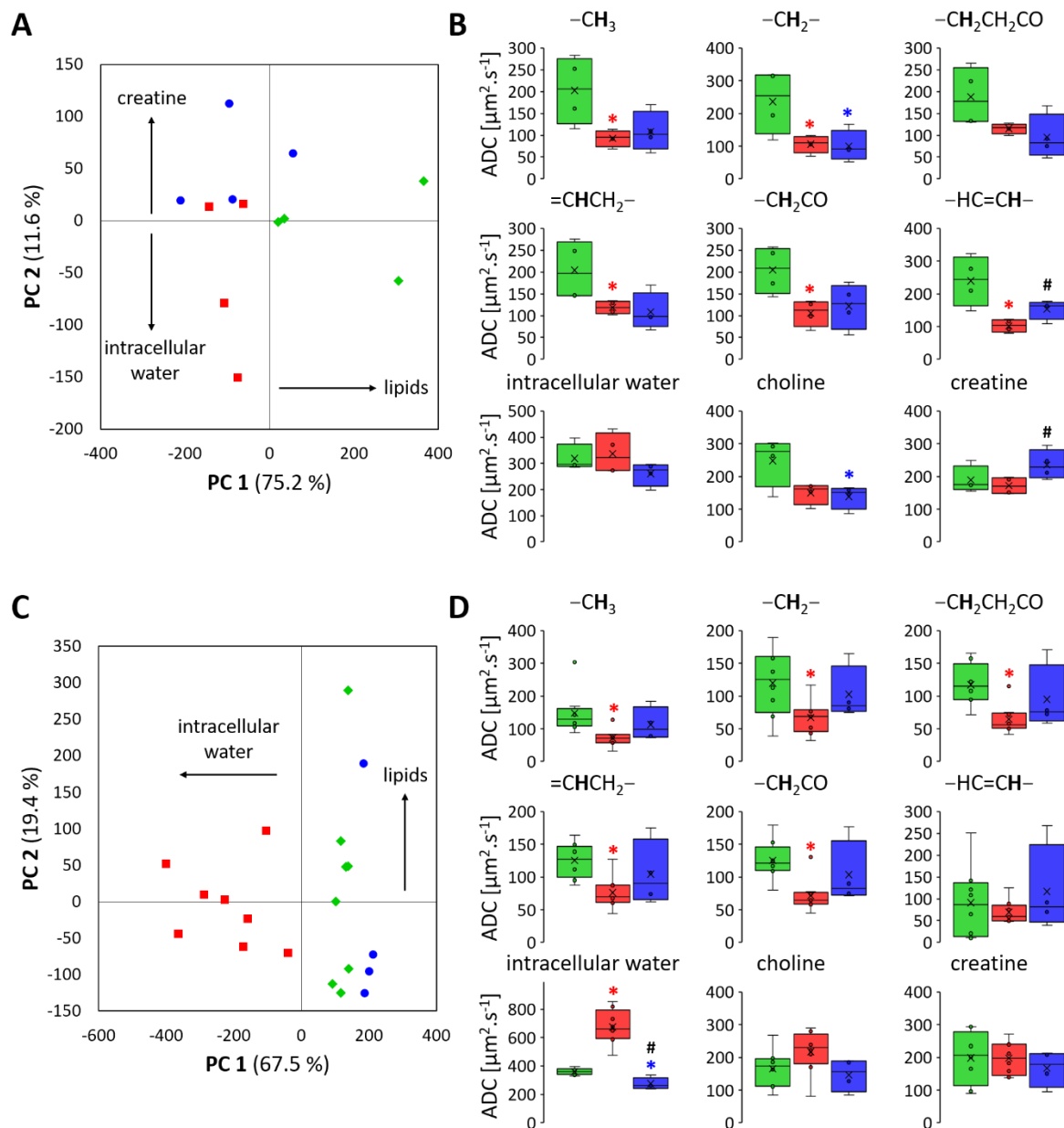


Figure 5.8. Statistical analysis of NMR-based diffusion data of intact cells after (A, B) 24- and (C, D) 48-hour treatments: control (♦ green), cisplatin (■ red), and etoposide (● blue). A&C Two-dimensional PCA score plot derived from the diffusion data of selected metabolites. One data point represents one sample; arrows represent metabolites that are responsible for separation in respective directions. The two principal components (PC) explained >85% of the total variation in diffusion data for both time points. B&D Box-whisker plots comparing apparent diffusion coefficients (ADC) for each metabolite signal across control (green), cisplatin (red), and etoposide (blue). The box covers the 25th and 75th percentiles, the line in the box represents the median value, the cross represents the mean, and the whiskers indicate the minimum and maximum values. Outliers are shown as points. Significant perturbation assessed by ANOVA with post hoc Fisher's test: *control vs cisplatin, *control vs etoposide, # cisplatin vs etoposide, FDR adjusted $p < 0.05$.

treatment (**Figure 5.8B**). Moreover, the ADCs of creatine and $-\text{HC}=\text{CH}-$ lipids were significantly higher for etoposide as compared to the cisplatin samples.

For the 48-hour treatment (**Figure 5.8C**), group separation along PC1 accounted for 67.5% of the total variation and PC2 accounted for 19.4%. Six ADCs showed significant discriminative power between the control and cisplatin samples ($-\text{CH}_3$, $-\text{CH}_2-$, $-\text{CH}_2\text{CH}_2\text{CO}$, $=\text{CHCH}_2-$, $-\text{CH}_2\text{CO}$, and intracellular water), while only the ADC of intracellular water was able to discriminate between control and etoposide treatment (**Figure 5.8D**).

For both time points, the cisplatin group was characterized by the significantly decreased ADC of lipids. Interestingly, the ADC values of lipids were better predictors of cisplatin-induced apoptosis after 24 h. After 48h, the ADC value of intracellular water was the main contributor to group separation.

5.4.2.3. Necrotic cells.

To investigate the effect of membrane damage on metabolite mobilities, I measured the ADCs of selected metabolites in heat-treated C2C12 myotubes. Heat treatment induces acute necrosis, which is characterized by sudden cell rupture and membrane damage.¹⁶⁸ **Figure 5.9** shows changes in the ADCs of lipid and non-lipid metabolites in necrotic cells as compared to control cells. The ADCs of lipids in necrotic cells were not significantly different except for unsaturated lipids ($=\text{CHCH}_2-$ and $-\text{HC}=\text{CH}-$), for which the ADCs increased as compared to the controls.

The ADC values for choline compounds and intracellular water increased for necrotic cells as compared to the controls. Similar behaviour was observed for other intracellular metabolites including glucose and lactate, however, the ADC of creatine remained constant (**Figure 5.9**).

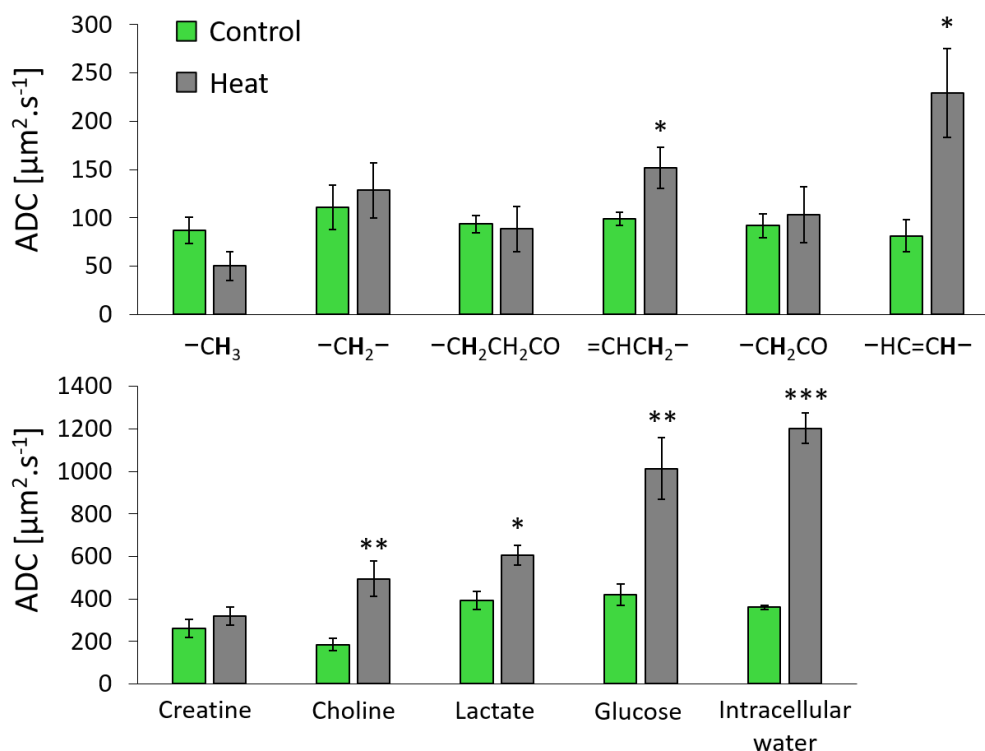


Figure 5.9. Apparent diffusion coefficients of metabolites and water in intact cells measured by HRMAS ^1H NMR spectroscopy: control (green) and heat-treated cells (grey). Error bars represent SEM (biological replicates, $n > 3$), Student *t*-test: * $p < 0.05$, ** $p < 0.01$, *** $p < 0.001$.

5.4.2.4. Apoptotic vs necrotic cells

In order to facilitate a comparison between apoptotic and necrotic treatments, the ADCs were converted into fold change relative to the control samples. The values were calculated by dividing the ADC of treated cells by the ADC of respective control cells. **Table 5.3** summarises the fold change in ADCs of selected metabolites for apoptotic and necrotic treatments as compared to their respective controls.

The results highlighted that the mobilities of metabolites in necrotic cells are different from the mobilities of metabolites in apoptotic cells. Apoptotic cells showed a clear decreasing trend for the ADCs of NMR-visible lipids while necrotic cells were characterized by no change in the ADCs of saturated lipids and an increase in the ADCs of unsaturated lipids. The ADCs of choline and intracellular water could also be used to discriminate between early apoptosis and necrosis/late apoptosis. The ADC of creatine did not change significantly either for necrotic or apoptotic cells.

Table 5.3. Fold change apparent diffusion coefficient as compared to respective controls ($ADC_{treatment}/ADC_{control}$) for selected metabolites, ANOVA with post hoc Fisher's test: * FDR-adjusted $p < 0.05$. intra. – intracellular.

Metabolite	Cisplatin 24 h	Etoposide 24 h	Cisplatin 48 h	Etoposide 48 h	Heat-treated
–CH ₃	0.46±0.04*	0.54±0.10	0.49±0.06*	0.73±0.15	0.58±0.17
–CH ₂ –	0.45±0.05*	0.42±0.09*	0.47±0.06*	0.68±0.14	1.16±0.26
–CH ₂ CH ₂ CO	0.61±0.03	0.51±0.12	0.55±0.07*	0.81±0.19	0.95±0.25
–HC=CHCH ₂ –	0.58±0.03*	0.53±0.09	0.61±0.07*	0.76±0.19	1.53±0.21*
–COCH ₂ –	0.52±0.06*	0.60±0.11	0.57±0.07*	0.75±0.19	1.13±0.32
–HC=CH–	0.63±0.05*	0.94±0.08	0.45±0.06*	0.57±0.18	2.82±0.56*
creatine	0.91±0.06	1.25±0.10	1.00±0.08	0.84±0.12	1.23±0.17
choline	0.60±0.06	0.56±0.06*	1.32±0.14	1.07±0.15	2.67±0.44*
intra. water	1.06±0.11	0.82±0.06	1.87±0.13*	0.76±0.05*	3.34±0.2*

5.4.2.5. High gradient diffusion

The diffusion measurements for metabolites in intact cells measured at relatively low gradient strengths ($b = 124 - 1571 \text{ s.mm}^{-2}$) captured fast diffusing species only. In order to explore the diffusion of metabolites at slower rates, I investigated a wider range of gradient strengths than had been used previously.

The impact of gradient strength was investigated using a high gradient diffusion probe (Diff50, $b = 6 - 420951 \text{ s.mm}^{-2}$). A larger range of gradient strengths enabled us to better investigate lipids diffusing at slower rates. **Figure 5.10** shows a Stejskal-Tanner plot generated using this new wide range-gradient approach.³¹⁸ Fitting the data to single and bi-exponential models was explored but neither described the data satisfactorily. The solid line presented in **Figure 5.10** shows the fit using a 3-component model, which provided the best fit to the diffusion data. The fastest apparent diffusion rate measured using the high gradient strength probe was similar to the ADCs measured by HRMAS ¹H NMR spectroscopy. The apparent diffusion constant values for the –CH₂– lipid signal are $120.1 \mu\text{m}^2.\text{s}^{-1}$ and $175.8 \mu\text{m}^2.\text{s}^{-1}$ as measured with the HRMAS probe and the Diff50 probe, respectively. Using the higher gradient strength, it was possible to resolve two other lipid species with ADCs of $41.7 \mu\text{m}^2.\text{s}^{-1}$ and $0.582 \mu\text{m}^2.\text{s}^{-1}$.

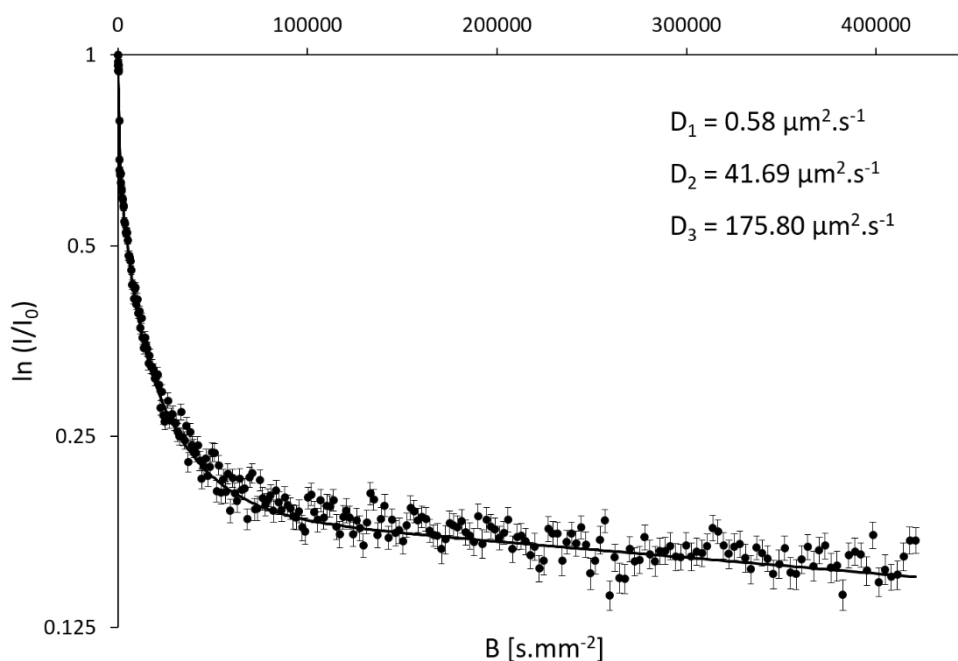


Figure 5.10. A tri-exponential diffusion fit for the $-\text{CH}_2-$ signal displayed as a Stejskal-Tanner plot. Diffusion data collected for untreated cells packed in 3 mm tubes using a high gradient 5 mm probe (diff50). Error bars correspond to the line fitting errors.

5.4.3. Microscopy compared with HRMAS ^1H NMR spectroscopy of mobile lipids

The standard approach for measuring the size of LDs in intact cells is fluorescence microscopy. **Figure 5.11A, B, C** shows images of labelled LDs in the control and treated cells. The size of the LDs was determined by image analysis. The analysis of the LD populations showed that the average LD cross-sectional areas were $0.26 \pm 0.03 \mu\text{m}^2$, $0.40 \pm 0.03 \mu\text{m}^2$, and $0.36 \pm 0.04 \mu\text{m}^2$ in the control, cisplatin, and etoposide-treated cells, respectively. Of these, only the size of the LD in cisplatin samples was confirmed to be statistically significant for group differentiation over all samples (FDR-adjusted $p = 0.04$, ANOVA).

According to the Stokes-Einstein equation (**Equation 5.2**), LD size is inversely related to the droplet's diffusion coefficient. Therefore, the correlation between HRMAS ^1H NMR-based diffusion measurements and the size of LDs measured by fluorescence confocal microscopy was investigated. **Figure 5.11D** shows the plot of the ADCs determined by HRMAS ^1H NMR spectroscopy against LD size from microscopy. The ADCs for the individual lipid signals: $-\text{CH}_3$, $-\text{CH}_2-$, $-\text{HC}=\text{CHCH}_2-$, $-\text{COCH}_2-$, and $-\text{HC}=\text{CH}-$ correlated with the mean LD area. The experimental data from the 24 h and 48 h time points were fitted using two separate

regression models. In both cases, the data are highly correlated ($R^2 = 0.90$ for 24 h and $R^2 = 0.92$ for 48 h).

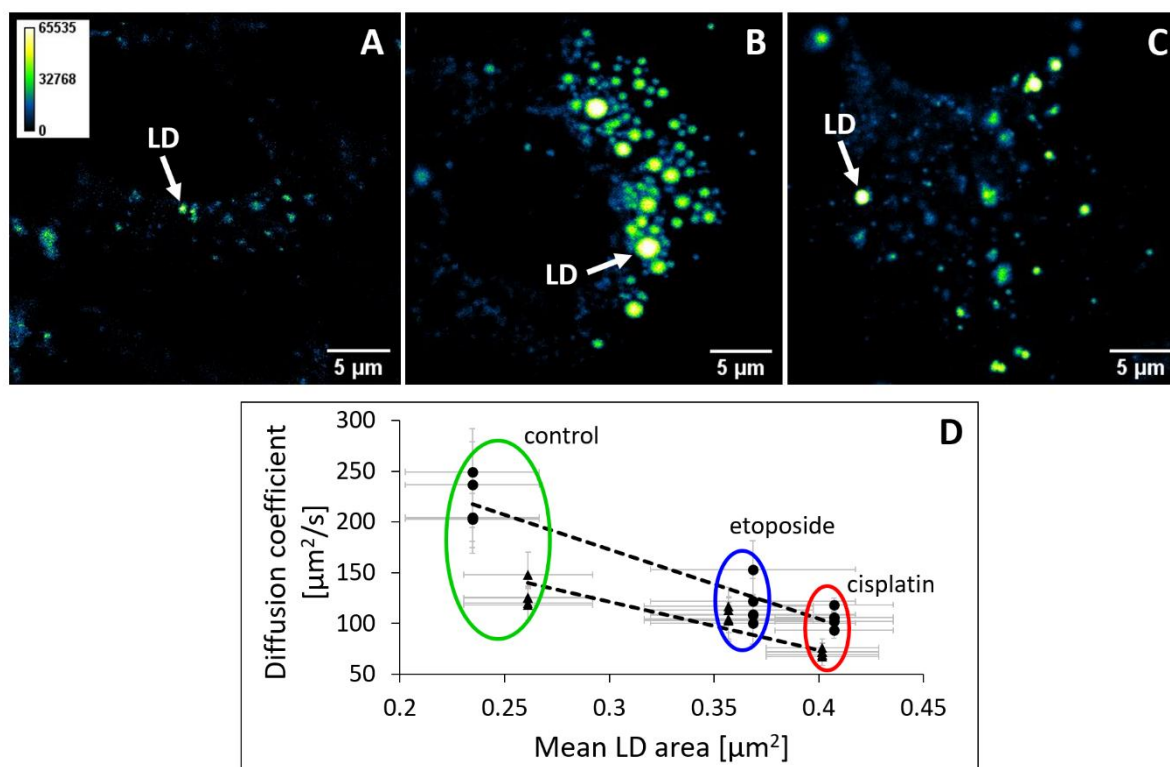


Figure 5.11. Correlation of microscopy-based LD size estimates and HRMAS ^1H NMR-based mean diffusion coefficients. Representative images of fluorescence-labeled LDs in a single cell: **A)** control, **B)** cisplatin treatment, **C)** etoposide treatment. Arrows indicate neutral lipids in LD stained with BODIPY dye. Images were taken after 48 h incubation. **D)** Regression analysis for mean LD size and NMR-based diffusion rates for control (○ green), cisplatin (○ red), and etoposide (○ blue) samples at ● 24 h and ▲ 48 h incubation times. Four dots aligned vertically represent four chemical groups ($-\text{CH}_3$, $-\text{CH}_2-$, $-\text{COCH}_2-$, $-\text{CH}=\text{CHCH}_2-$). The graph represents the collective diffusion coefficient from each chemical group. Error bars indicate standard error. Separate regression fits for the two incubation times are shown ($R^2 = 0.90$ for 24 h and $R^2 = 0.92$ for 48 h).

5.4.4. Viscosity of cytoplasm

Since LD size by microscopy and mobile lipid diffusion by NMR spectroscopy were highly correlated, I investigated if combining the HRMAS ^1H NMR-based diffusion data and fluorescence microscopy measurements would lead to correct estimation of the cytoplasmic viscosity. If we assume that LDs are ideal spheres, a constant temperature (300 K), and no cytoplasmic changes occur due to different ways in which the samples were treated, we can deduce the viscosity from the modified Stokes-Einstein equation as shown in **Equation 5.4**.

$$D = b + \frac{kT}{6\nu\pi} \left(\frac{1}{r} \right) \quad \text{Equation 5.4}$$

Where: b – constant [m²·s⁻¹].

The viscosity can be determined from the slope of the graph of $D \sim \frac{1}{r}$. Using data described in **Figure 5.11D**, the cytoplasmic viscosity was calculated. The values obtained for each lipid signal and their average are listed in **Table 5.4** and the $D \sim \frac{1}{r}$ graphs for each lipid signal are shown in **Appendix 2 (Figure S2.6)**.

Table 5.4. The viscosity (ν) of cytoplasm calculated from HRMAS ¹H NMR-based diffusion data and fluorescence microscopy for cells at 24 h and 48 h incubation time points. For comparison, literature values are included, measured using T₁ relaxation times of ¹⁹F-labelled proteins in cells by ¹⁹F NMR spectroscopy.³³⁴

Lipid signal	ν 24 h [mPa·s]	ν 48 h [mPa·s]	ν ¹⁹ F [mPa·s]
–CH ₃	1.75	2.13	
–CH ₂ –	1.37	3.20	
=CHCH ₂ –	2.04	3.33	
–COCH ₂ –	1.97	3.05	
AVERAGE	1.74 ± 0.13	2.93 ± 0.24	1.7 - 2.55

5.4.5. Determination of mean displacement

To further validate the HRMAS ¹H NMR-based diffusion measurements in intact cells, mean square displacements of mobile lipids measured by microscopy and HRMAS ¹H NMR spectrometry were compared. By tracking individual lipid droplets in intact cells for the control and cisplatin samples, it was possible to calculate the mean square displacement and compare it with the value determined by HRMAS ¹H NMR diffusion measurements. **Equation 5.5** describes the relationship between one dimensional diffusion (D), diffusion time (t), and mean displacement $\langle r \rangle$.³³⁵

$$\langle r \rangle^2 = 2Dt \quad \text{Equation 5.5}$$

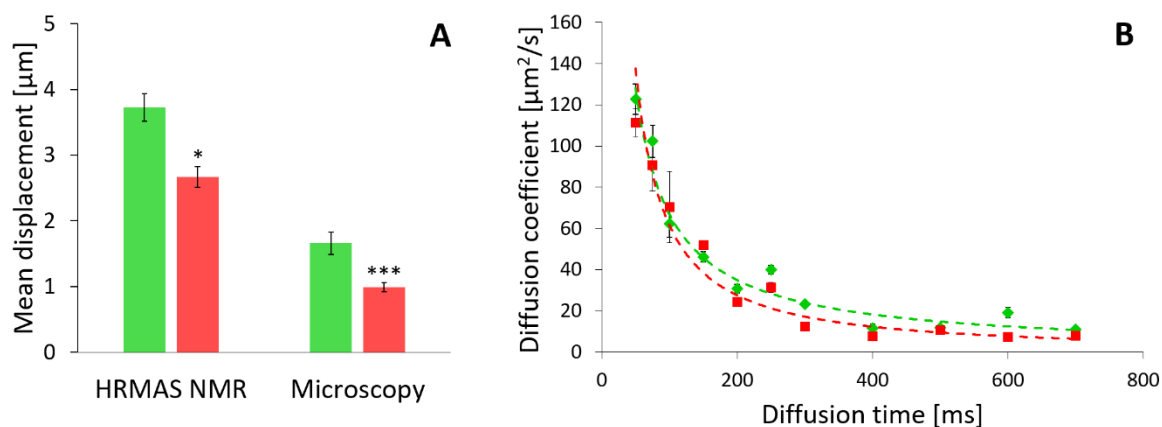


Figure 5.12. *A)* Mean and SEM values of LD displacement calculated from HRMAS ^1H NMR diffusion data and confocal fluorescence microscopy. *B)* Diffusion coefficients of LDs in intact cells as a function of diffusion time. Data correspond to the control (\blacklozenge green) and cisplatin (\blacksquare red) treated cells at 24 h. Error bars correspond to standard errors; asterisks represent statistical significance (Student *t*-test): * $p < 0.05$, *** $p < 0.001$.

Figure 5.12A shows a comparison between LD mean displacement values calculated from NMR diffusion data with mean displacements measured by microscopy tracking. Both the microscopy-based and NMR-based mean square displacements for cisplatin were shorter than for the control group, which is consistent with the formation of bigger LDs that diffuse slower. However, the microscopy-based mean displacements were shorter than the NMR-based mean displacements.

In addition, I tested if the NMR-based diffusion rates correspond to free or restricted diffusion by running variable diffusion time NMR experiments over the range of 50 - 700 ms. The results showed that the ADCs of mobile lipids in both control and treated cells decreased with increasing diffusion time (**Figure 5.12B**), which is characteristic for restricted diffusion³²². The data were described well by single exponential fits.

5.5. Discussion

5.5.1. T_2 relaxation times of metabolites in intact cells

In **Chapter 4**, I discussed the possibility of cellular disintegration during apoptosis and necrosis as detected by an increase in the NMR-visibility of certain metabolites. Comparing intact cells profiles and cell extract profiles suggested that the increased NMR-signal might be due to

cellular disintegration, leading to increased metabolite mobility (**Chapter 4, Section 4.1.1**). The T_2 relaxation experiment should have been a good way to test this hypothesis. Increased metabolite mobility results in a small average magnetic field variation and is characterized by longer T_2 relaxation times. Contrariwise, short T_2 values correspond to restricted mobility due to larger molecular sizes or engagement in semi-rigid structures.

The T_2 relaxation times of selected metabolites in intact cells measured here were consistent with the values previously reported by Griffin and colleagues⁷⁰ (**Table 5.5**). The T_2 values for water in skeletal muscle tissue reported by Kasturi and colleagues are also included for comparison.³³⁶ In general, the values are in good agreement except for the choline compounds. This may suggest a significant role of mobile choline compounds in muscle cells as essential nutrients, for example.³³⁷

Table 5.5. Comparison of T_2 relaxation times of selected metabolites and water for mouse muscle cells reported in this study, for endometrial cells reported by Griffin et al, and for skeletal muscle tissue reported by Kasturi et al; n/r – not reported.

Metabolites	Muscle cells ^a		Endometrial cells ⁷⁰		Muscle tissue ³³⁶
	Mean [ms]	SEM [ms]	Mean [ms]	SEM [ms]	Mean [ms]
lipid 0.9 ppm	240	34	210	40	n/r
lipid 1.6 ppm	132	11		n/r	n/r
lipid 2.0 ppm	237	23	290	40	n/r
lipid 2.2 ppm	155	17	320	30	n/r
lipid 5.3 ppm	279	10		n/r	n/r
creatine	753	22		n/r	n/r
choline	903	37	260	30	n/r
restricted water	302	36		n/r	n/r
restricted water 2	30	10		n/r	40-50 ^b

^a control cells harvested at 8 h

^b depending on the muscle fiber orientation with respect to the static field

The T_2 measurements of metabolites were not significantly different between healthy and apoptotic cells (**Figure 5.6**). However, the separation between healthy and necrotic cells is noteworthy (**Table 5.1**). Shorter T_2 values for necrotic cells would suggest decreased molecular tumbling, possibly as a consequence of cell shrinkage following the heat shock. It has previously been shown that the T_1 and T_2 values of cellular water depend on cell volume.³³⁸ Another possible explanation is increased cell permeability, which increases transmembrane exchange rate between T_2 of intracellular metabolites and T_2 of extracellular metabolites.

Bailey and colleagues described a model in which fast exchange decreased T_2 values of intracellular water and therefore needed to be accounted for in an accurate estimation of molecular dynamics.¹⁶⁶ Interestingly, the shrinkage of apoptotic cells did not influence T_2 , suggesting that only severe shrinkage or formation of apoptotic bodies can be captured by the selected T_2 NMR experiment.

The T_2 relaxation results did not exclude that cellular disintegration was not present in apoptotic cells. Rather, the results showed that T_2 measurements, under the selected HRMAS ^1H NMR parameters, failed to distinguish between healthy and apoptotic cells. The spin echo delays selected for the T_2 experiment (0.01 – 0.41 s) were tailored to measure shorter T_2 values, as expected for mobile lipids in intact cells (0.2 – 0.3 s).⁷⁰ In some cases, this targeted sampling of T_2 data can be advantageous for differentiating structural changes.³³⁹ Fast relaxing and slowly relaxing molecules require a different range of echo delays for accurate assessment of relaxation rates. For intact cells, it was crucial to keep the total experiment time to a minimum, which limited the number of data points collected.

Bi-exponential analysis of the relaxation data yielded two T_2 values: the fast-relaxing component (< 0.04 s, data not shown) and the moderately fast relaxing component attributed to metabolites with restricted motional freedom. The short T_2 value of water, most likely attributed to water bound to macromolecules, was similar to the values measured in skeletal muscle tissue by Kasturi and colleagues³³⁶ (**Table 5.5**). For the short T_2 of metabolites, the standard errors were greater than 50% of the mean measurements; hence, the data was excluded from the analysis. Kasturi acquired data with echo delays < 0.06 s, which is a more suitable data sampling approach for fast T_2 relaxation rates. The data presented here was acquired at echo delays > 0.01 s with only three data points corresponding to initial fast decay. Even though the short T_2 measurements were not reliable, incorporating the bi-exponential model improved the accuracy of the faster component.

T_2 variations depend on the qualitative and quantitative modification of metabolites in intact cells, namely the total content of intra- and extra-cellular metabolites, the variation in the ratio between cytosolic metabolites and structure-bound metabolites, and the balance between the signals from overlapping metabolites. Other factors that affect T_2 relaxation rates are cell density and the echo delay.^{340,341} Thus, these experiments in intact cells proved to be complex and challenging to interpret.

5.5.2. Diffusion of metabolites in intact cells

Another useful NMR experiment that can probe changes in cellular environment is measuring the diffusion properties of metabolites in intact cells. The changes in diffusion rates may be a sign of the restructuring of cellular membranes or compartmentalisation.

The ADC values reported here (**Figure 5.7**) are consistent with literature values. Griffin and colleagues have previously reported the ADCs of lipids in intact endometrial cells measured by HRMAS ^1H NMR spectroscopy.⁷⁰ A comparison of the apparent diffusion rates is shown in **Table 5.6**. Those for $-\text{CH}_3$, $-\text{CH}_2-$, and choline compounds showed a good agreement whereas those for $-\text{HC}=\text{CHCH}_2-$, $-\text{COCH}_2-$, and $-\text{HC}=\text{CH}-$ are much higher in endometrial cells. This may be due to the overlap of different peaks in the NMR spectrum, differences in metabolic profiles of different cell lines, and the size and shape of the cells.

Table 5.6. Mean ADCs of selected lipid signals for untreated muscle cells and endometrial cells and rat glioma tissue, \pm values refer to standard error, * value corresponds to restricted diffusion.

Lipid	Muscle cells [$\mu\text{m}^2/\text{s}$]	Endometrial cells ⁷⁰ [$\mu\text{m}^2/\text{s}$]	Rat glioma tissue ²²⁶ [$\mu\text{m}^2/\text{s}$]
$-\text{CH}_3$	148.1 \pm 22.4	200 \pm 10	
$-\text{CH}_2-$	120.1 \pm 14.0	200 \pm 10	46 \pm 17*
$-\text{HC}=\text{CHCH}_2-$	125.2 \pm 7.1	600 \pm 40	
$-\text{COCH}_2-$	125.4 \pm 7.9	800 \pm 50	
$-\text{HC}=\text{CH}-$	91.1 \pm 27.4	500 \pm 30	
choline	164.7 \pm 12.1	200 \pm 10	

The content and concentration of small metabolites and lipids vary from cell line to cell line. The NMR region between 2.0 – 2.5 ppm, corresponding to $-\text{HC}=\text{CHCH}_2-$ and $-\text{COCH}_2-$ lipid signals, was crowded with peaks from other small metabolites such as acetyl groups and glutamate, which diffuse much faster. The contribution of these metabolites resulted in higher ADCs for lipids and it is important to exclude them. This was achieved by starting the diffusion experiment at a non-zero gradient value ($b = 124 \text{ s}\cdot\text{mm}^{-2}$) (**Appendix 2, Figure S2.5**). Moreover, the chemical groups under investigation belong to a series of different fatty acids which in turn can be components of different lipids (e.g., free fatty acids, triacylglycerols,

phosphatidylcholines) and these will have different mobilities. DOSY ^1H NMR spectroscopy measured an average ADC across the whole ensemble, which should be considered when interpreting the lipid ADCs.

5.5.2.1. Choline compounds

A decrease in the ADC of choline after anticancer gene therapy has been previously reported *in vivo* by Hakumäki and colleagues.³⁴² During the early stages of apoptosis, the plasma membrane retains its integrity and choline-containing species of cytoplasmic origin contribute to the ^1H NMR resonance (free choline, phosphocholine, and glycerophosphocholine).³⁴² The reduced ADC of choline may represent increased restrictions within apoptotic cells (**Figure 5.7**), such as cell shrinkage and increased macromolecular crowding.³²⁵ In this scenario, we would also expect the ADC of other metabolites to follow the same decreasing trend. However, this was not observed for intracellular water and creatine (**Figure 5.7**), for which the ADCs do not change significantly during early apoptosis (8 and 24 h). Thus, another factor is likely to contribute to reduced choline mobility, which is unique for cytoplasmic choline.

It is worth noting that the ADC of choline is inversely proportional to choline levels (as reported in **Chapter 4, Section 4.4.2**). 1D HRMAS ^1H NMR data of intact cells demonstrated that the level of choline-containing compounds increased in the early stage of apoptosis (8 – 24 h) and decreased in the late stage of apoptosis (48 h). The data may suggest significant perturbation of physiologic regulation of cytosolic choline or the formation of small endosomes during apoptosis that can contribute to the resonances of NMR-visible choline compounds.²⁸⁸ Further experiments are needed to understand the decreased ADC of choline compounds during apoptosis.

An increasing trend in the ADC of choline between 24-48 h of apoptotic treatment may be an early sign of secondary necrosis and membrane disintegration. Similarly, an increase in the ADC of intracellular water at 48 h of cisplatin treatment may indicate early stages of secondary necrosis. This was further investigated by measuring ADC values of metabolites in necrotic cells, for which membrane disintegration was one of the prominent morphological features (**Section 5.4.2.3**).

Increased mobility of choline compounds in necrotic cells (**Figure 5.9**) might be linked to the cellular disintegration phase of necrosis and late-stage apoptosis in the absence of phagocytic

capacity.³⁴² Berghe and colleagues reported a sequence of subcellular events during different types of necrosis, including lysosomal membrane permeabilization, mitochondrial hyperpolarization, oxidative burst, and plasma membrane permeabilization.³⁴³ Events involving membrane permeabilization are likely to contribute to an increase in the ADC of choline compounds, as they are loosened and released from the membrane. Another possible contribution to the increased diffusivity of choline is leakage from compromised organelles into intracellular or extracellular space.

In vitro necrosis is characterized by cytoplasmic swelling and the presence of dilated organelles,³⁴⁴ which may affect the mobility of intracellular metabolites and water. This finding is in agreement with a previous MRI study by Sundgren and colleagues, who reported elevated ADCs of water in patients with oedema and in necrotic tissue after radiation treatment.³⁴⁵ An elevated ADC of water in tumour-related necrotic tissue has also been reported by others,^{346,347,348,349} and reflects increased mobility of water in necrotic tissue.

5.5.2.2. Mobile lipids

The ADC values of NMR-visible lipids in intact cells significantly decreased during apoptosis (**Figure 5.7**), which suggested an increased deposition of neutral lipids into LDs. Visualisation of LDs by fluorescence microscopy confirmed this hypothesis (**Figure 5.11**). Monitoring lipid droplet formation by microscopy is a well-established method.^{350,351} A good correlation between NMR-based diffusion results and microscopy proved that the observed changes in the ADCs of lipids correspond to relevant biological events induced by apoptosis. The results also demonstrated that NMR-based diffusion measurements, unlike T_2 relaxation measurements, could facilitate the discrimination between control and apoptotic cells and could have potential applications in monitoring LD size during apoptotic-based treatments in intact cells.

ADCs of mobile lipids have been previously measured *ex vivo* by ^1H MRS.²²⁶ Remy *et al.* reported two values of ADCs for mobile lipids in rat glioma: $46 \pm 17 \mu\text{m}^2\text{s}^{-1}$ for a mean LD radius of $0.485 \mu\text{m}$ and $11.0 \mu\text{m}^2\text{s}^{-1}$ for an equivalent spherical diameter of $4.27 \pm 0.71 \mu\text{m}$.²²⁷ The discrepancy between these two measurements was explained by differences in the range of gradient strengths and differences in tumor growth. The higher value was measured with $b = 0 - 8000 \text{ s}\cdot\text{mm}^{-2}$ and the slower rate with $b = 0 - 50000 \text{ s}\cdot\text{mm}^{-2}$.

My ADC measurements of mobile lipids in intact cells using high-gradient NMR spectroscopy identified slower moving lipid species (**Figure 5.10**), which may correspond to lipids located in different cellular environments (for example, the viscosity and molecular crowding is different in the nucleus and cytoplasm^{352–354}) or even in lipid rafts where the movement of lipids is highly restricted.²²¹ This approach opens new opportunities for investigating lipid behavior in intact cells.

A comparison between the Diff50 and HRMAS probes is also interesting from the sample packing perspective. Diff50 is a solution-state NMR probe and therefore the sample packing (rotor vs 3 mm tube) and experimental conditions (spinning vs no spinning) could have potentially affected the ADC measurements. However, the highest values of ADCs measured using the solution-state and HRMAS ¹H NMR spectroscopy were comparable regardless of the probe type.

A literature search revealed that the ADC values of lipids has not been used for the characterization of necrotic cells. The results are particularly interesting because of the different diffusion behaviour of the saturated and unsaturated lipid components (**Figure 5.9**), even though the lipid content decreased for all lipid species as measured by 1D HRMAS ¹H NMR spectroscopy (**Chapter 4, Figure 4.7**). The increased ADCs of unsaturated lipids in necrotic cells suggest an increased mobility. This decrease may be caused by the heat-induced breakdown of unsaturated lipids, which are less stable than saturated lipids.^{355,356} Further studies are needed to understand the differences in diffusion of saturated and unsaturated lipids during necrosis.

5.5.3. Validating NMR-based diffusion measurements of metabolites in intact cells

5.5.3.1. Viscosity

The intracellular viscosity values reported in various cell lines and by different methods vary widely: 0.75 – 18 mPa·s at 300 K.³⁵⁷ The viscosity values calculated based on HRMAS ¹H NMR diffusion data are in agreement with values from Ye et al, who reported cytosolic viscosities in the range 1.7 – 2.55 mPa·s as measured by ¹⁹F NMR spectroscopy.³³⁴

In addition, the viscosity calculated for cells incubated for 24 h was significantly different from the viscosity of cells incubated for 48 h ($p = 0.01$). The different values of viscosity determined

for the 24 h and 48 h samples may be explained by cytoplasmic changes during cell maturation/cell growth. This difference was also observed in control cells, which had different stages of cellular differentiation at 24 and 48 h. Control cells also Changes in the cytoplasmic viscosity have been reported during germination;³⁵⁸ and the cytoplasm viscosity is sensitive to changes in the concentration of Ca^{2+} , Mg^{2+} , and ATP.³⁵⁹ This suggests that HRMAS ^1H NMR-based diffusion measurements may be able to detect not only changes in mobile lipids but also changes in cytosol viscosity.

5.5.3.2. Mean squared displacement

Both the microscopy-based and NMR-based mean square displacements for cisplatin were shorter than for the control group, which is consistent with bigger LDs that diffuse more slowly. However, the microscopy-based mean displacements were shorter than the NMR-based mean displacements (**Figure 5.12**).

It is interesting to consider the discrepancy between the results as the two methods have different spatial and temporal detection limits. The spatial resolution of the microscopy used here allows the ADC values of LDs to be monitored.³⁶⁰ Conversely, the HRMAS ^1H NMR-based diffusion experiments in this thesis describe the mobility of LD-associated lipid molecules. Therefore, ADCs and hence mean displacements measured by the two methods correspond to different biological processes: microscopy implies that decreased ADCs ought to be prevalent in apoptotic cells due to larger LDs, and HRMAS ^1H NMR spectroscopy most likely captures decreased ADCs of mobile lipids, which can be linked to a more crowded environment within larger LDs.

The results are in contrast to a study by Perez and colleagues, who reported similar sizes of LDs obtained from microscopy and NMR experiments.³³⁰ Following the same approach (diameter = mean displacement $\times \sqrt{10}$), I calculated mobile lipid compartment sizes based on NMR mean displacement and obtained values of 5.9 μm and 4.22 μm for control and cisplatin-treated cells, respectively. The results suggest that the NMR experiment reported here does not measure changes in LD size per se, but changes in the mobility of lipids within LDs.

In addition, other subcellular organelles can contribute to NMR-based mean square displacement values, such as small endosomes. Martin-Sitjar and colleagues reported that the increasing MAS spinning rate resulted in a reversible increase in the intensities of NMR-visible

lipid resonances and attributed this effect to the fatty acyl chains of phospholipids in intracellular endosomes.²⁹⁴ Indeed, I also detected an increase in choline containing compounds (**Chapter 4, Figure 4.16**), which supported endosomal phospholipid detection by HRMAS NMR spectroscopy. The viability of cells in the MAS rotor decreased by ~10% after data acquisition (**Chapter 3, Figure 3.5**), while this was not the case during the microscopy experiment. This could be another potential explanation for the discrepancy.

From a temporal perspective, NMR measures diffusion on a millisecond time scale (50 ms) while microscopy measures diffusion on a second time scale (5 – 6 s). This difference in observation time means that NMR-based diffusion measurements may be less sensitive to restricted diffusion. The results of variable diffusion time NMR experiments (**Figure 5.12B**) showed that the ADCs of mobile lipids in both control and treated cells are restricted. For free diffusion we expect a constant value for diffusion coefficients regardless of the duration of the experimental diffusion delay time.³²¹ For the diffusion data presented in **Figure 5.12A** the diffusion time was 50 ms. During this time, lipid molecules travel an average distance of 3.5 μm (**Equation 5.5**) and are prone to collisions with the compartment boundary and collisions with other molecules. While there is a clear difference in LDs between control and apoptotic samples regardless of the analytical method used, more experiments are needed to investigate the reasons behind the relationship between the size of LDs and NMR-based diffusion measurements.

5.6. Conclusions

Chapter 5 describes the application of time domain NMR experiments, namely T_2 relaxation and diffusion measurements, for differentiating between control, apoptotic, and necrotic cells.

It was demonstrated that the T_2 relaxation times of metabolites in intact cells treated with apoptotic agents were not significantly different from the corresponding T_2 relaxation times in the control cells. This suggested that, under the constraints of the selected NMR parameters, the T_2 experiments were not sensitive enough to discriminate between control and apoptotic cells. Further study is needed to investigate whether T_2 experiments with longer echo times could provide useful information about changes in cellular environments during apoptosis.

Necrotic cells, on the other hand, showed significantly lower T_2 relaxation times as compared to the controls. Two explanations were proposed: 1) decreased molecular tumbling in necrotic

cells as a consequence of cell shrinkage following the heat shock; or 2) increased cell permeability, which increases the transmembrane exchange rate between the T_2 values of intracellular metabolites and those of extracellular metabolites. Further experiments employing longer echo delays are needed to investigate the broader ranges of cellular environments in necrotic cells.

HRMAS ^1H NMR-based diffusion data showed a significant decrease in ADCs of NMR-visible lipids at 50 ms diffusion time upon apoptosis, and this correlated well with an increase in LD size measured with fluorescence microscopy. Moreover, microscopy and NMR-based mean displacements were shorter for cisplatin-treated cells compared to the control group, further validating the use of DOSY experiments as a means to discriminate between control and apoptotic cells.

Necrosis could be differentiated from control cells based on increases in the ADC values of unsaturated lipids and non-lipid metabolites. This demonstrates that DOSY could discriminate between changes in cellular environments of intact cells induced by different types of cell death.

High gradient strength diffusion experiments revealed a broader range of diffusion environments than were seen by standard NMR techniques. This could have an application in probing slower-moving lipid species, which are located in more restricted cellular environments or even in lipid rafts where the movement of lipids is highly restricted.

HRMAS ^1H NMR spectroscopy offers a label-free approach for monitoring changes in lipid behaviour during apoptosis and could provide a minimally invasive technique for monitoring this molecular event *in vitro* and *ex vivo*.

Chapter 6. Study of lipid remodelling by mass spectrometry-based lipidomics and transcriptomics.

6.1. Introduction

In previous chapters, I demonstrated that lipid levels and the physical behaviour of LDs are significantly different in apoptotic cells as compared to control cells. HRMAS ¹H NMR spectroscopy can track these changes in intact cells providing a useful means to monitor apoptotic-based treatment *in vitro*. Nevertheless, NMR spectroscopy is not able to identify the individual lipid species that contribute to lipid remodelling during apoptosis. To better understand the abnormal formation of LDs during apoptosis, I investigated changes in lipid composition and lipid-related gene expression. In this chapter, a mass spectrometry-based lipidomics approach was applied to examine the lipid composition of whole-cell extracts and isolated lipid droplets. I also analysed the presence and quantity of mRNA in cell samples to investigate disruptions in the cellular transcriptome.

6.1.1. Lipidomics of apoptosis

Mass spectrometry-based lipidomics can provide information at the level of individual lipid species, and it is used to analyse the lipidomes of cells and tissues. It aims to identify and quantify many lipids including fatty acids (FA), triacylglycerols (TAG), diacylglycerols (DAG), phospholipids (PL), sphingolipids (SL), and sterols. It has been demonstrated that lipidomic analysis of cell extracts or isolated organelle extracts enables the phenotyping of pathologies including cancer, non-alcoholic fatty liver disease, inflammation, obesity, diabetes, and influenza infections.^{361–367} Lipidomics of total cell lysates is useful for studying global changes in cellular lipids; however, spatial information is lost during sample preparation. Some changes in lipid composition occur in all organelles, whereas other changes are unique to a

single organelle.³⁶³ Therefore, a number of studies have analysed the lipidomes of isolated organelles to preserve spatial distribution. For example, the lipidomes of cellular membranes, mitochondria, nuclei, lysosomes, and lipid droplets have been studied to understand metabolic states of health and disease.^{368–371}

The majority of lipidomic studies on apoptosis involve analysing phospholipids as they play an important role in cytoplasmic and mitochondrial membrane remodeling.^{372–375} The accumulation of TAGs during apoptosis has also been well established. Brindle and colleagues reported an increase in TAGs during apoptosis.²⁰⁶ Pacia and colleagues characterized the composition of apoptosis-induced LDs focusing on lipid classes (unsaturated neutral lipids, cholesterol, and phospholipids) without identifying chemically distinct lipid species.³⁷⁶ Even though the accumulation of TAGs during apoptosis has been reported on a number of occasions, their role in the cell is poorly understood. Li and colleagues reported the accumulation of specific polyunsaturated TAG species in apoptosis-induced LDs and hypothesized that they play a protective role to prevent lipid-mediated toxicity.³⁷⁷ Listenberger and colleagues demonstrated that channelling FAs to TAG pools prevented lipotoxicity and, consequently, FA-induced apoptosis.³⁷⁸ Nevertheless, the molecular mechanisms behind the activation and fine-tuning of TAGs are yet to be elucidated. Combining lipidome and transcriptome analysis could provide a powerful integrated approach to unravel the complex relationship between lipid metabolism and apoptosis.

6.1.2. Lipid-related transcriptomics apoptosis

RNA-Seq is routinely used to investigate the functional element of the genome of any organism. The method is based on Next Generation Sequencing (NGS) of mRNA and allows the entire transcriptomic profile to be characterized, which contributes to an understanding of molecular mechanisms behind system perturbations. It involves mRNA purification followed by fragmentation and the synthesis of cDNA by reverse transcriptase. Adapter-ligated cDNA is then amplified using PCR prior to NGS and mapping of the sequence reads to a reference genome (**Figure 6.1**).

RNA-Seq has been used for detecting differential expression in apoptosis. Several apoptotic pathways have been explored and their connection to the dysregulation of lipid metabolism studied.³⁷⁹ The link between ceramides (a key intermediate in sphingolipid metabolism) and apoptosis has been studied extensively for the last couple of decades.³⁸⁰ In addition, integrin

signalling, which regulates anti-apoptotic signalling pathways has been associated with sphingomyelin metabolism.³⁸¹ The expression of genes associated with phospholipid metabolisms such as LPCAT2 and AGPAT2 has been shown to prevent or offset the induction of apoptosis.^{382,383}

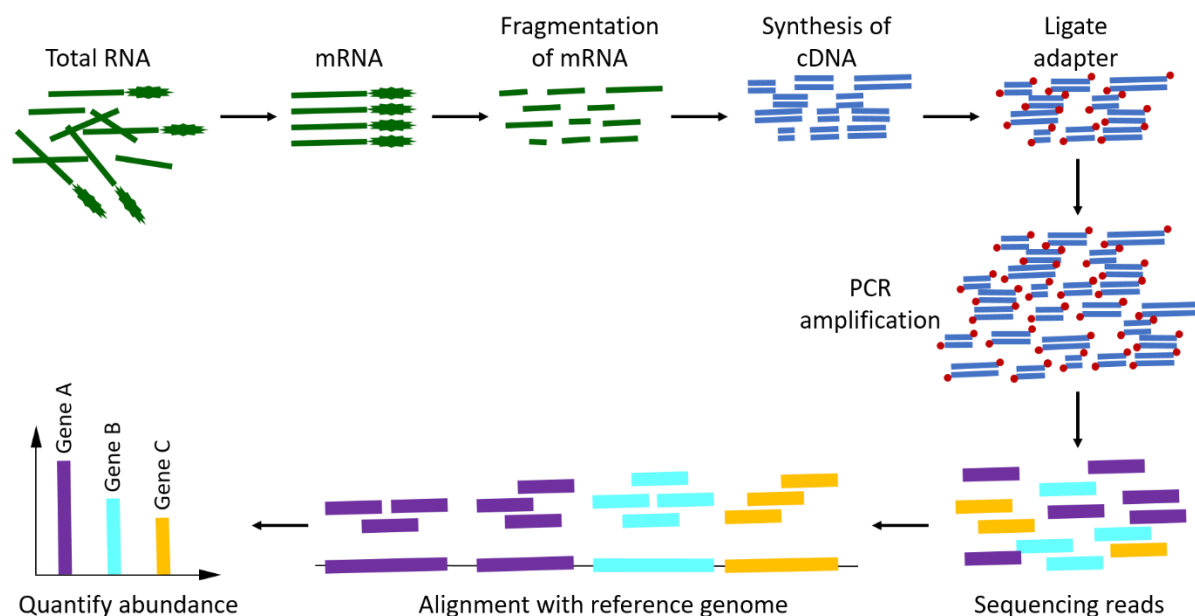


Figure 6.1. RNA-Seq workflow overview. First, RNA is extracted from cells; second, mRNA molecules are isolated, randomly fragmented and converted to complementary DNA (cDNA) by reverse transcription; next, sequencing adaptors (which contain functional elements permitting sequencing) are ligated to the ends of the cDNA fragments. Following amplification by PCR, NGS of the cDNA library produces sequencing reads, which are aligned to a genome of reference and assembled to produce an RNA sequence map.

The effect of apoptosis on the gene expression associated with metabolism and trafficking of TAG has also been studied. Gao and colleagues reported that apoptosis-related pathways (PI3K/AKT-TOR, cAMP/PKA/CREB, and LKB1/AMPK-FOXO), regulate changes in hepatic lipid metabolism in fish and mammals.³⁸⁴ They reported upregulation of lipogenesis and downregulation of lipolysis, β -oxidation and lipid transport that led to lipid accumulation upon apoptosis induced by methionine deficiency. Zhang and colleagues identified interactions between TAG lipases (enzymes that hydrolyse TAGs) and apoptosis signalling pathways.³⁸⁵ However, lipid-related pathways involved in apoptosis-induced lipid droplet formation have yet to be identified.

6.2. Aims

In **Chapter 6**, I apply an integrated transcriptomics and lipidomics approach to gain insight into molecular processes behind the lipid droplet formation induced by cisplatin and etoposide.

First, using MS-based lipidomics, I compare apoptosis-induced global changes in the TAG profiles of cell extracts with localized changes in isolated lipid droplets. I compare MS-based with previously reported NMR-based (**Chapter 4**) conclusions to cross-validate the results and demonstrate the advantages of analysing isolated lipid droplets. In addition, I identify TAG species that are significantly altered during apoptosis and highlight treatment-specific alterations.

Second, I use transcriptomics data to examine a correlation between apoptosis and TAG metabolism. Using the pathway enrichment approach, I identify several lipid-related pathways that are enriched in cisplatin- and etoposide-treated samples. In particular, I explore the remodelling of lipid particle organization, including LDs and peroxisomes, and their role in apoptosis progression.

Finally, I combine lipidomics and transcriptomics to gain insight into the remodelling of TAG metabolism and to better understand the origin of polyunsaturated fatty acids detected during apoptosis.

6.3. Methods

All experimental methods for collecting, processing, and analysing data are defined in **Chapter 2**.

6.4. Results

6.4.1. MS-based lipidomics

MS-based lipidomics was used to investigate changes in lipid composition in C2C12 myotubes treated with 60 μM cisplatin or 120 μM etoposide for 48 h. The changes were investigated globally, in whole cell extracts, and locally, in isolated LDs. A total of 94 (isolated LDs) and 63 (whole cell extracts) neutral lipid species, including DAGs and TAGs, were compared across the control, cisplatin, and etoposide groups. To identify the largest differences between

the groups relative to sample differences within the groups, PLS-DA was performed on the two data sets (**Figure 6.2**, unsupervised PCA in **Appendix 3, Figure S3.1**). Leave-One-Out Cross-Validation was performed to assess model performance for 1, 2, and 3 PCs. Two important metrics were returned: 1) R^2 measures the degree to which the independent variables explain the dependent variable, and 2) Q^2 estimates the predictive ability of the model. The PLS-DA model works independently of the specific data set that is used to train the model when $Q^2 \approx R^2$.

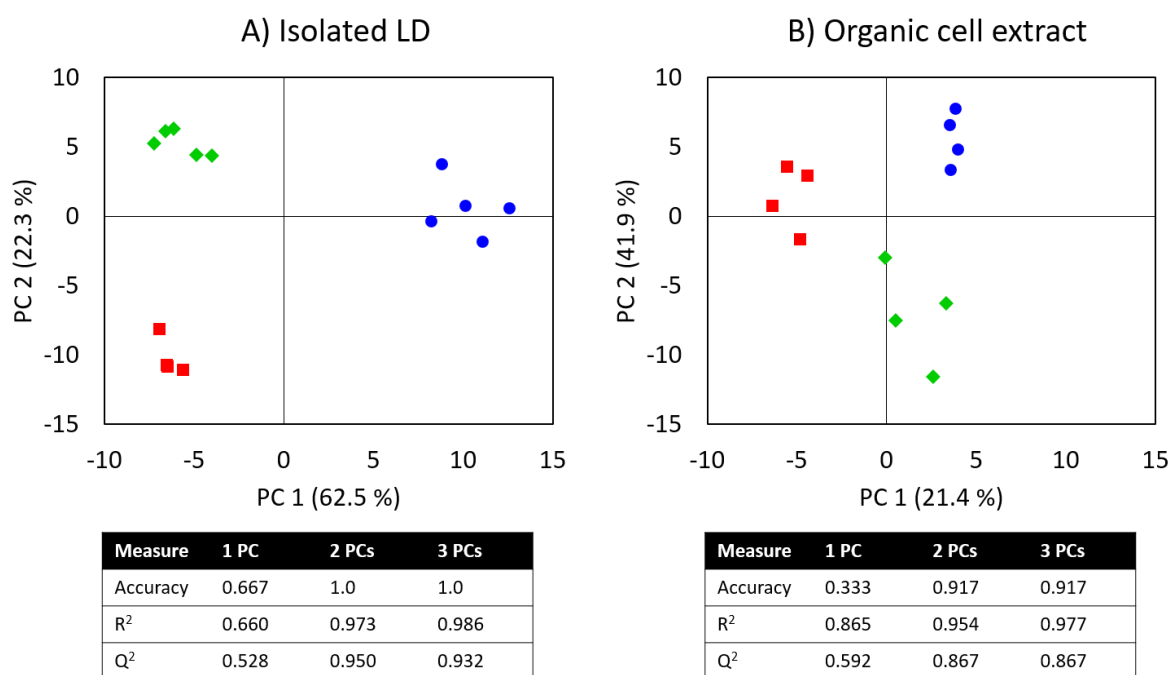


Figure 6.2. PLS-DA analysis of TAG and DAG species extracted from A) isolated LDs and B) organic fraction of cell extracts for control (♦ green), cisplatin (■ red), and etoposide (● blue) samples. The tables below contain quality metrics for each model: R^2 – goodness of fit, Q^2 – goodness of prediction. The analysis was performed after total sum normalization and Pareto scaling; $n = 5$ for isolated LD samples and $n = 4$ for cell extracts.

The PLS-DA models based on TAG and DAG abundance as measured by mass spectrometry readily separated the treatment groups across PCs 1 and 2. Both isolated LD and whole cell extract data sets yielded good PLS-DA models with a high fit and accuracy. The PLS-DA model of the isolated LD data set achieved an accuracy of 100%, R^2 of 0.97, and Q^2 of 0.95 with only two PCs. The PLS-DA model of the whole cell extract data set also produced a good model (accuracy 92%, $R^2 = 0.98$ and $Q^2 = 0.87$ for 3 PCs). The analysis revealed that the

separation between the groups was more pronounced for isolated LD samples as compared to the whole cell extracts.

A detailed list of analysed TAG and DAG species is listed in **Table S3.1** and **Table S3.2** in **Appendix 3**. To investigate lipid unsaturation patterns during apoptosis, I calculated the degree of unsaturation (DOU) for each lipid (number of double bonds/number of carbons) and plotted it against fold change abundance relative to the control group (**Figure 6.3**). This analysis showed that lipid species in isolated LD samples had a distinct unsaturation pattern as compared to whole cell extracts. In isolated LDs, highly unsaturated TAGs and DAGs (DOU between 0.1-0.2) increased during apoptosis, while lipids with fewer double bonds (DOU between 0.03-0.1) decreased during apoptosis. This effect was not observed in the whole cell extracts. However, another interesting pattern emerged for lipids in whole cell samples. When considering the same number of double bonds (for example MUFAs, **Figure 6.3B**), the level of TAGs containing longer FA chains decreased during apoptosis, while TAGs containing shorter FA chains increased. This diagonal pattern is also observed for TAGs containing two and three double bonds (DOU: ~0.04 and ~0.05, respectively).

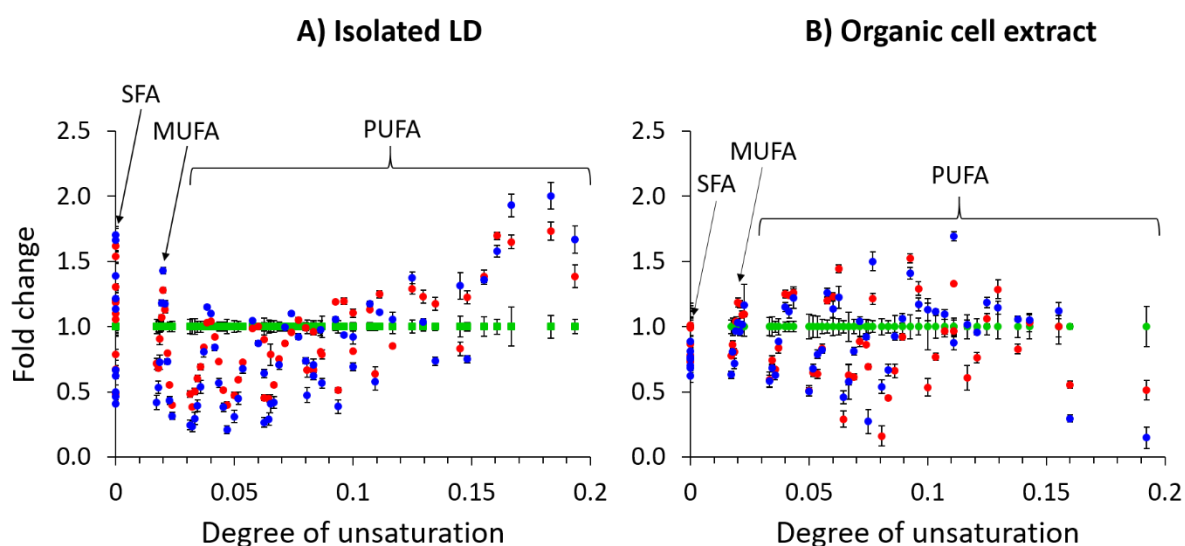


Figure 6.3. Unsaturation analysis of TAGs and DAGs extracted from A) isolated LD and B) whole cells after apoptotic treatment: cisplatin (●red) and etoposide (●blue). Fold changes for each lipid in apoptotic cells was calculated relative to the control group (●green): $Abundance_{treatment}/Abundance_{control}$ or $Abundance_{control}/Abundance_{control}$. Abundance is the total ion count for a given ion. Each ion corresponds to a mass-to-charge ratio (m/z), which is used to assign the lipid species. The list of individual species is reported in **Appendix 3, Table S3.1, and S3.2**. SFA – saturated fatty acids, MUFA – monounsaturated fatty acids, PUFA – polyunsaturated fatty acids; $n = 5$ for isolated LD samples and $n = 4$ for cell extracts.

To facilitate further comparison of apoptosis-induced changes in lipid composition, I analysed the top 20 lipid species ranked by the Variable's Importance in the Projection (VIP) score (**Figure 6.4**). VIP represents the contribution of a lipid species to the PLS-DA model (**Figure 6.2**) – the highest VIP score corresponds to the lipid species which make the greatest contribution to the group discrimination. Twelve species (in bold) were identified in both isolated LD and organic cell extract samples and are compared in **Figure 6.5**. A discrepancy between the compositional changes in isolated LD and whole cell samples during apoptosis was apparent. For example, the levels of TAG (48:3) decreased locally in LDs but increased globally in whole cells during apoptosis. Interestingly, not all TAGs in LDs with a high VIP score increased as would be expected from NMR-based metabolic profiles or microscopy images of enlarged LDs. The levels of several TAGs, namely 46:1, 48:2, 48:3, 56:3 decreased in LDs during apoptosis. Moreover, the levels of TAG species such as 46:1, 48:2, 48:3, 50:3, 52:4 decreased in LDs but increased or did not change overall in the whole cells.

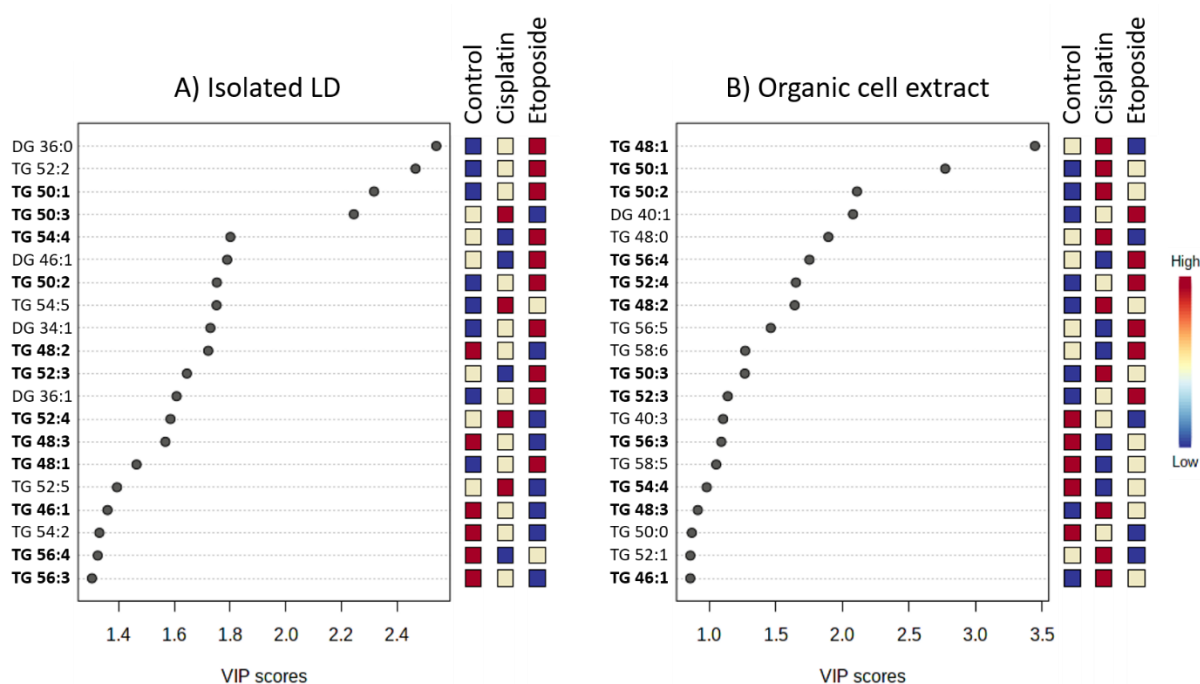


Figure 6.4. The top 20 lipid species ranked by VIP scores for A) isolated LDs and B) organic fraction of cell extracts. Species highlighted in bold are the same in isolated LD and cell extract samples. Squares represent the comparison of relative lipid abundance between control, cisplatin, and etoposide groups. TG - triacylglycerol, DG - diacylglycerol.

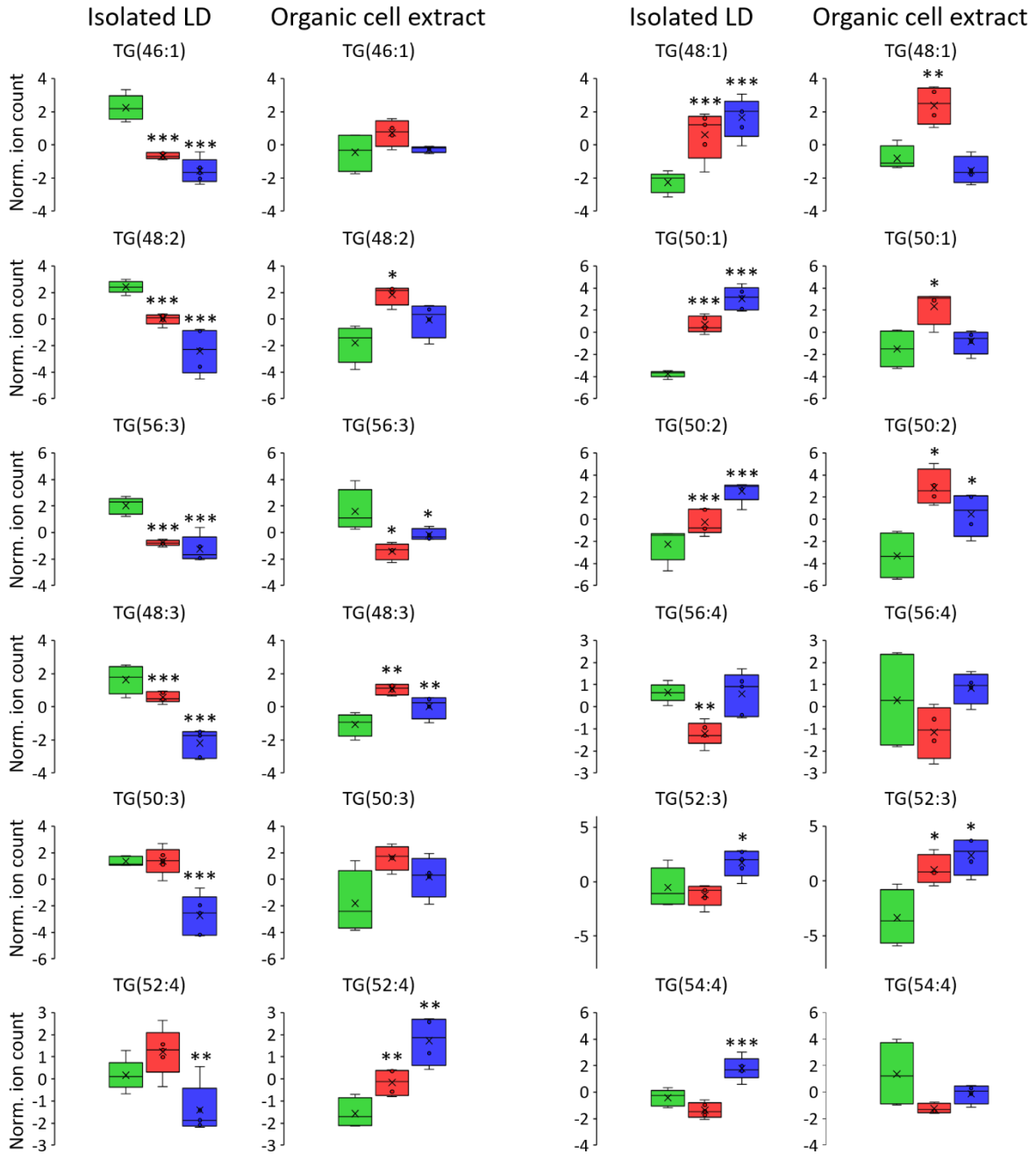


Figure 6.5. Comparison of selected lipid species extracted from isolated LDs and whole cells; control (green), cisplatin (red) and etoposide (blue). TG – triacylglycerol. ANOVA with post hoc Fisher’s test: * $p < 0.1$, ** $p < 0.01$, *** $p < 0.001$, FDR-adjusted; $n = 5$ for isolated LD samples and $n = 4$ for cell extracts.

6.4.2. Transcriptomics

RNA-Seq was performed to understand the changes in lipid-related pathways during cisplatin and etoposide treatments. I focused on genes with prior evidence for their role in lipid metabolism, apoptosis, cisplatin, or etoposide (based on the human gene database,

www.genecards.org). The expression profiles for these genes are represented by heat map diagrams in **Figure 6.6A**. Other processes were not considered relevant to the study and were excluded from the analysis. The targeted PCA showed significant discriminatory power of the selected genes (**Figure 6.6B**). The list of significantly regulated genes during the treatments is shown in **Appendix 3, Table S3.3** and **S3.4**.

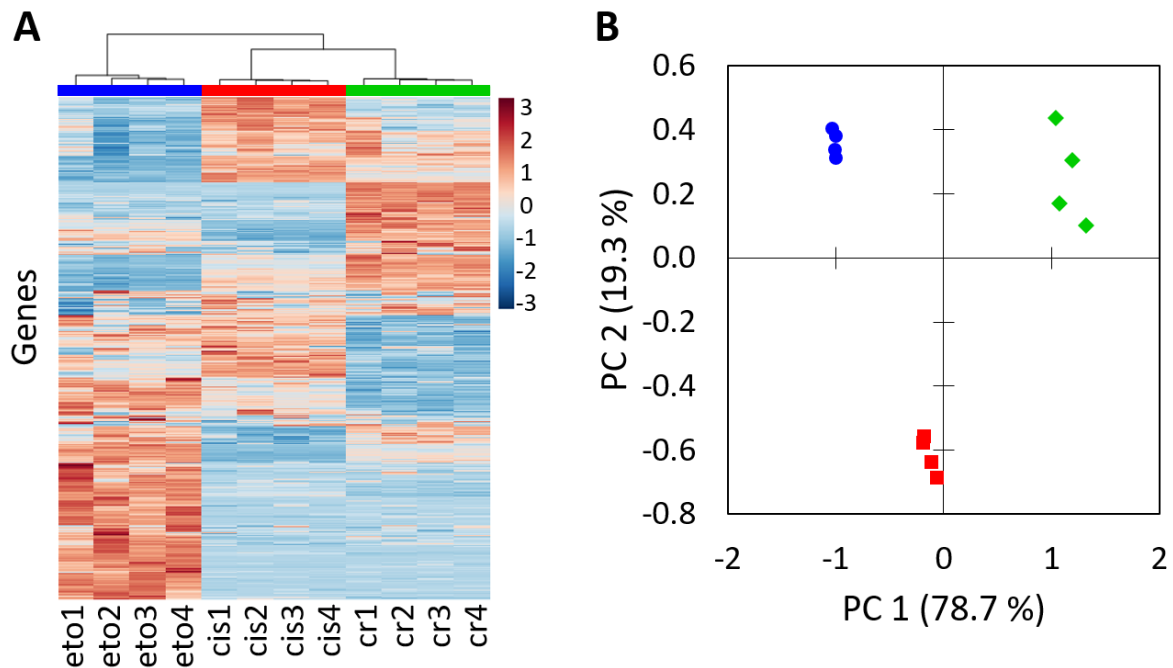


Figure 6.6. Gene expression profiles of apoptotic cells characterized by RNA-Seq. Only genes related to lipid metabolism and apoptosis are included in the analysis. **A)** Heat map comparing control (cr, green), cisplatin (cis, red), and etoposide (eto, blue) samples. Each coloured cell on the map corresponds to a normalized expression value, with samples in columns and genes in rows. **B)** PCA analysis of selected transcriptomic data. The list of significantly regulated genes is shown in **Appendix 3, Table S3.3** (apoptosis) and **S3.4** (lipid metabolism).

Quantitative reverse transcription-polymerase chain reaction (qRT-PCR) analysis of six randomly selected genes involved in lipid metabolism pathways (LIPE, PNPLA2, SOD1, ABCG1, ACOX1, ABHD5) was performed to validate the RNA-Seq results. The fold change values of each gene are the mean values of four independent samples calculated relatively to the respective controls. As shown in **Figure 6.7**, the qRT-PCR expression patterns were consistent with the gene counts measured by RNA-Seq ($R^2 = 0.823$).

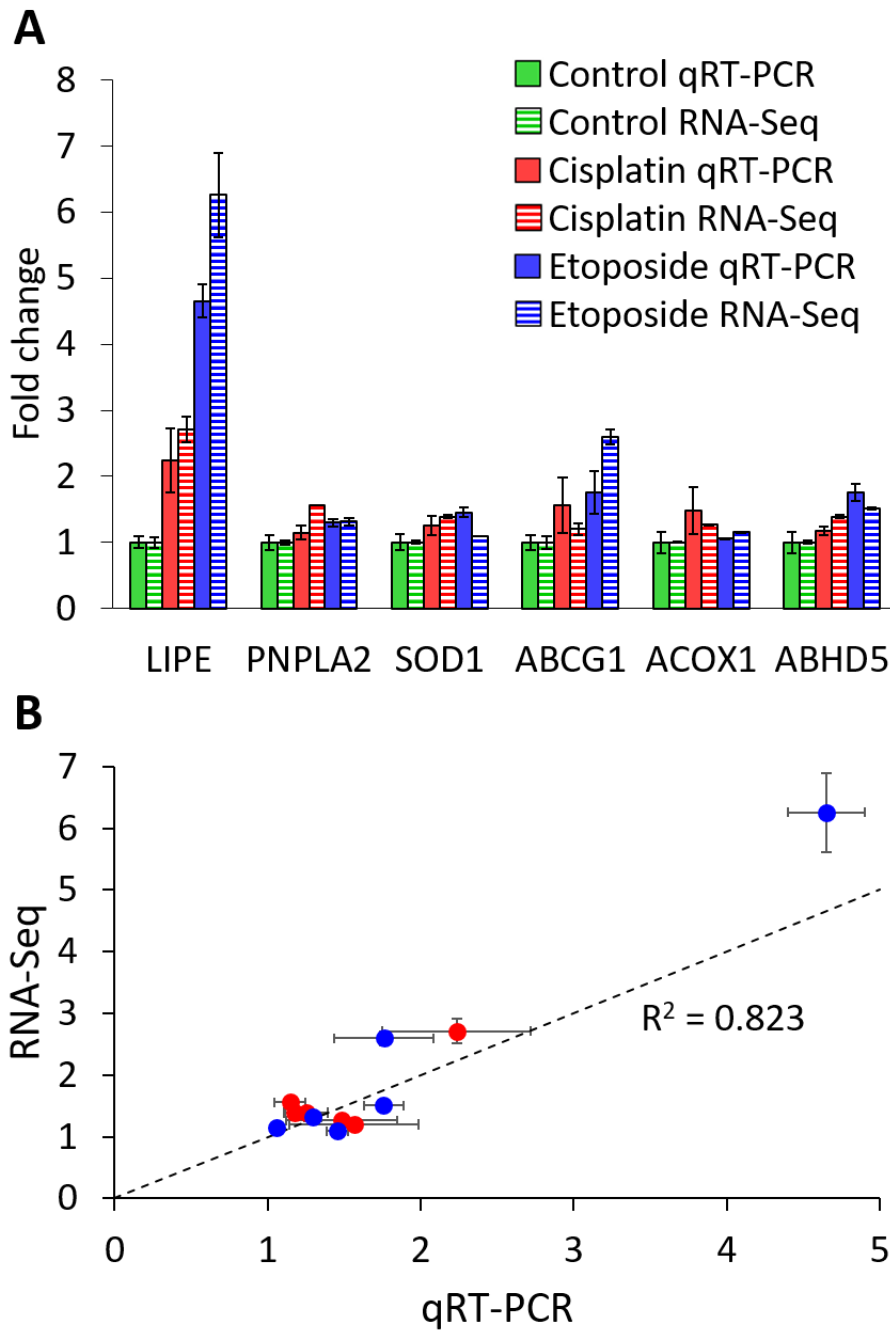


Figure 6.7. **A)** RNA-Seq results compared to qRT-PCR results for six genes involved in lipid metabolism. Mean fold changes in gene expression for cisplatin (red) and etoposide (blue) were calculated relative to the respective control group (green); error bars represent SEM of 4 independent cell samples. **B)** Correlation analysis between RNA-Seq and qRT-PCR, R^2 assesses goodness-of-fit for an idealized model ($y = x$).

6.4.2.1. Pathways enrichment analysis

All of the differentially expressed genes were mapped to the reference pathways in the REACTOME database (www.reactome.org) to identify transcriptional changes that promoted programmed cell death. The enriched pathways related to apoptosis, cell death, DNA damage response, cell cycle arrest, cell cycle progression, and cellular survival are shown in **Table S3.5** for cisplatin and **Table S3.6** for etoposide. Decreases in the expression of genes required for cell cycle progression, DNA synthesis, and DNA repair were observed for both treatments. Similarly, pathways involving pro-inflammatory cytokinesis were significantly upregulated for both treatments. Nevertheless, the transcriptome profiles were significantly different for the two treatments. For example, p53 mediated DNA damage response was upregulated for cisplatin but downregulated for the etoposide samples. Cisplatin triggered apoptosis by inactivation of the anti-apoptotic BCL-2, while etoposide activated the caspase pathway. This was expected since distinct mechanisms of action were reported for the two apoptotic agents. At the same time, other apoptotic pathways were downregulated (e.g. phosphorylation of Emi1, regulation of apoptosis, regulation of localization of FOXO transcription factors), and pathways involved in cell cycle progression were upregulated (e.g. APC/C:Cdc20 mediated degradation of securin, auto-degradation of Cdh1 by Cdh1:APC/C, SCF(Skp2)-mediated degradation of p27/p21).

Subsequently, I performed a pathway enrichment analysis to examine the metabolism of lipids during both apoptotic treatments. REACTOME returned several lipid metabolism pathways, which were affected by the treatments (**Table 6.1**). For example, fatty acyl-CoA biosynthesis, metabolism of sterols, and TAG catabolism decreased, while lipid transport across membranes and lipophagy increased for both apoptotic treatments. However, these changes were not statistically significant (PADOG differential expression analysis: $p > 0.05$).

Table 6.1. List of pathways linked to lipid metabolism regulated by cisplatin or etoposide in C2C12 cells. Legend: **↑↑** - significantly upregulated, **↑** - non-significantly upregulated, **↓** - non-significantly downregulated, **↓↓** - significantly downregulated. Pathways ID corresponds to Reactome pathway database.

Pathway ID	Pathway name	Cisplatin	Etoposide
R-HSA-8978868	Fatty acid metabolism		
R-HSA-75105	• Fatty acyl-CoA biosynthesis		
R-HSA-75876	○ Synthesis of very long-chain fatty acyl-CoAs	↓	↓
R-HSA-2142753	• Arachidonic acid metabolism		
R-HSA-2162123	○ Synthesis of Prostaglandins (PG) and Thromboxanes (TX)	↑	↑
R-HSA-2142691	○ Synthesis of Leukotrienes (LT) and Eoxins (EX)	↓	↓↓
R-HSA-2142688	○ Synthesis of 5-eicosatetraenoic acids	↓	↓
R-HSA-2142696	○ Synthesis of Hepoxilins and Trioxilins	↑	↑
R-HSA-2142712	○ Synthesis of 12-eicosatetraenoic acid derivatives	↑	↑
R-HSA-2142770	○ Synthesis of 15-eicosatetraenoic acid derivatives	↑	↑
R-HSA-2142670	○ Synthesis of epoxy (EET) and dihydroxyeicosatrienoic acids (DHET)	↓	↑↑
R-HSA-2142816	○ Synthesis of (16-20)-hydroxyeicosatetraenoic acids (HETE)	↓	↑↑
R-HSA-2046104	• α -linolenic (omega3) and linoleic (omega6) acid metabolism		
R-HSA-2046106	○ α -linolenic acid (ALA) metabolism	↓	↓
R-HSA-2046105	○ Linoleic acid (LA) metabolism	↓	↓
R-HSA-71262	• Carnitine synthesis	↓	↓
R-HSA-77289	• Mitochondrial Fatty Acid Beta-Oxidation		
R-HSA-77286	○ Mitochondrial fatty acid β -oxidation of saturated fatty acids	↑	↓
R-HSA-77288	○ Mitochondrial fatty acid β -oxidation of unsaturated fatty acids	↑	↓
R-HSA-71032	○ Propionyl-CoA catabolism	↓	↓
R-HSA-390918	• Peroxisomal lipid metabolism		
R-HSA-390247	○ β -oxidation of very long chain fatty acids	↑	↑
R-HSA-389599	○ Alpha-oxidation of phytanate	↑	↑
R-HSA-389887	○ Beta-oxidation of pristanoyl-CoA	↑	↓
R-HSA-8979227	Triglyceride metabolism		
R-HSA-75109	• Triglyceride biosynthesis	↑	↓
R-HSA-163560	• Triglyceride catabolism	↓	↓
R-HSA-1483257	Phospholipid metabolism		
R-HSA-1483206	• Glycerophospholipid biosynthesis		

R-HSA-1483166	○ Synthesis of PA	↑	↓
R-HSA-1482883	○ Acyl chain remodeling of DAG and TAG	↑	↑
R-HSA-1483213	○ Synthesis of PE	↑	↑
R-HSA-1482839	○ Acyl chain remodeling of PE	↑	↓↓
R-HSA-1483152	○ Hydrolysis of LPE	↓	↑
R-HSA-1483191	○ Synthesis of PC	↓	↓
R-HSA-1483196	○ PI and PC transport between ER and Golgi membranes	↓	↓
R-HSA-1482788	○ Acyl chain remodeling of PC	↑	↓↓
R-HSA-1483115	○ Hydrolysis of LPC	↑	↓
R-HSA-1483148	○ Synthesis of PG	↑	↓
R-HSA-1482925	○ Acyl chain remodeling of PG	↓	↓
R-HSA-1483101	○ Synthesis of PS	↓	↓
R-HSA-1482801	○ Acyl chain remodeling of PS	↑	↓
R-HSA-1483226	○ Synthesis of PI	↑	↓
R-HSA-1482922	○ Acyl chain remodeling of PI	↑	↓
R-HSA-1483076	○ Synthesis of CL	↓	↓
R-HSA-1482798	○ Acyl chain remodeling of CL	↓	↓
R-HSA-1483255	● Phosphatidylinositol metabolism		
R-HSA-1483248	○ Synthesis of PIPs at the ER membrane	↓	↑
R-HSA-1483196	○ PI and PC transport between ER and Golgi membranes	↓	↓
R-HSA-1660514	○ Synthesis of PIPs at the Golgi membrane	↓	↓
R-HSA-1660499	○ Synthesis of PIPs at the plasma membrane	↑	↓
R-HSA-1660516	○ Synthesis of PIPs at the early endosome membrane	↑	↑
R-HSA-1660517	○ Synthesis of PIPs at the late endosome membrane	↑	↑
R-HSA-6814848	○ Glycerophospholipid catabolism	↑	↑
R-HSA-8847453	○ Synthesis of PIPs in the nucleus	↑	↓↓
R-HSA-428157	Sphingolipids metabolism		
R-HSA-1660661	● Sphingolipid de novo biosynthesis	↑	↓
R-HSA-1660662	● Glycosphingolipid metabolism	↓↓	↓
R-HSA-8957322	Metabolism of steroids	↓	↓
R-HSA-74182	Ketone body metabolism		
R-HSA-77108	● Utilization of Ketone Bodies	↓	↓
R-HSA-77111	● Synthesis of Ketone Bodies	↓	↓
R-HSA-9018678	Biosynthesis of specialized pro-resolving mediators (SPMs)		
R-HSA-2142700	● Synthesis of Lipoxins (LX)	↓↓	↓↓
R-HSA-9018677	● Biosynthesis of DHA-derived SPMs	↓	↓↓
R-HSA-9018679	● Biosynthesis of EPA-derived SPMs	↓	↓↓

R-HSA-9018683	• Biosynthesis of DPA-derived SPMs		
R-HSA-9025106	○ Biosynthesis of DPAn-6 SPMs	↑	↑
R-HSA-9025094	○ Biosynthesis of DPAn-3 SPMs	↓↓	↓↓
R-HSA-9027604	• Biosynthesis of electrophilic ω -3 PUFA oxo-derivatives	↓↓	↓↓
R-HSA-1369062	ABC transporters in lipid homeostasis	↑	↑
R-HSA-9613354	Lipophagy	↑	↑
R-HSA-9029558	NR1H2 & NR1H3 regulate gene expression linked to lipogenesis	↑	↑
R-HSA-9031528	NR1H2 & NR1H3 regulate gene expression linked to triglyceride lipolysis in adipose	↑	↑
R-HSA-419408	Lysosphingolipid and LPA receptors	↑	↓
R-HSA-1483249	Inositol phosphate metabolism	↓	↓

For cisplatin samples, glycosphingolipid metabolism and biosynthesis of specialized pro-resolving mediators including ω -3 PUFA oxo-derivatives were significantly downregulated, which may have contributed to the accumulation of unused lipid precursors redirected to LDs. Similarly, for etoposide samples, downregulation of the synthesis of leukotrienes (LT), eoxins (EX), phosphatidylinositol phosphate (PIPs), and specialized pro-resolving mediators (SPM) including ω -3 PUFA oxo-derivatives may have contributed to the increased formation of LDs. Acyl chain remodelling of PE and PC was significantly downregulated most likely due to membrane disintegration during etoposide treatment.

The transcriptomics data of lipid metabolism did not provide clear evidence for increased *de novo* lipid synthesis, which could account for the accumulation of neutral lipids in LDs as detected by NMR and MS. Therefore, I investigated genes involved in lipid particle organization. **Figure 6.8** illustrates differentially expressed genes induced by cisplatin or etoposide. The pathway enrichment analysis showed that the expression of genes associated with lipid droplet formation (CIDEA, CIDEA, HILPDA, PLIN1, CAV1, HSD17B13) significantly increased and the increase was greater for the etoposide samples. This is in contradiction to the NMR and microscopy data, which suggested higher concentration of mobile lipids and the larger LDs in the cisplatin samples.

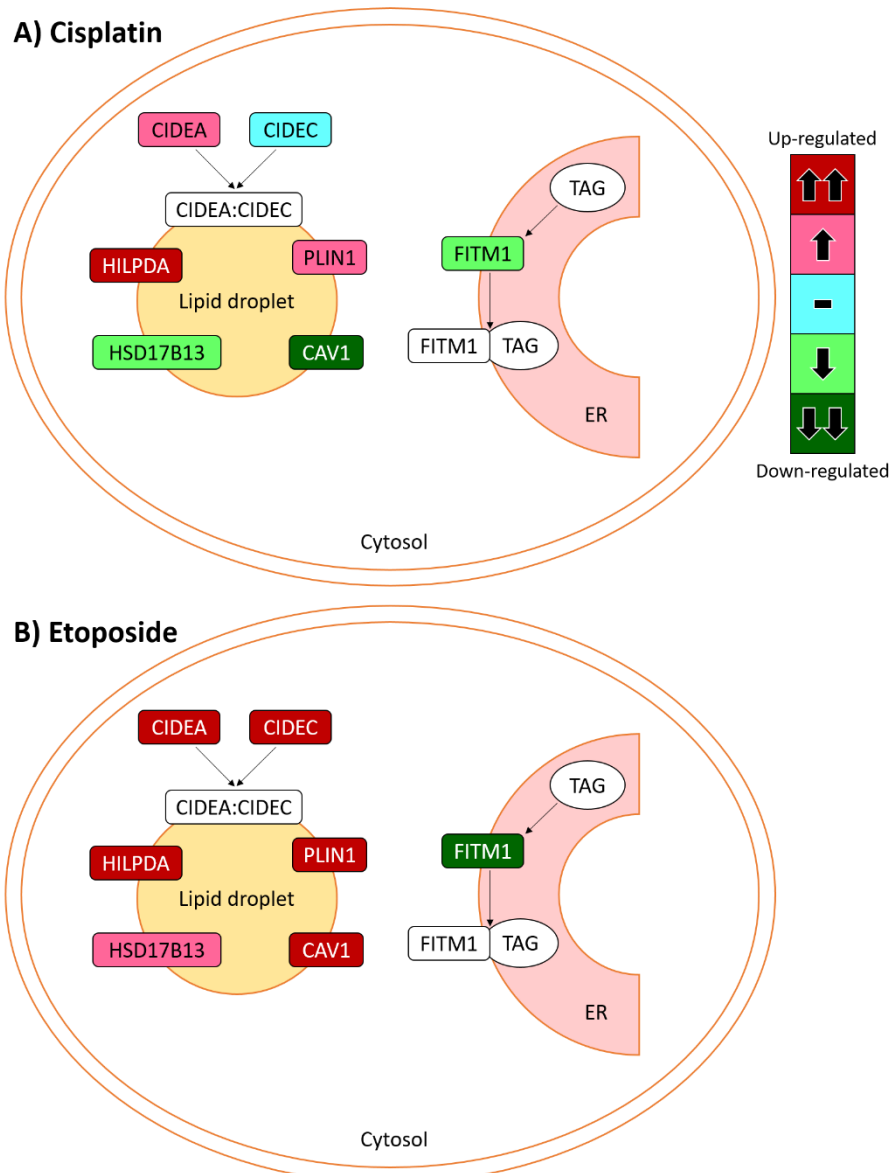


Figure 6.8. Regulation of lipid particle organization during **A) cisplatin** and **B) etoposide** treatments. Cell-death-inducing like effector A and C (**CIDEA** and **CIDEDEC**) bind to LDs and regulate their enlargement, by restricting lipolysis, favouring storage, and promoting net neutral lipid transfer from smaller to larger LDs. The fat storage-inducing transmembrane proteins 1 (**FITM1**), associated with the endoplasmic reticulum (**ER**) membrane, mediate binding and partitioning of TAGs into LDs. Hydroxysteroid 17-Beta Dehydrogenase 13 (**HSD17B13**) is an LD-associated enzyme of unknown physiological function. Hypoxia-inducible lipid droplet-associated protein (**HILPDA**) is an LD protein and stimulates intracellular lipid accumulation. Caveolin 1 (**CAV1**) affects the distribution of phospholipids and neutral lipids in mature LDs. Perilipin 1 (**PLIN1**) protects LDs from being broken down by hormone-sensitive lipase.

To investigate the alternative origin of NMR-visible lipids in cisplatin and etoposide samples, I analysed genes involved in intracellular lipid trafficking. Changes in the expression of genes related to lipid transporters are shown in **Figure 6.9** and their function is described in **Table 6.2**. The data demonstrated that the most affected transporters in cisplatin treatment are related to macrophage lipid metabolism (Abca2), lipophilic anion extrusion (Abcc10), peroxisomal lipid metabolism (Abcd1), and drug resistance (Abcf2). On the other hand, transporters related to translocation of phospholipids (Abca1, Abca4, Abcb1, Abcb4, Abcg1), lipid homeostasis (Abca6, Abca9) and peroxisomal lipid metabolism (Abcd2) increased for etoposide but not for cisplatin, as compared to the control.

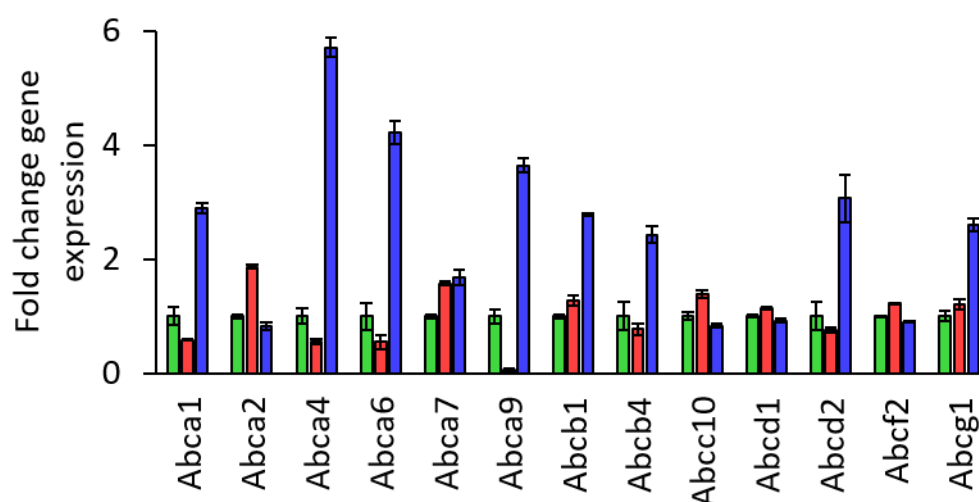


Figure 6.9. Lipid transporter expressions in C2C12 myotubes treated with cisplatin (red) or etoposide (blue). Mean fold changes in gene expressions were calculated relative to the control group (green); error bars represent SEM of four independent cell samples. All changes are statistically significant (FDR-adjusted $p < 0.05$).

Further analysis of genes involved in pathways regulating lipid storage and trafficking such as lipid droplets and peroxisomes is shown in **Figure 6.10**. These genes were selected to emphasize the differences between cisplatin and etoposide treatment. A full description of gene functions is included in **Appendix 3, Table S3.7**. The data revealed distinct characteristics in the formation and maintenance of specialized vesicles during apoptosis induced by cisplatin or etoposide. A different set of genes were regulated depending on the type of treatment. For cisplatin, the significantly upregulated genes, which were associated with LD formation, included Dgat2, Pnpla, Atg2a, and Aup1. For etoposide-induced LD the key genes included Lipe, Plin2, Cav, and Hilpda. Similarly, the expression of genes involved in peroxisomes was unique for the two treatments. Cisplatin upregulated the biogenesis of peroxisomes (Pex6,

Pex11a, Pex16, Pex11g), peroxisomal targeting (Pex5), and the import of FA (Abcd1, Tysnd1, Pex10). In contrast, etoposide upregulates genes that are involved in FA export from peroxisomes to cellular organelles (Acbd5, Crot).

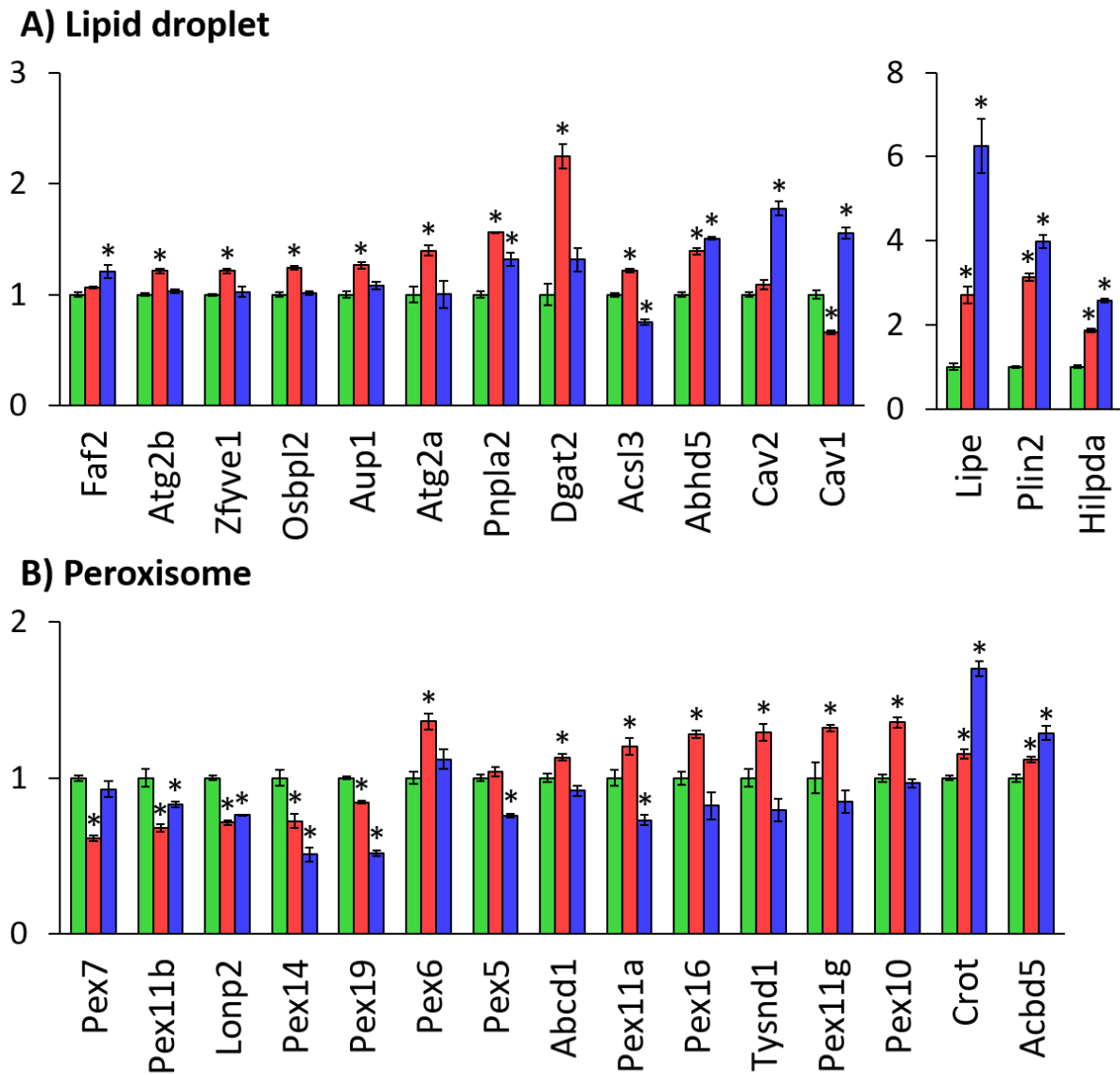


Figure 6.10. Differentially expressed genes related to **A)** lipid droplets, and **B)** peroxisomes in C2C12 myotubes treated with cisplatin (red) and etoposide (blue). Mean fold changes in gene expressions were calculated relative to the control group (green); error bars represent SEM of four independent cell samples. * indicates statistically significant changes as compared to the controls (ANOVA: FDR-adjusted P -value < 0.05 , see **Appendix 3, Table S3.7**)

Table 6.2. List of lipid transporters differentially expressed in apoptotic cells (**Figure 6.9**). Upregulated transporters after cisplatin and etoposide treatment are shown in red and blue, respectively. Cr – control, cis – cisplatin, eto – etoposide. Source: GeneCards (www.genecards.org).

Gene	Function	FDR	Fisher's tests
Abca1	Plasma membrane transporter; catalyses the translocation of specific phospholipids from the cytoplasmic to the extracellular/luminal leaflet of membrane coupled to the hydrolysis of ATP	$2.20 \cdot 10^{-6}$	cr - cis; eto - cis; eto - cr
Abca2	Plasma membrane transporter; may have a role in macrophage lipid metabolism	$1.78 \cdot 10^{-6}$	cr - cis; eto - cis; eto - cr
Abca4	Plasma membrane transporter; catalyses the translocation of specific phospholipids from the extracellular/luminal to the cytoplasmic leaflet of membrane coupled to the hydrolysis of ATP	$2.27 \cdot 10^{-8}$	cr - cis; eto - cis; eto - cr
Abca6	Plasma membrane transporter; may play a role in lipid homeostasis	$4.79 \cdot 10^{-6}$	cr - cis; eto - cis; eto - cr
Abca7	Plasma membrane transporter; catalyses the translocation of specific phospholipids from the cytoplasmic to the extracellular/luminal leaflet of membrane coupled to the hydrolysis of ATP; involved in lipid raft organization; plays a role in phagocytosis of apoptotic cells by macrophages	$1.34 \cdot 10^{-3}$	cr - cis; eto - cis; eto - cr
Abca9	Plasma membrane transporter; may play a role in lipid homeostasis	$8.04 \cdot 10^{-8}$	cr - cis; eto - cis; eto - cr
Abcb1	Plasma membrane transporter; translocates drugs and phospholipids across the membrane; energy-dependent efflux pump responsible for decreased drug accumulation in multidrug-resistant cells	$1.55 \cdot 10^{-7}$	cr - cis; eto - cis; eto - cr
Abcb4	Plasma membrane transporter; energy-dependent phospholipid efflux translocator; plays a role in the recruitment of phospholipids and sphingolipids to non-raft membranes and raft membranes	$9.14 \cdot 10^{-4}$	cr - cis; eto - cis; eto - cr
Abcc10	ATP-dependent transporter probably involved in cellular detoxification through lipophilic anion extrusion	$1.19 \cdot 10^{-3}$	cr - cis; eto - cis; eto - cr
Abcd1	Peroxisomal membrane transporter; plays a role in the transport of free very-long-chain fatty acids (VLCFAs) as well as their CoA-esters across the peroxisomal membrane; regulates VLCFAs by beta-oxidation	$4.35 \cdot 10^{-3}$	cr - cis; eto - cis; eto - cr
Abcd2	Peroxisomal membrane transporter; function unknown; may function as a dimerization partner of ABCD1 and/or other peroxisomal ABC transporters	$1.82 \cdot 10^{-3}$	eto - cis; eto - cr
Abcf2	Modulates drug resistance, including cisplatin resistance	$1.19 \cdot 10^{-6}$	cr - cis; eto - cis; eto - cr
Abcg1	Catalyses the efflux of phospholipids coupled to the hydrolysis of ATP; lipid efflux is ALB-dependent; an active component of the macrophage lipid export complex; may be involved in intracellular lipid transport processes	$1.83 \cdot 10^{-5}$	cr - cis; eto - cis; eto - cr

6.5. Discussion

6.5.1. Composition of apoptosis-induced LDs

MS-based lipidomics served to investigate changes in the composition of neutral lipid species during apoptosis. Lipidome analysis included the characterization of DAGs and TAGs in whole cell extracts, which aided the understanding of the global changes in lipid profiles during apoptosis. Additionally, the composition of isolated LDs was examined to understand the compartmentalization of lipids during apoptosis.

The analysis unravelled clear lipid phenotypes as judged by patterns seen in both whole cells and isolated LDs (**Figure 6.2**). Since about 98 mol% of total LD lipids belong to the TAG lipid class,³⁷⁰ they were the main contributors to group separation in LDs and were therefore studied in more detail. Not all TAGs, which were found in isolated LDs, were present in cell extracts. Similarly, several TAGs present in the whole cell extract were not found in LDs (**Table S3.1 and S3.2, Appendix 3**). Moreover, apoptosis-induced changes in TAGs measured in isolated LDs and whole cell extracts showed little resemblance (**Figure 6.5**). These findings confirmed the compartmentalization of lipid metabolism in LDs. Compartmentalization is also evident when studying lipid unsaturation patterns by mass spectrometry (**Figure 6.3**) and NMR spectroscopy (**Figure 4.16, Chapter 4**). Both techniques demonstrated that studying isolated LDs provided specific information about localized lipid remodelling during apoptosis.

LD formation may potentially aid in adaptation to stress responses or the re-establishment of lipid homeostasis disrupted by apoptotic treatments, such as remodelling of phospholipid membranes or lipid synthesis and catabolism. Li and colleagues demonstrated that an increased number of LDs reduced the extent of cell death during an apoptotic treatment.³⁷⁷ Listenberger and colleagues demonstrated that sequestering toxic lipids in lipid droplets serves as a means of protecting cells from lipotoxicity and subsequent apoptosis.³⁷⁸ Mammalian cells with defects in the conversion of FA to TAG and LD biogenesis were sensitive to FA-induced toxicity. However, Fei and colleagues demonstrated that the absence of LDs did not compromise cell viability under ER stress, suggesting that LDs were not essential to cell survival under ER stress.³⁸⁶

MS-based lipidomics data analysis showed that several TAGs decreased in both whole cells and isolated lipid droplets (**Figure 6.5**), suggesting that sequestration of excess lipids may not be the only reason for abnormal LD accumulation during apoptosis. In yeast, LD form as a

response to defects in phospholipid synthesis, thereby restoring lipid metabolism homeostasis.³⁸⁷ Evidence has been reported that during ER-stress, LDs can also serve as a temporary depot for proteins designated for degradation.³⁸⁸ Li and colleagues demonstrated that specific TAGs accumulated during 5-FU-induced apoptosis, and they hypothesised that TAGs had unique roles in that process.³⁸⁹ Interestingly, they observed accumulation of PUFA in whole cell extracts whereas I observed accumulation of PUFA mainly in isolated LDs and to a lesser degree in the whole cell organic extracts. Similar conclusions were made in **Chapter 4** when comparing NMR lipid profiles of intact cells (mobile lipids) and cell extracts (total lipids) using NMR spectroscopy. However, the transcriptomics analysis revealed that the conversion of SFA to MUFA and PUFA catalysed by enzymes such as FADS, SCD, and DEG, was not significantly upregulated (**Figure S3.2, Appendix 3**). This finding ruled out the possibility that desaturation of SFA contributed to increased PUFA levels during apoptotic treatments, at least in terms of regulation by transcription. Further studies are needed to measure the reaction rates catalysed by these enzymes as they might increase without apparent changes in the transcriptome.

6.5.2. Mechanism of lipid accumulation is treatment specific

To determine the underlying molecular changes induced by cisplatin and etoposide, I screened differentially expressed genes using RNA-Seq. The expression of genes involved in cell death and the cell cycle confirmed the activation of apoptotic pathways for both cisplatin and etoposide samples (**Appendix 3, Table S3.3, S3.5, and S3.6**). Cisplatin regulated mainly the p53 and necrosis factor (NF) pathways, and etoposide regulated the caspase-dependent pathways. The results were generally consistent with previously described molecular mechanisms.^{275,277} It is worth noting that downregulation of several apoptotic pathways was also observed, implying conflicting transcriptional changes. However, downregulation and upregulation of different apoptotic pathways have previously been reported in apoptotic cells.³⁹⁰ This is a common feature of pathological signalling pathways, which converge on a downstream effect from different pathways.³⁹¹

Analysis of the transcriptome associated with lipid metabolism and transport demonstrated that a large number of genes was differentially expressed (**Appendix 3, Table S3.4**). Pathway enrichment analysis (**Figure 6.1**) showed that while FA biosynthesis was not increased per se, TAG biosynthesis increased for cisplatin, potentially contributing to LD formation. In

particular, the upregulation of two enzymes, DGAT1 and DGAT2, which catalyse the final step in TAG synthesis, was likely to regulate excessive LD formation. However, the upregulation of β -oxidation in mitochondria and peroxisomes might counteract this effect. Increased β -oxidation was also supported by MS lipidomics of whole extracts (**Figure 6.3B**), showing an increase in shorter FAs but a decrease in longer FAs.

Genes encoding LD-associated proteins provided an interesting insight into lipid particle organization during apoptosis (**Figure 6.8**). These proteins regulate the morphology and size of LDs, stabilize the membrane monolayer, and protect LD content from oxidation.^{392,393} Surprisingly, transcriptomics data showed that genes associated with the formation of LD in etoposide-treated cells were significantly upregulated, which was not the case for cisplatin. This would suggest that LDs in etoposide-treated samples should be larger than in cisplatin samples, which was not the case as demonstrated by NMR diffusion and fluorescence microscopy experiments (**Chapter 5**). In line with this, I hypothesised that the mechanism of lipid accumulation was different in cisplatin and etoposide. Cisplatin may induce LD formation by upregulating genes associated with DAG \rightarrow TAG conversion inside LDs, whereas etoposide may upregulate genes, which isolate LD content from β -oxidation.

To test this, I analysed the expression of lipid membrane transporters responsible for intracellular lipid flux. ATP binding cassette (ABC) transporters are transmembrane proteins that facilitate the transport of substrates into an organelle or outside the cell.³⁹⁴ They are known to regulate intracellular lipid distribution precisely. For example, defects in ABCD1 function lead to the impaired import of VLCFA into peroxisomes and subsequently decrease β -oxidation leading to the accumulation of lipids.³⁹⁵ I examined 13 lipid transporters (**Figure 6.9, Table 6.2**), which are expressed in the plasma membrane or peroxisomes. Interestingly, the expression of lipid transporters was highly upregulated for etoposide and only small changes were observed for cisplatin. This would be consistent with a mechanism, whereby TAGs were synthesized in LDs rather than transported to LDs from the ER or other organelles. In contrast, in etoposide-treated cells, TAG biosynthesis was downregulated, hence high levels of lipid trafficking could be the main contributor to enlarged LDs. In addition, the expression of Cav1 and Cav2 increased for the etoposide samples only. These are proteins that target lipids to lipid rafts and drive caveolae formation.³⁹⁶ Therefore, it is possible that lipids were redirected from LDs to lipid rafts, which would not be detected by NMR spectroscopy and could not be distinguished by microscopy (**Figure 5.11, Chapter 5**).

6.5.3. Peroxisomes also accumulate lipids

Peroxisomes are cellular organelles that catalyse oxidation reactions, leading to the production of hydrogen peroxide.³⁹⁶ In mammalian cells, fatty acids can be oxidized in both mitochondria and peroxisomes.³⁹⁷ Very long chain fatty acids (VLCFA) enter peroxisomes via ABCD transporters, where they undergo α - and β -oxidation (**Figure 6.11**). My transcriptomics data showed that the ABCD1 transporter was upregulated for cisplatin and unchanged for etoposide. Increased ABCD1 expression and no changes or a decrease in oxidation enzymes (Hsd17b4, Ehhadh, Acaa1) may suggest the accumulation of lipid intermediates in peroxisomes during the cisplatin treatment. It has been shown that peroxisomes can enlarge in parallel with LDs when excess lipids are present in yeast.³⁹⁸ Moreover, LDs and peroxisomes can interact with each other and exchange organelle-specific enzymes.³⁹⁹ In contrast, etoposide induced the export of FA from peroxisomes, suggesting that peroxisomes were unlikely to accumulate lipids in this case.

Peroxisomes and LDs could not be differentiated in the microscopy images (**Figure 5.11, Chapter 5**) since BODIPY is a generic dye with a high affinity to neutral lipids in any cellular organelle. In addition, there is a substantial overlap in the sizes of peroxisomes (0.1 – 1 μm) and lipid droplets (0.04 – 100 μm). Similarly, NMR-based diffusion experiments will have detected any mobile lipids included in LDs, endosomes, or peroxisomes. More experiments are needed to discriminate between these two lipid-containing organelles.

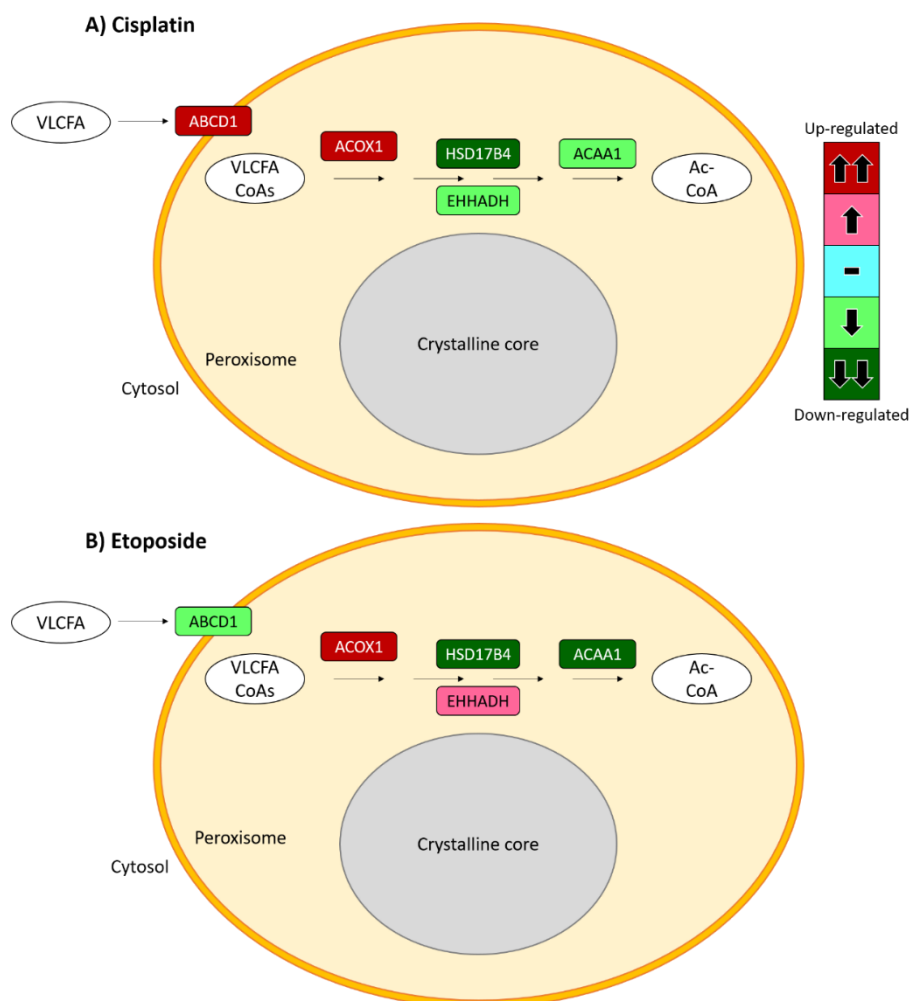


Figure 6.11. Regulation of very long chain fatty acid (VLCFA) catabolism in peroxisomes during **A)** cisplatin and **B)** etoposide treatments. Saturated and unsaturated VLCFAs enter the peroxisome as coenzyme A (CoA) esters via the ABC transporter *DI*. Four enzymes are involved in the peroxisomal β -oxidation pathways: 1) Acyl-CoA Oxidase 1 (*ACOX1*) catalyzes desaturation of acyl-CoAs; 2) bi-functional Hydroxysteroid 17-Beta Dehydrogenase 4 (*HSD17B4*) catalyzes dehydrogenation and hydration of acyl-CoAs; 3) bi-functional Enoyl-CoA Hydratase And 3-Hydroxyacyl CoA Dehydrogenase (*EHHADH*) catalyzes dehydrogenation and hydration of acyl-CoAs; 4) Acetyl-CoA Acyltransferase 1 (*ACAA1*) catalyzes the final step in the peroxisomal β -oxidation forming a fatty acid chain shortened by 2 carbons; Ac-CoA – Acetyl-CoA.

6.6. Conclusions

Chapter 6 describes the application of MS-based lipidomics and transcriptomics to probe the formation of LDs in apoptotic cells. The aim was to better understand the driving forces behind LD formation and their potential functions.

Both lipidomics and transcriptomics approaches were able to discriminate not only between control and apoptotic cells but also between the two apoptotic treatments. Compositional changes in TAGs were different in isolated LDs and whole cell lipid extracts, which is consistent with the compartmentalization of lipid metabolism. In addition, global and localised profiles of PUFA containing TAGs were consistent across MS and NMR techniques. These findings demonstrated the importance of studying localized changes in cellular organelles.

My analysis of genes related to lipid particle organization and trafficking gave an insight into the treatment-dependent mechanism of LD formation. It was proposed that cisplatin-induced LDs form because of increased TAG synthesis inside LDs, whereas etoposide-induced LDs are likely to form because of increased lipid trafficking and the preservation of LD content. It was also proposed that peroxisomes could accumulate excess lipids in cisplatin samples, potentially contributing to mobile lipid resonances in NMR spectra.

Increased β -oxidation was demonstrated both by the unsaturation patterns of TAGs in whole cell extracts and the transcriptomics of FA metabolism. In the future, it would be interesting to study localized TAG profiles of isolated mitochondria and peroxisomes. Specific fluorescence tagging of organelles would help discriminate between peroxisomes and LD by microscopy. This could aid a better understanding of the lipid metabolism in cisplatin- and etoposide-treated cells.

This chapter demonstrated that a combined lipidomics and transcriptomics approach provided a better mechanistic insight into apoptosis-induced LDs, and validated the NMR data reported in **Chapters 4 and 5**.

Chapter 7. Conclusions and future perspective

Monitoring apoptosis progression is an important strategy in evaluating cancer treatments. Whereas many analytical techniques exist that allow for the identification and quantitation of apoptotic cells *in vitro*, non-invasive *in vivo* agents for monitoring apoptosis could have significant clinical benefits. Apoptosis is a complex process involving many pathways, which may be upregulated or downregulated depending on an apoptotic trigger and its mechanism of action. Often more than one pathway is activated during apoptosis. Biochemical assays focus on signalling pathways that are affected by apoptotic agents, and usually target one or two proteins involved in these pathways. Consequently, the most effective assays for unambiguous identification of apoptosis measure final downstream effects such as DNA fragmentation. However, these assays do not give specific information about which or how many apoptotic pathways have been activated. Biochemical assays that measure specific upstream effects provide more details about the mechanism of apoptosis, but the negative results cannot exclude the absence of apoptosis. Thus, upstream assays often are used in conjunction with other assays to confirm apoptosis. This was demonstrated in **Chapter 4** when low-dose etoposide treatment did not induce apoptosis as measured by a caspase-3 activity assay, but clearly did induce apoptosis as measured by cell death. Furthermore, HRMAS ¹H NMR-based metabolic profiles of etoposide-treated cells were different from those of control cells and followed the pattern of cisplatin-treated cells, which showed increased caspase-3 activity. The findings suggests that NMR-based metabolomics on intact cells may be more sensitive to subtle changes during programmed cell death.

A good apoptotic assay is characterised by high specificity. This can be achieved, for example, by measuring all known apoptotic pathways at once. RNA-Seq is one of the approaches that could fulfil this requirement. In fact, the transcriptomics analysis in **Chapter 6** show that several apoptotic pathways were induced by cisplatin and etoposide. It also demonstrated that the apoptotic mechanisms were treatment dependent, which often cannot be established with a

simple biochemical assay. Even though transcriptomics is an information-rich approach, it has its limitations. For example, the abundance of mRNA encoding an enzyme may not be a reliable indicator of enzyme activity if this is regulated by other non-transcriptional factors. In contrast, metabolites are the end products of biochemical processes and hence are direct measures of underlying biochemical activities and the metabolic states of cells or organisms. It seems that metabolomics could be a suitable candidate for an all-in-one apoptotic assay. In this thesis I demonstrated an application of HRMAS ^1H NMR spectroscopy to differentiating between mechanisms of apoptosis (cisplatin vs etoposide), and necrosis in intact cells.

This work and previously published literature have identified a number of metabolites as potential NMR-detectable biomarkers of apoptosis. The changes in many of these metabolites depend on cell lines and apoptotic treatments, which makes it difficult to establish a universal biomarker of apoptosis. Moreover, HRMAS ^1H NMR data on intact cells is relatively less common as compared to solution-state ^1H NMR spectroscopy or MS. The need for specialised equipment (a HRMAS NMR probe) with niche applications and limited sensitivity may be a bottleneck in generating this sort of data. At present, published studies describe metabolic changes induced by different treatments, doses, incubation times and in various cell lines, which cannot be compared with each other systematically. A practical application of HRMAS ^1H NMR spectroscopy to study the effects of drugs in intact cells will depend on standardised database curating of HRMAS NMR-based metabolic changes so that different labs can compare their results. Machine learning algorithms embedded in the database would be an excellent resource for comparison and prediction of different apoptotic pathways in intact cells at the metabolomic level. Given that HRMAS NMR spectroscopy can monitor metabolism in living cells, it could complement solution-state NMR and MS metabolomics data.

HRMAS ^1H NMR spectroscopy, when compared to MS lags behind in terms of the smaller number of metabolites which can be detected, and greater amounts of biological material needed for the analysis. However, it provides other information that cannot be derived from MS data. For example, I demonstrated that we can monitor compartmentalisation of lipids during apoptosis (**Figure 4.16, Chapter 4**) or transitions of metabolites between different cellular environments (e.g., the membrane damage/disintegration described in **Chapter 4**), which are overlooked by solution-state NMR and MS on cell extracts. After HRMAS NMR analysis, intact cells were recovered and used for another biochemical experiment (the viability assay as shown in **Chapter 3**). This approach allows a direct correlation of NMR and non-NMR experiments performed on the same sample. In addition, HRMAS NMR samples can be

recovered for further rounds of growth in cell culture (**Chapter 3**), presenting the possibility of longitudinal studies. The practical application of this concept is yet to be demonstrated.

The ability to conduct short studies on living cells is an important advantage of HRMAS ^1H NMR spectroscopy. As demonstrated in **Chapter 3**, these studies need to be carefully designed and will depend on cell fragility, but they have the potential of following live metabolic changes in intact cells. A snapshot of such an application, developed during my PhD, is presented in **BOX 7.1**. In the future, it would be interesting to measure if metabolic reaction rates are correlated with pharmaceutical outcomes and therefore could predict drug efficacy.

BOX 7.1. Metabolic reaction rates in intact cells by HRMAS ^1H NMR spectroscopy.

Background: Curcumin is an active ingredient of turmeric with known therapeutic benefits such as anti-inflammatory, antioxidant and anticancer activities. Curcumin is poorly soluble in water, which hinders its bioavailability. Currently, the majority of *in vitro* studies use DMSO as a vehicle for delivering curcumin into cells but PEG300 has also been used.

Objective: To test if HRMAS ^1H NMR spectroscopy can discriminate between different solvents delivering the same curcumin treatment in intact cells.

Methods: C2C12 cells were cultured as described in Chapter 2. Curcumin treatment (final concentration: 50 μM or 200 μM) was delivered with DMSO or PEG300 to intact cells inside a MAS rotor as shown in **Figure 7.1**. Ten mM final concentrations of uniformly labelled ^{13}C -glucose were added to each cell sample. Glucose consumption and lactate accumulation were monitored by HRMAS ^1H NMR spectroscopy (CPMG, Chapter 2). Eleven spectra were recorded consecutively, one after another: total experiment time ~ 4 h. The spectra were normalised to total integral. MNOVA was used for relative quantification of glucose and lactate.

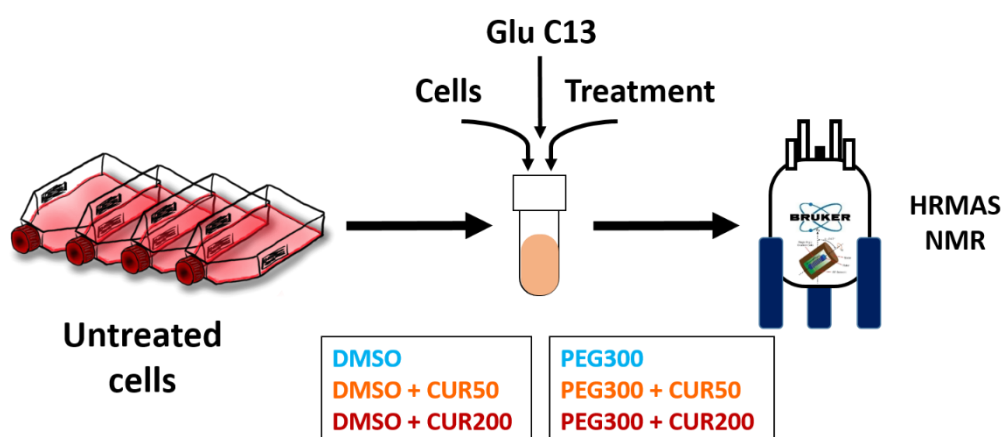


Figure 7.1. Schematic representation of monitoring metabolic reaction rates in intact cells by HRMAS ^1H NMR spectroscopy.

BOX 7.1. continued

Results: Curcumin increased glucose accumulation rate by $50 \pm 13\%$ or $52 \pm 13\%$ for DMSO and no significant change for PEG (**Figure 7.2A**). Curcumin increased lactate accumulation rate by $82 \pm 9\%$ or $61 \pm 14\%$ for DMSO and only $35 \pm 9\%$ for PEG (**Figure 7.2B**).

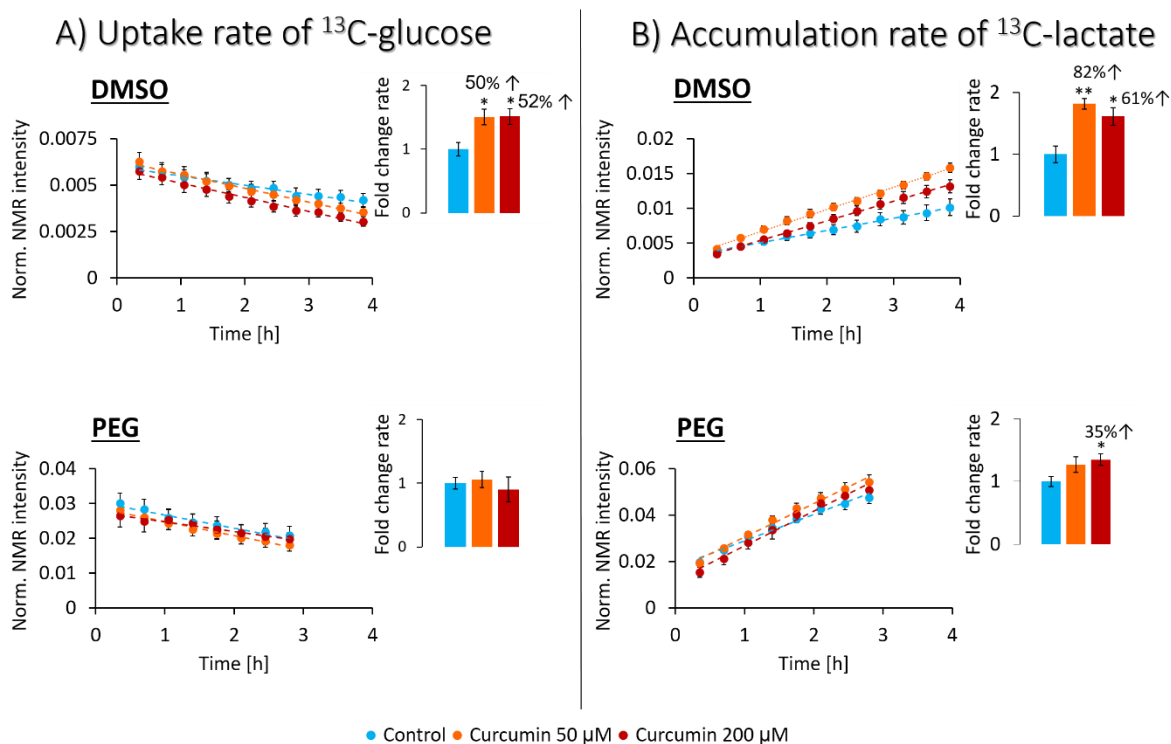


Figure 7.2. ^{13}C glucose consumption (A) and ^{13}C lactate accumulation (B) rates in intact cells treated with curcumin 50 μM (orange) and 200 μM (red) in DMSO or PEG as measured by HRMAS ^1H NMR spectroscopy. Student *t*-test: * $p < 0.05$, ** $p < 0.01$, $n = 3$. The fold change in reaction rates were calculated from the slope of the curve of the normalised NMR intensity versus time, relative to the control (blue).

Conclusion: Cellular response on the same treatment depends on the delivery vehicle. This may have potential applications in monitoring drug uptake *in vitro* by HRMAS ^1H NMR spectroscopy. Future experiments could involve comparing different pharmaceutical agents and measuring the accumulation rates of other metabolites such as lipids, myo-inositol, choline, acetate and creatine.

NMR-visible lipids have previously been demonstrated as a reliable biomarker of apoptosis. In **Chapter 5**, I described NMR-based diffusion measurements of mobile lipids as a means to discriminate between control, apoptotic and necrotic cells. This novel methodology for following apoptosis based on structural changes in intact cells treated with a pharmaceutical compound could be applied to NMR-based cellular assay for monitoring the effectiveness of drug treatments *in vitro* and as an aid in early stages drug discovery. The current method could be improved by shortening the DOSY pulse sequence to minimise MAS spinning effects on

the viability of intact cells. The implementation of a micro-HRMAS NMR probe would reduce the cell volume needed for a single experiment and also moderate the effect of centrifugal force, limiting the extent of damage to cells. In addition, adjusting NMR diffusion times and gradient strengths could facilitate the capture of signals from slower-moving species (lipid rafts as discussed in **Chapter 5**), or faster moving molecules (glucose, lactate, choline-compound and *myo*-inositol) to probe the cellular environments of non-lipid metabolites.

It is interesting that at the transcriptional level etoposide has the biggest effect on the formation of LDs but when analysing NMR or microscopy data it is cisplatin that forms bigger LDs. RNA-Seq revealed other potential origins of mobile lipid resonances in cisplatin treated cells, with a number of pathways associated with peroxisomes shown to be altered. At present little is known regarding the mobility of lipids inside peroxisomes. To the best of my knowledge, HRMAS NMR-visible lipid resonances have not previously been associated with peroxisomes and it is unknown how rigid the peroxisomal environment is (apart from its crystalline core). The morphology of peroxisomes resembles that of LDs rather than mitochondria (an organelle which also facilitates lipid β -oxidation). Peroxisomes are also known to move across the cytoskeleton from the ER to the cellular peripheries in a similar manner to LDs suggesting that their mobility could potentially be detected by HRMAS ^1H NMR spectroscopy. Considering the crucial role of peroxisomes in lipid metabolism it would be worthwhile testing if they contribute to NMR-visible lipid resonances. This could be done by fluorescence tagging of LDs and peroxisomes and observing their formation and mutual interactions during cisplatin and etoposide treatments by microscopy.

In conclusion, this PhD thesis describes the first investigation into the application of HRMAS ^1H NMR-based diffusion for following cisplatin and etoposide treatment and it might pave the way towards the monitoring of many other compounds in intact cells. It demonstrates that implementing HRMAS ^1H NMR spectroscopy could be a valuable addition to the drug discovery process.

References

1. Hasin Y, Seldin M, Lusi A. Multi-omics approaches to disease. *Genome Biol.* 2017;18(1):1-15. doi:10.1186/s13059-017-1215-1
2. Ryan D, Robards K. Metabolomics: The greatest omics of them all? *Anal Chem.* 2006;78(23):7954-7958. doi:10.1021/ac0614341

3. Weckwerth W. Metabolomics in Systems Biology. *Annu Rev Plant Biol.* 2003;54:669-689. doi:10.1146/annurev.arplant.54.031902.135014
4. Kell DB. Metabolomics and systems biology: Making sense of the soup. *Curr Opin Microbiol.* 2004;7(3):296-307. doi:10.1016/j.mib.2004.04.012
5. Oliver S, Böttcher C, Neumann S, et al. Systematic functional analysis of the yeast genome. *Trends Biotechnol.* 1998;16(9):373-378. doi:10.1016/S0167-7799(98)01214-1
6. Fiehn O. Combining genomics, metabolome analysis, and biochemical modelling to understand metabolic networks. *Comp Funct Genomics.* 2001;2(3):155-168. doi:10.1002/cfg.82
7. Nicholson, J. K ; Lindon, J. C ; Holmes E. “Metabonomics”: understanding the metabolic responses of living systems to pathophysiological stimuli via multivariate statistical analysis of biological NMR spectroscopic data. *Xenobiotica.* 1999;29(11):1181-1189.
8. Wishart DS, Feunang YD, Marcu A, et al. HMDB 4.0: The human metabolome database for 2018. *Nucleic Acids Res.* 2018;46(D1):D608-D617. doi:10.1093/nar/gkx1089
9. Griffith CM, Williams PB, Tinoco LW, Dinges MM, Wang Y, Larive CK. 1H NMR Metabolic Profiling of Earthworm (*Eisenia fetida*) Coelomic Fluid, Coelomocytes, and Tissue: Identification of a New Metabolite - Malylglutamate. *J Proteome Res.* 2017;16(9):3407-3418. doi:10.1021/acs.jproteome.7b00439
10. Safer S, Cicek SS, Pieri V, et al. Metabolic fingerprinting of *Leontopodium* species (Asteraceae) by means of 1H NMR and HPLC-ESI-MS. *Phytochemistry.* 2011;72(11-12):1379-1389. doi:10.1016/j.phytochem.2011.04.006
11. Pope GA, MacKenzie DA, Defernez M, et al. Metabolic footprinting as a tool for discriminating between brewing yeasts. *Yeast.* 2007;24:667-679. doi:10.1002/yea
12. Chen Y, Xu J, Zhang R, Abliz Z. Methods used to increase the comprehensive coverage of urinary and plasma metabolomes by MS. *Bioanalysis.* 2016;8(9):981-997. doi:10.4155/bio-2015-0010
13. Lindon JC, Nicholson JK, Holmes E, eds. *The Handbook of Metabonomics and Metabolomics.* First edit. Amsterdam: Elsevier; 2007.
14. Robertson DG, Lindon JC, Nicholson JK, Holmes E, eds. *Metabonomics in Toxicity Assessment.* First edit. Boca Raton: Taylor & Francis; 2005.
15. Metz TO, ed. *Metabolic Profiling. Methods and Protocols.* First edit. New York: Humana Press; 2011.
16. Bowen BP, Northen TR. Dealing with the unknown: metabolomics and metabolite atlases. *J Am Soc Mass Spectrom.* 2010;21(9):1471-1476. doi:10.1016/j.jasms.2010.04.003
17. Allwood JW, Winder CL, Dunn WB, Goodacre R. *Methodologies for Metabolomics.* (Wevers NWLJVSRA, ed.). New York: Cambridge University Press; 2012. doi:10.1017/CBO9780511996634

18. Griffin JL, Shockcor JP. Metabolic profiles of cancer cells. *Nat Rev Cancer*. 2004;4:551-561. doi:10.1038/nrc1390
19. Alonso A, Marsal S, Juliá A. Analytical Methods in Untargeted Metabolomics: State of the Art in 2015. *Front Bioeng Biotechnol*. 2015;3(March):1-20. doi:10.3389/fbioe.2015.00023
20. Dunn WB, Broadhurst DI, Atherton HJ, Goodacre R, Griffin JL. Systems level studies of mammalian metabolomes : the roles of mass spectrometry and nuclear magnetic resonance spectroscopy. *Chem Soc Rev*. 2011;40:387-426. doi:10.1039/b906712b
21. Bingol K, Brüschweiler R. Two elephants in the room: new hybrid nuclear magnetic resonance and mass spectrometry approaches for metabolomics. *Curr Opin Clin Nutr Metab Care*. 2015;18(5):471-477. doi:10.1097/MCO.0000000000000206
22. Chan ECY, Koh PK, Mal M, et al. Metabolic profiling of human colorectal cancer using high-resolution magic angle spinning nuclear magnetic resonance (HR-MAS NMR) spectroscopy and gas chromatography mass spectrometry (GC/MS). *J Proteome Res*. 2009;8(1):352-361. doi:10.1021/pr8006232
23. Schultz BH. A new method of measuring intensities of magnetization. *Physica*. 1939;6(2):137-144. doi:10.1016/S0031-8914(39)80004-0
24. Gerlach W, Stern O. Der experimentelle Nachweis der Richtungsquantelung im Magnetfeld. *Zeitschrift für Phys*. 1922;9(1):349-352. doi:10.1007/BF01326983
25. Sartoris FJ, Bock C, Pörtner HO. Temperature-dependent pH regulation in eurythermal and stenothermal marine fish: An interspecies comparison using ³¹P-NMR. *J Therm Biol*. 2003;28(5):363-371. doi:10.1016/S0306-4565(03)00012-3
26. Probert F, Rice P, Scudamore CL, et al. ¹H NMR metabolic profiling of plasma reveals additional phenotypes in knockout mouse models. *J Proteome Res*. 2015;14(5):2036-2045. doi:10.1021/pr501039k
27. Everett JR, Jennings KR, WG, MJ. B. Spin-echo ¹H NMR spectroscopy: a new method for studying penicillin metabolism. *J Chem Soc Chem Commun*. 1984;(894):894-895.
28. Kikuchi J, Tsuboi Y, Komatsu K, Gomi M, Chikayama E, Date Y. SpinCouple: Development of a Web Tool for Analyzing Metabolite Mixtures via Two-Dimensional J-Resolved NMR Database. *Anal Chem*. 2016;88(1):659-665. doi:10.1021/acs.analchem.5b02311
29. Bell JD, Brown JC, Sadler PJ. NMR studies of body fluids. *NMR Biomed*. 1989;2(5-6):246-256.
30. Adosraku RK, Choi GTY, Constantinou-kokotos V, Anderson MM, Gibbons WA. NMR lipid profiles of cells , tissues , and body fluids : proton NMR analysis of human erythrocyte lipids. 1994;35:1925-1931.
31. Reily MD, Niemitz M, Schilling B, et al. NMR-based metabolomics of mammalian cell and tissue cultures. *J Biomol NMR*. 2011;49(3-4):195-206. doi:10.1007/s10858-011-9490-8

32. Freedberg DI, Selenko P. Live cell NMR. *Annu Rev Biophys.* 2014;43:171-192. doi:10.1146/annurev-biophys-051013-023136
33. Stattin P, Riklund K, Bergh A, Stenlund H, Stenman K, Gröbner G. ¹H HRMAS NMR Derived Biomarkers Related to Tumor Grade, Tumor Cell Fraction, and Cell Proliferation in Prostate Tissue Samples. *Biomark Insights.* 2011;6:BMI.S6794. doi:10.4137/bmi.s6794
34. Kim, H. K.; Choi, Y. H.; Verpoorte R. NMR-based metabolomic analysis of plants. *Nat Protoc.* 2010;5(MARCH 2010):536-549. doi:10.1038/nprot.2009.237
35. Valentini M, Ritota M, Cafiero C, Cozzolino S, Leita L, Sequi P. The HRMAS-NMR tool in foodstuff characterisation. *Magn Reson Chem.* 2011;49(SUPPL. 1). doi:10.1002/mrc.2826
36. Schwalbe H. Editorial: New 1.2 GHz NMR Spectrometers— New Horizons? *Angew Chemie - Int Ed.* 2017;56(35):10252-10253. doi:10.1002/anie.201705936
37. Lee JH, Okuno Y, Cavagnero S. Sensitivity enhancement in solution NMR: Emerging ideas and new frontiers. *J Magn Reson.* 2014;241(1):18-31. doi:10.1016/j.jmr.2014.01.005
38. Webb A. Increasing the sensitivity of magnetic resonance spectroscopy and imaging. *Anal Chem.* 2012;84(1):9-16. doi:10.1021/ac201500v
39. Wishart DS. NMR metabolomics: A look ahead. *J Magn Reson.* 2019;306:155-161. doi:10.1016/j.jmr.2019.07.013
40. Larive CK, Barding GA, Dinges MM. NMR spectroscopy for metabolomics and metabolic profiling. *Anal Chem.* 2015;87(1):133-146. doi:10.1021/ac504075g
41. Emwas AH, Roy R, McKay RT, et al. Nmr spectroscopy for metabolomics research. *Metabolites.* 2019;9(7). doi:10.3390/metabo9070123
42. Nagana Gowda GA, Djukovic D. Overview of Mass Spectrometry-Based Metabolomics: Opportunities and Challenges. *Methods Mol Biol.* 2014;1198:3-12. doi:10.1007/978-1-4939-1258-2
43. Ren JL, Zhang AH, Kong L, Wang XJ. Advances in mass spectrometry-based metabolomics for investigation of metabolites. *RSC Adv.* 2018;8(40):22335-22350. doi:10.1039/c8ra01574k
44. Tayyari F, Gowda GAN, Gu H, Raftery D. ¹⁵N-Cholamine - A smart isotope tag for combining NMR- and MS-based metabolite profiling. *Anal Chem.* 2013;85(18):8715-8721. doi:10.1021/ac401712a
45. Esmaeili M, Bathen TF, Engebråten O, Mælandsmo GM, Gribbestad IS, Moestue SA. Quantitative ³¹P HR-MAS MR spectroscopy for detection of response to PI3K/mTOR inhibition in breast cancer xenografts. *Magn Reson Med.* 2014;71(6):1973-1981. doi:10.1002/mrm.24869
46. Wilson ID, Nicholson JK, Ghauri FYK, Blackledge CA. Use of high-field nuclear magnetic resonance spectroscopy for the analysis of biological fluids. *Anal Proc.* 1991;28(7):217-223. doi:10.1039/AP9912800217

47. Johnson CH, Gonzalez FJ. Challenges and opportunities of metabolomics. *J Cell Physiol.* 2012;227(8):2975-2981. doi:10.1002/jcp.24002
48. Duarte IF, Marques J, Ladeiras AF, et al. Analytical approaches toward successful human cell metabolome studies by NMR spectroscopy. *Anal Chem.* 2009;81(12):5023-5032. doi:10.1021/ac900545q
49. Emwas AHM, Salek RM, Griffin JL, Merzaban J. NMR-based metabolomics in human disease diagnosis: Applications, limitations, and recommendations. *Metabolomics.* 2013;9(5):1048-1072. doi:10.1007/s11306-013-0524-y
50. Powers R. The current state of drug discovery and a potential role for NMR metabolomics. *J Med Chem.* 2014;57(14):5860-5870. doi:10.1021/jm401803b
51. Boisseau R, Charrier B, Massou S, Portais JC, Akoka S, Giraudeau P. Fast spatially encoded 3D NMR strategies for ¹³C-based metabolic flux analysis. *Anal Chem.* 2013;85(20):9751-9757. doi:10.1021/ac402155w
52. Wang C, He L, Li D-W, Bruschweiler-Li L, Marshall AG, Brüschweiler R. Accurate Identification of Unknown and Known Metabolic Mixture Components by Combining 3D NMR with Fourier Transform Ion Cyclotron Resonance Tandem Mass Spectrometry. *J Proteome Res.* 2017;16(10):3774–3786. doi:10.1021/acs.jproteome.7b00457
53. Bharti SK, Roy R. Metabolite identification in NMR-based metabolomics. *Curr Metabolomics.* 2014;2:163-173. doi:10.2174/2213235X02666140924211244
54. Dona AC, Kyriakides M, Scott F, et al. A guide to the identification of metabolites in NMR-based metabonomics / metabolomics experiments. *Comput Struct Biotechnol J.* 2016;14:135-153. doi:10.1016/j.csbj.2016.02.005
55. Trefi S, Gilard V, Balaýssac S, Malet-Martino M, Martino R. The usefulness of 2D DOSY and 3D DOSY-COSY ¹H NMR for mixture analysis: Application to genuine and fake formulations of sildenafil (Viagra). *Magn Reson Chem.* 2009;47. doi:10.1002/mrc.2490
56. Liu J, Litt L, Segal MR, Kelly MJS, Pelton JG, Kim M. Metabolomics of oxidative stress in recent studies of Endogenous and exogenously administered intermediate metabolites. *Int J Mol Sci.* 2011;12(10):6469-6501. doi:10.3390/ijms12106469
57. Lindon JC, Holmes E, Nicholson JK. Metabonomics techniques and applications to pharmaceutical research & development. *Pharm Res.* 2006;23(6):1075-1088. doi:10.1007/s11095-006-0025-z
58. Dona AC, Jimenez B, Schafer H, et al. Precision High-Throughput Proton NMR Spectroscopy of Human Urine, Serum, and Plasma for Large-Scale Metabolic Phenotyping. *Anal Chem.* 2014;86(19):9887-9894. doi:DOI 10.1021/ac5025039
59. Coen M, Holmes E, Lindon JC, Nicholson JK. NMR-based metabolic profiling and metabonomic approaches to problems in molecular toxicology. *Chem Res Toxicol.* 2008;21(1):9-27.

doi:10.1021/tx700335d

60. Spratlin JL, Serkova NJ, Eckhardt SG. Clinical applications of metabolomics in oncology: A review. *Clin Cancer Res.* 2009;15(2):431-440. doi:10.1158/1078-0432.CCR-08-1059
61. Hu JM, Sun HT. Serum proton NMR metabolomics analysis of human lung cancer following microwave ablation. *Radiat Oncol.* 2018;13(1):1-10. doi:10.1186/s13014-018-0982-5
62. Peyraud R, Kiefer P, Christen P, Massou S, Portais J-C, Vorholt J a. Demonstration of the ethylmalonyl-CoA pathway by using ¹³C metabolomics. *Proc Natl Acad Sci U S A.* 2009;106(12):4846-4851. doi:10.1073/pnas.0810932106
63. Fonville JM, Maheir AD, Coen M, Holmes E, Lindon JC, Nicholson JK. Evaluation of full-resolution J-resolved ¹H NMR projections of biofluids for metabolomics information retrieval and biomarker identification. *Anal Chem.* 2010;82(5):1811-1821. doi:10.1021/ac902443k
64. Griffin JL, Williams HJ, Sang E, Nicholson JK. Abnormal lipid profile of dystrophic cardiac tissue as demonstrated by one- and two-dimensional magic-angle spinning ¹H NMR spectroscopy. *Magn Reson Med.* 2001;46(2):249-255. doi:10.1002/mrm.1185
65. Bingol K, Brusweiler-li L. Customized Metabolomics Database for the Analysis of NMR ¹H – ¹H TOCSY and ¹³C – ¹H HSQC-TOCSY Spectra of Complex Mixtures. 2014. doi:10.1021/ac500979g
66. Öman T, Tessem M, Bathen TF, et al. Identification of metabolites from 2D ¹H- ¹³C HSQC NMR using peak correlation plots. 2014:1-8. doi:10.1186/s12859-014-0413-z
67. Nicholson JK, Foxall PJD, Spraul M, Farrant RD, Lindon JC. 750 MHz ¹H and ¹H-¹³C NMR Spectroscopy of Human Blood Plasma. *Anal Chem.* 1995;67(5):793-811. doi:10.1021/ac00101a004
68. Dumas ME, Canlet C, Andf F, Vercauteren J, Paris A. Metabonomic assessment of physiological disruptions using ¹H-¹³C HMBC-NMR spectroscopy combined with pattern recognition procedures performed on filtered variables. *Anal Chem.* 2002;74(10):2261-2273. doi:10.1021/ac0156870
69. Tang H, Wang Y, Nicholson JK, Lindon JC. Use of relaxation-edited one-dimensional and two dimensional nuclear magnetic resonance spectroscopy to improve detection of small metabolites in blood plasma. 2004;325:260-272. doi:10.1016/j.ab.2003.10.033
70. Griffin JL, Pole JCM, Nicholson JK, Carmichael PL. Cellular environment of metabolites and a metabonomic study of tamoxifen in endometrial cells using gradient high resolution magic angle spinning ¹H NMR spectroscopy. *Biochim Biophys Acta - Gen Subj.* 2003;1619(2):151-158. doi:10.1016/S0304-4165(02)00475-0
71. Lowe IJ. Free induction decays of rotating solids. *Phys Rev Lett.* 1959;2(7):285-287. doi:10.1103/PhysRevLett.2.285
72. Andrew E, Bradbury A, Eades R. Removal of Dipolar Broadening of Nuclear Magnetic Resonance Spectra of Solids by Specimen Rotation. *Nature.* 1959;183:1802-1803.

73. Forbes J, Husted C, Oldfield E. High-Field, High-Resolution Proton “Magic-Angle” Sample-Spinning Nuclear Magnetic Resonance Spectroscopic Studies of Gel and Liquid Crystalline Lipid Bilayers and the Effects of Cholesterol. *J Am Chem Soc.* 1988;110(4):1059-1065. doi:10.1021/ja00212a010
74. Pielak GJ, Tian F. Membrane proteins, magic-angle spinning, and in-cell NMR. *Proc Natl Acad Sci.* 2012;109(13):4715-4716. doi:10.1073/pnas.1201502109
75. Garrod S, Humpfer E, Spraul M, et al. High-resolution magic angle spinning 1H NMR spectroscopic studies on intact rat renal cortex and medulla. *Magn Reson Med.* 1999;41(6):1108-1118. doi:10.1002/(SICI)1522-2594(199906)41:6<1108::AID-MRM6>3.0.CO;2-M
76. Cheng LL, Ma MJ, Becerra L, et al. Quantitative neuropathology by high resolution magic angle spinning proton magnetic resonance spectroscopy. *Proc Natl Acad Sci U S A.* 1997;94(12):6408-6413. doi:10.1073/pnas.94.12.6408
77. Lindon JC, Beckonert OP, Holmes E, Nicholson JK. High-resolution magic angle spinning NMR spectroscopy: Application to biomedical studies. *Prog Nucl Magn Reson Spectrosc.* 2009;55(2):79-100. doi:10.1016/j.pnmrs.2008.11.004
78. Beckonert O, Coen M, Keun HC, et al. High-resolution magic-angle-spinning NMR spectroscopy for metabolic profiling of intact tissues. *Nat Protoc.* 2010;5(6):1019-1032. doi:10.1038/nprot.2010.45
79. Jenkins JE, Holland GP, Yarger JL. High resolution magic angle spinning NMR investigation of silk protein structure within major ampullate glands of orb weaving spiders. *Soft Matter.* 2012;8(6):1947-1954. doi:10.1039/c2sm06462f
80. Griffin JL, Bollard M, Nicholson JK, Bhakoo K. Spectral profiles of cultured neuronal and glial cells derived from HRMAS 1H NMR spectroscopy. *NMR Biomed.* 2002;15(6):375-384. doi:10.1002/nbm.792
81. Huster D, Kuhn K, Kadereit D, Waldmann H, Arnold K. H high-resolution magic angle spinning NMR spectroscopy for the investigation of a ras lipopeptide in a lipid membrane. *Angew Chemie - Int Ed.* 2001;40(6):1056-1058. doi:10.1002/1521-3773(20010316)40:6<1056::AID-ANIE10560>3.0.CO;2-7
82. Bollard ME, Murray AJ, Clarke K, Nicholson JK, Griffin JL. A study of metabolic compartmentation in the rat heart and cardiac mitochondria using high-resolution magic angle spinning H NMR spectroscopy. *FEBS Lett.* 2003;553:73-78. doi:10.1016/S0014-5793(03)00969-4
83. Goldenberg JM, Pagel MD. Assessments of tumor metabolism with CEST MRI. *NMR Biomed.* 2019;32(10):1-12. doi:10.1002/nbm.3943
84. Kishimoto S, Oshima N, Krishna MC, Gillies RJ. Direct and indirect assessment of cancer metabolism explored by MRI. *NMR Biomed.* 2019;32(10):1-16. doi:10.1002/nbm.3966
85. Leach MO. Magnetic resonance spectroscopy (MRS) in the investigation of cancer at the Royal Marsden Hospital and the Institute of Cancer Research. *Phys Med Biol.* 2006;51(13). doi:10.1088/0031-9155/51/13/R05

86. Protoview P, Vol B, Ringgold B. Magnetic Resonance Imaging of the Brain and Spine , 5th Edition (online access included). 2016;3:1-2.
87. Davis JT, Kwatra N, Schooler GR. Pediatric whole-body MRI: A review of current imaging techniques and clinical applications. *J Magn Reson Imaging*. 2016;44(4):783-793. doi:10.1002/jmri.25259
88. Zöllner FG, Konstandin S, Lommen J, et al. Quantitative sodium MRI of kidney. *NMR Biomed*. 2016;29(2):197-205. doi:10.1002/nbm.3274
89. Tang C, Brown MA, Semelka RC. MRI: Basic Principles and Applications. *Radiat Res*. 1996;145(2):243. doi:10.2307/3579182
90. Serkova NJ, Van Rheen Z, Tobias M, Pitzer JE, Wilkinson JE, Stringer KA. Utility of magnetic resonance imaging and nuclear magnetic resonance-based metabolomics for quantification of inflammatory lung injury. *Am J Physiol - Lung Cell Mol Physiol*. 2008;295(1):152-161. doi:10.1152/ajplung.00515.2007
91. Lilimatainen T, Hakumäki JM, Kauppinen RA, Ala-Korpela M. Monitoring of gliomas in vivo by diffusion MRI and 1H MRS during gene therapy-induced apoptosis: Interrelationships between water diffusion and mobile lipids. *NMR Biomed*. 2009;22(3):272-279. doi:10.1002/nbm.1320
92. Huuse EM, Jensen Line R, Goa Pål E, et al. Monitoring the Effect of Docetaxel Treatment in MCF7 Xenografts Using Multimodal In Vivo and Ex Vivo Magnetic Resonance Methods, Histopathology, and Gene Expression. *Transl Oncol*. 2010;3(4):252-263. doi:10.1593/tlo.09322
93. Canese R, Palombelli G, Chirico M, et al. Integration of MRI and MRS approaches to monitor molecular imaging and metabolomic effects of trabectedin on a preclinical ovarian cancer model. *NMR Biomed*. 2019;32(10):1-11. doi:10.1002/nbm.4016
94. Chung YL, Madhu B, Griffiths JR. Metabolism and metabolomics by MRS. *eMagRes*. 2015;4(3):689-698. doi:10.1002/9780470034590.emrstm1461
95. An YJ, Cho HR, Kim TM, et al. An NMR metabolomics approach for the diagnosis of leptomeningeal carcinomatosis in lung adenocarcinoma cancer patients. *Int J Cancer*. 2015;136(1):162-171. doi:10.1002/ijc.28949
96. Griffin JL, Kauppinen RA. Tumour metabolomics in animal models of human cancer. *J Proteome Res*. 2007;6:498-505. doi:10.1021/pr060464h
97. Ahmed N, Bezabeh T, Ijare OB, et al. Metabolic signatures of lung cancer in sputum and exhaled breath condensate detected by 1H magnetic resonance spectroscopy: a feasibility study. *Magn Reson Insights*. 2016;9:29-35. doi:10.4137/MRIS40864
98. Glunde K, Bhujwalla ZM, Ronen SM. Choline metabolism in malignant transformation. *Nat Rev Cancer*. 2011;(November). doi:10.1038/nrc3162
99. Holmes HE, Powell NM, Ma D, et al. Comparison of In Vivo and Ex Vivo MRI for the Detection of

- Structural Abnormalities in a Mouse Model of Tauopathy. 2017;11(March):1-15.
doi:10.3389/fninf.2017.00020
100. Lehtimäki KK, Valonen PK, Griffin JL, et al. Metabolite Changes in BT4C Rat Gliomas Undergoing Ganciclovir-Thymidine Kinase Gene Therapy-induced Programmed Cell Death as Studied by ¹H NMR Spectroscopy in Vivo, ex Vivo, and in Vitro. *J Biol Chem*. 2003;278(46):45915-45923.
doi:10.1074/jbc.M306209200
 101. Hall Z, Chu Y, Griffin JL. Liquid Extraction Surface Analysis Mass Spectrometry Method for Identifying the Presence and Severity of Nonalcoholic Fatty Liver Disease. *Anal Chem*. 2017;89(9):5161-5170. doi:10.1021/acs.analchem.7b01097
 102. Abdel AM, Pawling J, Ryczko M, Caudy AA, Dennis JW. Targeted metabolomics in cultured cells and tissues by mass spectrometry: method development and validation. *Anal Chim Acta*. 2014;845:53-61.
doi:10.1016/j.aca.2014.06.012
 103. Khamis MM, Adamko DJ, El-aneed A. Mass spectrometric based approaches in urine metabolomics and biomarker discovery. *Mass Spectrom Rev*. 2017;36:115-134. doi:10.1002/mas
 104. Dunn WB, Broadhurst D, Begley P, Zelena E, Francis-mcintyre S, Anderson N. Procedures for large-scale metabolic profiling of serum and plasma using gas chromatography and liquid chromatography coupled to mass spectrometry. *Nat Protoc*. 2011;6(7):1060-1083. doi:10.1038/nprot.2011.335
 105. Stanley EG, Jenkins BJ, Walker CG, et al. Lipidomics profiling of human adipose tissue identifies a pattern of lipids associated with fish oil supplementation. *J Proteome Res*. 2017;16:3168-3179.
doi:10.1021/acs.jproteome.7b00161
 106. Ibanez C, Simo C, Palazoglu M, Cifuentes A. GC-MS based metabolomics of colon cancer cells using different extraction solvents. *Anal Chim Acta*. 2017;986:48-56. doi:10.1016/j.aca.2017.07.019
 107. Ghulam Musharraf S, Mazhar S, Jabbar Siddiqui A, Iqbal Choudhary M, Atta-ur-Rahman. Metabolite profiling of human plasma by different extraction methods through gas chromatography mass spectrometry — An objective comparison. *Anal Chim Acta*. 2013;804:180-189.
doi:10.1016/j.aca.2013.10.025
 108. El Rammouz R, Létisse F, Durand S, Portais J, Wadih Moussa Z, Fernandez X. Analysis of skeletal muscle metabolome: evaluation of extraction methods for targeted metabolite quantification using liquid chromatography tandem mass spectrometry. *Anal Biochem*. 2010;398(2):169-177.
doi:10.1016/j.ab.2009.12.006
 109. Gong Z, Hu J, Wu X, Xu Y. The recent developments in sample preparation for mass spectrometry-based metabolomics. *Crit Rev Anal Chem*. 2017;47(4):325-331. doi:10.1080/10408347.2017.1289836
 110. Bhattacharya SK. *Lipidomics*. 1st ed. New York: Humana Press; 2017. doi:10.1007/978-1-4939-6996-8
 111. Gori SS, Lorkiewicz P, Ehringer DS, et al. Profiling thiol metabolites and quantification of cellular glutathione using FT-ICR-MS spectrometry. *Anal Bioanal Chem*. 2014;406:4371-4379.

doi:10.1007/s00216-014-7810-z

112. Ulrich S. Solid-phase microextraction in biomedical analysis. *J Chromatogr A*. 2000;902:167-194.
113. Tsikas D. Affinity chromatography as a method for sample preparation in gas chromatography/mass spectrometry. *J Biochem Biophys Methods*. 2001;49:705-731.
114. Lockwood GB. Techniques for gas chromatography of volatile terpenoids from a range of matrices. *J Chromatogr A*. 2001;936:23-31.
115. Pirman DA, Efuet E, Ding XP, et al. Changes in Cancer Cell Metabolism Revealed by Direct Sample Analysis with MALDI Mass Spectrometry. *PLoS One*. 2013;8(4):19-21.
doi:10.1371/journal.pone.0061379
116. Fletcher JS, Kotze HL, Armitage EG, Lockyer NP, Vickerman JC. Evaluating the challenges associated with time-of-flight secondary ion mass spectrometry for metabolomics using pure and mixed metabolites. *Metabolomics*. 2013;9(3):535-544. doi:10.1007/s11306-012-0487-4
117. Lei Z, Huhman D V., Sumner LW. Mass spectrometry strategies in metabolomics. *J Biol Chem*. 2011;286(29):25435-25442. doi:10.1074/jbc.R111.238691
118. Lee DY, Bowen BP, Northen TR. Mass spectrometry-based metabolomics, analysis of metabolite-protein interactions, and imaging. *Biotechniques*. 2010;49(2):557-565. doi:10.2144/000113451
119. Kamleh MA, Dow JAT, Watson DG. Applications of mass spectrometry in metabolomic studies of animal model and invertebrate systems. *Briefings Funct Genomics Proteomics*. 2009;8(1):28-48.
doi:10.1093/bfpg/eln052
120. Dettmer K, Aronov PA, Hammock BD. Mass spectrometry-based metabolomics. *Mass Spectrom Rev*. 2007;26(1):51-78. doi:10.1038/jid.2014.371
121. Aichele F, Li J, Hoene M, Lehmann R, Xu G, Kohlbacher O. Retention Time Prediction Improves Identification in Nontargeted Lipidomics Approaches. *Anal Chem*. 2015;87(15):7698-7704.
doi:10.1021/acs.analchem.5b01139
122. Aretz I, Meierhofer D. Advantages and pitfalls of mass spectrometry based metabolome profiling in systems biology. *Int J Mol Sci*. 2016;17(5). doi:10.3390/ijms17050632
123. Ghaste M, Mistrik R, Shulaev V. Applications of fourier transform ion cyclotron resonance (FT-ICR) and orbitrap based high resolution mass spectrometry in metabolomics and lipidomics. *Int J Mol Sci*. 2016;17(6):816-838. doi:10.3390/ijms17060816
124. Rochat B. Recent Advances in Analytical Chemistry. In: Ince M, Ince OK, eds. *IntechOpen*. I. IntechOpen; 2018:13. doi:10.5772/intechopen.81285
125. Benito S, Sánchez A, Unceta N, et al. LC-QTOF-MS-based targeted metabolomics of arginine-creatine metabolic pathway-related compounds in plasma: Application to identify potential biomarkers in pediatric chronic kidney disease. *Anal Bioanal Chem*. 2016;408(3):747-760. doi:10.1007/s00216-015-

126. Magnusson M, Lewis GD, Ericson U, et al. A diabetes-predictive amino acid score and future cardiovascular disease. *Eur Heart J*. 2013;34(26):1982-1989. doi:10.1093/eurheartj/ehs424
127. Murgia A, Hinz C, Liggi S, et al. Italian cohort of patients affected by inflammatory bowel disease is characterised by variation in glycerophospholipid, free fatty acids and amino acid levels. *Metabolomics*. 2018;14(10):1-14. doi:10.1007/s11306-018-1439-4
128. Witting M, Lucio M, Tziotis D, et al. DI-ICR-FT-MS-based high-throughput deep metabolotyping: a case study of the *Caenorhabditis elegans*-*Pseudomonas aeruginosa* infection model. *Anal Bioanal Chem*. 2015;407(4):1059-1073. doi:10.1007/s00216-014-8331-5
129. de Falco B, Lanzotti V. NMR spectroscopy and mass spectrometry in metabolomics analysis of *Salvia*. *Phytochem Rev*. 2018;17(5):951-972. doi:10.1007/s11101-018-9550-8
130. Marshall DD, Powers R. Beyond the paradigm: Combining mass spectrometry and nuclear magnetic resonance for metabolomics. *Prog Nucl Magn Reson Spectrosc*. 2017;100:1-16. doi:10.1016/j.pnmrs.2017.01.001
131. Dias DA, Jones OAH, Beale DJ, et al. Current and future perspectives on the structural identification of small molecules in biological systems. *Metabolites*. 2016;6(4). doi:10.3390/metabo6040046
132. Pan Z, Raftery D. Comparing and combining NMR spectroscopy and mass spectrometry in metabolomics. *Anal Bioanal Chem*. 2007;387(2):525-527. doi:10.1007/s00216-006-0687-8
133. Shockcor JP, Unger SE, Wilson ID, Foxall PJD, Nicholson JK, Lindon JC. Combined HPLC, NMR Spectroscopy, Mass Spectrometry with Application to the Detection and Characterization of Xenobiotic and Endogenous Metabolites in Human Urine. *Anal Chem*. 1996;68(24):4431-4435.
134. Chen H, Pan Z, Talaty N, Raftery D, Cooks GR. Combining desorption electrospray ionization mass spectrometry and nuclear magnetic resonance for differential metabolomics without sample preparation. *Rapid Commun Mass Spectrom*. 2006;20:1577-1584. doi:10.1002/rcm.2474
135. Lanza IR, Zhang S, Ward LE, Karakelides H, Raftery D, Sreekumaran Nair K. Quantitative metabolomics by ¹H-NMR and LC-MS/MS confirms altered metabolic pathways in diabetes. *PLoS One*. 2010;5(5):e10538. doi:10.1371/journal.pone.0010538
136. Bingol K, Brüscheweiler R. NMR/MS translator for the enhanced simultaneous analysis of metabolomics mixtures by NMR spectroscopy and mass spectrometry: Application to human urine. *J Proteome Res*. 2015;14(6):2642-2648. doi:10.1021/acs.jproteome.5b00184
137. Hao J, Liebeke M, Sommer U, Viant MR, Bundy JG, Ebbels TMD. Statistical Correlations between NMR Spectroscopy and Direct Infusion FT-ICR Mass Spectrometry Aid Annotation of Unknowns in Metabolomics. *Anal Chem*. 2016;88(5):2583-2589. doi:10.1021/acs.analchem.5b02889
138. Saccenti E, Hoefsloot HCJ, Smilde AK, Westerhuis JA, Hendriks MMWB. Reflections on univariate

- and multivariate analysis of metabolomics data. *Metabolomics*. 2014;10(3):361-374.
doi:10.1007/s11306-013-0598-6
139. Cambiaghi A, Ferrario M, Masseroli M. Analysis of metabolomic data: Tools, current strategies and future challenges for omics data integration. *Brief Bioinform*. 2017;18(3):498-510.
doi:10.1093/bib/bbw031
140. Puchades-carrasco L, Palomino-scha M, Pineda-lucena A. Bioinformatics tools for the analysis of NMR metabolomics studies focused on the identification of clinically relevant biomarkers. *Brief Bioinform*. 2016;17(3):541-552. doi:10.1093/bib/bbv077
141. Worley B, Powers R. Multivariate analysis in metabolomics. *Curr Metabolomics*. 2013;1(1):92-107.
doi:10.2174/2213235X11301010092
142. Goodpaster AM, Romick-Rosendale LE, Kennedy MA. Statistical significance analysis of nuclear magnetic resonance-based metabolomics data. *Anal Biochem*. 2010;401(1):134-143.
doi:10.1016/j.ab.2010.02.005
143. Sud M, Fahy E, Cotter D, et al. Metabolomics Workbench: An international repository for metabolomics data and metadata, metabolite standards, protocols, tutorials and training, and analysis tools. *Nucleic Acids Res*. 2016;44(D1):D463-D470. doi:10.1093/nar/gkv1042
144. Wittig U, De Beuckelaer a. Analysis and comparison of metabolic pathway databases. *Brief Bioinform*. 2001;2(2):126-142. doi:10.1093/bib/2.2.126
145. Ellinger JJ, Chylla R a, Ulrich EL, Markley JL. Databases and Software for NMR-Based Metabolomics. *Curr Metabolomics*. 2013;1(1):1-22. doi:10.2174/2213235X11301010028.Databases
146. Misra BB. New tools and resources in metabolomics: 2016–2017. *Electrophoresis*. 2018;39(7):909-923.
doi:10.1002/elps.201700441
147. Gil de la Fuente A, Grace Armitage E, Otero A, Barbas C, Godzien J. Differentiating signals to make biological sense – A guide through databases for MS-based non-targeted metabolomics. *Electrophoresis*. 2017;38(18):2242-2256. doi:10.1002/elps.201700070
148. Elmore S. Apoptosis: A Review of Programmed Cell Death. *Toxicol Pathol*. 2007;35(4):495-516.
doi:10.1080/01926230701320337
149. Bejarano I, Rodríguez AB, Pariente JA. Apoptosis is a demanding selective tool during the development of fetal male germ cells. *Front Cell Dev Biol*. 2018;6(JUN):1-7. doi:10.3389/fcell.2018.00065
150. Sarvothaman S, Undi RB, Pasupuleti SR, Gutti U, Gutti RK. Apoptosis: Role in myeloid cell development. *Blood Res*. 2015;50(2):73-79. doi:10.5045/br.2015.50.2.73
151. Rai NK, Tripathi K, Sharma D, Shukla VK. Apoptosis: A basic physiologic process in wound healing. *Int J Low Extrem Wounds*. 2005;4(3):138-144. doi:10.1177/1534734605280018
152. Greenhalgh DG. The role of apoptosis in wound healing. *Int J Biochem Cell Biol*. 1998;30(9):1019-

1030. doi:10.1016/S1357-2725(98)00058-2
153. Häcker G. Apoptosis in infection. *Microbes Infect.* 2018;20(9-10):552-559. doi:10.1016/j.micinf.2017.10.006
154. Brunner T, Mueller C. Apoptosis in disease: About shortage and excess. *Essays Biochem.* 2003;39:119-130. doi:10.1042/bse0390119
155. Roshal M, Zhu Y, Planelles V. Apoptosis in AIDS. *Apoptosis.* 2001;6(1-2):103-116. doi:10.1023/A:1009636530839
156. Beutler B. Autoimmunity and apoptosis: The Crohn's connection. *Immunity.* 2001;15(1):5-14. doi:10.1016/S1074-7613(01)00176-5
157. Lowe SW, Lin a W. Apoptosis in cancer. *Carcinogenesis.* 2000;21(3):485-495. doi:10.1093/carcin/21.3.485
158. Fouad YA, Aanei C. Revisiting the hallmarks of cancer. *Am J Cancer Res.* 2017;7(5):1016-1036.
159. Kaleigh F, Kurokawa M. Evading apoptosis in cancer. *Trends Cell Biol.* 2013;23(12):620-633. doi:10.1038/jid.2014.371
160. Schmitt CA, Lowe SW. Apoptosis and therapy. *J Pathol.* 1999;187:127-137.
161. Baig S, Seevasant I, Mohamad J, Mukheem A, Huri HZ, Kamarul T. Potential of apoptotic pathway-targeted cancer therapeutic research: where do we stand? *Cell Death Dis.* 2016;7:1-11. doi:10.1038/cddis.2015.275
162. Kornienko A, Rastogi SK, Lefranc F, Kiss R. Therapeutic agents triggering nonapoptotic cancer cell death. *J Med Chem.* 2013;56:4823-4839. doi:10.1021/jm400136m
163. Hassan M, Watari H, Abualmaaty A, Ohba Y, Sakuragi N. Apoptosis and molecular targeting therapy in cancer. *Biomed Res Int.* 2014;2014:1-23. doi:10.1155/2014/150845
164. Letai A. Apoptosis and cancer. *Annu Rev Cancer Biol.* 2017;1:275-294. doi:10.1146/annurev-cancerbio-050216-121933
165. Bruin EC De, Medema JP. Apoptosis and non-apoptotic deaths in cancer development and treatment response. *Cancer Treat Rev.* 2008;34:737-749. doi:10.1016/j.ctrv.2008.07.001
166. Bailey C, Giles A, Czarnota GJ, Stanisz GJ. Detection of apoptotic cell death in vitro in the presence of Gd-DTPA-BMA. *Magn Reson Med.* 2009;62(1):46-55. doi:10.1002/mrm.21972
167. Baskar R, Dai J, Wenlong N, Yeo R, Yeoh KW. Biological response of cancer cells to radiation treatment. *Front Mol Biosci.* 2014;1(NOV):1-9. doi:10.3389/fmolb.2014.00024
168. Duprez L, Wirawan E, Berghe T Vanden, Vandenabeele P. Major cell death pathways at a glance. *Microbes Infect.* 2009;11(13):1050-1062. doi:10.1016/j.micinf.2009.08.013

169. Galluzzi L, Vitale I, Abrams JM, et al. Molecular definitions of cell death subroutines: Recommendations of the Nomenclature Committee on Cell Death 2012. *Cell Death Differ.* 2012;19(1):107-120. doi:10.1038/cdd.2011.96
170. Fiers W, Beyaert R, Declercq W, Vandenabeele P. More than one way to die: apoptosis, necrosis and reactive oxygen damage. *Oncogene.* 1999;18:7719-7730.
171. Fulda S, Debatin KM. Extrinsic versus intrinsic apoptosis pathways in anticancer chemotherapy. *Oncogene.* 2006;25(34):4798-4811. doi:10.1038/sj.onc.1209608
172. Lopez J, Tait SWG. Mitochondrial apoptosis: Killing cancer using the enemy within. *Br J Cancer.* 2015;112(6):957-962. doi:10.1038/bjc.2015.85
173. Hoves S, Trapani JA, Voskoboinik I. The battlefield of perforin/granzyme cell death pathways. *J Leukoc Biol.* 2010;87(2):237-243. doi:10.1189/jlb.0909608
174. Saito Y, Nishio K, Ogawa Y, et al. Turning point in apoptosis/necrosis induced by hydrogen peroxide. *Free Radic Res.* 2006;40(6):619-630.
175. Yin XM, Dong Z. Chapter 27. Necrosis: Molecular Mechanisms and Physiological Roles. In: *Essentials of Apoptosis: A Guide for Basic and Clinical Research*; . ; 2009:599-633. doi:10.1007/978-1-60327-381-7
176. Golstein P, Kroemer G. Cell death by necrosis: towards a molecular definition. *Trends Biochem Sci.* 2007;32(1):37-43. doi:10.1016/j.tibs.2006.11.001
177. Tonnus W, Meyer C, Paliege A, et al. The pathological features of regulated necrosis. *J Pathol.* 2019;247(5):697-707. doi:10.1002/path.5248
178. Clarke PGH. Apoptosis Versus Necrosis. In: Koliatsos VE, Ratan RR, eds. *Cell Death and Diseases of the Nervous System.* Totowa, NJ: Humana Press; 1999:3-28. doi:10.1007/978-1-4612-1602-5_1
179. Tsujimoto Y. Apoptosis and necrosis: Intracellular ATP level as a determinant for cell death modes. *Cell Death Differ.* 1997;4(6):429-434. doi:10.1038/sj.cdd.4400262
180. Silva MT. Secondary necrosis: The natural outcome of the complete apoptotic program. *FEBS Lett.* 2010;584(22):4491-4499. doi:10.1016/j.febslet.2010.10.046
181. Bank HL. Assessment of islet cell viability using fluorescent dyes. *Diabetologia.* 1987;30(10):812-816. doi:10.1007/BF00275748
182. Krysko D V, Vanden T, Herde KD, Vandenabeele P. Apoptosis and necrosis : Detection , discrimination and phagocytosis. *Methods.* 2008;44:205-221. doi:10.1016/j.ymeth.2007.12.001
183. Méry B, Guy JB, Vallard A, et al. In Vitro Cell Death Determination for Drug Discovery: A Landscape Review of Real Issues. *J Cell Death.* 2017;10:1-8. doi:10.1177/1179670717691251
184. Kepp O, Galluzzi L, Lipinski M, Yuan J, Kroemer G. Cell death assays for drug discovery. *Nat Rev*

- Drug Discov.* 2011;10(3):221-237. doi:10.1038/nrd3373
185. Dong H, Shen W, Cheung MTW, et al. Rapid detection of apoptosis in mammalian cells by using intact cell MALDI mass spectrometry. *Analyst.* 2011;136(24):5181-5189. doi:10.1039/c1an15750g
186. Halama A, Riesen N, Möller G, Hrabě de Angelis M, Adamski J. Identification of biomarkers for apoptosis in cancer cell lines using metabolomics: Tools for individualized medicine. *J Intern Med.* 2013;274(5):425-439. doi:10.1111/joim.12117
187. Halama A, Möller G, Adamski J. Metabolic signatures in apoptotic human cancer cell lines. *Omi A J Integr Biol.* 2011;15(5):325-335. doi:10.1089/omi.2010.0121
188. Pradelli LA, Villa E, Zunino B, Marchetti S, Ricci JE. Glucose metabolism is inhibited by caspases upon the induction of apoptosis. *Cell Death Dis.* 2014;5(9):e1406-7. doi:10.1038/cddis.2014.371
189. Lu S, Lu R, Song H, et al. Metabolomic study of natrin-induced apoptosis in SMMC-7721 hepatocellular carcinoma cells by ultra-performance liquid chromatography-quadrupole/time-of-flight mass spectrometry. *Int J Biol Macromol.* 2019;124:1264-1273. doi:10.1016/j.ijbiomac.2018.11.060
190. Lutz NW. From metabolic to metabolomic NMR spectroscopy of apoptotic cells. *Metabolomics.* 2005;1(3):251-268. doi:10.1007/s11306-005-0005-z
191. Lutz NW. Contributions of metabol(om)ic NMR spectroscopy to the investigation of apoptosis. *Comptes Rendus Chim.* 2006;9(3-4):445-451. doi:10.1016/j.crci.2005.06.017
192. Zietkowski D, Payne GS, Nagy E, Mobberley MA, Ryder TA, Desouza NM. Comparison of NMR lipid profiles in mitotic arrest and apoptosis as indicators of paclitaxel resistance in cervical cell lines. *Magn Reson Med.* 2012;68(2):369-377. doi:10.1002/mrm.23265
193. Shih C, Ko W, Yang L. Detection of Apoptosis and Necrosis in Normal Human Lung Cells Using ¹H NMR. *Ann NY Acad Sci 1042.* 2005;1042:488-496. doi:10.1196/annals.1338.042
194. Rainaldi G, Romano R, Indovina P, et al. Metabolomics using ¹H NMR of apoptosis and necrosis in HL60 leukemia cells: differences between the two types of cell death and independence from the stimulus of apoptosis used. *Radiat Res.* 2008;169(2):170-180. doi:10.1667/RR0958.1
195. Bezabeh T, Mowat MR, Jarolim L, Greenberg a H, Smith IC. Detection of drug-induced apoptosis and necrosis in human cervical carcinoma cells using ¹H NMR spectroscopy. *Cell Death Differ.* 2001;8(3):219-224. doi:10.1038/sj.cdd.4400802
196. Vermathen M, Paul LEH, Diserens G, Vermathen P, Furrer J. ¹H HR-MAS NMR based metabolic profiling of cells in response to treatment with a hexacationic ruthenium metallaprism as potential anticancer drug. *PLoS One.* 2015;10(5). doi:10.1371/journal.pone.0128478
197. Tiziani S, Lodi A, Khanim FL, Viant MR, Bunce CM, Günther UL. Metabolomic profiling of drug responses in acute myeloid leukemia cell lines. *PLoS One.* 2009;4(1):1-10. doi:10.1371/journal.pone.0004251

198. D'Alessandro G, Quaglio D, Monaco L, et al. ¹H-NMR metabolomics reveals the Glabrescione B exacerbation of glycolytic metabolism beside the cell growth inhibitory effect in glioma. *Cell Commun Signal*. 2019;17(1):1-12. doi:10.1186/s12964-019-0421-8
199. Al-Saffar NMS, Titley JC, Robertson D, et al. Apoptosis is associated with triacylglycerol accumulation in Jurkat T-cells. *Br J Cancer*. 2002;86(6):963-970. doi:10.1038/sj.bjc.6600188
200. Di Vito M, Lenti L, Knijn A, et al. ¹H NMR-visible mobile lipid domains correlate with cytoplasmic lipid bodies in apoptotic T-lymphoblastoid cells. *Biochim Biophys Acta - Mol Cell Biol Lipids*. 2001;1530(1):47-66. doi:10.1016/S1388-1981(00)00165-7
201. Delikatny EJ, Chawla S, Leung DJ, Poptani H. MR-visible lipids and the tumor microenvironment. *NMR Biomed*. 2011;24(6):592-611. doi:10.1002/nbm.1661
202. Brisdelli F, Iorio E, Knijn A, et al. Two-step formation of ¹H NMR visible mobile lipids during apoptosis of paclitaxel-treated K562 cells. *Biochem Pharmacol*. 2003;65(8):1271-1280. doi:10.1016/S0006-2952(03)00080-7
203. T. Musacchio; M. Toniutti; R. Kautz; and V.P. Torchilin. ¹H NMR detection of mobile lipids as a marker for apoptosis: the case of anti-cancer drug-loaded liposomes and polymeric micelles. *Mol Pharm*. 2009;6(6):1876–1882. doi:10.1158/0008-5472.CAN-10-4002.BONE
204. Pan X, Wilson M, McConville C, et al. Increased unsaturation of lipids in cytoplasmic lipid droplets in DAOY cancer cells in response to cisplatin treatment. *Metabolomics*. 2013;9(3):722-729. doi:10.1007/s11306-012-0483-8
205. Milkevitch M, Shim H, Pilatus U, et al. Increases in NMR-visible lipid and glycerophosphocholine during phenylbutyrate-induced apoptosis in human prostate cancer cells. *Biochim Biophys Acta - Mol Cell Biol Lipids*. 2005;1734(1):1-12. doi:10.1016/j.bbalip.2005.01.008
206. Boren J, Brindle KM. Apoptosis-induced mitochondrial dysfunction causes cytoplasmic lipid droplet formation. *Cell Death Differ*. 2012;19(9):1561-1570. doi:10.1038/cdd.2012.34
207. Griffin JL, Lehtimaki KK, Valoneu PK, et al. Assignment of ¹H Nuclear Magnetic Resonance Visible Polyunsaturated Fatty Acids in BT4C Gliomas Undergoing Ganciclovir-Thymidine Kinase Gene Therapy-induced Programmed Cell Death. *Cancer Res*. 2003;63(20):3195-3201.
208. Iorio E, Di Vito M, Spadaro F, et al. Triacsin C inhibits the formation of ¹H NMR-visible mobile lipids and lipid bodies in HuT 78 apoptotic cells. *Biochim Biophys Acta - Mol Cell Biol Lipids*. 2003;1634(1-2):1-14. doi:10.1016/j.bbalip.2003.07.001
209. Lyng H, Sitter B, Bathen TF, et al. Metabolic mapping by use of high-resolution magic angle spinning ¹H MR spectroscopy for assessment of apoptosis in cervical carcinomas. *BMC Cancer*. 2007;7:1-12. doi:10.1186/1471-2407-7-11
210. Cooper WA, Bartier WA, Rideout DC, Delikatny EJ. ¹H NMR visible lipids are induced by phosphonium salts and 5-fluorouracil in human breast cancer cells. *Magn Reson Med*. 2001;45(6):1001-

1010. doi:10.1002/mrm.1133
211. Schmitz JE, Kettunen MI, Hu DE, Brindle KM. ¹H MRS-visible lipids accumulate during apoptosis of lymphoma cells in vitro and in vivo. *Magn Reson Med*. 2005;54(1):43-50. doi:10.1002/mrm.20529
212. Griffin JL, Blenkiron C, Valonen PK, Caldas C, Kauppinen RA. High-resolution magic angle spinning ¹H NMR spectroscopy and reverse transcription-PCR analysis of apoptosis in a rat glioma. *Anal Chem*. 2006;78(5):1546-1552. doi:10.1021/ac051418o
213. Pike LJ. Lipid rafts: Bringing order to chaos. *J Lipid Res*. 2003;44(4):655-667. doi:10.1194/jlr.R200021-JLR200
214. Simons K, Sampaio JL. Membrane Organization and Lipid Rafts. *Cold Spring Harb Perspect Biol*. 2011;(3):1-17. doi:10.1101/cshperspect.a004697
215. Rajendran L, Simons K. Lipid rafts and membrane dynamics. *J Cell Sci*. 2005;118(6):1099-1102. doi:10.1242/jcs.01681
216. Cary LA, Cooper JA. Molecular switches in lipid rafts. *Nature*. 2000;404(6781):945-947. doi:10.1038/35010257
217. McIntosh TJ. *Lipid Rafts*. Torowa, New Jersey: Humana Press; 2007.
218. Gaede HC, Gawrisch K. Lateral diffusion rates of lipid, water, and a hydrophobic drug in a multilamellar liposome. *Biophys J*. 2003;85(3):1734-1740. doi:10.1016/S0006-3495(03)74603-7
219. Filippov A, Orädd G, Lindblom G. Lipid Lateral Diffusion in Ordered and Disordered Phases in Raft Mixtures. *Biophys J*. 2004;86(2):891-896. doi:10.1016/S0006-3495(04)74164-8
220. Ferretti A, Knijn A, Raggi C, Sargiacomo M. High-resolution proton NMR measures mobile lipids associated with Triton-resistant membrane domains in haematopoietic K562 cells lacking or expressing caveolin-1. *Eur Biophys J*. 2003;32(2):83-95. doi:10.1007/s00249-002-0273-8
221. Ceñido JF, Itin B, Stark RE, et al. Characterization of lipid rafts in human platelets using nuclear magnetic resonance: A pilot study. *Biochem Biophys Reports*. 2017;10(March):132-136. doi:10.1016/j.bbrep.2017.03.005
222. Wang CW. Lipid droplets, lipophagy, and beyond. *Biochim Biophys Acta - Mol Cell Biol Lipids*. 2016;1861(8):793-805. doi:10.1016/j.bbalip.2015.12.010
223. Onal G, Kutlu O, Gozuacik D, Dokmeci Emre S. Lipid droplets in health and disease. *Lipids Health Dis*. 2017;16(1):1-15. doi:10.1186/s12944-017-0521-7
224. Gross DA, Silver DL. Cytosolic lipid droplets: From mechanisms of fat storage to disease. *Crit Rev Biochem Mol Biol*. 2014;49(4):304-326. doi:10.3109/10409238.2014.931337
225. Hashemi HF, Goodman JM. The life cycle of lipid droplets. *Curr Opin Cell Biol*. 2015;33:119-124. doi:10.1016/j.ceb.2015.02.002

226. Remy C, Fouilhã N, Barba I, et al. Evidence that mobile lipids detected in rat brain glioma by ¹H nuclear magnetic resonance correspond to lipid droplets. *Cancer Res.* 1997;57:407-4014.
227. Decorps M, Lahrech H, Zoula S, Farion R, Remy C. In vivo measurement of the size of lipid droplets in an intracerebral glioma in the rat. *Magn Reson Med.* 2002;45(3):409-414. doi:10.1002/1522-2594(200103)45:3<409::aid-mrm1053>3.0.co;2-o
228. Zietkowski D, DeSouza MN, Davidson RL, Payne GS. Characterisation of mobile lipid resonances in tissue biopsies from patients with cervical cancer and correlation with cytoplasmic lipid droplets. *NMR Biomed.* 2013;26:1096-1102. doi:10.1002/nbm.2923
229. Hakumäki JM, Kauppinen RA. ¹H NMR visible lipids in the life and death of cells. *Trends Biochem Sci.* 2000;25(8):357-362. doi:10.1016/S0968-0004(00)01614-5
230. Pan X, Wilson M, McConville C, Arvanitis TN, Kauppinen RA, Peet AC. The size of cytoplasmic lipid droplets varies between tumour cell lines of the nervous system: a ¹H NMR spectroscopy study. *Magn Reson Mater Physics, Biol Med.* 2012;25(6):479-485. doi:10.1007/s10334-012-0315-x
231. Pan X, Wilson M, McConville C, et al. The lipid composition of isolated cytoplasmic lipid droplets from a human cancer cell line, BE(2)M17. *Mol Biosyst.* 2012;8(6):1694-1700. doi:10.1039/c2mb05485j
232. Holland GP, McIntyre SK, Alam TM. Distinguishing individual lipid headgroup mobility and phase transitions in raft-forming lipid mixtures with ³¹P MAS NMR. *Biophys J.* 2006;90(11):4248-4260. doi:10.1529/biophysj.105.077289
233. Kostidis S, Addie RD, Morreau H, Mayboroda OA, Giera M. Quantitative NMR analysis of intra- and extracellular metabolism of mammalian cells: A tutorial. *Anal Chim Acta.* 2017;980:1-24. doi:10.1016/j.aca.2017.05.011
234. Fernie AR, Trethewey RN, Krotzky AJ. *To Systems Biology.* 2004;5(September):1-7. doi:10.1038/nrm1451
235. Le Belle JE, Harris NG, Williams SR, Bhakoo KK. A comparison of cell and tissue extraction techniques using high-resolution ¹H NMR spectroscopy. *NMR Biomed.* 2002;15(1):37-44. doi:10.1002/nbm.740
236. Schleucher J, Schwendinger M, Sattler M, et al. A general enhancement scheme in heteronuclear multidimensional NMR employing pulsed field gradients. *J Biomol NMR.* 1994;4(2):301-306. doi:10.1007/BF00175254
237. Nagayama K, Kumar A, Wüthrich K, Ernst R. Experimental techniques of two-dimensional correlated spectroscopy. *J Magn Reson.* 1980;40(2):321-334. doi:10.1016/0022-2364(80)90255-3
238. Wu, D.; Chen, A.; Johnson SC. An improved diffusion-ordered spectroscopy experiment incorporating bipolar-gradient pulses. *J Magn Reson Ser A.* 1995;115(2):260-264. doi:10.1006/jmra.1995.1176
239. Xia J, Sinelnikov I V., Han B, Wishart DS. MetaboAnalyst 3.0-making metabolomics more meaningful.

- Nucleic Acids Res.* 2015;43:W251-W257. doi:10.1093/nar/gkv380
240. Cajka T, Fiehn O. Increasing lipidomic coverage by selecting optimal mobile-phase modifiers in LC-MS of blood plasma. *Metabolomics.* 2016;12(2):1-11. doi:10.1007/s11306-015-0929-x
241. Sud M, Fahy E, Cotter D, et al. LMSD: LIPID MAPS structure database. *Nucleic Acids Res.* 2007;35(SUPPL. 1):527-532. doi:10.1093/nar/gkl838
242. Livak KJ, Schmittgen TD. Analysis of relative gene expression data using real-time quantitative PCR and the 2- $\Delta\Delta$ CT method. *Methods.* 2001;25(4):402-408. doi:10.1006/meth.2001.1262
243. Trapnell C, Pachter L, Salzberg SL. TopHat: Discovering splice junctions with RNA-Seq. *Bioinformatics.* 2009;25(9):1105-1111. doi:10.1093/bioinformatics/btp120
244. Croft D, Mundo AF, Haw R, et al. The Reactome pathway knowledgebase. *Nucleic Acids Res.* 2014;42(D1):472-477. doi:10.1093/nar/gkt1102
245. Tinevez JY, Perry N, Schindelin J, et al. TrackMate: An open and extensible platform for single-particle tracking. *Methods.* 2017;115:80-90. doi:10.1016/j.ymeth.2016.09.016
246. Jafari M, Ansari-Pour N. Why, when and how to adjust your P values? *Cell J.* 2019;20(4):604-607. doi:10.22074/cellj.2019.5992
247. Li W, Lee REB, Lee RE, Li J. Methods for acquisition and assignment of multidimensional high-resolution magic angle spinning NMR of whole cell bacteria. *Anal Chem.* 2005;77(18):5785-5792. doi:10.1021/ac050906t
248. Zandomenighi G, Ilg K, Aebi M, Meier BH. On-cell MAS NMR: Physiological clues from living cells. *J Am Chem Soc.* 2012;134(42):17513-17519. doi:10.1021/ja307467p
249. Fredlund E, Broberg A, Boysen ME, Kenne L, Schnürer J. Metabolite profiles of the biocontrol yeast *Pichia anomala* J121 grown under oxygen limitation. *Appl Microbiol Biotechnol.* 2004;64(3):403-409. doi:10.1007/s00253-003-1464-7
250. Gjersing EL, Herberg JL, Horn J, Schaldach CM, Maxwell RS. NMR metabolomics of planktonic and biofilm modes of growth in *Pseudomonas aeruginosa*. *Anal Chem.* 2007;79(21):8037-8045. doi:10.1021/ac070800t
251. Aime S, Bruno E, Cabella C, Colombatto S, Digilio G, Mainero V. HR-MAS of cells: A “cellular water shift” due to water-protein interactions? *Magn Reson Med.* 2005;54(6):1547-1552. doi:10.1002/mrm.20707
252. Weybright P, Millis K, Campbell N, Cory DG, Singer S. Gradient, high-resolution, magic angle spinning 1H nuclear magnetic resonance spectroscopy of intact cells. *Magn Reson Med.* 1998;39:337-345. doi:10.1002/mrm.1910390302
253. Valonen PK, Griffin JL, Va TH, et al. Metabolite changes in BT4C rat gliomas undergoing ganciclovir-thymidine kinase gene therapy-induced programmed cell death as studied by 1H NMR spectroscopy in

- vivo, ex vivo, and in vitro. *J Biol Chem.* 2003;278(46):45915-45923. doi:10.1074/jbc.M306209200
254. van Asten JJA, Vettukattil R, Buckle T, et al. Increased levels of choline metabolites are an early marker of docetaxel treatment response in BRCA1-mutated mouse mammary tumors: An assessment by ex vivo proton magnetic resonance spectroscopy. *J Transl Med.* 2015;13(1):1-8. doi:10.1186/s12967-015-0458-4
255. Renault M, Shintu L, Piotto M, Caldarelli S. Slow-spinning low-sideband HR-MAS NMR spectroscopy: delicate analysis of biological samples. *Sci Rep.* 2013;3:3349. doi:10.1038/srep03349
256. Alam TM, Jenkins JE. HR-MAS NMR Spectroscopy in Material Science. In: *Advanced Aspects of Spectroscopy.* Alam and Jenkins; 2012:279-304. doi:10.5772/48340
257. Sodickson AD. Spatial Aspects of Nuclear Magnetic Resonance Spectroscopy: Static and Radio-frequency Magnetic Field Gradients in Principle and Practice. 1997.
258. Oliveira AL, Martinelli BCB, Liao LM, Pereira FC, Silveira-Lacerda EP, Alcantara GB. 1H HR-MAS NMR and S180 cells: metabolite assignment and evaluation of pulse sequence. *Short Rep.* 2014;25(6):656-657. doi:dx.doi.org/10.5935/0103-5053.20140070
259. McKay RT. How the 1D-NOESY suppresses solvent signal in metabonomics NMR spectroscopy: An examination of the pulse sequence components and evolution. *Concepts Magn Reson Part A.* 2011;38(5):1-6197-6220. doi:10.1002/cmr.a.20223
260. Rooney OM, Troke J, Nicholson JK, Griffin JL. High-Resolution Diffusion and Relaxation-Edited Magic Angle Spinning 1H NMR Spectroscopy of Intact Liver Tissue. *Magn Reson Med.* 2003;50:925-930. doi:10.1002/mrm.10620
261. Giraudeau P. Quantitative 2D liquid-state NMR. *Magn Reson Chem.* 2014;52(6). doi:10.1002/mrc.4068
262. Jézéquel T, Deborde C, Maucourt M, Zhendre V, Moing A, Giraudeau P. Absolute quantification of metabolites in tomato fruit extracts by fast 2D NMR. *Metabolomics.* 2015;11(5):1231-1242. doi:10.1007/s11306-015-0780-0
263. Rio P, Loiseau D, Demidem A, et al. Quantitative two-dimensional HRMAS 1H-NMR spectroscopy-based metabolite profiling of human cancer cell lines and response to chemotherapy. *Magn Reson Med.* 2010;63(5):1172-1183. doi:10.1002/mrm.22303
264. Gladden LB. Lactate metabolism: A new paradigm for the third millennium. *J Physiol.* 2004;558(1):5-30. doi:10.1113/jphysiol.2003.058701
265. Petrushanko IY, Simonenko O V., Burnysheva KM, et al. The ability of cells to adapt to low-oxygen conditions is associated with glutathionylation of Na,K-ATPase. *Mol Biol.* 2015;49(1):153-160. doi:10.1134/S0026893315010148
266. Poluektov YM, Petrushanko IY, Undrovinas NA, et al. Glutathione-related substances maintain cardiomyocyte contractile function in hypoxic conditions. *Sci Rep.* 2019;9(1):1-12. doi:10.1038/s41598-

267. Degani H, Eliyahu G, Maril N. Choline Metabolism: Meaning and Significance. *Metab Clin Exp*.
268. Mylonis I, Simos G, Paraskeva E. Hypoxia-Inducible Factors and the Regulation of Lipid Metabolism. *Cells*. 2019;8(3):214. doi:10.3390/cells8030214
269. Cerofolini L, Giuntini S, Barbieri L, et al. Real-Time Insights into Biological Events: In-Cell Processes and Protein-Ligand Interactions. *Biophys J*. 2019;116(2):239-247. doi:10.1016/j.bpj.2018.11.3132
270. Jin X, Kang S, Tanaka S, Park S. Monitoring the Glutathione Redox Reaction in Living Human Cells by Combining Metabolic Labeling with Heteronuclear NMR. *Angew Chemie - Int Ed*. 2016;55(28):7939-7942. doi:10.1002/anie.201601026
271. Carvalho J, Alves S, Castro MMCA, et al. Development of a bioreactor system for cytotoxic evaluation of pharmacological compounds in living cells using NMR spectroscopy. *J Pharmacol Toxicol Methods*. 2019;95(September 2018):70-78. doi:10.1016/j.vascn.2018.11.004
272. Opstad KS, Bell BA, Griffiths JR, Howe FA. An investigation of human brain tumour lipids by high-resolution magic angle spinning 1H MRS and histological analysis. *NMR Biomed*. 2008;21:677-685. doi:10.1002/nbm.1239
273. Dietz C, Ehret F, Palmas F, et al. Applications of high - resolution magic angle spinning MRS in biomedical studies II — Human diseases. *NMR Biomed*. 2017;30:1-31. doi:10.1002/nbm.3784
274. Baccam A, Benoni-Sviercovich A, Rocchi M, et al. The mechanical stimulation of myotubes counteracts the effects of tumor-derived factors through the modulation of the activin/follistatin ratio. *Front Physiol*. 2019;10(APR):1-9. doi:10.3389/fphys.2019.00401
275. Shaloam Dasari and Paul Bernard Tchounwou. Cisplatin in cancer therapy: molecular mechanisms of action. *Eur J Pharmacol*. 2015;5(0):364-378. doi:10.1016/j.ejphar.2014.07.025.Cisplatin
276. Hande KR. Clinical Oncology Update Etoposide : Four Decades of Development of a Topoisomerase II Inhibitor. *Eur J Cancer*. 1998;34(10):1514-1521.
277. Montecucco A, Zanetta F, Biamonti G. Molecular mechanisms of etoposide. *EXCLI J*. 2015;14:95-108. doi:10.17179/excli2014-561
278. von Stechow L, Ruiz-Aracama A, van de Water B, Peijnenburg A, Danen E, Lommen A. Identification of Cisplatin-Regulated Metabolic Pathways in Pluripotent Stem Cells. *PLoS One*. 2013;8(10). doi:10.1371/journal.pone.0076476
279. Duarte IF, Marques J, Marques MPM, Blaise BJ, Gil AM. Nuclear Magnetic Resonance (NMR) Study of the Effect of Cisplatin on the Metabolic Profile of MG-63 Osteosarcoma Cells. *J Proteome Res*. 2010;9:5877-5886. doi:10.1021/pr100635n
280. Carneiro TJ, Araújo R, Vojtek M, et al. Multi-organ NMR metabolomics to assess in vivo overall metabolic impact of cisplatin in mice. *Metabolites*. 2019;9(11):1-17. doi:10.3390/metabo9110279

281. Kell DB, Brown M, Davey HM, Dunn WB, Spasic I, Oliver SG. Metabolic footprinting and systems biology: the medium is the message. *Nat Rev Microbiol*. 2005;3:557-565. doi:10.1038/nrmicro1177
282. Feng J, Li J, Wu H, Chen Z. Metabolic responses of HeLa cells to silica nanoparticles by NMR-based metabolomic analyses. *Metabolomics*. 2013;9(4):874-886. doi:10.1007/s11306-013-0499-8
283. Larsen BD, Rampalli S, Burns LE, Brunette S, Dilworth FJ, Megeney LA. Caspase 3/caspase-activated DNase promote cell differentiation by inducing DNA strand breaks. *Proc Natl Acad Sci U S A*. 2010;107(9):4230-4235. doi:10.1073/pnas.0913089107
284. Griffin JL, Shockcor JP. Metabolic profiles of cancer cells. *Nat Rev Cancer*. 2004;4(7):551-561. doi:10.1038/nrc1390
285. Bruni E, Reichle A, Scimeca M, Bonanno E, Ghibelli L. Lowering etoposide doses shifts cell demise from caspase-dependent to differentiation and caspase-3-independent apoptosis via DNA damage response, inducing AML culture extinction. *Front Pharmacol*. 2018;9(NOV):1-13. doi:10.3389/fphar.2018.01307
286. Gey C, Seeger K. Metabolic changes during cellular senescence investigated by proton NMR-spectroscopy. *Mech Ageing Dev*. 2013;134(3-4):130-138. doi:10.1016/j.mad.2013.02.002
287. Daskalaki E, Pillon NJ, Krook A, Wheelock CE, Checa A. The influence of culture media upon observed cell secretome metabolite profiles: The balance between cell viability and data interpretability. *Anal Chim Acta*. 2018;1037:338-350. doi:10.1016/j.aca.2018.04.034
288. Quintero MR, Cabañas ME, Arús C. A possible cellular explanation for the NMR-visible mobile lipid (ML) changes in cultured C6 glioma cells with growth. *Biochim Biophys Acta - Mol Cell Biol Lipids*. 2007;1771(1):31-44. doi:10.1016/j.bbalip.2006.10.003
289. Anthony ML, Zhao M, Brindle KM. Inhibition of phosphatidylcholine biosynthesis following induction of apoptosis in HL-60 cells. *J Biol Chem*. 1999;274(28):19686-19692. doi:10.1074/jbc.274.28.19686
290. Cui Z, Houweling M. Phosphatidylcholine and cell death. *Biochim Biophys Acta - Mol Cell Biol Lipids*. 2002;1585(2-3):87-96. doi:10.1016/S1388-1981(02)00328-1
291. Fagone P, Jackowski S. Phosphatidylcholine and the CDP-choline cycle. *Biochim Biophys Acta - Mol Cell Biol Lipids*. 2013;1831(3):523-532. doi:10.1016/j.bbalip.2012.09.009
292. Gibbons E, Pickett KR, Streeter MC, Warcup AO, Judd AM, Bell JD. Molecular details of membrane fluidity changes during apoptosis and relationship to phospholipase A2 activity. *Biochim Biophys Acta*. 2013;1828(2):887-895. doi:10.1016/j.bbamem.2012.08.024.Molecular
293. Nielson KH, Olsen CA, Allred D V, Neill KLO, Burton GF, Y JDB. Susceptibility of S49 lymphoma cell membranes to hydrolysis by secretory phospholipase A2 during early phase of apoptosis. *Biochim Biophys Acta*. 2000;1484:163-174.
294. Martín-Sitjar J, Delgado-Goñi T, Cabañas ME, Tzen J, Arús C. Influence of the spinning rate in the HR-

- MAS pattern of mobile lipids in C6 glioma cells and in artificial oil bodies. *Magn Reson Mater Physics, Biol Med.* 2012;25(6):487-496. doi:10.1007/s10334-012-0327-6
295. Mason EF, Rathmell JC. Cell metabolism: An essential link between cell growth and apoptosis. *Biochim Biophys Acta - Mol Cell Res.* 2011;1813(4):645-654. doi:10.1016/j.bbamcr.2010.08.011
296. Chhetri DR. Myo-inositol and its derivatives: Their emerging role in the treatment of human diseases. *Front Pharmacol.* 2019;10(October):1-8. doi:10.3389/fphar.2019.01172
297. Majerus PW, Zou J, Marjanovic J, Kisseleva M V., Wilson MP. The role of inositol signaling in the control of apoptosis. *Adv Enzyme Regul.* 2008;48:10-17. doi:10.1016/j.advenzreg.2008.04.001.
298. Hayashi E, Maeda T, Tomita T. The effect of myo-inositol deficiency on lipid metabolism in rats. *Biochim Biophys Acta.* 1974;360:146-155.
299. Agarwal R, Mumtaz H, Ali N. Role of inositol polyphosphates in programmed cell death. *Mol Cell Biochem.* 2009;328(1-2):155-165. doi:10.1007/s11010-009-0085-6
300. Circu ML, Aw TY. Glutathione and modulation of cell apoptosis. *Biochim Biophys Acta - Mol Cell Res.* 2012;1823(10):1767-1777. doi:10.1016/j.bbamcr.2012.06.019
301. De Nicola M, Ghibelli L. Glutathione depletion in survival and apoptotic pathways. *Front Pharmacol.* 2014;5(NOV):1-4. doi:10.3389/fphar.2014.00267
302. Franco R, Cidlowski JA. Apoptosis and glutathione: Beyond an antioxidant. *Cell Death Differ.* 2009;16(10):1303-1314. doi:10.1038/cdd.2009.107
303. Elstad CA, Meadows GG, Abdallah RM. Specificity of the suppression of metastatic phenotype by tyrosine and phenylalanine restriction. *Clin Exp Metastasis.* 1990;8(5):393-416. doi:10.1007/BF00058152
304. Meadows GG, Pierson HF, Abdallah RM, Desai PR. Dietary Influence of Tyrosine and Phenylalanine on the Response of B16 Melanoma to Carbidopa-Levodopa Methyl Ester Chemotherapy. *Cancer Res.* 1982;42(8):3056-3063.
305. Ge X, Fu YM, Li YQ, Meadows GG. Activation of caspases and cleavage of Bid are required for tyrosine and phenylalanine deficiency-induced apoptosis of human A375 melanoma cells. *Arch Biochem Biophys.* 2002;403(1):50-58. doi:10.1016/S0003-9861(02)00211-4
306. Yan Y, Wang Y, Wang X, et al. The effects of jolkinolide B on HepG2 cells as revealed by 1H-NMR-based metabolic profiling. *Eur J Pharmacol.* 2019;842(July 2018):10-19. doi:10.1016/j.ejphar.2018.10.025
307. Medina CB, Mehrotra P, Arandjelovic S, et al. Metabolites released from apoptotic cells act as tissue messengers. *Nature.* 2020;580(7801):130-135. doi:10.1038/s41586-020-2121-3
308. Ma D, Gulani V, Seiberlich N, et al. Magnetic resonance fingerprinting. *Nature.* 2013;495(7440):187-192. doi:10.1038/nature11971

309. Torrey HC. Transient nutations in nuclear magnetic resonance. *Phys Rev.* 1949;76(8):1059-1068. doi:10.1103/PhysRev.76.1059
310. Bloch F. Nuclear induction. *Phys Rev.* 1946;70(7-8):460-474. doi:10.1103/PhysRev.70.460
311. Meiboom S, Gill D. Modified spin-echo method for measuring nuclear relaxation times. *Rev Sci Instrum.* 1958;29(8):688-691. doi:10.1063/1.1716296
312. Siminovitich DJ, Ruocco MJ, Olejniczak ET, Das Gupta SK, Griffin RG. Anisotropic ²H-nuclear magnetic resonance spin-lattice relaxation in cerebroside- and phospholipid-cholesterol bilayer membranes. *Biophys J.* 1988;54(3):373-381. doi:10.1016/S0006-3495(88)82970-9
313. Pottumarthi V. Prasad, ed. *Magnetic Resonance Imaging: Methods and Biologic Applications*. Totowa, New Jersey: Humana Press; 2006.
314. Liimatainen TJ, Hakumäki JM. ¹H NMR Spectroscopic Study of Lipid T₁ - and T₂ -Relaxation in BT4C Rat Gliomas In Vivo. *Proc Intl Soc Mag Reson Med.* 2004;11:610.
315. Truszkiewicz A, Aebisher D, Bartusik-Aebisher D. Assessment of spin-lattice T₁ and spin-spin T₂ relaxation time measurements in breast cell cultures at 1.5 Tesla as a potential diagnostic tool in vitro. *Med Res J.* 2020;23-33. doi:10.5603/mrj.a2020.0005
316. Callahan DE, Trapane TL, Deamomd SF, Kao G, Ts'o POP, Kan LS. Studies of the T₁ and T₂ of intracellular water as a function of frequency in normal and transformed fetal cells. *Cell Biophys.* 1991;18(3):193-202. doi:10.1007/BF02989813
317. Chapman BE, Kuchel PW. Diffusion-Ordered (DOSY) NMR of Solute Exchange Across the Human Erythrocyte Membrane : including an application of Post- Widder Laplace inversion. *Diffus Fundam.* 2007;4(2007):8.1-8.15.
318. Stejskal EO, Tanner JE. Spin diffusion measurements: Spin echoes in the presence of a time-dependent field gradient. *J Chem Phys.* 1965;42(1):288-292. doi:10.1063/1.1695690
319. Johnson, C.S J. Diffusion ordered nuclear magnetic resonance spectroscopy: principles and applications. *Prog Nucl Magn Reson Spectrosc.* 1999;34:203-256.
320. Bihan D Le. Apparent diffusion coefficient and beyond: What diffusion MR imaging can tell us about tissue structure. *Radiology.* 2013;268(2):318-322. doi:10.1148/radiol.13130420
321. White NS, McDonald CR, Farid N, et al. Diffusion-weighted imaging in cancer: physical foundations and applications of restriction spectrum imaging. *Cancer Res.* 2014;74(17):4638-4652. doi:10.1158/0008-5472.CAN-13-3534
322. Li X, Cox JC, Flumerfelt RW. Determination of emulsion size distribution by NMR restricted diffusion measurement. *AIChE J.* 1992;38(10):1671-1674. doi:10.1002/aic.690381019
323. Kono K, Inoue Y, Nakayama K, et al. The role of diffusion-weighted imaging in patients with brain tumors. *Am J Neuroradiol.* 2001;22(6):1081-1088.

324. Bonekamp S, Corona-Villalobos CP, Kamel IR. Oncologic applications of diffusion-weighted MRI in the body. *J Magn Reson Imaging*. 2012;35(2):257-279. doi:10.1002/jmri.22786
325. Kauppinen RA. Monitoring cytotoxic tumour treatment response by diffusion magnetic resonance imaging and proton spectroscopy. *NMR Biomed*. 2002;15(1):6-17. doi:10.1002/nbm.742
326. Ababneha ZQ, Beloeilb H, Berdeb CB, Ababneha AM, Maierc SE, Mulkern R V. In vivo lipid diffusion coefficient measurements in rat bone marrow. *Magn Reson Imaging*. 2009;27(6):859-864. doi:10.1038/jid.2014.371
327. Steidle G, Eibofner F, Schick F. Quantitative diffusion imaging of adipose tissue in the human lower leg at 1.5 T. *Magn Reson Med*. 2011;65(4):1118-1124. doi:10.1002/mrm.22699
328. Wu M, Gmach O, Skurk T, et al. Measuring large lipid droplet sizes by probing restricted lipid diffusion effects with diffusion-weighted MRS at 3T. *Magn Reson Med*. 2019:1-13. doi:10.1002/mrm.27651
329. Cao P, Fan SJ, Wang AM, et al. Diffusion magnetic resonance monitors intramyocellular lipid droplet size in vivo. *Magn Reson Med*. 2015;73(1):59-69. doi:10.1002/mrm.25116
330. Pérez Y, Lahrech H, Cabañas ME, et al. Measurement by nuclear magnetic resonance diffusion of the dimensions of the mobile lipid compartment in C6 cells. *Cancer Res*. 2002;62(20):5672-5677.
331. Ronczka M, Müller-Petke M. Optimization of CPMG sequences to measure NMR transverse relaxation time T2 in borehole applications. *Geosci Instrumentation, Methods Data Syst*. 2012;1(2):197-208. doi:10.5194/gi-1-197-2012
332. Levoguer C. Using laser diffraction to measure particle size and distribution. *Met Powder Rep*. 2013;68(3):15-18. doi:10.1016/S0026-0657(13)70090-0
333. Bakshi AS, Smith DE. Effect of Fat Content and Temperature on Viscosity in Relation to Pumping Requirements of Fluid Milk Products. *J Dairy Sci*. 1984;67(6):1157-1160. doi:10.3168/jds.S0022-0302(84)81417-4
334. Ye Y, Liu X, Zhang Z, et al. ¹⁹F NMR spectroscopy as a probe of cytoplasmic viscosity and weak protein interactions in living cells. *Chemistry*. 2013;19(38):12705-12710. doi:10.1002/chem.201301657
335. Einstein A. On the motion of small particles suspended in a stationary liquid. *Ann Phys*. 1905;322:549-560. doi:10.1002/andp.19053220806
336. Kasturi SR, Chang DC, Hazlewood CF. Study of anisotropy in nuclear magnetic resonance relaxation times of water protons in skeletal muscle. *Biophys J*. 1980;30(3):369-381. doi:10.1016/S0006-3495(80)85102-2
337. Moretti A, Paoletta M, Liguori S, Bertone M, Toro G, Iolascon G. Choline: An Essential Nutrient for Skeletal Muscle. *Nutrients*. 2020;12:2144-2155. doi:10.3390/nu12072144
338. Fabry ME, Eisenstadt M. Water exchange across red cell membranes: II. Measurement by nuclear magnetic resonance T1, T2, and T12 hybrid relaxation. The effects of osmolarity, cell volume, and

- medium. *J Membr Biol.* 1978;42(4):375-398. doi:10.1007/BF01870357
339. Marjańska M, Emir UE, Deelchand DK, Terpstra M. Faster Metabolite 1H Transverse Relaxation in the Elder Human Brain. *PLoS One.* 2013;8(10):1-7. doi:10.1371/journal.pone.0077572
340. Jackson PR. Multiexponential T2 and Diffusion Magnetic Resonance Measurements of Glioma Cells. 2012. doi:10.1017/CBO9781107415324.004
341. Fenrich FRE, Beaulieu C, Allen PS. Relaxation times and microstructures. *NMR Biomed.* 2001;14(2):133-139. doi:10.1002/nbm.685
342. Krysko D V., D'Herde K, Vandenabeele P. Clearance of apoptotic and necrotic cells and its immunological consequences. *Apoptosis.* 2006;11(10):1709-1726. doi:10.1007/s10495-006-9527-8
343. Berghe T Vanden, Vanlangenakker N, Parthoens E, et al. Necroptosis, necrosis and secondary necrosis converge on similar cellular disintegration features. *Cell Death Differ.* 2010;17(6):922-930. doi:10.1038/cdd.2009.184
344. Degterev A, Yuan J. Expansion and evolution of cell death programmes. *Nat Rev Mol Cell Biol.* 2008;9:378-390. doi:doi.org/10.1038/nrm2393
345. Sundgren PC, Fan X, Weybright P, et al. Differentiation of recurrent brain tumor versus radiation injury using diffusion tensor imaging in patients with new contrast-enhancing lesions. *Magn Reson Imaging.* 2006;24(9):1131-1142. doi:10.1016/j.mri.2006.07.008
346. Castillo M, Smith JK, Kwock L, Wilber K. Apparent diffusion coefficients in the evaluation of high-grade cerebral gliomas. *Am J Neuroradiol.* 2001;22(1):60-64.
347. Stadnik TW, Chaskis C, Michotte A, et al. Diffusion-weighted MR imaging of intracerebral masses: Comparison with conventional MR imaging and histologic findings. *Am J Neuroradiol.* 2001;22(5):969-976.
348. Mannelli L, Kim S, Hajdu CH, Babb JS, Clark TWI, Taouli B. Assessment of tumor necrosis of hepatocellular carcinoma after chemoembolization: Diffusion-weighted and contrast-enhanced MRI with histopathologic correlation of the explanted liver. *Am J Roentgenol.* 2009;193(4):1044-1052. doi:10.2214/AJR.08.1461
349. Lyng H, Haraldseth O, Rofstad EK. Measurement of cell density and necrotic fraction in human melanoma xenografts by diffusion weighted magnetic resonance imaging. *Magn Reson Med.* 2000;43(6):828-836. doi:10.1002/1522-2594(200006)43:6<828::AID-MRM8>3.0.CO;2-P
350. Daemen S, van Zandvoort MAMJ, Parekh SH, Hesselink MKC. Microscopy tools for the investigation of intracellular lipid storage and dynamics. *Mol Metab.* 2016;5(3):153-163. doi:10.1016/j.molmet.2015.12.005
351. Digel M, Eehalt R, Füllekrug J. Lipid droplets lighting up: Insights from live microscopy. *FEBS Lett.* 2010;584(11):2168-2175. doi:10.1016/j.febslet.2010.03.035

352. Lang I, Scholz M, Peters R. Molecular mobility and nucleocytoplasmic flux in hepatoma cells. *J Cell Biol.* 1986;102(4):1183-1190. doi:10.1083/jcb.102.4.1183
353. Liang L, Xing D, Chen T, Pei Y. Nucleoplasmic viscosity of living cells investigated by fluorescence correlation spectroscopy. *Opt Heal Care Biomed Opt III.* 2007;6826(January 2008):68262T. doi:10.1117/12.760226
354. García-Pérez AI, López-Beltrán EA, Klüner P, Luque J, Ballesteros P, Cerdán S. Molecular crowding and viscosity as determinants of translational diffusion of metabolites in subcellular organelles. *Arch Biochem Biophys.* 1999;362(2):329-338. doi:10.1006/abbi.1998.1051
355. Neidleman SL. Effects of temperature on lipid unsaturation. *Biotechnol Genet Eng Rev.* 1987;5(1):245-268. doi:10.1080/02648725.1987.10647839
356. Peerawat Charuwat, Boardman G, Bott C, Novak JT. Thermal Degradation of Long Chain Fatty Acids. *Water Environ Res.* 2018;90(3):278-287.
357. Puchkov EO. Intracellular viscosity: methods of measurement and role in metabolism. *Biochem Suppl Ser A Membr Cell Biol.* 2013;7(4):270-279. doi:10.1134/s1990747813050140
358. Dijksterhuis J, Nijssse J, Hoekstra FA, Golovina EA. High viscosity and anisotropy characterize the cytoplasm of fungal dormant stress-resistant spores. *Eukaryot Cell.* 2007;6(2):157-170. doi:10.1128/EC.00247-06
359. Adams DS. Mechanisms of cell shape change: the cytomechanics of cellular response to chemical environment and mechanical loading. *J Cell Biol.* 1992;117(1):83-93. doi:10.1083/jcb.117.1.83
360. Wilflinga F, Haasb JT, Walthera TC, Farese Jr R V. Lipid droplet biogenesis. *Curr Opin Cell Biol.* 2014;29:39-45. doi:10.1016/j.bbi.2017.04.008
361. Burch TC, Isaac G, Booher CL, et al. Comparative metabolomic and lipidomic analysis of phenotype stratified prostate cells. *PLoS One.* 2015;10(8):1-16. doi:10.1371/journal.pone.0134206
362. Llorente A, Skotland T, Sylvänne T, et al. Molecular lipidomics of exosomes released by PC-3 prostate cancer cells. *Biochim Biophys Acta - Mol Cell Biol Lipids.* 2013;1831(7):1302-1309. doi:10.1016/j.bbalip.2013.04.011
363. Andreyev AY, Fahy E, Guan Z, et al. Subcellular organelle lipidomics in TLR-4-activated macrophages. *J Lipid Res.* 2010;51(9):2785-2797. doi:10.1194/jlr.M008748
364. Leiria LO, Tseng YH. Lipidomics of brown and white adipose tissue: Implications for energy metabolism. *Biochim Biophys Acta - Mol Cell Biol Lipids.* 2020;1865(10):158788. doi:10.1016/j.bbalip.2020.158788
365. Chitraju C, Trötz Müller M, Hartler J, et al. Lipidomic analysis of lipid droplets from murine hepatocytes reveals distinct signatures for nutritional stress. *J Lipid Res.* 2012;53(10):2141-2152. doi:10.1194/jlr.M028902

366. Markgraf DF, Al-Hasani H, Lehr S. Lipidomics—Reshaping the analysis and perception of type 2 diabetes. *Int J Mol Sci.* 2016;17(11). doi:10.3390/ijms17111841
367. Tam VC, Quehenberger O, Oshansky CM, et al. Lipidomic Profiling of Influenza Infection Identifies Mediators that Induce and Resolve Inflammation. *Cell.* 2013;154(1):213-227. doi:10.1016/j.cell.2013.05.052.Lipidomic
368. Gaudio A, Garcia-Rozas P, Casarejos MJ, Pastor O, Rodriguez-Navarro JA. Lipidomic alterations in the mitochondria of aged Parkin null mice relevant to autophagy. *Front Neurosci.* 2019;13(APR):1-12. doi:10.3389/fnins.2019.00329
369. Symons JL, Cho K-J, Chang JT, et al. Lipidomic atlas of mammalian cell membranes reveals hierarchical variation induced by culture conditions, subcellular membranes, and cell lineages. *Soft Matter.* 2020. doi:10.1039/d0sm00404a
370. Hartler J, Köfeler HC, Trötz Müller M, Thallinger GG, Spener F. Assessment of lipidomic species in hepatocyte lipid droplets from stressed mouse models. *Sci Data.* 2014;1:1-12. doi:10.1038/sdata.2014.51
371. Aviram R, Manella G, Kopelman N, et al. Lipidomics Analyses Reveal Temporal and Spatial Lipid Organization and Uncover Daily Oscillations in Intracellular Organelles. *Mol Cell.* 2016;62(4):636-648. doi:10.1016/j.molcel.2016.04.002
372. Corsetto PA, Ferrara G, Buratta S, et al. Changes in lipid composition during manganese-induced apoptosis in PC12 cells. *Neurochem Res.* 2016;41(1-2):258-269. doi:10.1007/s11064-015-1785-9
373. Yang S, Qiao B, Lu SH, Yuan YJ. Comparative lipidomics analysis of cellular development and apoptosis in two *Taxus* cell lines. *Biochim Biophys Acta - Mol Cell Biol Lipids.* 2007;1771(5):600-612. doi:10.1016/j.bbalip.2007.02.011
374. Crimi M, Esposti MD. Apoptosis-induced changes in mitochondrial lipids. *Biochim Biophys Acta - Mol Cell Res.* 2011;1813(4):551-557. doi:10.1016/j.bbamcr.2010.09.014
375. Tyurin VA, Tyurina YY, Ritov VB, et al. Oxidative Lipidomics of Apoptosis: Quantitative Assessment of Phospholipid Hydroperoxides in Cells and Tissues. *Methods Mol Biol.* 2010;610:353-374. doi:10.1007/978-1-60327-029-8
376. Pacia MZ, Sternak M, Mateuszuk L, Stojak M, Kaczor A, Chlopicki S. Heterogeneity of chemical composition of lipid droplets in endothelial inflammation and apoptosis. *Biochim Biophys Acta - Mol Cell Res.* 2020;1867(6):118681. doi:10.1016/j.bbamcr.2020.118681
377. Li N, Sancak Y, Frasor J, Atilla-Gokcumen GE. A Protective Role for Triacylglycerols during Apoptosis. *Biochemistry.* 2018;57(1):72-80. doi:10.1021/acs.biochem.7b00975
378. Listenberger LL, Han X, Lewis SE, et al. Triglyceride accumulation protects against fatty acid-induced lipotoxicity. *Proc Natl Acad Sci U S A.* 2003;100(6):3077-3082. doi:10.1073/pnas.0630588100

379. Huang C, Freter C. Lipid metabolism, apoptosis and cancer therapy. *Int J Mol Sci*. 2015;16(1):924-949. doi:10.3390/ijms16010924
380. Mullen TD, Obeid LM. Ceramide and apoptosis: exploring the enigmatic connections between sphingolipid metabolism and programmed cell death. *Anticancer Agents Med Chem*. 2012;12(4):340-363. doi:10.2174/187152012800228661
381. Shyu P, Wong XFA, Crasta K, Thibault G. Dropping in on lipid droplets: Insights into cellular stress and cancer. *Biosci Rep*. 2018;38(5):1-20. doi:10.1042/BSR20180764
382. Triantafyllou EA, Georgatsou E, Mylonis I, Simos G, Paraskeva E. Expression of AGPAT2, an enzyme involved in the glycerophospholipid/triacylglycerol biosynthesis pathway, is directly regulated by HIF-1 and promotes survival and etoposide resistance of cancer cells under hypoxia. *Biochim Biophys Acta - Mol Cell Biol Lipids*. 2018;1863(9):1142-1152. doi:10.1016/j.bbalip.2018.06.015
383. Cotte AK, Aires V, Fredon M, et al. Lysophosphatidylcholine acyltransferase 2-mediated lipid droplet production supports colorectal cancer chemoresistance. *Nat Commun*. 2018;9(1). doi:10.1038/s41467-017-02732-5
384. Song YF, Gao Y, Hogstrand C, Li DD, Pan YX, Luo Z. Upstream regulators of apoptosis mediates methionine-induced changes of lipid metabolism. *Cell Signal*. 2018;51(August):176-190. doi:10.1016/j.cellsig.2018.08.005
385. Zhang G, He P, Tan H, et al. Integration of metabolomics and transcriptomics revealed a fatty acid network exerting growth inhibitory effects in human pancreatic cancer. *Clin Cancer Res*. 2013;19(18):4983-4993. doi:10.1158/1078-0432.CCR-13-0209
386. Fei W, Wang H, Fu X, Bielby C, Yang H. Conditions of endoplasmic reticulum stress stimulate lipid droplet formation in *Saccharomyces cerevisiae*. *Biochem J*. 2009;424(1):61-67. doi:10.1042/BJ20090785.
387. Vevea JD, Garcia EJ, Chan RB, et al. Role for Lipid Droplet Biogenesis and Microlipophagy in Adaptation to Lipid Imbalance in Yeast. *Dev Cell*. 2015;35(5):584-599. doi:10.1016/j.devcel.2015.11.010
388. Thibault G, Shui G, Kim W, et al. The membrane stress response buffers the lethal effects of lipid disequilibrium by reprogramming the protein homeostasis network. *Mol Cell*. 2012;48(1):16-27. doi:10.1016/j.molcel.2012.08.016.The
389. Li N, Lizardo DY, Atilla-Gokcumen GE. Specific Triacylglycerols Accumulate via Increased Lipogenesis during 5-FU-Induced Apoptosis. *ACS Chem Biol*. 2016;11(9):2583-2587. doi:10.1021/acscchembio.6b00410
390. Blackham S, Baillie A, Al-Hababi F, et al. Gene Expression Profiling Indicates the Roles of Host Oxidative Stress, Apoptosis, Lipid Metabolism, and Intracellular Transport Genes in the Replication of Hepatitis C Virus. *J Virol*. 2010;84(10):5404-5414. doi:10.1128/jvi.02529-09

391. Solary E, Droin N, Bettaieb A, Corcos L, Dimanche-Boitrel MT, Garrido C. Positive and negative regulation of apoptotic pathways by cytotoxic agents in hematological malignancies. *Leukemia*. 2000;14(10):1833-1849. doi:10.1038/sj.leu.2401902
392. Olzmann JA, Carvalho P. Dynamics and functions of lipid droplets. *Nat Rev Mol Cell Biol*. 2019;20(3):137-155. doi:10.1038/s41580-018-0085-z
393. Ayyappan JP, Paul A, Goo YH. Lipid droplet-associated proteins in atherosclerosis (Review). *Mol Med Rep*. 2016;13(6):4527-4534. doi:10.3892/mmr.2016.5099
394. Tarling EJ, Vallim TQ d. A, Edwards PA. Role of ABC transporters in lipid transport and human disease. *Trends Endocrinol Metab*. 2013;24(7):342-350. doi:10.1016/j.tem.2013.01.006
395. Kemp S, Theodoulou FL, Wanders RJA. Mammalian peroxisomal ABC transporters: From endogenous substrates to pathology and clinical significance. *Br J Pharmacol*. 2011;164(7):1753-1766. doi:10.1111/j.1476-5381.2011.01435.x
396. Rajendran L, Le Lay S, Illges H. Raft association and lipid droplet targeting of flotillins are independent of caveolin. *Biol Chem*. 2007;388(3):307-314. doi:10.1515/BC.2007.034
397. Demarquoy J, Borgne F Le. Crosstalk between mitochondria and peroxisomes. *World J Biol Chem*. 2015;6(4):301. doi:10.4331/wjbc.v6.i4.301
398. Veenhuis M, Mateblowski M, Kunau WH, Harder W. Proliferation of microbodies in *Saccharomyces cerevisiae*. *Yeast*. 1987;3:77-84. doi:10.1002/yea.320030204
399. Binns D, Januszewski T, Chen Y, et al. An intimate collaboration between peroxisomes and lipid bodies. *J Cell Biol*. 2006;173(5):719-731. doi:10.1083/jcb.200511125
400. Ferrante G, Sykora S. *Technical Aspects of Fast Field Cycling*. Vol 57.; 2005. doi:10.1016/S0898-8838(05)57009-0

Appendix 1. Supporting information for Chapter 4

S1.1. Supporting information for cellular disintegration of necrotic cells by ¹H NMR spectroscopy.

Table S1.1. *Fold change integral for selected metabolites in aqueous fraction of cell extracts: control and heat-treated cells. * $p < 0.05$, ** $p < 0.01$, *** $p < 0.001$ for control vs treatment, FDR adjusted.*

Metabolite	Range	Control		Heat	
		Mean	SEM	Mean	SEM
Isoleucine+ leucine	0.99 - 0.97	1.00	0.03	1.22	0.11
Valine	1.06 - 1.03	1.00	0.01	1.28	0.12
Lactate	1.35 - 1.31	1.00	0.02	0.32***	0.06
Alanine	1.49 - 1.46	1.00	0.02	0.52***	0.06
Lysine	1.75 - 1.70	1.00	0.02	0.91	0.09
Acetate	1.93 - 1.91	1.00	0.04	1.23	0.18
Glutamine +glutamate	2.20 - 2.11	1.00	0.08	0.43**	0.10
Glutamate	2.37 - 2.33	1.00	0.03	0.29***	0.04
Succinate	2.41 - 2.39	1.00	0.05	1.20	0.22
Glutamine	2.47 - 2.44	1.00	0.10	0.47*	0.15
Glutathione	2.58 - 2.50	1.00	0.01	0.40***	0.05
DMA	2.71 - 2.68	1.00	0.01	0.39**	0.16
Creatine	3.05 - 3.03	1.00	0.02	0.11***	0.02
Choline compounds	3.24 - 3.22	1.00	0.01	0.65***	0.06
Glycine	3.56 - 3.53	1.00	0.01	0.57***	0.05
Myo-inositol	4.08 - 4.04	1.00	0.02	0.32***	0.04
Glucose	5.25 - 5.22	1.00	0.03	2.48***	0.20
Tyrosine	6.92 - 6.86	1.00	0.01	0.93	0.10
Phenylalanine	7.35 - 7.31	1.00	0.01	1.07	0.10
Methylhistidine	7.69 - 7.67	1.00	0.16	6.58***	0.84
ADP/ATP	8.29 - 8.26	1.00	0.06	0.11***	0.04

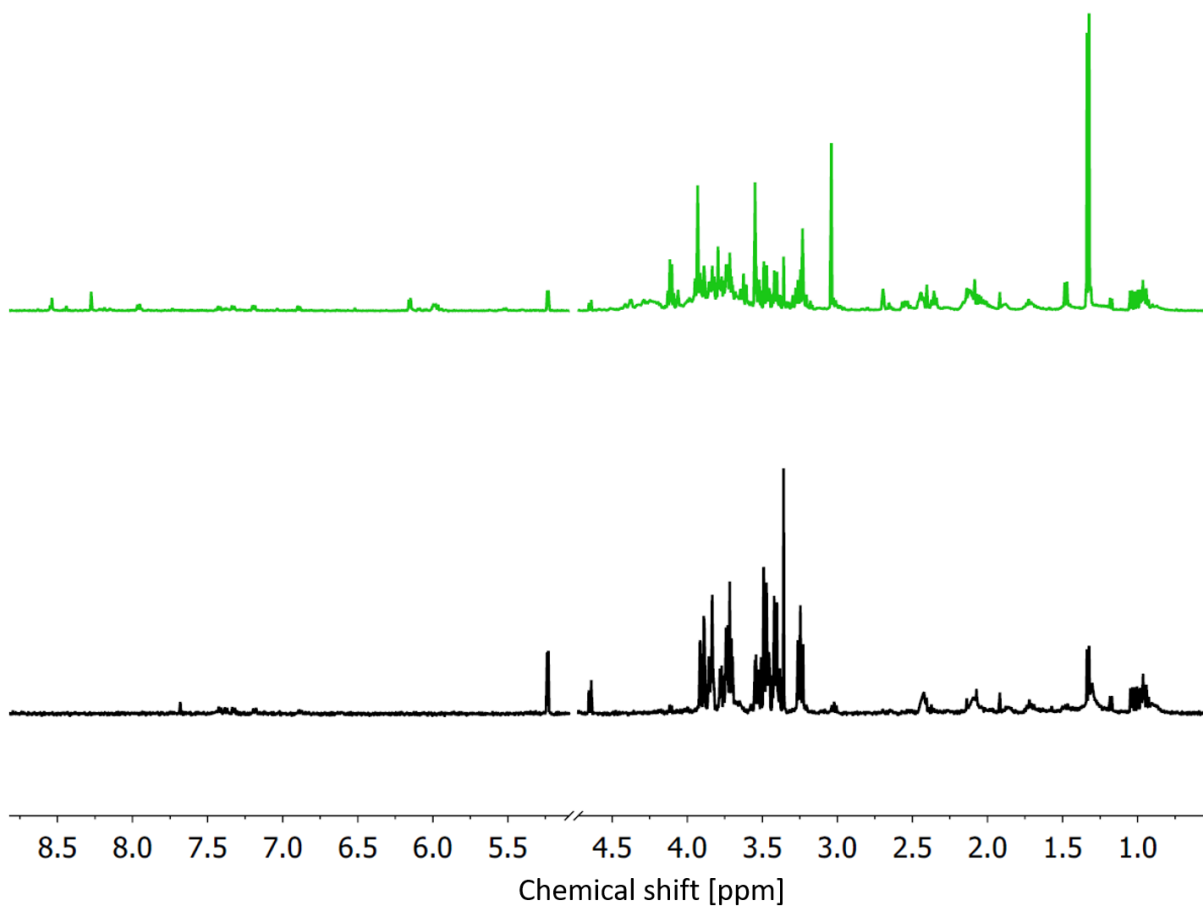


Figure S1.1. 500 MHz ¹H NMR spectra of control (green) and heat-treated (black) cell extracts (aqueous fraction). All spectra were normalised to the total integral.

S1.2. Supporting information for data reported in **Table 4.1** in **Chapter 4**.

S1.2.1. Growth media

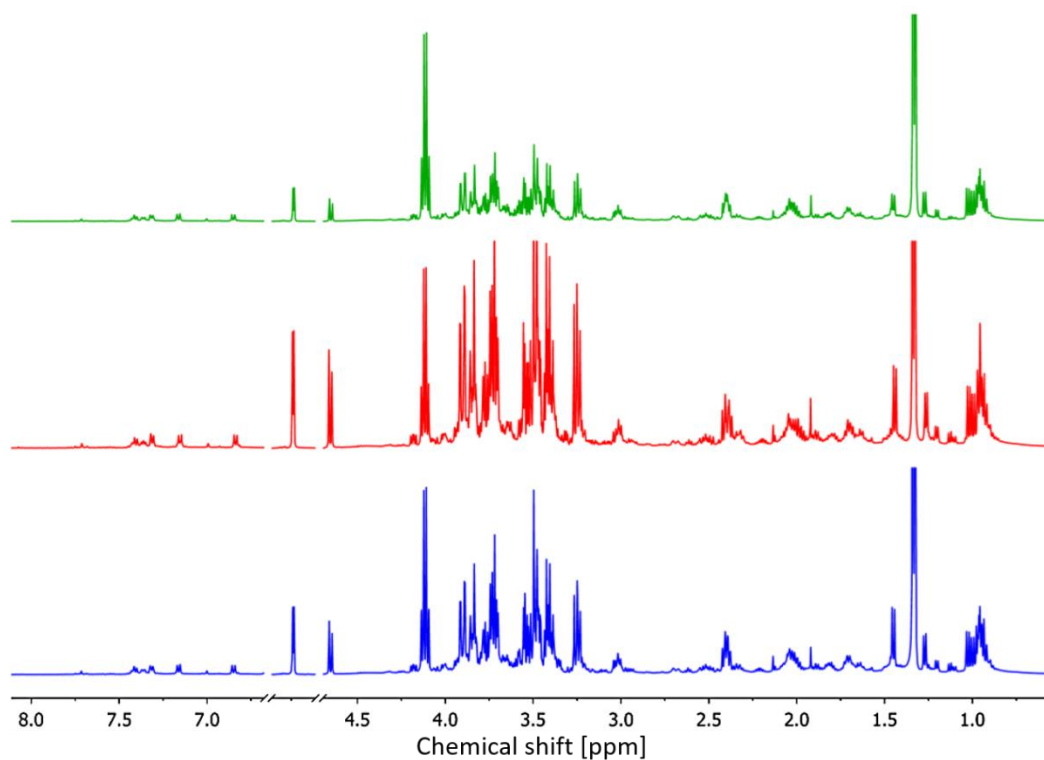


Figure S1.2. 500 MHz ^1H NMR spectra of culture media collected after 48 h treatments: control (green), cisplatin (red) and etoposide (blue). All spectra were normalised to the total integral. Partially suppressed water peak was removed.

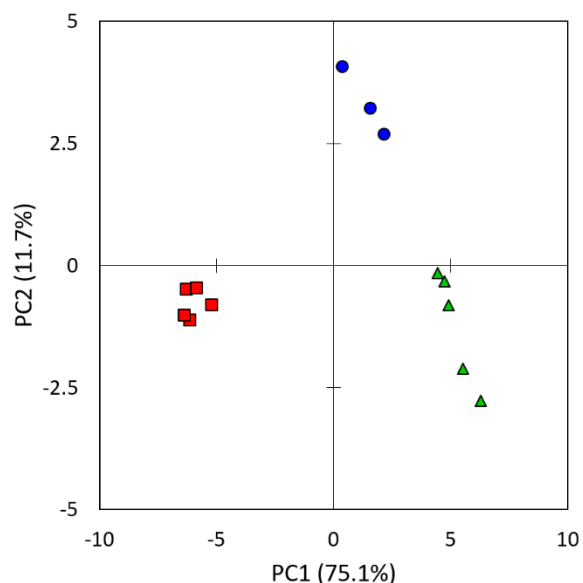


Figure S1.3. Two-dimensional PCA score plot derived from the ^1H NMR spectra of growth media samples: control (green triangles), cisplatin (red squares), etoposide (blue circles); $n = 3$ for etoposide, $n = 5$ for control and cisplatin. The numbers in brackets represent the percentage of variability explain by each principal component (PC). Spectral pre-processed with total integral normalisation and Pareto scaling.

Table S1.2. Fold change integral for selected metabolites in growth media. * $p < 0.05$, ** $p < 0.01$, *** $p < 0.001$ for control vs treatment; # $p < 0.05$, for cisplatin vs etoposide, FDR adjusted.

Metabolites	Range [ppm]	Control		Cisplatin		Etoposide	
		Mean	SEM	Mean	SEM	Mean	SEM
Isoleucine + leucine	0.97 - 0.91	1.000	0.025	1.176***	0.012	1.008#	0.005
Valine	1.04 - 0.99	1.000	0.024	0.858***	0.004	0.905*#	0.011
Lactate	1.35 - 1.31	1.000	0.029	0.475***	0.004	0.800***#	0.029
Lactate	4.15 - 4.07	1.000	0.016	0.486***	0.006	0.789***#	0.024
Alanine	1.47 - 1.42	1.000	0.039	1.128*	0.006	1.235***#	0.005
Lysine	1.75 - 1.67	1.000	0.010	0.967*	0.004	0.984#	0.003
Lysine	3.05 - 2.99	1.000	0.017	0.951	0.009	0.997#	0.003
Acetate	1.93 - 1.91	1.000	0.017	1.019	0.004	0.832***#	0.006
Glutamine + glutamate	2.09 - 1.93	1.000	0.009	0.952**	0.006	0.944**	0.001
Glutamate	2.35 - 2.28	1.000	0.022	1.462***	0.006	1.077#	0.008
Glutamine	2.43 - 2.36	1.000	0.018	0.963	0.002	0.993#	0.002
Glutathione	2.56 - 2.46	1.000	0.012	0.846***	0.004	0.877***#	0.006
Glucose	5.26 - 5.22	1.000	0.034	1.850***	0.018	1.433***#	0.025
Tyrosine	6.89 - 6.80	1.000	0.013	1.024	0.007	0.997#	0.003
Phenylalanine	7.44 - 7.29	1.000	0.011	0.996	0.005	0.987	0.004

S1.2.2. Cell extracts - organic fraction

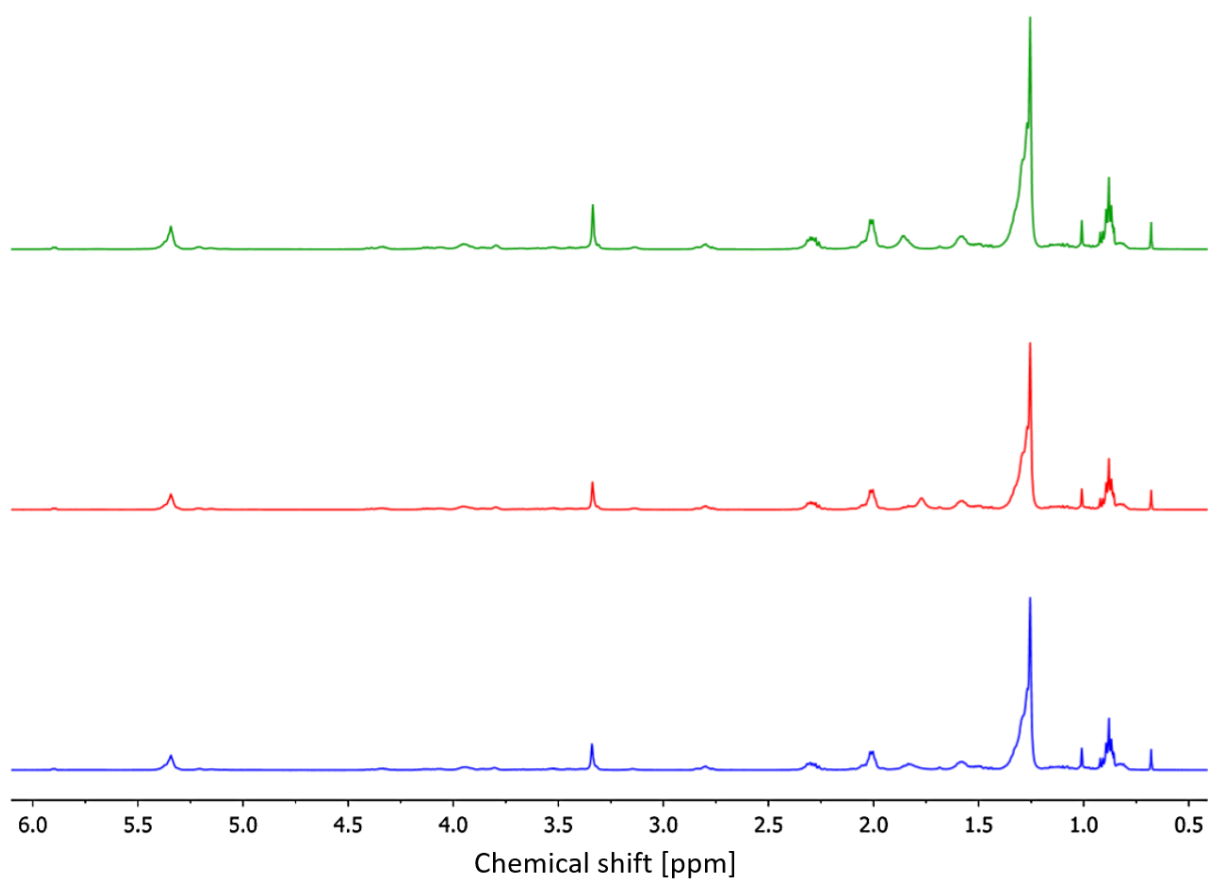


Figure S1.4. 500 MHz ¹H NMR spectra of cell extract (organic fraction) collected after 48 h of the following treatments: control (green), cisplatin (red) and etoposide (blue). All spectra were normalised to the total integral.

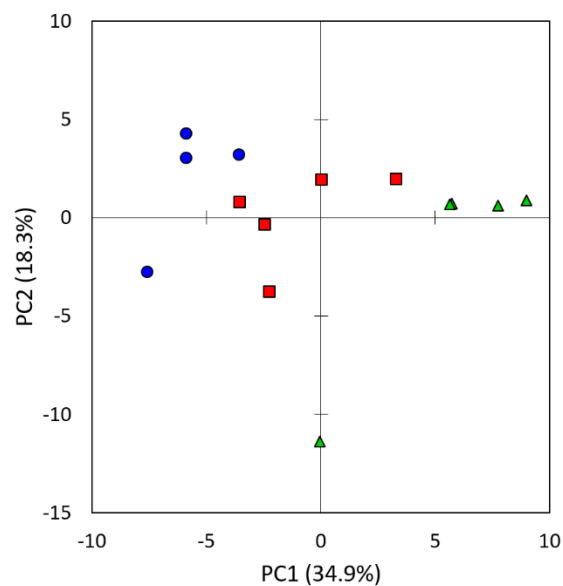


Figure S1.5. Two-dimensional PCA score plot derived from the ^1H NMR spectra of organic fraction of cell extract samples: control (green triangles), cisplatin (red squares), etoposide (blue circles); $n = 4$ for etoposide, $n = 5$ for control and cisplatin. The numbers in brackets represent the percentage of variability explain by each principal component (PC). Spectral pre-processed with total integral normalisation and pareto scaling.

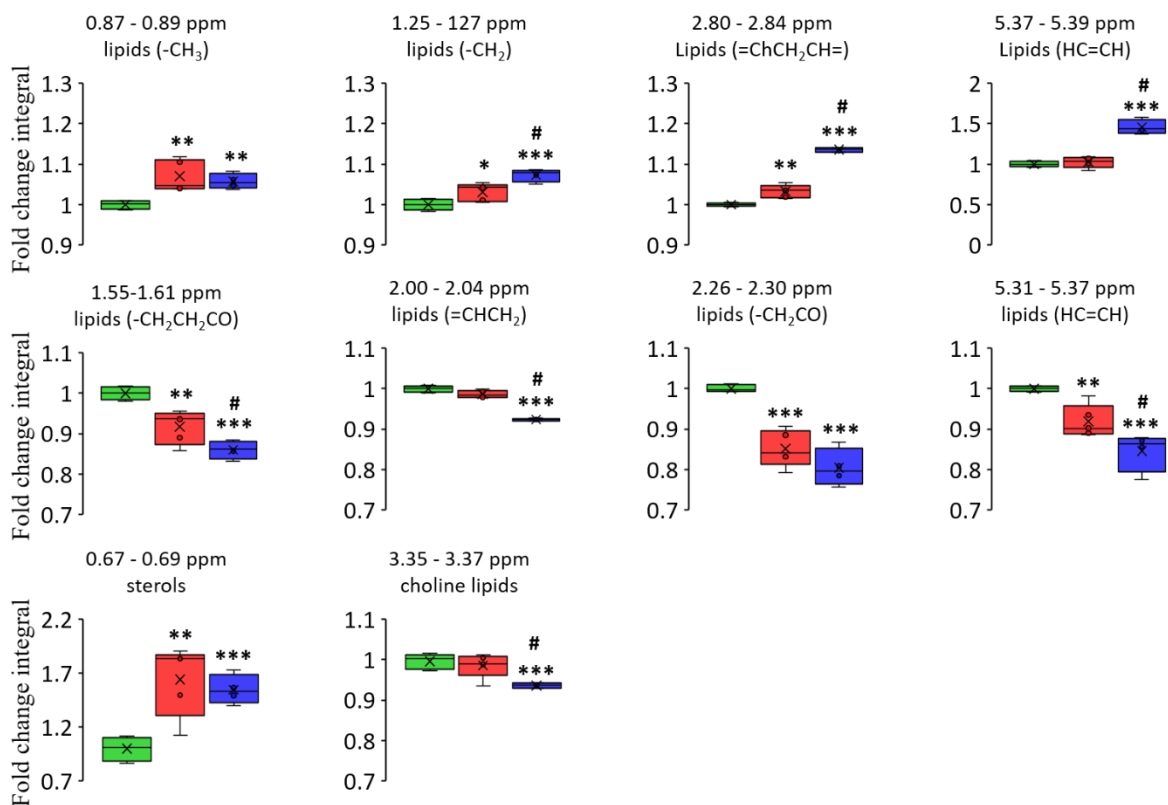


Figure S1.6. Comparison of fold change integral for selected lipids in organic fraction of cell extracts: control (green), cisplatin (red) and etoposide (blue). * $p < 0.05$, ** $p < 0.01$, *** $p < 0.001$ for control vs treatment; # $p < 0.05$ for cisplatin vs etoposide, FDR adjusted.

S1.2.3. Cell extract - aqueous fraction

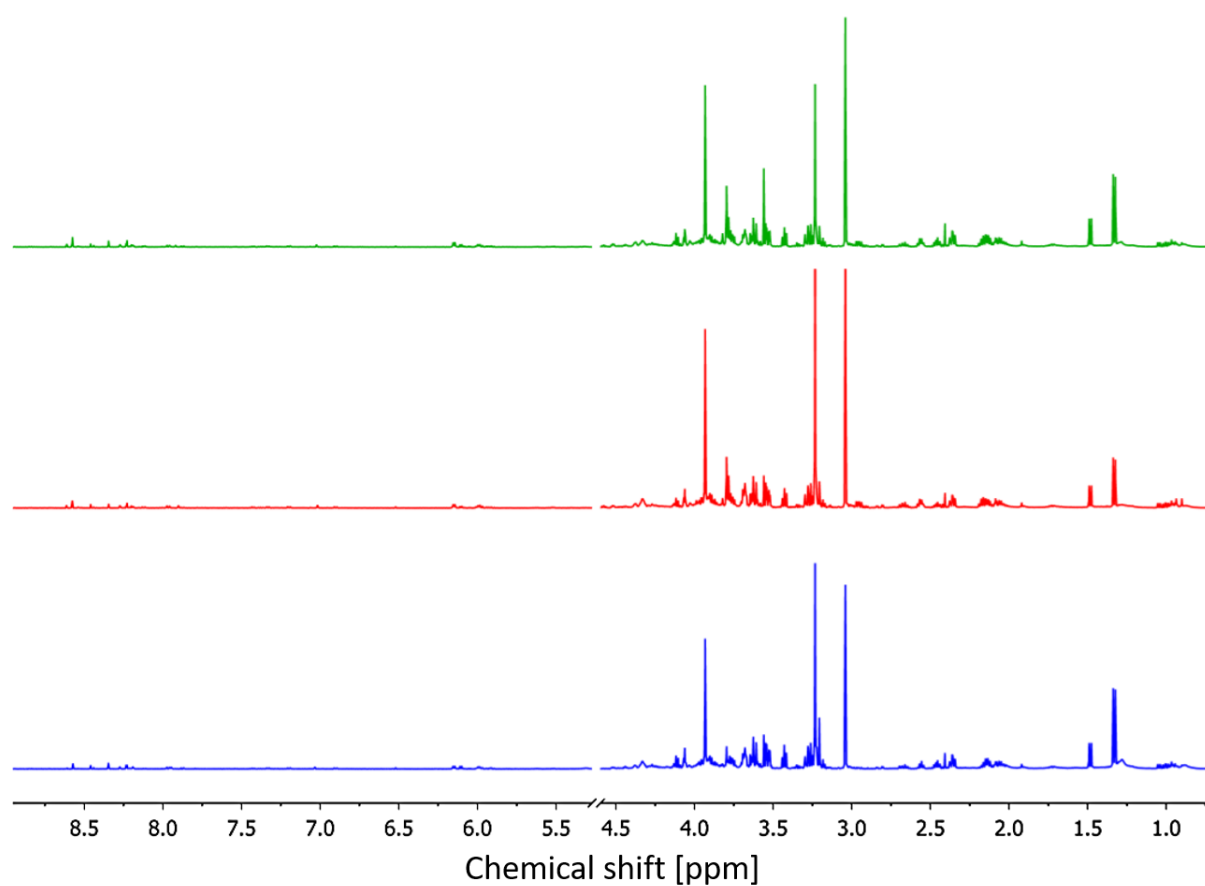


Figure S1.7. 500 MHz ¹H NMR spectra of cell extract (aqueous fraction) collected after 48 h of the following treatments: control (green), cisplatin (red) and etoposide (blue). All spectra were normalised to the total integral.

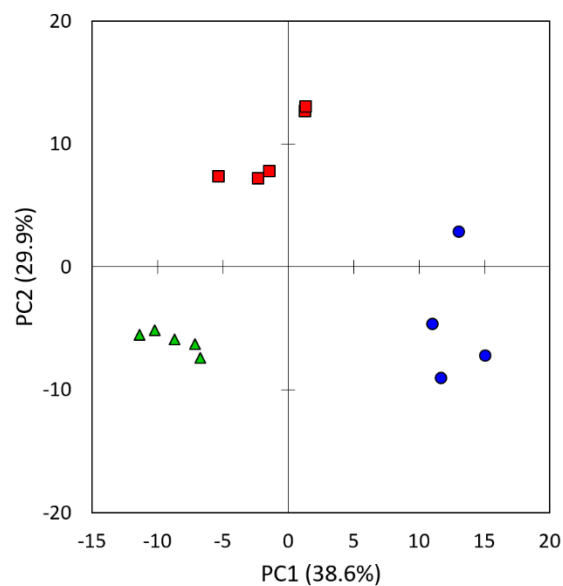


Figure S1.8. Two-dimensional PCA score plot derived from the ^1H NMR spectra of aqueous fraction of cell extract samples: control (green triangles), cisplatin (red squares), etoposide (blue circles); $n = 4$ for etoposide, $n = 5$ for control and cisplatin. The numbers in brackets represent the percentage of variability explain by each principal component (PC). Spectral pre-processed with total integral normalisation and Pareto scaling.

Table S1.3. Fold change integral for selected metabolites in aqueous fraction of cell extracts.
 * $p < 0.05$, ** $p < 0.01$, *** $p < 0.001$ for control vs treatment; # $p < 0.05$, for cisplatin vs etoposide, FDR adjusted.

Metabolite	Range [ppm]	Control		Cisplatin		Etoposide	
		Mean	SEM	Mean	SEM	Mean	SEM
Pantothenate	0.91 - 0.89	1.000	0.036	1.293*	0.103	0.819#	0.140
Pantothenate	0.94 - 0.93	1.000	0.022	1.718***	0.036	0.762***#	0.048
Isoleucine+ leucine	0.98 - 0.95	1.000	0.021	0.953	0.023	1.003	0.049
Valine	1.06 - 1.02	1.000	0.010	1.001	0.033	1.091	0.065
Lactate	1.34 - 1.32	1.000	0.028	0.723***	0.007	1.270***#	0.057
Alanine	1.50 - 1.47	1.000	0.006	0.828***	0.010	0.969#	0.036
Lysine	1.75 - 1.71	1.000	0.018	0.879**	0.019	0.948	0.037
Acetate	1.92 - 1.91	1.000	0.044	0.710*	0.095	0.777	0.087
Succinate	2.42 - 2.40	1.000	0.036	0.784***	0.018	0.814*	0.061
Glutamate	2.13 - 2.11	1.000	0.022	0.735***	0.016	0.844***#	0.019
Glutamate	2.39 - 2.34	1.000	0.019	0.808***	0.007	0.860***#	0.014
Glutamine	2.46 - 2.45	1.000	0.025	0.749***	0.020	0.968#	0.049
Glutathione	2.59 - 2.53	1.000	0.015	1.0488	0.010	0.542***#	0.008
Glutathione	3.01 - 2.99	1.000	0.021	0.877	0.065	0.583***#	0.015
DMA	2.69 - 2.66	1.000	0.011	0.964	0.069	0.844*	0.048
Creatine	3.05 - 3.03	1.000	0.015	1.138**	0.028	0.840***#	0.038
Creatine	3.94 - 3.92	1.000	0.012	1.149**	0.032	0.870*#	0.043
Choline	3.24 - 3.23	1.000	0.005	1.587***	0.055	1.388***	0.067
Myo-inositol	3.28 - 3.24	1.000	0.007	1.159*	0.069	1.280**	0.074
Myo-inositol	4.07 - 4.05	1.000	0.015	1.144**	0.039	1.374***#	0.044
Glucose	3.55 - 3.51	1.000	0.012	1.165**	0.047	1.279***	0.048
Glycine	3.56 - 3.55	1.000	0.011	0.486***	0.016	0.492***	0.010
ADP/ATP	4.40 - 4.36	1.000	0.029	0.834**	0.004	0.720***#	0.017
Fumarate	6.53 - 6.51	1.000	0.053	1.486**	0.132	1.408**	0.217
Tyrosine	6.92 - 6.88	1.000	0.015	1.161***	0.018	1.227*	0.081
Phenylalanine	7.35 - 7.32	1.000	0.024	1.037	0.016	1.036	0.068
Succinate	2.42 - 2.40	1.000	0.036	0.784**	0.018	0.814*	0.061

Appendix 2. Supporting information for Chapter 5

S2.1. T_2 bi-exponential fits

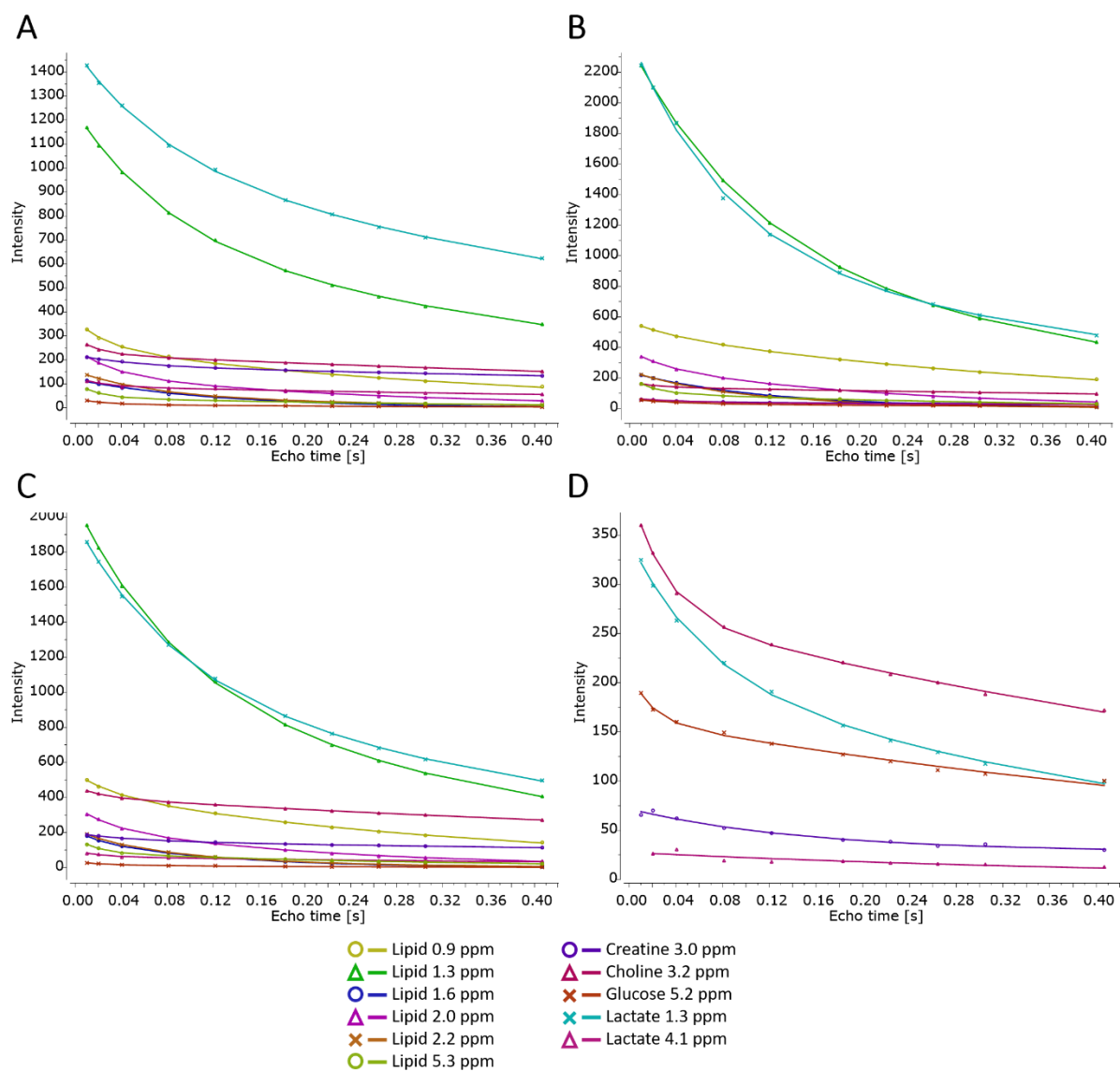


Figure S2.1. Representative examples of bi-exponential T_2 fits of signal intensity for selected metabolites versus echo time for control (A), cisplatin (B), etoposide (C) and heat (D) treated cells.

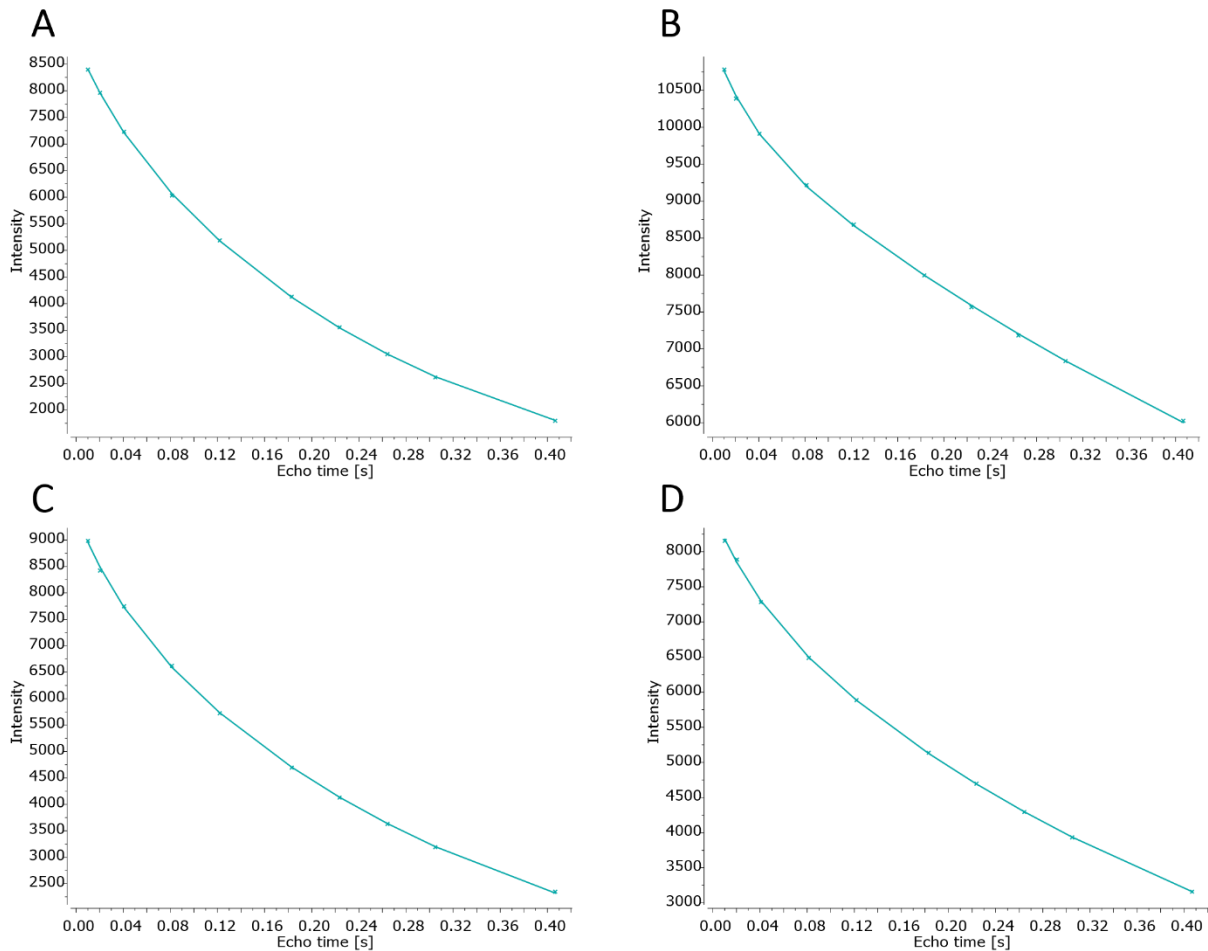


Figure S2.2. Representative examples of bi-exponential T_2 fits of signal intensity for water versus echo time for control (A), cisplatin (B), etoposide (C) and heat (D) treated cells.

S2.2. Fitting errors for T_2 bi-exponential model

$y(t) = B_1 \cdot \exp(-t \cdot F_1) + B_2 \cdot \exp(-t \cdot F_2) \rightarrow T_2 = 1/F_1$ or $1/F_2$, where: $y(t)$ – signal intensity; t – echo time; B_1, B_2, F_1, F_2 – empirical parameters; T_2 – T_2 relaxation time. The error is the quadratic error of the fit (error in values of ‘y’) ⁴⁰⁰

Lipid 0.9 ppm

$B_1=496.3; F_1=2.388; B_2=72.52; F_2=27.44; \text{error: } 4.598$

Lipid 1.3 ppm

$B_1=1042; F_1=2.335; B_2=1345; F_2=9.306; \text{error: } 8.333$

Lipid 1.6 ppm

$B_1=201.4; F_1=9.557; B_2=36.34; F_2=3.925; \text{error: } 1.603$

Lactate 1.3 ppm

$B_1=1032; F_1=1.923; B_2=1413; F_2=12.01; \text{error: } 65.17$

Lipid 2.0 ppm

$B_1=98.24; F_1=34.03; B_2=284.3; F_2=4.704; \text{error: } 5.457$

Lipid 2.2 ppm

B1=86.17; F1=16.91; B2=159.9; F2=7.381; error: 2.378

Creatine 3.0 ppm

B1=22.18; F1=22.24; B2=41.78; F2=0.8147; error: 2.154

Choline 3.25 ppm

B1=35.23; F1=49.20; B2=141.3; F2=0.9622; error: 1.930

Lactate 4.1 ppm

B1=36.93; F1=0.9127; B2=31.37; F2=19.86; error: 3.334

Glucose 5.2 ppm

B1=34.83; F1=2.452; B2=29.34; F2=32.61; error: 2.168

Lipid 5.3 ppm

B1=109.2; F1=58.45; B2=104.8; F2=3.023; error: 4.937

Water 4.7 ppm

B1=1066; F1=29.64; B2=1.010e+4; F2=1.279; error: 62.33

S2.3. Diffusion bi-exponential fits

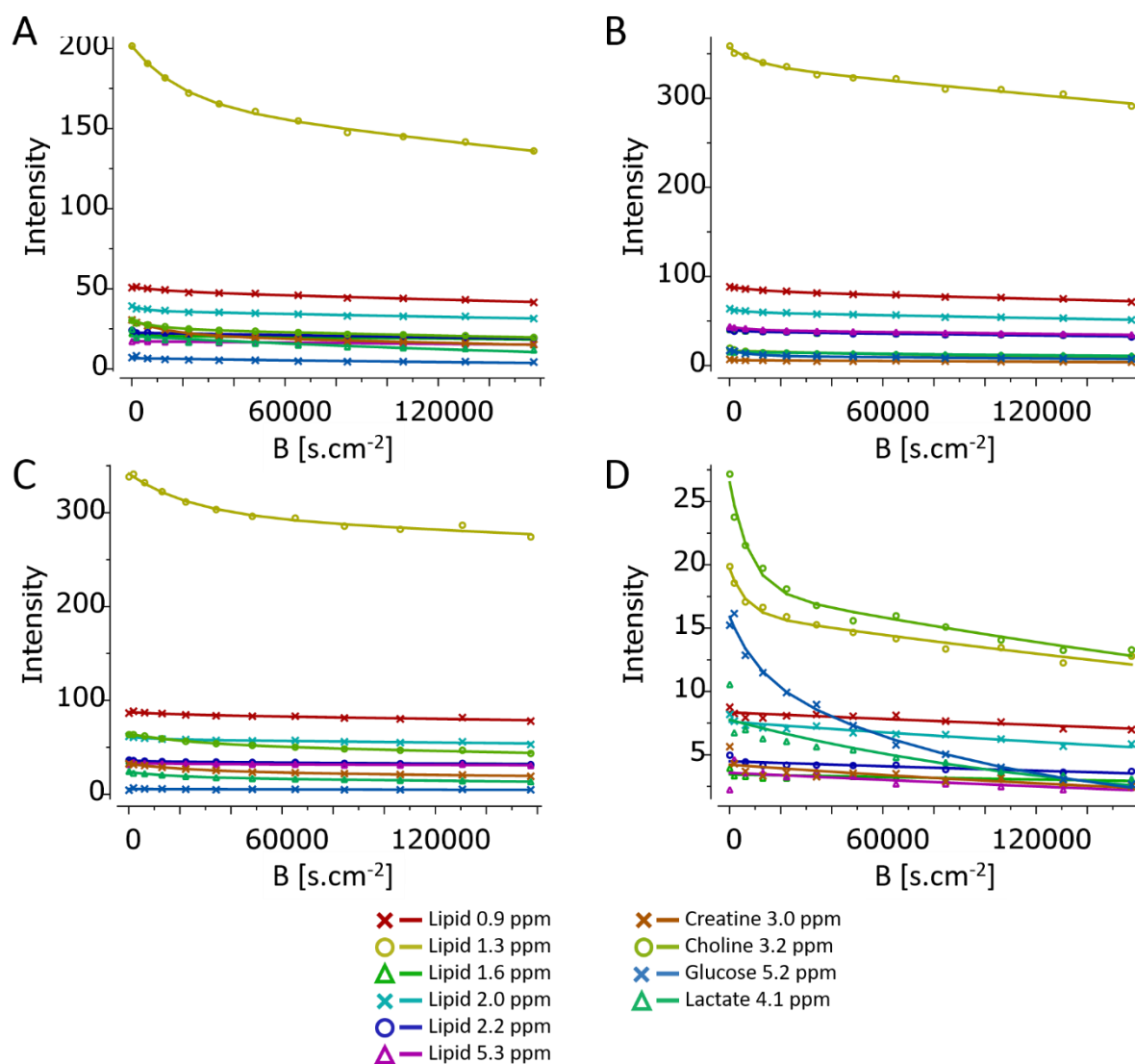


Figure S2.3. Representative examples of bi-exponential diffusion fits of signal intensity for selected metabolites versus b -value for control (A), cisplatin (B), etoposide (C) and heat treated cells (D).

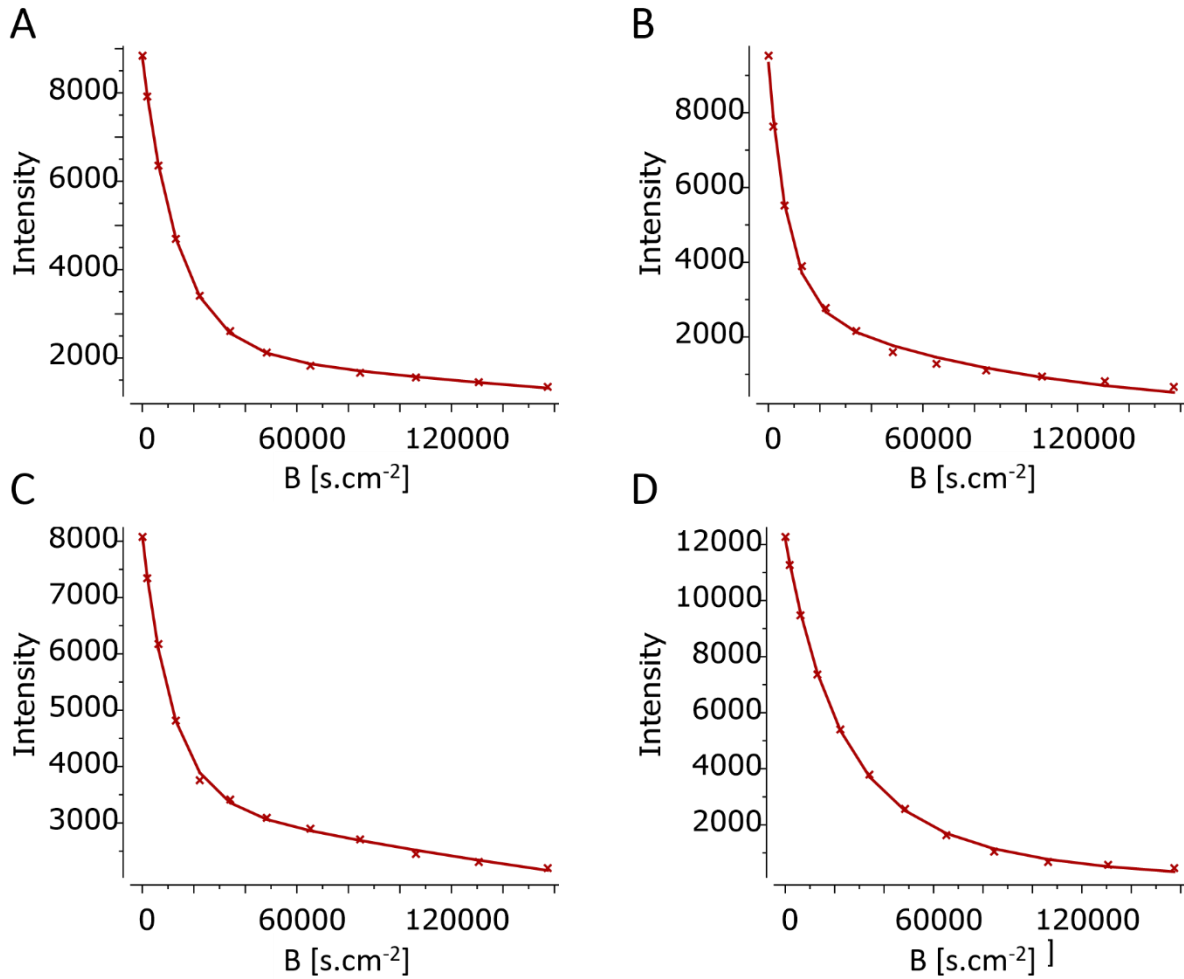


Figure S2.4. Representative examples of bi-exponential diffusion fits of signal intensity for water versus b-value for control (A), cisplatin (B), etoposide (C) and heat (D) treated cells.

S2.4. Fitting errors for diffusion bi-exponential model

$y(B) = B1 \cdot \exp(-B \cdot F1) + B2 \cdot \exp(-B \cdot F2)$, where: $y(B)$ – signal intensity; $B = \gamma^2 G^2 \delta^2 (\Delta - \delta/3)$; $B1, B2, F1, F2$ – empirical parameters; G – gradient strength, δ – gradient duration, Δ – diffusion time. The error is the quadratic error of the fit (error in values of ‘y’) ⁴⁰⁰.

Lipids 0.9 ppm

$B1=2.440$; $F1=0.00007596$; $B2=48.78$; $F2=9.914e-7$; Error: 1.199

Lipid 1.3 ppm

$B1=166.1$; $F1=0.000001270$; $B2=35.33$; $F2=0.00005059$; Error: 2.951

Lipid 1.6 ppm

$B1=1.444$; $F1=0.0001973$; $B2=20.68$; $F2=7.493e-7$; Error: 0.5361

Lipid 2.0 ppm

$B1=2.741$; $F1=0.0001806$; $B2=36.24$; $F2=8.991e-7$; Error: 1.225

Lipid 2.25 ppm

B1=1.792; F1=0.001903; B2=22.58; F2=0.000001104; Error: 0.5883

Lipid 5.3 ppm

B1=21.63; F1=8.186e-7; B2=-4.373; F2=8.186e-7; Error: 0.9697

Creatine 3.0 ppm

B1=9.063; F1=0.00007101; B2=21.38; F2=0.000002251; Error: 0.7377

Choline 3.25 ppm

B1=4.875; F1=0.00009306; B2=25.15; F2=0.000001574; Error: 0.8836

Lactate 4.1 ppm

B1=24.48; F1=0.000004201; B2=-4.073; F2=0.000004201; Error: 5.298

Glucose 5.2 ppm

B1=-15.56; F1=0.000003739; B2=22.28; F2=0.000003739; Error: 1.997

Water 4.7

B1=6556; F1=0.00007287; B2=2264; F2=0.000003424; Error: 116.9

S2.5. Signal to noise calculated for key resonances at the highest b-value for HRMAS NMR and high-gradient solution-state NMR spectroscopy.

For HRMAS NMR

Noise(mean) = 0.285 Noise(rms) = 0.095

PPM	INTENSITY	SNR
0.85	12.2	129.2
1.26	26.0	274.0
2.00	9.0	94.8
2.21	4.9	51.2
5.28	4.1	42.9

For high-gradient solution-state NMR

Noise(mean) = 0.635 Noise(rms) = 0.205

PPM	INTENSITY	SNR
0.91	7.1	34.8
1.31	6.4	31.3
2.03	6.8	33.1
2.29	4.4	21.3

S2.6. Contribution of non-lipid metabolites to apparent diffusion coefficients of mobile lipids.

The contribution of lactate at 1.3 ppm (and more broadly for other small, non-lipid metabolites) to the apparent diffusion of mobile lipids was excluded by taking advantage of the significant difference between the apparent diffusion coefficients of lipids and lactate. The attached figure shows two apparent diffusion coefficients calculated based on a model using a biexponential fit for the resonance at 1.3 ppm. The larger diffusion component ($1.37 \cdot 10^{-8} \text{ m}^2 \text{ s}^{-1}$) that corresponded to lactate was excluded from ADC calculations ($b > 124 \text{ s} \cdot \text{mm}^{-2}$). The ADC values for glucose and creatine in intact cells have been reported previously as $3\text{-}4 \cdot 10^{-8} \text{ m}^2 \text{ s}^{-1}$, and for lactate it is expected to be in a similar range. Moreover, we measured lactate accumulation during cisplatin and etoposide treatments. The NMR signal integral at 4.09 – 4.13 ppm did not increase much after 48 h of treatment, as shown in the below figure, and so we feel the majority of the signal intensity increase at 1.3 ppm is a change in the $-\text{CH}_2-$ lipid resonance intensity.

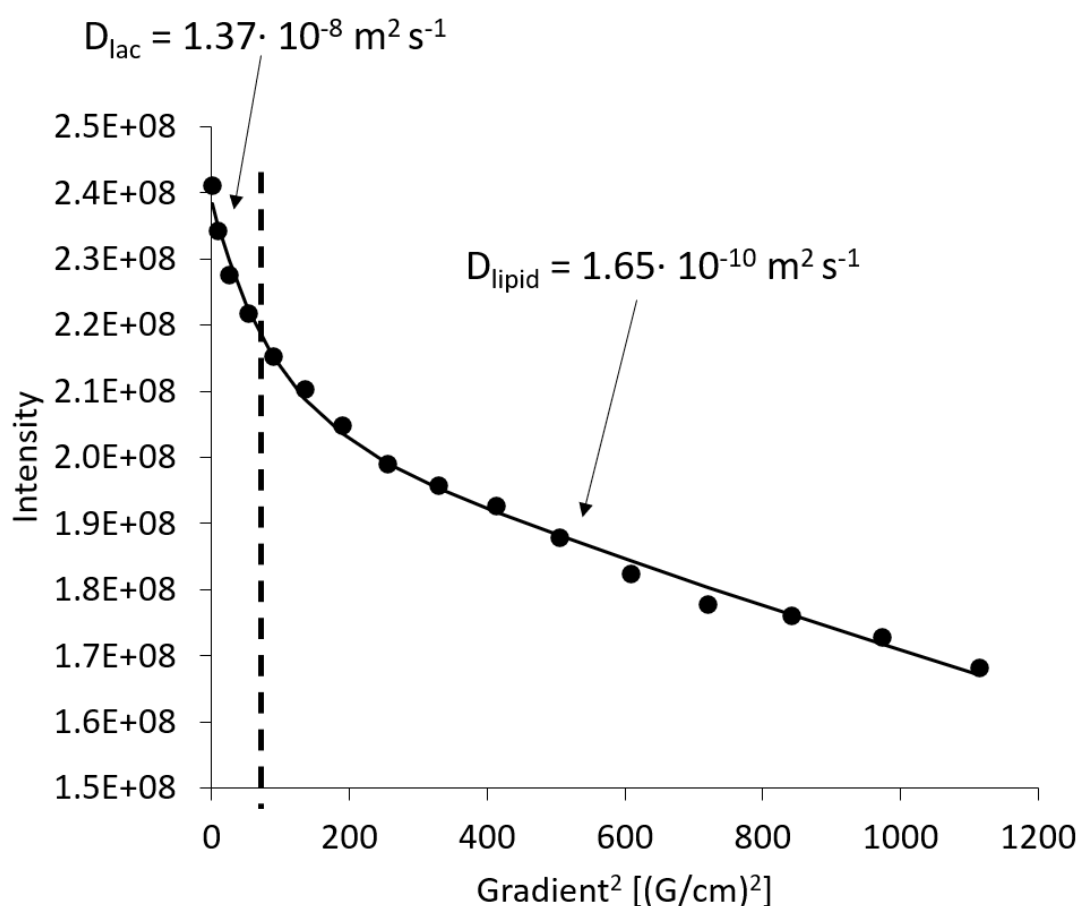


Figure S2.5. A biexponential diffusion fit for the $-\text{CH}_2$ signal at 1.3 ppm. The faster apparent diffusion component ($1.37 \cdot 10^{-8} \text{ m}^2/\text{s}$, corresponding to lactate and excluded from ADC calculations) ($b > 124 \text{ s} \cdot \text{mm}^{-2}$).

S2.7. Determination of cytoplasmic viscosity from the slope of the $D \sim \frac{1}{r}$ graph (Equation 5.4) presented in Table 5.6.

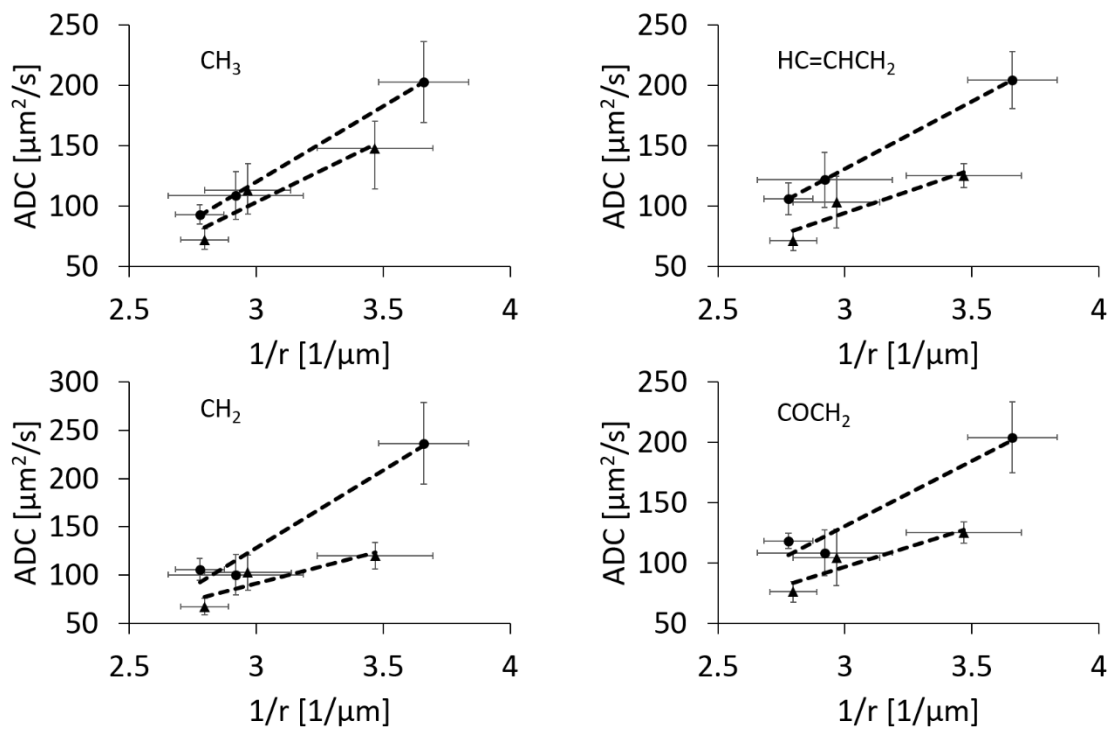


Figure S2.6. Correlation of LD size measured by fluorescence microscopy with diffusion coefficients measured by HRMAS ^1H NMR. ● 24 h and ▲ 48 h for four lipid signals.

Appendix 3. Supporting information for Chapter 6

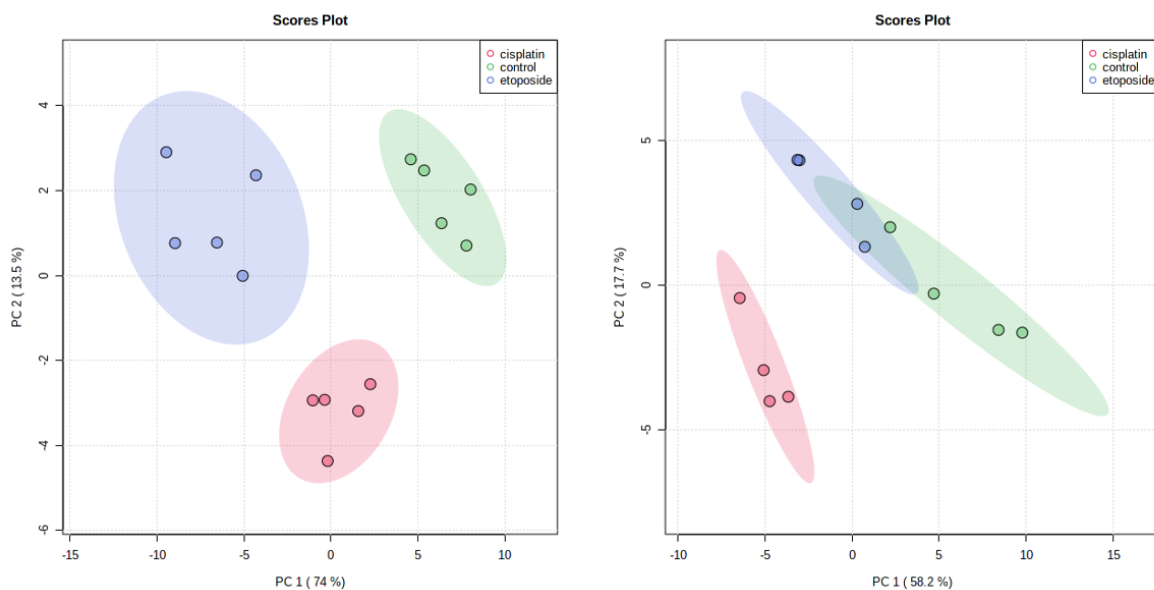


Figure S3.1. PCA analysis of TAG and DAG species extracted from A) isolated LDs and B) organic fraction of cell extracts for control (green), cisplatin (red), and etoposide (blue) samples. The analysis was performed after total sum normalization and Pareto scaling; $n = 5$ for isolated LD samples and $n = 4$ for cell extracts. The numbers in brackets represent the percentage of variability explained by each PC.

Table S3.1. TAG and DAGs species annotated from cell extracts treated with cisplatin and etoposide for 48h. Fold changes are reported relative to the control untreated samples. Included only lipid species with even number of carbon that formed NH₄ adducts. ANOVA: FRD-adjusted p-values, n≥3. Fisher's least significant difference (LSD) was used for ad hoc pairwise comparisons of the treatment groups. N/S – not significant; Lipid class (number of double bonds/ number of carbons)molecular weight_retention time [s]; cr – control, cis – cisplatin, eto – etoposide.

Lipid species	Degree of unsaturation	Control		Cisplatin		Etoposide		FDR p-value	Fisher's LSD
		Mean	SEM	Mean	SEM	Mean	SEM		
DG(32:0)586.5404_333.17	0.000	1.00	0.02	1.07	0.03	1.18	0.03	1.57E-02	eto - cis; eto - cr
DG(34:1)612.5509_336.95	0.029	1.00	0.07	0.89	0.06	0.64	0.02	1.02E-02	cis - eto; cr - eto
DG(34:2)610.5351_323.61	0.059	1.00	0.09	0.72	0.05	0.42	0.01	1.46E-03	cr - cis; cis - eto; cr - eto
DG(36:1)640.5816_350.57	0.028	1.00	0.06	0.87	0.03	0.54	0.05	2.30E-03	eto - cis; eto - cr
DG(38:3)664.5879_346.11	0.079	1.00	0.06	0.88	0.15	0.08	0.01	1.19E-03	eto - cis; eto - cr
DG(40:1)696.6456_335.36	0.025	1.00	0.06	1.21	0.08	1.64	0.05	1.46E-03	eto - cis; eto - cr
DG(42:3)720.6527_299.87	0.071	1.00	0.23	2.07	0.12	1.61	0.10	1.39E-02	cis - cr; eto - cr
TG(40:3)706.6029_351.99	0.075	1.00	0.05	0.69	0.02	0.27	0.09	5.16E-04	cr - cis; cis - eto; cr - eto
TG(44:0)768.7014_391.97	0.000	1.00	0.12	0.78	0.05	0.89	0.14	N/S	
TG(44:1)766.6862_384	0.023	1.00	0.07	1.09	0.08	1.17	0.16	N/S	
TG(46:0)796.7343_400.36	0.000	1.00	0.07	0.99	0.06	0.77	0.03	N/S	
TG(46:1)794.7186_392.05	0.022	1.00	0.04	1.09	0.03	1.02	0.01	N/S	
TG(46:2)792.7021_383.81	0.043	1.00	0.04	1.26	0.03	1.22	0.08	2.52E-02	cis - cr; eto - cr
TG(48:0)824.764_408.78	0.000	1.00	0.07	1.01	0.02	0.81	0.02	4.30E-02	cis - eto; cr - eto
TG(48:1)822.7471_400.01	0.021	1.00	0.02	1.18	0.03	0.96	0.03	9.57E-03	cis - cr; cis - eto
TG(48:2)820.733_392.08	0.042	1.00	0.04	1.24	0.02	1.12	0.05	3.64E-02	cis - cr
TG(48:3)818.7163_384.58	0.063	1.00	0.06	1.44	0.03	1.23	0.08	1.97E-02	cis - cr
TG(50:0)852.7957_414.2	0.000	1.00	0.12	0.87	0.02	0.75	0.01	N/S	
TG(50:1)850.7807_408.56	0.020	1.00	0.04	1.19	0.03	1.03	0.03	2.31E-02	cis - cr; cis - eto
TG(50:2)848.7711_403.26	0.040	1.00	0.04	1.25	0.03	1.15	0.04	1.01E-02	cr - cis; cr - eto
TG(50:3)846.7477_392.43	0.060	1.00	0.07	1.23	0.03	1.13	0.06	N/S	
TG(50:8)836.6841_351.78	0.160	1.00	0.02	0.56	0.03	0.30	0.03	5.34E-06	cr - cis; cis - eto; cr - eto
TG(52:0)880.8265_424.65	0.000	1.00	0.14	0.76	0.04	0.70	0.04	N/S	

TG(52:1)878.8119_416.29	0.019	1.00	0.04	1.04	0.04	0.97	0.01	9.01E-03	cr - cis; cr - eto
TG(52:10)860.6841_346.49	0.192	1.00	0.15	0.51	0.07	0.15	0.08	7.58E-03	cr - cis; cr - eto
TG(52:3)874.7844_400.05	0.058	1.00	0.05	1.20	0.03	1.26	0.03	1.26E-02	cr - cis; cr - eto
TG(52:4)872.7689_396.37	0.077	1.00	0.05	1.21	0.04	1.50	0.07	2.95E-03	cr - cis; cis - eto; cr - eto
TG(52:5)870.7474_389.55	0.096	1.00	0.07	1.29	0.05	1.17	0.05	4.28E-02	cis - cr
TG(54:0)908.8574_431.79	0.000	1.00	0.16	0.73	0.06	0.68	0.04	N/S	
TG(54:1)906.8501_428.15	0.019	1.00	0.02	0.80	0.02	0.72	0.04	1.86E-03	cr - cis; cr - eto
TG(54:2)904.8255_416.12	0.037	1.00	0.06	0.84	0.04	0.89	0.01	N/S	
TG(54:3)902.8084_405	0.056	1.00	0.06	0.83	0.04	0.82	0.02	N/S	
TG(54:4)900.7939_401.1	0.074	1.00	0.06	0.86	0.01	0.92	0.02	N/S	
TG(54:5)898.7801_394.41	0.093	1.00	0.09	1.52	0.04	1.41	0.05	1.48E-02	cr - cis; cr - eto
TG(54:6)896.7698_393.71	0.111	1.00	0.05	1.33	0.01	1.69	0.04	6.04E-05	cr - cis; cis - eto; cr - eto
TG(54:7)894.7494_386.61	0.130	1.00	0.09	1.29	0.07	1.15	0.05	N/S	
TG(56:0)936.8873_438.67	0.000	1.00	0.18	0.73	0.07	0.62	0.05	N/S	
TG(56:1)934.8724_430.97	0.018	1.00	0.07	0.86	0.03	0.81	0.00	N/S	
TG(56:2)932.8655_427.85	0.036	1.00	0.04	0.67	0.02	0.63	0.03	3.53E-04	cr - cis; cr - eto
TG(56:3)930.8387_411.94	0.054	1.00	0.08	0.64	0.03	0.79	0.03	3.96E-02	cr - cis
TG(56:4)928.8249_409.44	0.071	1.00	0.08	0.89	0.04	1.04	0.03	N/S	
TG(56:5)926.8099_402.89	0.089	1.00	0.08	0.92	0.03	1.06	0.04	N/S	
TG(56:6)924.795_397.98	0.107	1.00	0.08	0.97	0.02	1.10	0.04	N/S	
TG(56:7)922.7784_394.56	0.125	1.00	0.06	1.06	0.04	1.18	0.04	N/S	
TG(56:8)920.7622_387.14	0.143	1.00	0.09	1.03	0.07	1.05	0.04	N/S	
TG(58:1)962.9102_443.94	0.017	1.00	0.05	0.78	0.01	0.63	0.03	1.08E-03	cr - cis; cis - eto; cr - eto
TG(58:2)960.8879_430.06	0.034	1.00	0.08	0.74	0.04	0.68	0.03	4.76E-02	cr - cis; cr - eto
TG(58:3)958.8707_422.76	0.052	1.00	0.08	0.65	0.03	0.68	0.03	3.35E-02	cr - cis; cr - eto
TG(58:4)956.8547_415.95	0.069	1.00	0.06	0.62	0.02	0.81	0.03	8.53E-03	cr - cis; cis - eto; cr - eto
TG(58:5)954.8387_410.37	0.086	1.00	0.09	0.66	0.05	0.93	0.03	3.09E-02	cr - cis; eto - cis
TG(58:6)952.8238_405.36	0.103	1.00	0.09	0.77	0.03	1.11	0.02	1.95E-02	cr - cis; eto - cis
TG(58:7)950.8082_397.96	0.121	1.00	0.06	0.76	0.04	0.96	0.02	3.20E-02	cr - cis; eto - cis

TG(58:8)948.793_394.66	0.138	1.00	0.08	0.83	0.04	1.06	0.02	N/S	
TG(58:9)946.7783_387.89	0.155	1.00	0.13	1.00	0.08	1.12	0.06	N/S	
TG(60:2)988.9219_437.43	0.033	1.00	0.07	0.59	0.06	0.58	0.04	2.13E-02	cr - cis; cr - eto
TG(60:3)986.9038_429.93	0.050	1.00	0.10	0.51	0.04	0.50	0.03	1.48E-02	cr - cis; cr - eto
TG(60:4)984.8895_423.81	0.067	1.00	0.11	0.63	0.08	0.58	0.13	N/S	
TG(60:5)982.8789_422.33	0.083	1.00	0.05	0.45	0.01	0.67	0.04	1.79E-04	cr - cis; cis - eto; cr - eto
TG(60:6)980.8566_411.93	0.100	1.00	0.18	0.54	0.07	1.13	0.08	4.51E-02	cr - cis; eto - cis
TG(60:7)978.8398_405.14	0.117	1.00	0.09	0.61	0.09	1.02	0.04	3.20E-02	cr - cis; eto - cis
TG(62:4)1012.927_436.21	0.065	1.00	0.05	0.29	0.06	0.46	0.05	2.28E-04	cr - cis; cr - eto
TG(62:5)1010.9111_430.29	0.081	1.00	0.06	0.16	0.08	0.54	0.05	3.53E-04	cr - cis; cis - eto; cr - eto

Table S3.2. TAG and DAG species annotated from isolated lipid droplet from cells treated with cisplatin and etoposide for 48 h. Fold changes are reported relative to the control untreated samples. Included only lipid species with even number of carbon that formed NH₄ adducts. ANOVA: FRD-adjusted p-values, n≥3. Fisher's least significant difference (LSD) was used for ad hoc pairwise comparisons of the treatment groups. N/S – not significant; Lipid class (Number of carbons:number of double bonds)molecular weight_retention time [s]; cr – control, cis – cisplatin, eto – etoposide.

Lipid species	Degree of unsaturation	Control		Cisplatin		Etoposide		FDR	Fisher's LSD
		Mean	SEM	Mean	SEM	Mean	SEM	p-value	
DG(32:0)586.5391_343.92	0.000	1.00	0.02	1.05	0.03	2.71	0.06	5.21·10 ⁻¹¹	eto - cis; eto - cr
DG(32:1)584.5226_253.76	0.031	1.00	0.08	1.16	0.13	2.38	0.53	4.40·10 ⁻²	eto - cis; eto - cr
DG(34:1)612.5553_322.32	0.029	1.00	0.07	1.24	0.17	2.44	0.29	2.10·10 ⁻³	eto - cis; eto - cr
DG(34:2)610.5385_257.77	0.059	1.00	0.06	1.06	0.12	2.28	0.46	2.60·10 ⁻²	eto - cis; eto - cr
DG(36:0)642.6022_351.07	0.000	1.00	0.02	1.06	0.02	1.78	0.04	5.51·10 ⁻⁹	eto - cis; eto - cr
DG(36:1)640.5855_338.74	0.028	1.00	0.04	1.01	0.07	2.18	0.11	4.60·10 ⁻⁴	eto - cis; eto - cr
DG(36:2)638.5712_324.1	0.056	1.00	0.07	1.10	0.14	2.11	0.27	5.85·10 ⁻³	eto - cis; eto - cr
DG(36:3)636.5617_388.16	0.083	1.00	0.10	0.60	0.07	1.40	0.05	2.78·10 ⁻⁴	cr - cis; cis - eto; cr - eto
DG(36:4)634.5438_342.49	0.111	1.00	0.14	1.19	0.04	3.04	0.06	6.52·10 ⁻⁸	eto - cis; eto - cr
DG(38:3)664.5863_331.2	0.079	1.00	0.06	1.34	0.16	3.45	0.55	1.68·10 ⁻⁴	eto - cis; eto - cr
DG(38:4)662.5704_323.57	0.105	1.00	0.08	1.81	0.28	4.16	0.57	9.22·10 ⁻⁴	eto - cis; eto - cr
DG(40:1)696.6484_325.78	0.025	1.00	0.04	1.14	0.02	3.14	0.09	4.45·10 ⁻¹⁰	eto - cis; eto - cr
DG(46:1)780.7404_396.86	0.022	1.00	0.06	0.75	0.03	1.03	0.06	2.39·10 ⁻⁶	cr - cis; cis - eto; cr - eto
[TG(36:0)+NH4]656.5804_338.27	0.000	1.00	0.07	1.21	0.06	1.39	0.09	2.83·10 ⁻²	eto - cr
[TG(38:0)+NH4]684.612_358.52	0.000	1.00	0.06	1.19	0.05	1.66	0.09	3.52·10 ⁻⁴	eto - cis; eto - cr
[TG(42:0)+NH4]740.6742_375.27	0.000	1.00	0.03	0.48	0.01	0.41	0.01	1.49·10 ⁻⁸	cr - cis; cis - eto; cr - eto
[TG(42:1)+NH4]738.6594_366.68	0.024	1.00	0.04	0.40	0.01	0.32	0.03	2.62·10 ⁻⁷	cr - cis; cr - eto
[TG(44:0)+NH4]768.7064_384.37	0.000	1.00	0.02	0.67	0.01	0.63	0.02	7.14·10 ⁻⁷	cr - cis; cr - eto
[TG(44:1)+NH4]766.6891_376.04	0.023	1.00	0.04	0.55	0.01	0.43	0.03	6.79·10 ⁻⁷	cr - cis; cis - eto; cr - eto
[TG(44:2)+NH4]764.6741_367.57	0.045	1.00	0.03	0.51	0.01	0.38	0.03	5.60·10 ⁻⁷	cr - cis; cis - eto; cr - eto
[TG(46:0)+NH4]796.7372_391.61	0.000	1.00	0.01	1.10	0.03	1.14	0.04	4.86·10 ⁻²	eto - cr
[TG(46:1)+NH4]794.722_384.84	0.022	1.00	0.02	0.80	0.01	0.73	0.02	6.99·10 ⁻⁶	cr - cis; cis - eto; cr - eto

[TG(46:2)+NH4]792.705_376.71	0.043	1.00	0.04	0.73	0.01	0.57	0.04	$1.71 \cdot 10^{-5}$	cr - cis; cis - eto; cr - eto
[TG(46:3)+NH4]790.6898_368.55	0.065	1.00	0.04	0.79	0.08	0.41	0.07	$7.34 \cdot 10^{-4}$	eto - cis; eto - cr
[TG(46:4)+NH4]788.6733_364	0.087	1.00	0.08	0.79	0.04	0.57	0.04	$2.47 \cdot 10^{-3}$	cr - cis; cis - eto; cr - eto
[TG(48:0)+NH4]824.7675_401.42	0.000	1.00	0.02	1.62	0.04	1.70	0.07	$5.84 \cdot 10^{-6}$	cr - cis; cr - eto
[TG(48:1)+NH4]822.7511_392.58	0.021	1.00	0.01	1.13	0.03	1.18	0.02	$8.02 \cdot 10^{-4}$	cr - cis; cr - eto
[TG(48:2)+NH4]820.736_385.09	0.042	1.00	0.01	0.92	0.01	0.84	0.02	$7.75 \cdot 10^{-5}$	cr - cis; cis - eto; cr - eto
[TG(48:3)+NH4]818.7212_377.25	0.063	1.00	0.03	0.90	0.01	0.64	0.03	$2.70 \cdot 10^{-5}$	cr - cis; cis - eto; cr - eto
[TG(48:4)+NH4]816.7043_373.19	0.083	1.00	0.04	0.96	0.02	0.62	0.03	$6.31 \cdot 10^{-5}$	eto - cis; eto - cr
[TG(50:0)+NH4]852.7988_409.77	0.000	1.00	0.02	1.54	0.04	1.22	0.05	$2.82 \cdot 10^{-5}$	cr - cis; cis - eto; cr - eto
[TG(50:1)+NH4]850.7842_401.4	0.020	1.00	0.01	1.28	0.02	1.43	0.03	$6.49 \cdot 10^{-7}$	cr - cis; cis - eto; cr - eto
[TG(50:2)+NH4]848.7668_393.35	0.040	1.00	0.01	1.04	0.01	1.10	0.01	$3.22 \cdot 10^{-4}$	cr - cis; cis - eto; cr - eto
[TG(50:3)+NH4]846.7505_385.58	0.060	1.00	0.00	1.00	0.01	0.87	0.02	$1.77 \cdot 10^{-4}$	eto - cis; eto - cr
[TG(50:4)+NH4]844.7362_378.72	0.080	1.00	0.03	0.99	0.01	0.74	0.02	$3.23 \cdot 10^{-5}$	eto - cis; eto - cr
[TG(50:5)+NH4]842.7195_374.74	0.100	1.00	0.03	1.10	0.03	0.69	0.03	$2.13 \cdot 10^{-5}$	eto - cis; eto - cr
[TG(52:0)+NH4]880.8295_417.82	0.000	1.00	0.05	1.30	0.02	0.67	0.03	$3.46 \cdot 10^{-6}$	cr - cis; cis - eto; cr - eto
[TG(52:1)+NH4]878.8144_401.75	0.019	1.00	0.04	1.07	0.02	1.18	0.02	$5.97 \cdot 10^{-3}$	eto - cis; eto - cr
[TG(52:2)+NH4]876.7984_401.35	0.038	1.00	0.01	1.03	0.01	1.15	0.01	$1.37 \cdot 10^{-5}$	eto - cis; eto - cr
[TG(52:3)+NH4]874.7833_393.81	0.058	1.00	0.01	0.99	0.01	1.04	0.01	$1.83 \cdot 10^{-2}$	eto - cis; eto - cr
[TG(52:4)+NH4]872.7674_386.75	0.077	1.00	0.01	1.05	0.02	0.92	0.02	$6.50 \cdot 10^{-3}$	eto - cis; eto - cr
[TG(52:5)+NH4]870.75_383.18	0.096	1.00	0.02	1.19	0.02	0.93	0.02	$5.77 \cdot 10^{-5}$	cr - cis; eto - cis
[TG(52:7)+NH4]866.7202_371.74	0.135	1.00	0.03	1.17	0.05	0.74	0.03	$9.12 \cdot 10^{-5}$	cr - cis; cis - eto; cr - eto
[TG(54:0)+NH4]908.8622_425.52	0.000	1.00	0.04	1.06	0.01	0.46	0.02	$6.49 \cdot 10^{-7}$	eto - cis; eto - cr
[TG(54:1)+NH4]906.8451_417.45	0.019	1.00	0.05	0.91	0.05	0.73	0.06	$1.73 \cdot 10^{-2}$	eto - cis; eto - cr
[TG(54:2)+NH4]904.8293_409.52	0.037	1.00	0.02	0.84	0.01	0.80	0.04	$1.76 \cdot 10^{-3}$	cr - cis; cr - eto
[TG(54:4)+NH4]900.7972_394.98	0.074	1.00	0.01	0.96	0.01	1.10	0.02	$1.18 \cdot 10^{-4}$	eto - cis; eto - cr
[TG(54:5)+NH4]898.7831_388.15	0.093	1.00	0.03	1.19	0.01	1.06	0.02	$5.61 \cdot 10^{-4}$	cr - cis; eto - cis
[TG(54:6)+NH4]896.7666_383.9	0.111	1.00	0.03	1.25	0.03	1.11	0.01	$1.91 \cdot 10^{-4}$	cr - cis; cis - eto; cr - eto
[TG(54:7)+NH4]894.7524_380.32	0.130	1.00	0.03	1.23	0.05	1.04	0.02	$7.26 \cdot 10^{-3}$	cr - cis; eto - cis
[TG(54:8)+NH4]892.7359_372.3	0.148	1.00	0.03	1.22	0.05	0.75	0.03	$6.31 \cdot 10^{-5}$	cr - cis; cis - eto; cr - eto

[TG(56:0)+NH4]936.8867_425.71	0.000	1.00	0.05	0.79	0.04	0.50	0.06	2.79·10 ⁻⁴	cr - cis; cis - eto; cr - eto
[TG(56:1)+NH4]934.8779_424.84	0.018	1.00	0.04	0.68	0.02	0.54	0.05	4.98·10 ⁻⁵	cr - cis; cis - eto; cr - eto
[TG(56:2)+NH4]932.86_417.03	0.036	1.00	0.04	0.69	0.02	0.54	0.05	9.65·10 ⁻⁵	cr - cis; cis - eto; cr - eto
[TG(56:3)+NH4]930.8448_409.57	0.054	1.00	0.02	0.73	0.01	0.68	0.04	4.51·10 ⁻⁵	cr - cis; cr - eto
[TG(56:4)+NH4]928.8282_403.55	0.071	1.00	0.01	0.87	0.01	1.00	0.03	2.30·10 ⁻³	cr - cis; eto - cis
[TG(56:6)+NH4]924.7982_391.65	0.107	1.00	0.03	1.13	0.01	1.17	0.02	1.18·10 ⁻³	cr - cis; cr - eto
[TG(56:7)+NH4]922.7814_386.54	0.125	1.00	0.05	1.29	0.04	1.37	0.05	9.41·10 ⁻⁴	cr - cis; cr - eto
[TG(56:9)+NH4]918.7491_374.06	0.161	1.00	0.06	1.70	0.03	1.58	0.04	5.14·10 ⁻⁶	cr - cis; cr - eto
[TG(58:1)+NH4]962.9101_432.97	0.017	1.00	0.05	0.72	0.04	0.42	0.06	1.36·10 ⁻⁴	cr - cis; cis - eto; cr - eto
[TG(58:2)+NH4]960.8942_424.74	0.034	1.00	0.04	0.60	0.02	0.39	0.05	8.35·10 ⁻⁶	cr - cis; cis - eto; cr - eto
[TG(58:3)+NH4]958.8734_410.54	0.052	1.00	0.04	0.59	0.02	0.45	0.05	9.94·10 ⁻⁶	cr - cis; cis - eto; cr - eto
[TG(58:4)+NH4]956.8581_410.49	0.069	1.00	0.04	0.75	0.01	0.71	0.04	2.97·10 ⁻⁴	cr - cis; cr - eto
[TG(58:5)+NH4]954.8426_404.14	0.086	1.00	0.05	0.81	0.01	0.98	0.04	1.82·10 ⁻²	cr - cis; eto - cis
[TG(58:9)+NH4]946.781_382.03	0.155	1.00	0.07	1.39	0.05	1.36	0.03	1.76·10 ⁻³	cr - cis; cr - eto
[TG(60:10)+NH4]972.7986_382.96	0.167	1.00	0.15	1.65	0.05	1.93	0.09	6.51·10 ⁻⁴	cr - cis; cr - eto
[TG(60:11)+NH4]970.7835_379.06	0.183	1.00	0.09	1.73	0.07	2.00	0.10	8.65·10 ⁻⁵	cr - cis; cr - eto
[TG(60:2)+NH4]988.9228_432.26	0.033	1.00	0.06	0.50	0.03	0.30	0.05	8.00·10 ⁻⁶	cr - cis; cis - eto; cr - eto
[TG(60:3)+NH4]986.908_424.47	0.050	1.00	0.05	0.48	0.02	0.31	0.05	3.02·10 ⁻⁶	cr - cis; cis - eto; cr - eto
[TG(60:4)+NH4]984.8918_417.73	0.067	1.00	0.04	0.55	0.01	0.42	0.05	6.39·10 ⁻⁶	cr - cis; cis - eto; cr - eto
[TG(60:5)+NH4]982.8737_411.27	0.083	1.00	0.03	0.67	0.02	0.71	0.04	1.87·10 ⁻⁴	cr - cis; cr - eto
[TG(60:6)+NH4]980.86_407.23	0.100	1.00	0.03	0.81	0.01	0.92	0.06	3.78·10 ⁻²	cr - cis
[TG(60:7)+NH4]978.8448_399.3	0.117	1.00	0.05	0.85	0.01	1.05	0.05	4.91·10 ⁻²	eto - cis
[TG(62:12)+NH4]996.7965_379.01	0.194	1.00	0.05	1.39	0.09	1.67	0.10	1.93·10 ⁻³	cr - cis; cr - eto
[TG(62:2)+NH4]1016.9521_438.88	0.032	1.00	0.06	0.39	0.01	0.24	0.04	2.58·10 ⁻⁶	cr - cis; cis - eto; cr - eto
[TG(62:4)+NH4]1012.9215_425.14	0.065	1.00	0.05	0.45	0.02	0.29	0.05	3.02·10 ⁻⁶	cr - cis; cis - eto; cr - eto
[TG(62:5)+NH4]1010.9054_418.95	0.081	1.00	0.05	0.67	0.05	0.48	0.06	4.14·10 ⁻⁴	cr - cis; cis - eto; cr - eto
[TG(62:9)+NH4]1002.8443_395.94	0.145	1.00	0.08	0.83	0.05	1.31	0.10	1.16·10 ⁻²	eto - cis; eto - cr
[TG(64:2)+NH4]1044.9881_445.8	0.031	1.00	0.05	0.48	0.03	0.25	0.04	2.31·10 ⁻⁶	cr - cis; cis - eto; cr - eto
[TG(64:3)+NH4]1042.9705_438.48	0.047	1.00	0.05	0.40	0.02	0.21	0.03	7.14·10 ⁻⁷	cr - cis; cis - eto; cr - eto

[TG(64:4)+NH4]1040.9562_432.38	0.063	1.00	0.06	0.46	0.02	0.27	0.04	4.32·10 ⁻⁶	cr - cis; cis - eto; cr - eto
[TG(64:6)+NH4]1036.9223_422.24	0.094	1.00	0.05	0.51	0.02	0.39	0.05	1.17·10 ⁻⁵	cr - cis; cr - eto
[TG(64:7)+NH4]1034.9078_415.05	0.109	1.00	0.03	0.64	0.06	0.58	0.07	8.99·10 ⁻⁴	cr - cis; cr - eto

Table S3.3. Normalised read count for differentially expressed genes related to programmed cell death in the cells treated with cisplatin or etoposide versus controls. SEM represent biological variance (n = 4). ANOVA: FRD-adjusted p-values; Fisher's least significant difference (LSD) was used for ad hoc pairwise comparisons of the treatment groups. Green and orange backgrounds indicate upregulation and downregulation, respectively, compared to the controls; cr – control, cis – cisplatin, eto- etoposide.

Pathway	Gene	Control		Cisplatin		Etoposide		FDR p-values	Fisher's LSD
		Mean	SEM	Mean	SEM	Mean	SEM		
NRIF signals cell death from the nucleus	Sqstm1	13184	104	30261	336	25987	221	1.70·10 ⁻⁹	cr - cis cis - eto cr - eto
Apoptotic cleavage of cellular proteins, Caspase-mediated cleavage of cytoskeletal proteins, Apoptotic execution phase	Gsn	10113	301	13369	172	12862	563	1.67·10 ⁻³	cis - cr eto - cr
Intrinsic Pathway for Apoptosis, BH3-only proteins associate with and inactivate anti-apoptotic BCL-2 members	Stat3	7640.	209	9991	34	9793	198	4.44·10 ⁻⁵	cis - cr eto - cr
Regulation of Apoptosis, Stimulation of the cell death response by PAK-2p34, Apoptotic execution phase	Pak2	4754	85	5530	40	4859	147	3.01·10 ⁻³	cr - cis eto - cis
FOXO-mediated transcription of cell death genes, NR1H3 & NR1H2 regulate gene expression linked to cholesterol transport and efflux	Ep300	4492	248	6067	109	5533	281	7.90·10 ⁻³	cis - cr eto - cr
NF-kB activation through FADD/RIP-1 pathway mediated by caspase-8 and -10	Ikbkg	4050	63	5980	166	5965	131	2.02·10 ⁻⁵	cis - cr eto - cr
TP53 Regulates Transcription of Caspase Activators and Caspases, NF-kB activation through FADD/RIP-1 pathway mediated by caspase-8 and -10, FasL/CD95L signaling, Regulated Necrosis, Dimerization of procaspase-8, Caspase activation via extrinsic apoptotic signalling pathway, Caspase activation via Death Receptors in the presence of ligand, TP53 Regulates Transcription of Cell Death Genes	Cflar	3267	59	3661	66	4650	124	3.28·10 ⁻⁵	cr - cis cis - eto cr - eto
Apoptotic execution phase, Apoptotic cleavage of cellular proteins	Ptk2	2786	43	4776	136	4139	54	3.02·10 ⁻⁶	cr - cis cis - eto

									cr - eto
Apoptotic cleavage of cellular proteins, Apoptotic execution phase, Intrinsic Pathway for Apoptosis, Cytochrome c-mediated apoptotic response, Caspase-mediated cleavage of cytoskeletal proteins, Activation of caspases through apoptosome-mediated cleavage, Stimulation of the cell death response by PAK-2p34, Caspase activation via Dependence Receptors in the absence of ligand, Caspase activation via extrinsic apoptotic signalling pathway, Apoptosis induced DNA fragmentation, Apoptotic cleavage of cell adhesion proteins, SMAC(DIABLO)-mediated dissociation of IAP:caspase complexes	Casp3	2502	73	3373	44	3670	58	6.75·10 ⁻⁶	cr - cis cis - eto cr - eto
TRIF-mediated programmed cell death, Caspase activation via Death Receptors in the presence of ligand, Caspase activation via extrinsic apoptotic signalling pathway	Tlr4	2381	105	3651	113	4616	105	6.01·10 ⁻⁶	cr - cis cis - eto cr - eto
Intrinsic Pathway for Apoptosis, Release of apoptotic factors from the mitochondria, Activation, translocation and oligomerization of BAX, TP53 Regulates Transcription of Cell Death Genes	Bax	1946	80	4066	147	2444	288	3.64·10 ⁻⁴	cr - cis eto - cis
NF-kB activation through FADD/RIP-1 pathway mediated by caspase-8 and -10	Chuk	1760	41	2138	35	2423	126	2.99·10 ⁻³	cis - cr eto - cr
NRIF signals cell death from the nucleus	Traf6	1413	27	1721	8	1510	39	4.08·10 ⁻⁴	cr - cis eto - cis
TLR3-mediated TICAM1-dependent programmed cell death, NF-kB activation through FADD/RIP-1 pathway mediated by caspase-8 and -10, Regulated Necrosis, TNFR1-induced proapoptotic signaling, Dimerization of procaspase-8, TRIF-mediated programmed cell death, Caspase activation via extrinsic apoptotic signalling pathway, Caspase activation via Death Receptors in the presence of ligand	Ripk1	1041	29	1064	9	1290	62	9.15·10 ⁻³	eto - cis eto - cr
Intrinsic Pathway for Apoptosis, Cytochrome c-mediated apoptotic response, SMAC(DIABLO)-mediated dissociation of IAP:caspase complexes, TP53 Regulates Transcription of Caspase Activators and Caspases, TP53 Regulates Transcription of Cell Death Genes, Activation of caspases through apoptosome-mediated cleavage	Apaf1	914	61	1914	60	2093	97	2.39·10 ⁻⁵	cis - cr eto - cr
DAG and IP3 signaling, Apoptotic execution phase, Apoptotic cleavage of cellular proteins	Prkcd	911	26	1255	27	2108	38	6.89·10 ⁻⁸	cr - cis cis - eto cr - eto
Apoptotic cleavage of cellular proteins, Regulated Necrosis, Apoptotic execution phase	Birc2	814	31	1334	26	1260	57	9.63·10 ⁻⁵	cr - cis eto - cis
FOXO-mediated transcription of cell death genes	Ddit3	513	20	985	11	998	51	2.26·10 ⁻⁵	cis - cr

TLR3-mediated TICAM1-dependent programmed cell death, NF-kB activation through FADD/RIP-1 pathway mediated by caspase-8 and -10, FasL/ CD95L signaling, Regulated Necrosis, TNFR1-induced proapoptotic signaling, Dimerization of procaspase-8, TRIF-mediated programmed cell death, Caspase activation via extrinsic apoptotic signalling pathway, Caspase activation via Death Receptors in the presence of ligand	Fadd	305	6	410	10	369	6	9.66·10 ⁻⁵	eto - cr cr - cis cis - eto cr - eto
Apoptotic execution phase, Apoptotic cleavage of cellular proteins	Pparg	242	18	332	12	454	32	1.30·10 ⁻³	cr - cis cis - eto cr - eto
FasL/ CD95L signaling, Regulated Necrosis, Dimerization of procaspase-8, Caspase activation via extrinsic apoptotic signalling pathway, Fatty acyl-CoA biosynthesis, NR1H2 & NR1H3 regulate gene expression linked to lipogenesis, Caspase activation via Death Receptors in the presence of ligand	Fas	169	14	509	24	426	14	8.12·10 ⁻⁶	cr - cis cis - eto cr - eto
Apoptotic cleavage of cellular proteins, Apoptotic cleavage of cell adhesion proteins, Apoptotic execution phase	Cdh1	114	5	145	6	363	6	3.05·10 ⁻⁸	cr - cis cis - eto cr - eto
Intrinsic Pathway for Apoptosis, FOXO-mediated transcription of cell death genes, TP53 Regulates Transcription of Cell Death Genes, BH3-only proteins associate with and inactivate anti-apoptotic BCL-2 members	Bbc3	108	13	245	13	147	15	8.97·10 ⁻⁴	cr - cis eto - cis
Apoptosis induced DNA fragmentation	Dffb	39	4	89	8	109	6.10	3.90·10 ⁻⁴	cis - cr eto - cr
TP53 Regulates Transcription of Cell Death Genes, TP53 Regulates Transcription of Caspase Activators and Caspases	Casp1	36	6	40	3	129	12.02	1.37·10 ⁻⁴	eto - cis eto - cr
Intrinsic Pathway for Apoptosis, Activation, translocation and oligomerization of BAX, Release of apoptotic factors from the mitochondria	Dhdh	35	2	44	2	83	4	1.89·10 ⁻⁵	eto - cis eto - cr
TP53 Regulates Transcription of Cell Death Genes, TP53 regulates transcription of several additional cell death genes whose specific roles in p53-dependent apoptosis remain uncertain	Perp	23	1	221	6	672	12	5.89·10 ⁻⁹	cr - cis cis - eto cr - eto
Regulated Necrosis	Birc3	6	1	8	1	21	1	6.62·10 ⁻⁵	eto - cis eto - cr
NRIF signals cell death from the nucleus	Ngfr	6	2	16	1	140	6	4.61·10 ⁻⁸	eto - cis eto - cr
Caspase-mediated cleavage of cytoskeletal proteins	Vim	73328	1611	71829	867	80975	2601	3.40·10 ⁻²	eto - cis eto - cr
Intrinsic Pathway for Apoptosis	Ywhah	7759	92	7690	91	9570	155	1.43·10 ⁻⁵	eto - cis

										eto - cr
Intrinsic Pathway for Apoptosis, Cytochrome c-mediated apoptotic response, SMAC(DIABLO)-mediated dissociation of IAP:caspase complexes , Regulated Necrosis, Activation of caspases through apoptosome-mediated cleavage	Xiap	2798	52	2783	115	3471	185	1.81·10 ⁻²		eto - cis eto - cr
Intrinsic Pathway for Apoptosis	Akt3	2026	55	965	37	2078	76	4.39·10 ⁻⁶		cr - cis eto - cis
TP53 Regulates Transcription of Caspase Activators and Caspases, TP53 Regulates Transcription of Cell Death Genes	Atm	885	48	702	75	1067	55	1.84·10 ⁻²		eto - cis cr - cis
Intrinsic Pathway for Apoptosis, BH3-only proteins associate with and inactivate anti-apoptotic BCL-2 members	Bcl2	611	16	130	6	945	29	5.15·10 ⁻⁸		cis - eto cr - eto
Regulated Necrosis	Mkl1	497	22	487	11	638	25	3.10·10 ⁻³		eto - cis eto - cr
Apoptotic cleavage of cellular proteins, Caspase-mediated cleavage of cytoskeletal proteins, Apoptotic execution phase	Gas2	320	18	58	6	328	33	9.29·10 ⁻⁵		cr - cis eto - cis
TLR3-mediated TICAM1-dependent programmed cell death, TRIF-mediated programmed cell death, Regulated Necrosis	Ripk3	176	6	131	11	177	12	3.69·10 ⁻²		cr - cis eto - cis
NRIF signals cell death from the nucleus	Ngf	64	3	51	3	149	6	2.05·10 ⁻⁶		eto - cis eto - cr
Regulated Necrosis, Dimerization of procaspase-8, Caspase activation via extrinsic apoptotic signalling pathway, Caspase activation via Death Receptors in the presence of ligand	Tnfsf10	5	1	2	0.3	23	4	1.90·10 ⁻³		eto - cis eto - cr
Apoptotic cleavage of cellular proteins, Breakdown of the nuclear lamina, Apoptotic execution phase	Lmna	15679	1253	16520	788	5688	836	2.39·10 ⁻⁴		eto - cis eto - cr
Intrinsic Pathway for Apoptosis	Akt2	11894	149	12956	149	6436	119	1.79·10 ⁻⁸		cr - cis cis - eto cr - eto
Regulation of Apoptosis	Psmc4	4307	66	5732	69	3258	19	3.55·10 ⁻⁸		cr - cis cis - eto cr - eto
FOXO-mediated transcription of cell death genes, TP53 Regulates Transcription of Cell Death Genes, TP53 regulates transcription of several additional cell death genes whose specific roles in p53-dependent apoptosis remain uncertain	Bcl6	3253	50	3454	59	842	16	4.23·10 ⁻⁹		cr - cis cis - eto cr - eto
Intrinsic Pathway for Apoptosis, TP53 Regulates Transcription of Cell Death Genes, BH3-only proteins associate with and inactivate anti-apoptotic BCL-2 members	Pmaip1	3104	76	3804	45	3020	74	1.67·10 ⁻⁴		cr - cis eto - cis

NRIF signals cell death from the nucleus	Psen1	3057	67	3191	65	2449	61	2.40·10 ⁻⁴	eto - cis eto - cr
FOXO-mediated transcription of cell death genes	Foxo3	2659	53	3477	41	2608	43	5.27·10 ⁻⁶	cr - cis eto - cis
Intrinsic Pathway for Apoptosis, Activation and oligomerization of BAK protein, Release of apoptotic factors from the mitochondria	Bak1	2445	81	2732	59	1802	89	2.35·10 ⁻⁴	cr - cis cis - eto cr - eto
FOXO-mediated transcription of cell death genes	Stk11	2434	115	3509	71	1785	133	3.84·10 ⁻⁵	cr - cis cis - eto cr - eto
Intrinsic Pathway for Apoptosis, Activation, myristoylation of BID and translocation to mitochondria, Activation, translocation and oligomerization of BAX, TP53 Regulates Transcription of Cell Death Genes, Activation and oligomerization of BAK protein, BH3-only proteins associate with and inactivate anti-apoptotic BCL-2 members	Bid	2257	25	3517	94	1220	32	8.36·10 ⁻⁸	cr - cis cis - eto cr - eto
Intrinsic Pathway for Apoptosis, Cytochrome c-mediated apoptotic response, Release of apoptotic factors from the mitochondria, SMAC(DIABLO)-mediated dissociation of IAP:caspase complexes	Diablo	2019	65	2418	73	1834	52	1.50·10 ⁻³	cr - cis eto - cis
FOXO-mediated transcription of cell death genes	Crebbp	1703	41	2156	55	1552	158	1.51·10 ⁻²	cr - cis eto - cis
TNFR1-induced proapoptotic signaling	Tnfaip3	1189	37	1224	2	1063	17	7.71·10 ⁻³	eto - cis eto - cr
Intrinsic Pathway for Apoptosis, Cytochrome c-mediated apoptotic response, SMAC(DIABLO)-mediated dissociation of IAP:caspase complexes , Activation of caspases through apoptosome-mediated cleavage, Caspase activation via Dependence Receptors in the absence of ligand, Caspase activation via extrinsic apoptotic signalling pathway	Casp9	1066	15	1159	34	974	45	2.97·10 ⁻²	cis - eto eto - cis
Apoptosis induced DNA fragmentation, Apoptotic execution phase	Dffa	1036	29	1097	17	920	31	1.02·10 ⁻²	eto - cis eto - cr
TP53 Regulates Transcription of Cell Death Genes	Triap1	980	17	1057	30	876	12	2.63·10 ⁻³	eto - cis eto - cr
Intrinsic Pathway for Apoptosis, BH3-only proteins associate with and inactivate anti-apoptotic BCL-2 members	Bad	875	77	966	60	600	82	3.86·10 ⁻²	eto - cis eto - cr
Apoptotic cleavage of cellular proteins, Apoptotic execution phase, TP53 Regulates Transcription of Caspase Activators and Caspases, Breakdown of the	Casp6	654	24	688	19	498	34	5.35·10 ⁻³	eto - cis eto - cr

nuclear lamina, TP53 Regulates Transcription of Cell Death Genes, Phospholipid metabolism, Caspase-mediated cleavage of cytoskeletal proteins										
Regulated Necrosis, Dimerization of procaspase-8, Caspase activation via extrinsic apoptotic signalling pathway, Caspase activation via Death Receptors in the presence of ligand	Tradd	469	23	496	30	365	28	4.54·10 ⁻²	cis - cr eto - cr	
Intrinsic Pathway for Apoptosis	Ywhae	29187	516	22536	433	16045	223	2.90·10 ⁻⁷	cr - cis cis - eto cr - eto	
Intrinsic Pathway for Apoptosis	Ywhag	14362	243	14115	239	9358	441	1.97·10 ⁻⁵	eto - cis eto - cr	
Intrinsic Pathway for Apoptosis	Akt1	11409	245	9678	161	6459	161	1.26·10 ⁻⁶	cr - cis cis - eto cr - eto	
Intrinsic Pathway for Apoptosis	Ywhaq	9861	146	9406	199	8965	178	4.11·10 ⁻²	cr - eto	
Intrinsic Pathway for Apoptosis	Ywhab	9276	66	7812	181	7910	194	7.57·10 ⁻⁴	cis - cr eto - cr	
Apoptosis induced DNA fragmentation, Apoptotic execution phase	Hmgb1	4000	190	2197	57	2069	78	1.94·10 ⁻⁵	cis - cr eto - cr	
Intrinsic Pathway for Apoptosis, Cytochrome c-mediated apoptotic response, Suppression of apoptosis	Mapk3	3334	94	2764	99	2704	147	1.90·10 ⁻²	cis - cr eto - cr	
NRIF signals cell death from the nucleus, Intrinsic Pathway for Apoptosis	Mapk8	2189	53	1991	22	1781	50	1.57·10 ⁻³	cr - cis cis - eto cr - eto	
Regulated Necrosis, TNFR1-induced proapoptotic signaling, Dimerization of procaspase-8, Caspase activation via extrinsic apoptotic signalling pathway, Caspase activation via Death Receptors in the presence of ligand	Traf2	1437.00	32.92	1230.85	20.04	753.40	41	4.39·10 ⁻⁶	cr - cis cis - eto cr - eto	
TP53 regulates transcription of several additional cell death genes whose specific roles in p53-dependent apoptosis remain uncertain, TP53 Regulates Transcription of Cell Death Genes	Birc5	1359	29	79	5	50	3	5.89·10 ⁻⁹	cis - cr eto - cr	
Apoptotic cleavage of cellular proteins, Breakdown of the nuclear lamina, Apoptotic execution phase	Lmnb1	1352	37	340	12	323	9	1.67·10 ⁻⁸	cis - cr eto - cr	
Intrinsic Pathway for Apoptosis, Cytochrome c-mediated apoptotic response, SMAC(DIABLO)-mediated dissociation of IAP:caspase complexes , Release of apoptotic factors from the mitochondria, Activation of caspases through apoptosome-mediated cleavage	Cyca	1164	26	1145	16	967	53	1.66·10 ⁻²	cr - cis eto - cis	

Apoptotic cleavage of cellular proteins, Apoptotic execution phase, Intrinsic Pathway for Apoptosis, TLR3-mediated TICAM1-dependent programmed cell death, NF-kB activation through FADD/RIP-1 pathway mediated by caspase-8 and -10, FasL/ CD95L signaling, Activation, myristoylation of BID and translocation to mitochondria, Regulated Necrosis, TNFR1-induced proapoptotic signaling, Dimerization of procaspase-8, TRIF-mediated programmed cell death, Caspase activation via extrinsic apoptotic signalling pathway, Caspase activation via Death Receptors in the presence of ligand, Caspase-mediated cleavage of cytoskeletal proteins	Casp8	884	10	628	14	804	18	$1.48 \cdot 10^{-5}$	cr - cis cis - eto cr - eto
Apoptotic execution phase	Hmgb2	869	28	166	14	161	16	$6.74 \cdot 10^{-8}$	cis - cr eto - cr
TP53 Regulates Transcription of Cell Death Genes, TP53 Regulates Transcription of Caspase Activators and Caspases	Casp2	676	31	483	19	667	45	$1.30 \cdot 10^{-2}$	cr - cis eto - cis
Cytochrome c-mediated apoptotic response, Intrinsic Pathway for Apoptosis	Aven	579	22	230	6	410	22	$9.88 \cdot 10^{-6}$	cr - cis cis - eto cr - eto
NRIF signals cell death from the nucleus	Alg3	566	7	413	11	308	16	$3.45 \cdot 10^{-6}$	cr - cis cis - eto cr - eto
Apoptotic cleavage of cellular proteins, Apoptotic execution phase, Intrinsic Pathway for Apoptosis, Apoptotic factor-mediated response, Cytochrome c-mediated apoptotic response, SMAC(DIABLO)-mediated dissociation of IAP:caspase complexes , Activation of caspases through apoptosome-mediated cleavage, Caspase-mediated cleavage of cytoskeletal proteins	Casp7	304	15	181	11	292	7	$3.64 \cdot 10^{-4}$	cr - cis eto - cis

Table S3.4. Normalised read count for differentially expressed genes related to lipid metabolism in the cells treated with cisplatin or etoposide versus controls. SEM represent biological variance (n = 4). ANOVA: FRD-adjusted p-values; Fisher's least significant difference (LSD) was used for ad hoc pairwise comparisons of the treatment groups. Green and orange backgrounds indicate upregulation and downregulation, respectively, compared to the controls; cr – control, cis – cisplatin, eto- etoposide.

Pathway	Gene	Control		Cisplatin		Etoposide		FDR p-values	Fisher's LSD
		mean	SEM	mean	SEM	mean	SEM		
Glycosphingolipid metabolism, Biosynthesis of the N-glycan precursor (dolichol lipid-linked oligosaccharide, LLO) and transfer to a nascent protein	Ctsa	7096	137	7281	43	8423	70	3.87·10 ⁻⁵	eto - cis eto - cr
Regulation of lipid metabolism by PPARalpha, alpha-linolenic (omega3) and linoleic (omega6) acid metabolism, Beta-oxidation of very long chain fatty acids, Peroxisomal lipid metabolism	Acox1	6664	43	8425	70	7678	26	1.47·10 ⁻⁷	cr - cis cis - eto cr - eto
Glycosphingolipid metabolism	Hexa	6203	74	7206	119	7570	150	2.86·10 ⁻⁴	cis - cr eto - cr
Lipophagy, Regulation of lipid metabolism by PPARalpha	Plin2	5521	129	17360	500	22035	858	5.28·10 ⁻⁷	cr - cis cis - eto cr - eto
Regulation of lipid metabolism by PPARalpha, Regulation of cholesterol biosynthesis by SREBP (SREBF)	Sp1	5153	209	6026	165.33	6298	91	6.46·10 ⁻³	cis - cr eto - cr
Phospholipid metabolism, Glycerophospholipid biosynthesis	Abhd4	5066	100	10067	107	8057	197	1.47·10 ⁻⁷	cr - cis cis - eto cr - eto
Regulation of lipid metabolism by PPARalpha, FOXO-mediated transcription of cell death genes, NR1H3 & NR1H2 regulate gene expression linked to cholesterol transport and efflux	Ep300	4492	248	6067	109	5533	281	7.90·10 ⁻³	cis - cr eto - cr
Phospholipid metabolism, Inositol phosphate metabolism	Pten	4324	109	6538	138	6100	233	3.87·10 ⁻⁵	cis - cr eto - cr
Fatty acid metabolism, mitochondrial fatty acid beta-oxidation of saturated fatty acids	Acadvl	3777	66	4950	44	4657	29	1.72·10 ⁻⁶	cr - cis cis - eto cr - eto

Regulation of lipid metabolism by PPARalpha, Fatty acid metabolism, mitochondrial fatty acid beta-oxidation of unsaturated fatty acids, mitochondrial fatty acid beta-oxidation of saturated fatty acids	Acadm	3721	79	3851	122	4351	67	7.25·10 ⁻³	eto - cis eto - cr
Plasma lipoprotein clearance	Npc1	2394	80	2917	60.69	3116	125	3.74·10 ⁻³	cis - cr eto - cr
Glycosphingolipid metabolism	Gba	2169	40	2660	15	2481	26	3.87·10 ⁻⁵	cr - cis cis - eto cr - eto
Plasma lipoprotein remodeling, NR1H3 & NR1H2 regulate gene expression linked to cholesterol transport and efflux	Pltp	1913	86.	4334	60	5641	119	5.41·10 ⁻⁸	cr - cis cis - eto cr - eto
Plasma lipoprotein remodeling, Regulation of lipid metabolism by PPARalpha	Angptl4	1860	19	2992	93	3943	147	6.28·10 ⁻⁶	cr - cis cis - eto cr - eto
ABC transporters in lipid homeostasis	Abca7	1814	64	2851	57	3042	227	1.41·10 ⁻³	cis - cr eto - cr
Phospholipid metabolism	Pikfyve	1735	43	2275	51	3023	91	8.27·10 ⁻⁶	cr - cis cis - eto cr - eto
Triglyceride catabolism	Abhd5	1717	39	2388	45	2588	26	1.96·10 ⁻⁶	cr - cis cis - eto cr - eto
Glycosphingolipid metabolism	Cerk	1712	19	2256	45	2587	77	2.61·10 ⁻⁵	cr - cis cis - eto cr - eto
Fatty acid metabolism, Regulation of lipid metabolism by PPARalpha	Cpt2	1251	49	1333	27	1470	22	1.44·10 ⁻²	eto - cis eto - cr
Phospholipid metabolism, Glycerophospholipid biosynthesis	Taz	1239	32	1423	63	1567	35	7.36·10 ⁻³	cis - cr eto - cr
Lipophagy, Fatty acid metabolism	Prkaa2	1065	35	1524	15	1218.91	38.40	6.15·10 ⁻⁵	cr - cis cis - eto cr - eto
Glycosphingolipid metabolism	Galc	1052	30	1266	41	1823	68	3.23·10 ⁻⁵	cr - cis cis - eto cr - eto

Plasma lipoprotein assembly, ABC transporters in lipid homeostasis	Abca3	930	13	998	12	1312	22	1.65·10 ⁻⁶	cr - cis cis - eto cr - eto
Glycerophospholipid biosynthesis, Acyl chain remodeling of DAG and TAG, Phospholipid metabolism	Pnpla2	879	28	1370	4	1157	50	6.06·10 ⁻⁵	cr - cis cis - eto cr - eto
Glycosphingolipid metabolism, Biosynthesis of the N-glycan precursor (dolichol lipid-linked oligosaccharide, LLO) and transfer to a nascent protein	Neu1	854	30	1604	82	1424	82	4.22·10 ⁻⁴	cis - cr eto - cr
Plasma lipoprotein clearance	Ldlrap1	835	56	1131	31	841	67	1.47·10 ⁻²	cr - cis eto - cis
Glycerophospholipid catabolism, Phospholipid metabolism	Pnpla6	771	62	1213	32	1084	48	1.59·10 ⁻³	cis - cr eto - cr
Glycerophospholipid biosynthesis, Tag biosynthesis, Acyl chain remodeling of DAG and TAG, Phospholipid metabolism	Dgat1	768	28	962	27	856	6	2.76·10 ⁻³	cr - cis cis - eto cr - eto
TAG biosynthesis, Phospholipid metabolism, Glycerophospholipid biosynthesis	Lpin1	652	7	1625	40	1269	21	1.08·10 ⁻⁷	cr - cis cis - eto cr - eto
Phospholipid metabolism, Glycerophospholipid biosynthesis	Agpat2	571	16	956	17	625	23	4.18·10 ⁻⁶	cr - cis eto - cis
Fatty acid metabolism, Synthesis of 15-eicosatetraenoic acid derivatives, Synthesis of Prostaglandins (PG) and Thromboxanes (TX), Biosynthesis of DPA-derived SPMs, Biosynthesis of electrophilic omega-3 PUFA oxo-derivatives, Biosynthesis of DHA-derived SPMs, Biosynthesis of EPA-derived SPMs, Arachidonic acid metabolism	Ptgs2	508	31	1078	49	3024	143	5.21·10 ⁻⁷	cr - cis cis - eto cr - eto
Fatty acid metabolism, Mitochondrial Fatty Acid Beta-Oxidation	Mmaa	485	10	664	19	795	8	2.25·10 ⁻⁶	cr - cis cis - eto cr - eto
Sphingolipid de novo biosynthesis	Sphk1	479	20	511	17	676	59	2.59·10 ⁻²	eto - cis eto - cr
Glycosphingolipid metabolism	Gla	441	37	883	22	902	36	3.83·10 ⁻⁵	cis - cr eto - cr

Phospholipid metabolism	Nqo1	349	7	678	8	1421	47	$7.81 \cdot 10^{-8}$	cr - cis cis - eto cr - eto
Glycosphingolipid metabolism	Gba2	323	21	420	18	388	11	$2.45 \cdot 10^{-2}$	cis - cr eto - cr
Lipid particle organization	Hilpda	315	10	585	14	812	12	$6.20 \cdot 10^{-8}$	cr - cis cis - eto cr - eto
Regulation of lipid metabolism by PPARalpha, Apoptotic execution phase, Apoptotic cleavage of cellular proteins	Pparg	242	18	332	12	454	32	$1.30 \cdot 10^{-3}$	cr - cis cis - eto cr - eto
Glycerophospholipid biosynthesis	Gpd1	211	9	381	11	255	13	$3.59 \cdot 10^{-5}$	cr - cis cis - eto cr - eto
Glycerophospholipid biosynthesis, TAG biosynthesis, Acyl chain remodeling of DAG and TAG, Phospholipid metabolism	Dgat2	198	19	445	21	260	21	$1.97 \cdot 10^{-4}$	cr - cis eto - cis
Regulation of cholesterol biosynthesis by SREBP (SREBF), FasL/CD95L signaling, Regulated Necrosis, Dimerization of procaspase-8, Caspase activation via extrinsic apoptotic signalling pathway, Fatty acyl-CoA biosynthesis, NR1H2 & NR1H3 regulate gene expression linked to lipogenesis, Caspase activation via Death Receptors in the presence of ligand, Fatty acid metabolism	Fas	169	14	509	24	426	14	$8.12 \cdot 10^{-6}$	cr - cis cis - eto cr - eto
Regulation of lipid metabolism by PPARalpha	Tnfrsf21	158	5	191	3	251	7	$1.43 \cdot 10^{-5}$	cr - cis cis - eto cr - eto
Glycosphingolipid metabolism, Biosynthesis of the N-glycan precursor (dolichol lipid-linked oligosaccharide, LLO) and transfer to a nascent protein	Neu3	153	3	180	8	173	3	$3.67 \cdot 10^{-2}$	cis - cr cr - cis cis - eto cr - eto
Fatty acyl-CoA biosynthesis, Fatty acid metabolism	Elovl4	128	4	162	4	226	6	$5.54 \cdot 10^{-6}$	eto - cis eto - cr
Plasma lipoprotein remodeling, ABC transporters in lipid homeostasis, NR1H3 & NR1H2 regulate gene expression linked to cholesterol transport and efflux	Abcg1	100	10	120	9	260	12	$2.33 \cdot 10^{-5}$	

Transport of fatty acids, NR1H3 & NR1H2 regulate gene expression linked to cholesterol transport and efflux	Apod	73	5	145	7	257	13	$6.75 \cdot 10^{-6}$	cr - cis cis - eto cr - eto
Triglyceride catabolism	Lipe	67	5	181	13	418	43	$1.02 \cdot 10^{-4}$	cr - cis cis - eto cr - eto
Peroxisomal lipid metabolism	Acox2	19	5	21	2	75	7	$1.19 \cdot 10^{-4}$	eto - cis eto - cr
Fatty acid metabolism, Biosynthesis of DPAn-6 SPMs, Synthesis of Hepoxilins (HX) and Trioxilins (TrX), Synthesis of 12-eicosatetraenoic acid derivatives, Synthesis of Lipoxins (LX), Biosynthesis of specialized proresolving mediators (SPMs), Biosynthesis of DPA-derived SPMs, Biosynthesis of DHA-derived SPMs, Arachidonic acid metabolism	Alox12	9	0.5	15	1	83	3	$7.85 \cdot 10^{-8}$	eto - cis eto - cr
Fatty acid metabolism, Synthesis of 15-eicosatetraenoic acid derivatives, Arachidonic acid metabolism	Aloxe3	4	2	12	2	52	3	$6.56 \cdot 10^{-6}$	eto - cis eto - cr
Plasma lipoprotein clearance	Soat2	3	1	7	1	24	2	$2.95 \cdot 10^{-5}$	eto - cis eto - cr
Lipid particle organization	Cidea	1.24	1	3	1	33	4	$4.48 \cdot 10^{-5}$	eto - cis eto - cr
Triglyceride catabolism, NR1H2 & NR1H3 regulate gene expression linked to triglyceride lipolysis in adipose	Plin1	1	0.5	2	0.6	22	4	$5.47 \cdot 10^{-4}$	eto - cis eto - cr
Plasma lipoprotein clearance, Plasma lipoprotein assembly, Plasma lipoprotein remodeling	Apob	1	0.3	5	1	105	11	$1.14 \cdot 10^{-5}$	eto - cis eto - cr
Fatty acid metabolism, Biosynthesis of DHA-derived SPMs, Arachidonic acid metabolism, Synthesis of epoxy (EET) and dihydroxyeicosatrienoic acids (DHET)	Ephx2	1	0.4	1	0.5	67	3	$1.03 \cdot 10^{-7}$	eto - cis eto - cr
NR1H2 & NR1H3 regulate gene expression linked to lipogenesis, Plasma lipoprotein remodeling	Angptl3	0.6	0.5	2	1	30	3	$2.43 \cdot 10^{-5}$	eto - cis eto - cr

Fatty acid metabolism, Biosynthesis of DPAn-6 SPMs, Synthesis of Hepoxilins (HX) and Trioxilins (TrX), Synthesis of 12-eicosatetraenoic acid derivatives, Synthesis of 15-eicosatetraenoic acid derivatives, Synthesis of Lipoxins (LX), Biosynthesis of specialized proresolving mediators (SPMs), Biosynthesis of DPA-derived SPMs, Biosynthesis of DHA-derived SPMs, Biosynthesis of EPA-derived SPMs, Arachidonic acid metabolism	Alox15	0.3	0.2	0.4	0.3	83	10	2.44·10 ⁻⁵	eto - cis eto - cr
Plasma lipoprotein remodeling	Cidec	0.0	0.0	0.0	0.0	20	2.32	6.15·10 ⁻⁵	eto - cis eto - cr
Phospholipid metabolism, Glycerophospholipid biosynthesis	Cfi	0.0	0.0	0.2	0.2	23	3	8.50·10 ⁻⁵	eto - cis eto - cr
Fatty acid metabolism, Synthesis of 15-eicosatetraenoic acid derivatives, Biosynthesis of DHA-derived SPMs, Biosynthesis of EPA-derived SPMs, Arachidonic acid metabolism, Synthesis of 5-eicosatetraenoic acids	Gpx4	9264	458	11570	263	8364	564	6.19·10 ⁻³	cr - cis eto - cis
Fatty acid metabolism, mitochondrial fatty acid beta-oxidation of unsaturated fatty acids, mitochondrial fatty acid beta-oxidation of saturated fatty acids	Acadl	7763	183	9425	177	6744	118	2.71·10 ⁻⁵	cr - cis cis - eto cr - eto
Glycerophospholipid biosynthesis, mitochondrial fatty acid beta-oxidation of unsaturated fatty acids, Phospholipid metabolism, mitochondrial fatty acid beta-oxidation of saturated fatty acids, Fatty acid metabolism, Fatty acid metabolism	Hadha	6630	177	6789	145	5911	187	2.97·10 ⁻²	eto - cis eto - cr
Free fatty acids regulate insulin secretion, Fatty acyl-CoA biosynthesis, Intracellular metabolism of fatty acids regulates insulin secretion, Fatty acid metabolism	Acsl3	6430	114	7818	116	4812	167	3.68·10 ⁻⁶	cr - cis cis - eto cr - eto
Regulation of cholesterol biosynthesis by SREBP (SREBF), Fatty acyl-CoA biosynthesis, NR1H2 & NR1H3 regulate gene expression linked to lipogenesis, Fatty acid metabolism	Fasn	4569	118	6115	126	3179	353	1.65·10 ⁻⁴	cr - cis cis - eto cr - eto
Phospholipid metabolism, Glycerophospholipid biosynthesis	Gnpat	4568	25	4809	84	2890	89	5.96·10 ⁻⁷	eto - cis eto - cr
Phospholipid metabolism	Fig4	4175	50	5421	129	1598	30	2.26·10 ⁻⁸	cr - cis cis - eto cr - eto

Phospholipid metabolism, Glycerophospholipid biosynthesis	Stard7	3631	70	4360	132	2496	126	2.73·10 ⁻⁵	cr - cis cis - eto cr - eto
Peroxisomal lipid metabolism, Fatty acid metabolism	Crat	3344	271	3970	181	2204	213	4.03·10 ⁻³	eto - cis eto - cr
Biosynthesis of the N-glycan precursor (dolichol lipid-linked oligosaccharide, LLO) and transfer to a nascent protein	Dhdds	2623	59	3094	44	1717	49	8.60·10 ⁻⁷	cr - cis cis - eto cr - eto
Biosynthesis of the N-glycan precursor (dolichol lipid-linked oligosaccharide, LLO) and transfer to a nascent protein	Mpi	2460	69	2890	85	1495	44	5.77·10 ⁻⁶	cr - cis cis - eto cr - eto
Sphingolipid de novo biosynthesis, Lysosphingolipid and LPA receptors	Plpp1	2261	66	3335	81	1379	29	3.43·10 ⁻⁷	cr - cis cis - eto cr - eto
Glycerophospholipid biosynthesis, mitochondrial fatty acid beta-oxidation of unsaturated fatty acids, Phospholipid metabolism, mitochondrial fatty acid beta-oxidation of saturated fatty acids	Hadh	2045	14	2288	25	1319	23	2.40·10 ⁻⁸	cr - cis cis - eto cr - eto
Glycosphingolipid metabolism	Smpd1	1910	34	2185	39	1724	65	1.20·10 ⁻³	cr - cis cis - eto cr - eto
Regulation of cholesterol biosynthesis by SREBP (SREBF)	Scap	1859	138	2658	82	1759	127	3.09·10 ⁻³	cr - cis eto - cis
Fatty acid metabolism, mitochondrial fatty acid beta-oxidation of saturated fatty acids	Acads	1762	117	1885	61	1062	107	1.83·10 ⁻³	eto - cis eto - cr
Regulation of lipid metabolism by PPARalpha, Regulation of cholesterol biosynthesis by SREBP (SREBF), FOXO-mediated transcription of cell death genes	Crebbp	1703	41	2156	55	1552	158.27	1.51·10 ⁻²	cr - cis eto - cis
Regulation of lipid metabolism by PPARalpha, Regulation of cholesterol biosynthesis by SREBP (SREBF), NR1H2 & NR1H3 regulate gene expression linked to lipogenesis	Srebf1	1494	47	1514	17	1004	99.86	1.95·10 ⁻³	eto - cis eto - cr
Lipophagy	Prkab1	1196	45	1296	6	1028	12	9.04·10 ⁻⁴	cr - cis; cis - eto cr - eto

Glycosphingolipid metabolism	Smpd2	1084	13	1384	19	982	12	8.48·10 ⁻⁷	cr - cis; cis - eto cr - eto
Fatty acid metabolism, ABC transporters in lipid homeostasis, Linoleic acid (LA) metabolism, alpha-linolenic (omega3) and linoleic (omega6) acid metabolism, Beta-oxidation of very long chain fatty acids, Peroxisomal lipid metabolism	Abcd1	1011	29	1145	22.02	927	32	4.33·10 ⁻³	cr - cis eto - cis
Fatty acid metabolism	Ppard	936	51	942	35	650	92	3.82·10 ⁻²	eto - cis eto - cr
Biosynthesis of the N-glycan precursor (dolichol lipid-linked oligosaccharide, LLO) and transfer to a nascent protein	Dolk	843	24	903	16	775	18	1.29·10 ⁻²	cis - eto
Ketone body metabolism, Synthesis of Ketone Bodies	Hmgcl	748	20	1062	8	727	30	1.99·10 ⁻⁵	cr - cis eto - cis
Biosynthesis of the N-glycan precursor (dolichol lipid-linked oligosaccharide, LLO) and transfer to a nascent protein	Alg1	696	4	975	21	580	27	1.93·10 ⁻⁴	cr - cis eto - cis
Glycerophospholipid biosynthesis, Apoptotic cleavage of cellular proteins, Apoptotic execution phase, TP53 Regulates Transcription of Caspase Activators and Caspases, Breakdown of the nuclear lamina, TP53 Regulates Transcription of Cell Death Genes, Phospholipid metabolism, Caspase-mediated cleavage of cytoskeletal proteins	Casp6	654	24	688	19	498	34.49	5.35·10 ⁻³	eto - cis eto - cr
Phospholipid metabolism, Glycerophospholipid biosynthesis	Stard10	594	30	890	23	392	30	1.54·10 ⁻⁵	cr - cis cis - eto cr - eto
Fatty acid metabolism, Beta-oxidation of very long chain fatty acids, Peroxisomal lipid metabolism	Mlycd	483	3	722	30	347	13	7.33·10 ⁻⁶	cr - cis cis - eto cr - eto
Sphingolipid de novo biosynthesis	Cers1	185	10	195	9	20	2	2.02·10 ⁻⁶	eto - cis eto - cr
Fatty acid metabolism, Synthesis of Prostaglandins (PG) and Thromboxanes (TX), Arachidonic acid metabolism	Ptgs1	5704	196	5223	96	6797	202	1.47·10 ⁻³	eto - cis eto - cr
Fatty acyl-CoA biosynthesis, Fatty acid metabolism	Ppt1	5218	49	4271	74	5390	137	1.83·10 ⁻⁴	cr - cis eto - cis

Triglyceride catabolism	Cav1	4057	157	2680	78	6313	209	$2.83 \cdot 10^{-6}$	cr - cis cis - eto cr - eto
Plasma lipoprotein clearance	Soat1	3311	110	3279	97	4282	125	$8.19 \cdot 10^{-4}$	eto - cis eto - cr
Regulation of lipid metabolism by PPARalpha, Regulation of cholesterol biosynthesis by SREBP (SREBF), Cholesterol biosynthesis	Fdft1	1949	83	1360	6	2154	48	$6.15 \cdot 10^{-5}$	cr - cis cis - eto cr - eto
Glycosphingolipid metabolism	Hexb	1634	24	1341	43	1697	55	$2.14 \cdot 10^{-3}$	cr - cis eto - cis
Phospholipid metabolism	Ptpn13	1560	20	891	15	2601	48	$9.99 \cdot 10^{-9}$	cr - cis cis - eto cr - eto
Inositol phosphate metabolism	Braf	1154	81	1024	43	1539	81	$5.35 \cdot 10^{-3}$	eto - cis eto - cr
Biosynthesis of the N-glycan precursor (dolichol lipid-linked oligosaccharide, LLO) and transfer to a nascent protein	Pmm2	1056	32	927	39	1221	66	$1.74 \cdot 10^{-2}$	eto - cis
Sphingolipid de novo biosynthesis	Acer3	929	49	888	36	1978	50	$9.72 \cdot 10^{-7}$	eto - cis eto - cr
Plasma lipoprotein remodeling	Lpl	715	32	366	7	1338	40	$2.44 \cdot 10^{-7}$	cr - cis cis - eto cr - eto
Phospholipid metabolism, Glycerophospholipid biosynthesis	Chka	678	14	627	32	906	64	$8.09 \cdot 10^{-3}$	eto - cis eto - cr
Glycerophospholipid catabolism, Phospholipid metabolism	Pnpla7	621	26	594	18	722	33	$3.84 \cdot 10^{-2}$	eto - cis eto - cr
Phospholipid metabolism, Glycerophospholipid biosynthesis	Agk	597	36	387	17	621	27	$1.56 \cdot 10^{-3}$	cr - cis eto - cis
Glycerophospholipid biosynthesis, Synthesis of PG, Role of phospholipids in phagocytosis, Glycerophospholipid biosynthesis	Pld1	537	17	276	14	884	27	$4.23 \cdot 10^{-7}$	cr - cis cis - eto cr - eto
Role of phospholipids in phagocytosis, DAG and IP3 signaling	Itpr1	523	18	49	5	831	17	$1.34 \cdot 10^{-8}$	cr - cis cis - eto cr - eto

Peroxisomal lipid metabolism, Fatty acid metabolism	Phyh	452	15	394	14	483	16	$2.18 \cdot 10^{-2}$	cr - cis eto - cis
Regulation of lipid metabolism by PPARalpha, Plasma lipoprotein assembly, NR1H3 & NR1H2 regulate gene expression linked to cholesterol transport and efflux	Abca1	408	66	237	5	1182	38	$3.06 \cdot 10^{-6}$	cr - cis cis - eto cr - eto
Lipophagy, Fatty acid metabolism	Prkag2	299	21	241	16	821	19	$1.85 \cdot 10^{-7}$	eto - cis eto - cr
Plasma lipoprotein clearance	Cubn	180	6	17	1	950	64	$9.72 \cdot 10^{-7}$	cr - cis cis - eto cr - eto
DAG and IP3 signaling	Prkce	166	6	5	3	249	12	$2.91 \cdot 10^{-7}$	cr - cis cis - eto cr - eto
Fatty acid metabolism, Regulation of cholesterol biosynthesis by SREBP (SREBF)	Acacb	61	8	18	4	138	5	$6.75 \cdot 10^{-6}$	cr - cis cis - eto cr - eto
ABC transporters in lipid homeostasis	Abca4	60	8	33	3	340	10	$3.14 \cdot 10^{-8}$	eto - cis eto - cr
Mitochondrial Fatty Acid Beta-Oxidation	Acbd	34	4	28	4	113	6	$8.95 \cdot 10^{-6}$	eto - cis eto - cr
Glycerophospholipid biosynthesis, Phospholipid metabolism, Mitochondrial Fatty Acid Beta-Oxidation	Pctp	30	2	24	1	43	2	$3.10 \cdot 10^{-4}$	eto - cis eto - cr
Regulation of lipid metabolism by PPARalpha	Abcb4	21	5	16	2	51	3	$8.37 \cdot 10^{-4}$	eto - cis eto - cr
Regulation of lipid metabolism by PPARalpha, Regulation of cholesterol biosynthesis by SREBP (SREBF)	Ppara	21	8	1	0.3	31	2	$1.27 \cdot 10^{-2}$	cr - cis eto - cis
Plasma lipoprotein remodeling	Lipc	19	4	1	1	89	6	$3.89 \cdot 10^{-6}$	cr - cis cis - eto cr - eto
Triglyceride catabolism	Stard8	17	3	4	1	26	3	$2.14 \cdot 10^{-3}$	cr - cis eto - cis
Glycosphingolipid metabolism	Smpd3	16	0.5	8	2	105	5	$1.85 \cdot 10^{-7}$	eto - cis eto - cr
Phospholipid metabolism, Glycerophospholipid biosynthesis	Lpcat2	14	2	6	1	27	3	$3.09 \cdot 10^{-3}$	eto - cis eto - cr

Sphingolipid de novo biosynthesis	Cers3	12	2	2	1	48	3	2.04·10 ⁻⁶	cr - cis cis - eto cr - eto
Sphingolipid de novo biosynthesis	Acer2	12	2	11	2	52	4	2.80·10 ⁻⁵	eto - cis eto - cr
Mitochondrial Fatty Acid Beta-Oxidation, Fatty acid metabolism	Acot12	7	1	5	1	28	6	1.35·10 ⁻²	eto - cis eto - cr
ABC transporters in lipid homeostasis	Abca12	5	2	2	1	184	2	1.14·10 ⁻¹⁰	eto - cis eto - cr
Sphingolipid de novo biosynthesis	Acer1	5	1	3	0.7	30	1	1.94·10 ⁻⁶	eto - cis eto - cr
Triglyceride catabolism	Fabp4	2	1	2	0.4	48	8	5.22·10 ⁻⁴	eto - cis eto - cr
ABC transporters in lipid homeostasis, NR1H3 & NR1H2 regulate gene expression linked to cholesterol transport and efflux	Abcg8	2	1	0.2	0.1	42	3	1.05·10 ⁻⁶	eto - cis eto - cr
Muscle Contraction, Sphingolipid de novo biosynthesis	Spp1	159600	3490	29632	367	56730	1187	4.23·10 ⁻⁹	cr - cis cis - eto cr - eto
cell cell comunication, Glycosphingolipid metabolism	Psap	46846	653	45726	590	41353	1361	1.64·10 ⁻²	eto - cis eto - cr
Glycosphingolipid metabolism	Ugcg	13594	686	8057	121	4985	238	6.51·10 ⁻⁶	cr - cis cis - eto cr - eto
Fatty acid metabolism, Synthesis of Lipoxins (LX), Biosynthesis of specialized proresolving mediators (SPMs), Biosynthesis of DPA-derived SPMs, Biosynthesis of electrophilic omega-3 PUFA oxo-derivatives, Biosynthesis of DHA-derived SPMs, Biosynthesis of EPA-derived SPMs, Arachidonic acid metabolism, Synthesis of 5-eicosatetraenoic acids	Alox5	13107	335	5054	76	1354	68	6.81·10 ⁻⁹	cr - cis cis - eto cr - eto
Plasma lipoprotein clearance	Npc2	12598	86	9959	131	10654	146	3.97·10 ⁻⁶	cr - cis cis - eto cr - eto
Plasma lipoprotein clearance	Scarb2	8689	173	7803	105	7559	210	8.19·10 ⁻³	cis - cr eto - cr

Regulation of lipid metabolism by PPARalpha, Regulation of cholesterol biosynthesis by SREBP (SREBF), Regulation of lipid metabolism by PPARalpha, Regulation of cholesterol biosynthesis by SREBP (SREBF)	Srebf2	7330	200	5667	165	2630	144	7.97·10 ⁻⁷	cr - cis cis - eto cr - eto
ABC transporters in lipid homeostasis,	Pex19	6474	44	5460	68	3367	117	8.42·10 ⁻⁸	cr - cis cis - eto cr - eto
Glycosphingolipid metabolism	Asah1	4605	48	3663	45	4288	98	9.17·10 ⁻⁵	cr - cis cis - eto cr - eto
Fatty acid metabolism, Mitochondrial Fatty Acid Beta-Oxidation, Mitochondrial Fatty Acid Beta-Oxidation	Dbi	4283	48	4086	112	3762	43	8.12·10 ⁻³	eto - cis eto - cr
Arachidonic acid metabolism, Fatty acid metabolism	Abcc1	3183	131	2551	93	2837	115	2.83·10 ⁻²	cr - cis
Fatty acid metabolism, Regulation of cholesterol biosynthesis by SREBP (SREBF), Fatty acyl-CoA biosynthesis	Acaca	2950	97	1022	53	2911	115	2.31·10 ⁻⁶	cr - cis eto - cis
DAG and IP3 signaling	Prkca	2946	89	264	7	870	52	2.47·10 ⁻⁸	cr - cis cis - eto cr - eto
Regulation of lipid metabolism by PPARalpha, Fatty acid metabolism, Linoleic acid (LA) metabolism, alpha-linolenic (omega3) and linoleic (omega6) acid metabolism	Fads1	2845	53	2196	122	2254	50	2.27·10 ⁻³	cis - cr eto - cr
Cholesterol biosynthesis via desmosterol, Cholesterol biosynthesis	Ebp	2666	55	2426	30	1127	24	4.61·10 ⁻⁸	cr - cis cis - eto cr - eto
Regulation of lipid metabolism by PPARalpha, Regulation of cholesterol biosynthesis by SREBP (SREBF), Cholesterol biosynthesis	Hmgcr	2588	83	2000	88	2371	113	1.64·10 ⁻²	cr - cis eto - cis
Plasma lipoprotein clearance, Fatty acid metabolism, Biosynthesis of DPAn-6 SPMs, Synthesis of Hepoxilins (HX) and Trioxilins (TrX), Synthesis of 12-eicosatetraenoic acid derivatives, Synthesis of Lipoxins (LX), Biosynthesis of specialized proresolving mediators (SPMs), Biosynthesis of DPA-derived SPMs, Biosynthesis of DHA-derived SPMs, Arachidonic acid metabolism	Lipa	2455	64	1911	39	2398	108	4.23·10 ⁻³	cr - cis eto - cis

The fatty acid cycling model	Ucp2	2429	70	2334	24	1271	36	9.72·10 ⁻⁷	eto - cis eto - cr
Phospholipid metabolism, Glycerophospholipid biosynthesis	Agpat1	2272	115	2144	54	1710	112	1.89·10 ⁻²	eto - cis eto - cr
Plasma lipoprotein clearance, Phospholipid metabolism, Glycerophospholipid biosynthesis	Ldlr	2061	94	586	23	526	19	4.07·10 ⁻⁷	cis - cr eto - cr
Ketone body metabolism, Synthesis of Ketone Bodies, Utilization of Ketone Bodies	Cholesterol biosynthesis	1813	43	1265	65	904	48	2.06·10 ⁻⁵	cr - cis cis - eto cr - eto
Glycosphingolipid metabolism, Biosynthesis of the N-glycan precursor (dolichol lipid-linked oligosaccharide, LLO) and transfer to a nascent protein	Glb1	1726	26	703	15	1125	21	1.99·10 ⁻⁸	cr - cis cis - eto cr - eto
Glycosphingolipid metabolism	Arsb	1689	10	108	2	1202	21	1.23·10 ⁻¹⁰	cr - cis cis - eto cr - eto
Synthesis of PG, Phospholipid metabolism, Glycerophospholipid biosynthesis	Ptpmt1	1536	47	1524	61	1178	60	7.14·10 ⁻³	eto - cis eto - cr
Regulation of lipid metabolism by PPARalpha	Fhl2	1493	68	1049	35	938	51	4.86·10 ⁻⁴	cis - cr eto - cr
Phospholipid metabolism, Glycerophospholipid biosynthesis	Mboat2	1275	13	769.51	23.19	292	14	9.91·10 ⁻⁹	cr - cis cis - eto cr - eto
Biosynthesis of the N-glycan precursor (dolichol lipid-linked oligosaccharide, LLO) and transfer to a nascent protein	Dpagt1	1264	36	1153	49	905	52	4.05·10 ⁻³	eto - cis eto - cr
Cholesterol biosynthesis	Nsdhl	1215	28	596	16	639	22	3.73·10 ⁻⁷	cis - cr eto - cr
Phospholipid metabolism	Aatf	1159	33	1073	23	942	16	2.33·10 ⁻³	eto - cis eto - cr
Biosynthesis of the N-glycan precursor (dolichol lipid-linked oligosaccharide, LLO) and transfer to a nascent protein	Alg9	1114	53	416	16	666	7	4.03·10 ⁻⁶	cr - cis cis - eto cr - eto
Plasma lipoprotein clearance	Scarb1	1075	35	647	26	657	44	1.05·10 ⁻⁴	cis - cr eto - cr
Regulation of cholesterol biosynthesis by SREBP (SREBF), Cholesterol biosynthesis	Lbr	1003	15	872	23	827	16	9.90·10 ⁻⁴	cis - cr eto - cr

Lysosphingolipid and LPA receptors	Plpp3	990	40	799	14	981	19	4.04·10 ⁻³	cr - cis eto - cis
Phospholipid metabolism, Glycerophospholipid biosynthesis	Lpcat1	942	37	730	39	607	7	5.36·10 ⁻⁴	cr - cis; cis - eto cr - eto
Glycosphingolipid metabolism	Asah2	829	82	242	8	797	49	2.86·10 ⁻⁴	cr - cis eto - cis
Biosynthesis of the N-glycan precursor (dolichol lipid-linked oligosaccharide, LLO) and transfer to a nascent protein	Rft1	697	13	605	12	691	19	8.98·10 ⁻³	cr - cis eto - cis
Glycosphingolipid metabolism	Arsa	680	10	607	11	531	23	1.57·10 ⁻³	cr - cis cis - eto cr - eto
Glycerophospholipid biosynthesis, Triglyceride catabolism, Acyl chain remodeling of DAG and TAG, Arachidonate production from DAG, Phospholipid metabolism	Mgll	625	28	166	7	353	23	4.37·10 ⁻⁶	cr - cis cis - eto cr - eto
NRIF signals cell death from the nucleus, Biosynthesis of the N-glycan precursor (dolichol lipid-linked oligosaccharide, LLO) and transfer to a nascent protein	Alg3	566	7	413	11	308	16	3.45·10 ⁻⁶	cr - cis cis - eto cr - eto
Phospholipid metabolism, Glycerophospholipid biosynthesis	Brca1	506	29	78	4	177	22	5.78·10 ⁻⁶	cr - cis cis - eto cr - eto
Biosynthesis of the N-glycan precursor (dolichol lipid-linked oligosaccharide, LLO) and transfer to a nascent protein	Alg8	467	9	337	11	278	15	2.95·10 ⁻⁵	cr - cis cis - eto cr - eto
Plasma lipoprotein remodeling	Fgf21	366	16	219	8	32	2	2.56·10 ⁻⁷	cr - cis cis - eto cr - eto
Phospholipid metabolism, Glycerophospholipid biosynthesis	Ace	347	15	14	2	284	8	1.25·10 ⁻⁷	cr - cis cis - eto cr - eto
Regulation of lipid metabolism by PPARalpha, Free fatty acids regulate insulin secretion, Intracellular metabolism of fatty acids regulates insulin secretion	Cd36	346	16	151	11	95	8	4.17·10 ⁻⁶	cr - cis cis - eto cr - eto
Biosynthesis of the N-glycan precursor (dolichol lipid-linked oligosaccharide, LLO) and transfer to a nascent protein	Alg6	328	15	192	12	223	14	6.85·10 ⁻⁴	cis - cr eto - cr

Fatty acid metabolism, Arachidonic acid metabolism	Dpep1	280	19	201	11	54	1	$1.59 \cdot 10^{-5}$	cr - cis cis - eto cr - eto
Synthesis of glycosylphosphatidylinositol (GPI)	Chek2	265	29	152	11	185	23	$3.83 \cdot 10^{-2}$	cr - cis
Plasma lipoprotein remodeling	Lipg	144	7	10	2	143	7	$1.07 \cdot 10^{-6}$	cr - cis eto - cis
Sphingolipid de novo biosynthesis	Degs2	125	5	27	1	70	1	$1.80 \cdot 10^{-7}$	cr - cis cis - eto cr - eto
Plasma lipoprotein clearance	Pcsk9	84	9	48	1	52	4	$7.58 \cdot 10^{-3}$	cis - cr eto - cr

Table S3.5. List of cell death and cell cycle pathways significantly regulated by cisplatin treatment in C2C12. Legend: ↑ - significantly upregulated, ↓ - significantly downregulated; entities FDR – probability that the overlap between the query and the pathway has occurred by chance corrected for multiple comparison. Pathways ID corresponds to Reactome pathway database.

Pathway ID	Pathway name	Effect	Entities FDR	Association
R-HSA-111453	BH3-only proteins associate with and inactivate anti-apoptotic BCL-2 members	↑	$3.31 \cdot 10^{-2}$	apoptosis
R-HSA-69563	p53-Dependent G1 DNA Damage Response	↑	$1.83 \cdot 10^{-2}$	apoptosis
R-HSA-69580	p53-Dependent G1/S DNA damage checkpoint	↑	$1.83 \cdot 10^{-2}$	apoptosis
R-HSA-169911	Regulation of Apoptosis	↑	$1.98 \cdot 10^{-3}$	apoptosis
R-HSA-450408	AUF1 (hnRNP D0) binds and destabilizes mRNA	↑	$2.50 \cdot 10^{-3}$	apoptosis
R-HSA-174113	SCF-beta-TrCP mediated degradation of Emi1	↑	$4.60 \cdot 10^{-3}$	apoptosis
R-HSA-69613	p53-Independent G1/S DNA damage checkpoint	↑	$4.60 \cdot 10^{-3}$	apoptosis
R-HSA-69610	p53-Independent DNA Damage Response	↑	$4.60 \cdot 10^{-3}$	apoptosis
R-HSA-176417	Phosphorylation of Emi1	↓	$1.98 \cdot 10^{-3}$	apoptosis
R-HSA-69541	Stabilization of p53	↑	$2.11 \cdot 10^{-3}$	cell cycle
R-HSA-174154	APC/C:Cdc20 mediated degradation of Securin	↑	$6.35 \cdot 10^{-3}$	cell cycle
R-HSA-174084	Auto-degradation of Cdh1 by Cdh1:APC/C	↑	$9.28 \cdot 10^{-3}$	cell cycle
R-HSA-187577	SCF(Skp2)-mediated degradation of p27/p21	↑	$1.71 \cdot 10^{-2}$	cell cycle
R-HSA-69615	G1/S DNA Damage Checkpoints	↑	$3.73 \cdot 10^{-2}$	cell cycle
R-HSA-2980767	Activation of NIMA Kinases NEK9, NEK6, NEK7	↓	$1.81 \cdot 10^{-3}$	cell cycle
R-HSA-69618	Mitotic Spindle Checkpoint	↓	$5.17 \cdot 10^{-12}$	cell cycle
R-HSA-141444	Amplification of signal from unattached kinetochores via a MAD2 inhibitory signal	↓	$5.17 \cdot 10^{-12}$	cell cycle
R-HSA-141424	Amplification of signal from the kinetochores	↓	$5.17 \cdot 10^{-12}$	cell cycle
R-HSA-9648025	EML4 and NUDC in mitotic spindle formation	↓	$5.63 \cdot 10^{-12}$	cell cycle
R-HSA-69205	G1/S-Specific Transcription	↓	$6.25 \cdot 10^{-12}$	cell cycle
R-HSA-68877	Mitotic Prometaphase	↓	$6.36 \cdot 10^{-12}$	cell cycle
R-HSA-1538133	G0 and Early G1	↓	$1.96 \cdot 10^{-10}$	cell cycle
R-HSA-69278	Cell Cycle, Mitotic	↓	$8.26 \cdot 10^{-10}$	cell cycle
R-HSA-1640170	Cell Cycle	↓	$5.10 \cdot 10^{-8}$	cell cycle
R-HSA-1362277	Transcription of E2F targets under negative control by DREAM complex	↓	$2.49 \cdot 10^{-7}$	cell cycle

R-HSA-1362300	Transcription of E2F targets under negative control by p107 (RBL1) and p130 (RBL2) in complex with HDAC1	↓	$3.69 \cdot 10^{-7}$	cell cycle
R-HSA-73886	Chromosome Maintenance	↓	$4.10 \cdot 10^{-7}$	cell cycle
R-HSA-176187	Activation of ATR in response to replication stress	↓	$1.28 \cdot 10^{-6}$	cell cycle
R-HSA-774815	Nucleosome assembly	↓	$8.52 \cdot 10^{-6}$	cell cycle
R-HSA-606279	Deposition of new CENPA-containing nucleosomes at the centromere	↓	$8.52 \cdot 10^{-6}$	cell cycle
R-HSA-180786	Extension of Telomeres	↓	$1.01 \cdot 10^{-5}$	cell cycle
R-HSA-174417	Telomere C-strand (Lagging Strand) Synthesis	↓	$1.76 \cdot 10^{-5}$	cell cycle
R-HSA-8854518	AURKA Activation by TPX2	↓	$7.73 \cdot 10^{-5}$	cell cycle
R-HSA-2980766	Nuclear Envelope Breakdown	↓	$1.13 \cdot 10^{-4}$	cell cycle
R-HSA-380320	Recruitment of NuMA to mitotic centrosomes	↓	$4.40 \cdot 10^{-4}$	cell cycle
R-HSA-156711	Polo-like kinase mediated events	↓	$4.60 \cdot 10^{-4}$	cell cycle
R-HSA-2514853	Condensation of Prometaphase Chromosomes	↓	$1.10 \cdot 10^{-3}$	cell cycle
R-HSA-68911	G2 Phase	↓	$1.82 \cdot 10^{-3}$	cell cycle
R-HSA-8854050	FBXL7 down-regulates AURKA during mitotic entry and in early mitosis	↑	$3.27 \cdot 10^{-3}$	cell cycle arrest
R-HSA-75815	Ubiquitin-dependent degradation of Cyclin D (lack of Cyclin →impaired cell cycle)	↑	$1.72 \cdot 10^{-3}$	cell cycle
R-HSA-75893	TNF signaling	↑	$3.58 \cdot 10^{-2}$	cell death
R-HSA-211733	Regulation of activated PAK-2p34 by proteasome mediated degradation	↑	$6.17 \cdot 10^{-4}$	cell death
R-HSA-5676590	NIK→noncanonical NF-kB signaling	↑	$2.95 \cdot 10^{-3}$	cell death
R-HSA-5607761	Dectin-1 mediated noncanonical NF-kB signaling	↑	$3.30 \cdot 10^{-3}$	cell death
R-HSA-4641258	Degradation of DVL	↑	$1.89 \cdot 10^{-4}$	cell fate
R-HSA-4641257	Degradation of AXIN	↑	$1.20 \cdot 10^{-3}$	cell fate
R-HSA-195253	Degradation of beta-catenin by the destruction complex	↑	$2.64 \cdot 10^{-2}$	cell fate
R-HSA-5658442	Regulation of RAS by GAPs	↑	$3.10 \cdot 10^{-2}$	cell survival
R-HSA-2871837	FCERI mediated NF-kB activation	↑	$5.79 \cdot 10^{-3}$	cytokines
R-HSA-202424	Downstream TCR signaling	↑	$8.18 \cdot 10^{-3}$	cytokines
R-HSA-5668541	TNFR2 non-canonical NF-kB pathway	↑	$1.05 \cdot 10^{-2}$	cytokines
R-HSA-9020702	Interleukin-1 signaling	↑	$2.50 \cdot 10^{-2}$	cytokines
R-HSA-349425	Autodegradation of the E3 ubiquitin ligase COP1	↑	$1.97 \cdot 10^{-3}$	DNA damage
R-HSA-5651801	PCNA-Dependent Long Patch Base Excision Repair	↓	$1.19 \cdot 10^{-4}$	DNA repair
R-HSA-5358508	Mismatch Repair	↓	$3.58 \cdot 10^{-4}$	DNA repair

R-HSA-68962	Activation of the pre-replicative complex	↓	4.13·10 ⁻¹⁰	DNA repair
R-HSA-68952	DNA replication initiation	↓	4.00·10 ⁻³	DNA synthesis
R-HSA-69190	DNA strand elongation	↓	5.17·10 ⁻¹²	DNA synthesis
R-HSA-69186	Lagging Strand Synthesis	↓	1.40·10 ⁻⁸	DNA synthesis
R-HSA-69183	Processive synthesis on the lagging strand	↓	1.95·10 ⁻⁷	DNA synthesis
R-HSA-69166	Removal of the Flap Intermediate	↓	2.22·10 ⁻⁶	DNA synthesis
R-HSA-176974	Unwinding of DNA	↓	5.22·10 ⁻⁵	DNA synthesis
R-HSA-69109	Leading Strand Synthesis	↓	8.19·10 ⁻⁵	DNA synthesis
R-HSA-69091	Polymerase switching	↓	8.19·10 ⁻⁵	DNA synthesis

Table S3.6. List of cell death and cell cycle pathways significantly regulated by etoposide treatment in C2C12. Legend: ↑ - significantly upregulated, ↓ - significantly downregulated; entities FDR – probability that the overlap between the query and the pathway has occurred by chance corrected for multiple comparison. Pathways ID corresponds to Reactome pathway database.

Pathway ID	Pathway name	Effect	Entities FDR	Association
R-HSA-140534	Caspase activation via Death Receptors in the presence of ligand	↑	4.60·10 ⁻³	apoptosis
R-HSA-69610	p53-Independent DNA Damage Response	↓	4.60·10 ⁻³	apoptosis
R-HSA-69613	p53-Independent G1/S DNA damage checkpoint	↓	4.60·10 ⁻³	apoptosis
R-HSA-69615	G1/S DNA Damage Checkpoints	↓	3.73·10 ⁻²	apoptosis
R-HSA-169911	Regulation of Apoptosis	↓	1.98·10 ⁻³	apoptosis
R-HSA-9614399	Regulation of localization of FOXO transcription factors	↓	3.20·10 ⁻²	apoptosis
R-HSA-111448	Activation of NOXA and translocation to mitochondria	↓	3.68·10 ⁻²	apoptosis
R-HSA-211733	Regulation of activated PAK-2p34 by proteasome mediated degradation	↓	6.17·10 ⁻⁴	apoptosis
R-HSA-113501	Inhibition of replication initiation of damaged DNA by RB1/E2F1	↓	1.66·10 ⁻³	cell cycle
R-HSA-113510	E2F mediated regulation of DNA replication	↓	1.23·10 ⁻⁴	cell cycle
R-HSA-1362277	Transcription of E2F targets under negative control by DREAM complex	↓	2.49·10 ⁻⁷	cell cycle
R-HSA-1362300	Transcription of E2F targets under negative control by p107 (RBL1) and p130 (RBL2) in complex with HDAC1	↓	3.69·10 ⁻⁷	cell cycle

R-HSA-141405	Inhibition of the proteolytic activity of APC/C required for the onset of anaphase by mitotic spindle checkpoint components	↓	$3.08 \cdot 10^{-4}$	cell cycle
R-HSA-141424	Amplification of signal from the kinetochores	↓	$5.17 \cdot 10^{-12}$	cell cycle
R-HSA-141430	Inactivation of APC/C via direct inhibition of the APC/C complex	↓	$3.08 \cdot 10^{-4}$	cell cycle
R-HSA-141444	Amplification of signal from unattached kinetochores via a MAD2 inhibitory signal	↓	$5.17 \cdot 10^{-12}$	cell cycle
R-HSA-1538133	G0 and Early G1	↓	$1.96 \cdot 10^{-10}$	cell cycle
R-HSA-156711	Polo-like kinase mediated events	↓	$4.60 \cdot 10^{-4}$	cell cycle
R-HSA-1640170	Cell Cycle	↓	$5.10 \cdot 10^{-8}$	cell cycle
R-HSA-174048	APC/C:Cdc20 mediated degradation of Cyclin B	↓	$7.31 \cdot 10^{-4}$	cell cycle
R-HSA-174084	Autodegradation of Cdh1 by Cdh1:APC/C	↓	$9.28 \cdot 10^{-3}$	cell cycle
R-HSA-174113	SCF-beta-TrCP mediated degradation of Emi1	↓	$4.60 \cdot 10^{-3}$	cell cycle
R-HSA-174143	APC/C-mediated degradation of cell cycle proteins	↓	$5.03 \cdot 10^{-4}$	cell cycle
R-HSA-174154	APC/C:Cdc20 mediated degradation of Securin	↓	$6.35 \cdot 10^{-3}$	cell cycle
R-HSA-174178	APC/C:Cdh1 mediated degradation of Cdc20 and other APC/C:Cdh1 targeted proteins in late mitosis/early G1	↓	$3.97 \cdot 10^{-3}$	cell cycle
R-HSA-174184	Cdc20:Phospho-APC/C mediated degradation of Cyclin A	↓	$2.61 \cdot 10^{-3}$	cell cycle
R-HSA-176187	Activation of ATR in response to replication stress	↓	$1.28 \cdot 10^{-6}$	cell cycle
R-HSA-176407	Conversion from APC/C:Cdc20 to APC/C:Cdh1 in late anaphase	↓	$3.20 \cdot 10^{-8}$	cell cycle
R-HSA-176408	Regulation of APC/C activators between G1/S and early anaphase	↓	$1.86 \cdot 10^{-3}$	cell cycle
R-HSA-176409	APC/C:Cdc20 mediated degradation of mitotic proteins	↓	$7.50 \cdot 10^{-4}$	cell cycle
R-HSA-176412	Phosphorylation of the APC/C	↓	$3.80 \cdot 10^{-4}$	cell cycle
R-HSA-176814	Activation of APC/C and APC/C:Cdc20 mediated degradation of mitotic proteins	↓	$5.03 \cdot 10^{-4}$	cell cycle
R-HSA-179409	APC-Cdc20 mediated degradation of Nek2A	↓	$1.86 \cdot 10^{-4}$	cell cycle
R-HSA-179419	APC:Cdc20 mediated degradation of cell cycle proteins prior to satisfaction of the cell cycle checkpoint	↓	$1.86 \cdot 10^{-3}$	cell cycle
R-HSA-187577	SCF(Skp2)-mediated degradation of p27/p21	↓	$1.71 \cdot 10^{-2}$	cell cycle
R-HSA-2467813	Separation of Sister Chromatids	↓	$5.68 \cdot 10^{-8}$	cell cycle
R-HSA-2500257	Resolution of Sister Chromatid Cohesion	↓	$1.13 \cdot 10^{-13}$	cell cycle
R-HSA-2555396	Mitotic Metaphase and Anaphase	↓	$2.14 \cdot 10^{-7}$	cell cycle
R-HSA-2565942	Regulation of PLK1 Activity at G2/M Transition	↓	$5.43 \cdot 10^{-4}$	cell cycle
R-HSA-2980766	Nuclear Envelope Breakdown	↓	$1.13 \cdot 10^{-4}$	cell cycle
R-HSA-2995383	Initiation of Nuclear Envelope (NE) Reformation	↓	$4.00 \cdot 10^{-4}$	cell cycle

R-HSA-2995410	Nuclear Envelope (NE) Reassembly	↓	$4.33 \cdot 10^{-3}$	cell cycle
R-HSA-3301854	Nuclear Pore Complex (NPC) Disassembly	↓	$4.01 \cdot 10^{-3}$	cell cycle
R-HSA-380259	Loss of Nlp from mitotic centrosomes	↓	$8.69 \cdot 10^{-4}$	cell cycle
R-HSA-380270	Recruitment of mitotic centrosome proteins and complexes	↓	$5.83 \cdot 10^{-4}$	cell cycle
R-HSA-380284	Loss of proteins required for interphase microtubule organization from the centrosome	↓	$8.69 \cdot 10^{-4}$	cell cycle
R-HSA-380287	Centrosome maturation	↓	$5.83 \cdot 10^{-4}$	cell cycle
R-HSA-380320	Recruitment of NuMA to mitotic centrosomes	↓	$4.40 \cdot 10^{-4}$	cell cycle
R-HSA-4419969	Depolymerisation of the Nuclear Lamina	↓	$1.89 \cdot 10^{-2}$	cell cycle
R-HSA-453274	Mitotic G2-G2/M phases	↓	$2.61 \cdot 10^{-4}$	cell cycle
R-HSA-453276	Regulation of mitotic cell cycle	↓	$5.03 \cdot 10^{-4}$	cell cycle
R-HSA-453279	Mitotic G1 phase and G1/S transition	↓	$1.96 \cdot 10^{-7}$	cell cycle
R-HSA-6791312	TP53 Regulates Transcription of Cell Cycle Genes	↓	$4.58 \cdot 10^{-3}$	cell cycle
R-HSA-68875	Mitotic Prophase	↓	$4.35 \cdot 10^{-3}$	cell cycle
R-HSA-68877	Mitotic Prometaphase	↓	$6.36 \cdot 10^{-12}$	cell cycle
R-HSA-68882	Mitotic Anaphase	↓	$2.56 \cdot 10^{-7}$	cell cycle
R-HSA-68884	Mitotic Telophase/Cytokinesis	↓	$3.67 \cdot 10^{-3}$	cell cycle
R-HSA-68886	M Phase	↓	$1.20 \cdot 10^{-6}$	cell cycle
R-HSA-68911	G2 Phase	↓	$1.82 \cdot 10^{-3}$	cell cycle
R-HSA-69202	Cyclin E associated events during G1/S transition	↓	$6.98 \cdot 10^{-4}$	cell cycle
R-HSA-69205	G1/S-Specific Transcription	↓	$6.25 \cdot 10^{-12}$	cell cycle
R-HSA-69206	G1/S Transition	↓	$4.11 \cdot 10^{-7}$	cell cycle
R-HSA-69231	Cyclin D associated events in G1	↓	$8.39 \cdot 10^{-4}$	cell cycle
R-HSA-69236	G1 Phase	↓	$8.39 \cdot 10^{-4}$	cell cycle
R-HSA-69242	S Phase	↓	$4.04 \cdot 10^{-7}$	cell cycle
R-HSA-69273	Cyclin A/B1/B2 associated events during G2/M transition	↓	$1.93 \cdot 10^{-3}$	cell cycle
R-HSA-69275	G2/M Transition	↓	$4.87 \cdot 10^{-4}$	cell cycle
R-HSA-69278	Cell Cycle, Mitotic	↓	$8.26 \cdot 10^{-10}$	cell cycle
R-HSA-69481	G2/M Checkpoints	↓	$1.25 \cdot 10^{-2}$	cell cycle
R-HSA-69618	Mitotic Spindle Checkpoint	↓	$5.17 \cdot 10^{-12}$	cell cycle
R-HSA-69620	Cell Cycle Checkpoints	↓	$6.78 \cdot 10^{-7}$	cell cycle
R-HSA-69656	Cyclin A:Cdk2-associated events at S phase entry	↓	$1.06 \cdot 10^{-3}$	cell cycle

R-HSA-75815	Ubiquitin-dependent degradation of Cyclin D	↓	$1.72 \cdot 10^{-3}$	cell cycle
R-HSA-774815	Nucleosome assembly	↓	$8.52 \cdot 10^{-6}$	cell cycle
R-HSA-8852276	The role of GTSE1 in G2/M progression after G2 checkpoint	↓	$2.56 \cdot 10^{-2}$	cell cycle
R-HSA-8854050	FBXL7 down-regulates AURKA during mitotic entry and in early mitosis	↓	$3.27 \cdot 10^{-3}$	cell cycle
R-HSA-8854518	AURKA Activation by TPX2	↓	$7.73 \cdot 10^{-5}$	cell cycle
R-HSA-9615933	Post-mitotic nuclear pore complex (NPC) reformation	↓	$1.71 \cdot 10^{-2}$	cell cycle
R-HSA-9648025	EML4 and NUDC in mitotic spindle formation	↓	$5.63 \cdot 10^{-12}$	cell cycle
R-HSA-6804114	TP53 Regulates Transcription of Genes Involved in G2 Cell Cycle Arrest	↓	$5.79 \cdot 10^{-3}$	cell cycle arrest
R-HSA-6804116	TP53 Regulates Transcription of Genes Involved in G1 Cell Cycle Arrest	↓	$4.85 \cdot 10^{-3}$	cell cycle arrest
R-HSA-5669034	TNFs bind their physiological receptors	↑	$2.09 \cdot 10^{-2}$	cell death
R-HSA-5607761	Dectin-1 mediated non-canonical NF-kB signalling	↓	$3.30 \cdot 10^{-3}$	cell death
R-HSA-5676590	NIK → non-canonical NF-kB signalling	↓	$2.95 \cdot 10^{-3}$	cell death
R-HSA-6783783	Interleukin-10 signalling	↑	$1.77 \cdot 10^{-2}$	cytokines
R-HSA-877300	Interferon gamma signalling	↑	$4.64 \cdot 10^{-2}$	cytokines
R-HSA-909733	Interferon alpha/beta signalling	↑	$2.08 \cdot 10^{-3}$	cytokines
R-HSA-5658442	Regulation of RAS by GAPs	↓	$3.10 \cdot 10^{-2}$	cytokines
R-HSA-110320	Translation Synthesis by POLH	↓	$3.07 \cdot 10^{-2}$	DNA damage bypass
R-HSA-110373	Resolution of AP sites via the multiple-nucleotide patch replacement pathway	↓	$2.65 \cdot 10^{-3}$	DNA repair
R-HSA-5358508	Mismatch Repair	↓	$3.58 \cdot 10^{-4}$	DNA repair
R-HSA-5358565	Mismatch repair (MMR) directed by MSH2:MSH6 (MutSalpha)	↓	$4.91 \cdot 10^{-4}$	DNA repair
R-HSA-5358606	Mismatch repair (MMR) directed by MSH2:MSH3 (MutSbeta)	↓	$5.38 \cdot 10^{-5}$	DNA repair
R-HSA-5651801	PCNA-Dependent Long Patch Base Excision Repair	↓	$1.19 \cdot 10^{-4}$	DNA repair
R-HSA-5685942	HDR through Homologous Recombination (HRR)	↓	$5.03 \cdot 10^{-4}$	DNA repair
R-HSA-5693532	DNA Double-Strand Break Repair	↓	$5.27 \cdot 10^{-3}$	DNA repair
R-HSA-5693538	Homology Directed Repair	↓	$3.22 \cdot 10^{-3}$	DNA repair
R-HSA-5693567	HDR through Homologous Recombination (HRR) or Single Strand Annealing (SSA)	↓	$3.31 \cdot 10^{-3}$	DNA repair
R-HSA-5696397	Gap-filling DNA repair synthesis and ligation in GG-NER	↓	$2.27 \cdot 10^{-3}$	DNA repair
R-HSA-5696398	Nucleotide Excision Repair	↓	$4.41 \cdot 10^{-2}$	DNA repair
R-HSA-5696399	Global Genome Nucleotide Excision Repair (GG-NER)	↓	$2.79 \cdot 10^{-2}$	DNA repair
R-HSA-73933	Resolution of Abasic Sites (AP sites)	↓	$2.39 \cdot 10^{-3}$	DNA repair

R-HSA-176974	Unwinding of DNA	↓	$5.22 \cdot 10^{-5}$	DNA synthesis
R-HSA-68827	CDT1 association with the CDC6:ORC:origin complex	↓	$4.64 \cdot 10^{-2}$	DNA synthesis
R-HSA-68867	Assembly of the pre-replicative complex	↓	$4.61 \cdot 10^{-3}$	DNA synthesis
R-HSA-68949	Orc1 removal from chromatin	↓	$1.06 \cdot 10^{-2}$	DNA synthesis
R-HSA-68962	Activation of the pre-replicative complex	↓	$4.13 \cdot 10^{-10}$	DNA synthesis
R-HSA-69002	DNA Replication Pre-Initiation	↓	$4.00 \cdot 10^{-4}$	DNA synthesis
R-HSA-69017	CDK-mediated phosphorylation and removal of Cdc6	↓	$6.68 \cdot 10^{-3}$	DNA synthesis
R-HSA-69052	Switching of origins to a post-replicative state	↓	$1.19 \cdot 10^{-3}$	DNA synthesis
R-HSA-69091	Polymerase switching	↓	$8.19 \cdot 10^{-5}$	DNA synthesis
R-HSA-69109	Leading Strand Synthesis	↓	$8.19 \cdot 10^{-5}$	DNA synthesis
R-HSA-69166	Removal of the Flap Intermediate	↓	$2.22 \cdot 10^{-6}$	DNA synthesis
R-HSA-69183	Processive synthesis on the lagging strand	↓	$1.95 \cdot 10^{-7}$	DNA synthesis
R-HSA-69186	Lagging Strand Synthesis	↓	$1.40 \cdot 10^{-8}$	DNA synthesis
R-HSA-69190	DNA strand elongation	↓	$5.17 \cdot 10^{-12}$	DNA synthesis
R-HSA-69239	Synthesis of DNA	↓	$1.61 \cdot 10^{-5}$	DNA synthesis
R-HSA-69306	DNA Replication	↓	$2.33 \cdot 10^{-6}$	DNA synthesis

Table S3.7. Differentially expressed genes linked to lipid droplets, endosomes, lysosomes, and peroxisomes. ANOVA: FDR-adjusted p-values, post hoc Fisher's test: cr – control, cis – cisplatin, eto- etoposide, Source: GeneCards (www.genecards.org).

Lipid droplet

Gene	FDR	Post- hoc Fisher's test	Role
Faf2	1.7·10 ⁻²	eto - cis; eto - cr	involved in inhibition of LD degradation by binding to phospholipase PNPL2 and inhibiting its activity by promoting dissociation of PNPL2 from its endogenous activator, ABHD5 which inhibits the rate of triacylglycerol hydrolysis (PubMed:23297223).
Atg2b	6.4·10 ⁻⁵	cis - cr; cis - eto	required for both autophagosome formation and regulation of LD morphology and dispersion
Zfyve1	4.7·10 ⁻³	cis - cr; cis - eto	plays a role in the formation of LDs (PubMed:30970241); regulates the morphology, size and distribution of LDs (PubMed:31293035, PubMed:30970241); mediates the formation of endoplasmic reticulum-lipid droplets (ER-LD) contacts (PubMed:30970241).
Osbpl2	3.3·10 ⁻⁵	cis - cr; cis - eto	binds sterols and phospholipids and mediates lipid transport between intracellular compartments.
Aup1	3.6·10 ⁻³	cis - cr; cis - eto	involved in LD accumulation; reduced expression results in reduced LD clustering
Atg2a	3.7·10 ⁻²	cis - cr; cis - eto	regulates lipid droplets morphology and distribution within the cell
Pnpla2	6.7·10 ⁻⁵	all	catalyses the first step in the hydrolysis of TAGs in adipose tissue and non-adipocyte LDs; regulates adiposome size and degradation
Dgat2	2.2·10 ⁻⁴	cis - cr; cis - eto	catalyses final reaction in the synthesis of TAGs (DAG + long chain fatty acyl-CoAs); required for synthesis and storage of intracellular TAGs (PubMed:27184406); plays a central role in cytosolic lipid accumulation
Acsl3	4.2·10 ⁻⁶	all	converts free long-chain fatty acids into fatty acyl-CoA esters; plays a key role in lipid biosynthesis and fatty acid degradation; activates long-chain fatty acids for synthesis of cellular lipids and degradation via beta-oxidation
Abhd5	2.2·10 ⁻⁶	all	regulates the cellular storage of TAGs (PubMed:16679289)
Lipe	1.1·10 ⁻⁴	all	hydrolyzes stored TAGs to free fatty acids
Plin2	6.3·10 ⁻⁷	all	marker of lipid accumulation in diverse cell types and diseases
Hilpda	7.5·10 ⁻⁸	all	increases intracellular lipid accumulation
Cav2	1.3·10 ⁻⁵	eto - cis; eto - cr	acts as an accessory protein in conjunction with CAV1 in targeting to lipid rafts and driving caveolae formation
Cav1	3.1·10 ⁻⁶	all	forms a stable heterooligomeric complex with CAV2 that targets to lipid rafts and drives caveolae formation

Table S3.7. Continued.

Peroxisome			
Pex7	2.4·10 ⁻⁴	cr - cis; eto - cis	cytosolic receptor for peroxisomal matrix enzymes
Pex11b	2.4·10 ⁻³	all	facilitates peroxisomal proliferation
Lonp2	1.5·10 ⁻⁶	all	maintains overall peroxisome homeostasis
Pex14	9.5·10 ⁻⁴	all	essential component of the peroxisomal import machinery
Pex19	1.7·10 ⁻⁷	all	early peroxisomal biogenesis
Pex6	8.9·10 ⁻³	cis - cr; cis - eto	peroxisome biogenesis
Pex5	1.1·10 ⁻⁴	cis - eto; cr - eto	peroxisomal targeting signal
Abcd1	4.7·10 ⁻³	cis - cr; cis - eto	peroxisomal import of fatty acids and/or fatty acyl-CoAs in the organelle
Pex11a	1.0·10 ⁻⁵	all	involved in regulation of peroxisome maintenance and proliferation; increases peroxisome abundance
Pex16	3.6·10 ⁻³	cis - cr; cis - eto	restores the formation of new peroxisomes
Tysnd1	4.4·10 ⁻³	cis - cr; cis - eto	facilitates protein import into the peroxisome
Pex11g	1.3·10 ⁻²	cis - cr; cis - eto	regulates the number and size of peroxisomes
Pex10	5.9·10 ⁻⁵	cis - cr; cis - eto	involved in import of peroxisomal matrix proteins
Crot	5.8·10 ⁻⁶	all	converts 4,8-dimethylnonanoyl-CoA to its corresponding carnitine ester. This transesterification is necessary for transport of medium- and long- chain acyl-CoA molecules out of the peroxisome to the cytosol and mitochondria
Acbd5	1.8·10 ⁻³	all	transport and distribution of long chain acyl-Coenzyme A in cells

Desaturases analysis

I examined a possible transcriptomic explanation for increased in PUFAs during apoptosis, especially in the etoposide-treated cells (Fig of data MS). **Figure S3.** shows differentially expressed genes which encodes for desaturases (enzymes catalysing double bond formation in FA chains). The enzymes, which catalyse biosynthesis of unsaturated FAs (Fads1-3 and Scd2), were downregulated during apoptosis. The bi-functional enzyme, Degs2, which catalyses sphingolipid desaturation and mono-oxidation is also downregulated. In addition, two desaturases (Degs1 and Scd1) either increased or remained unchanged during apoptosis.

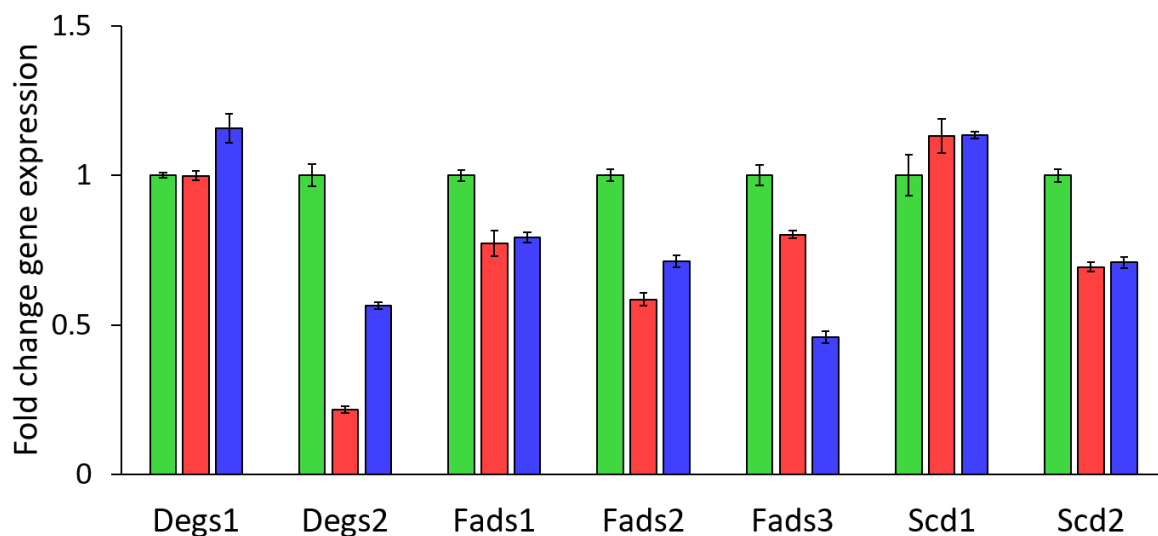


Figure S3.2. Differentially expressed genes linked to lipid desaturases in control (green), cisplatin- (red) and etoposide-treated (blue) C2C12 myotubes. Degs1-2 – sphingolipid desaturases, Fads1-3 and Scd1-2 – biosynthesis of unsaturated fatty acids. Mean fold changes in gene expressions were calculated relatively to the control group; error bars represent SEM of four independent cell samples. All changes are statistically significant (ANOVA: FDR-adjusted P -value < 0.05), except for Degs1 control vs cisplatin.

Appendix 4. Supporting information for Chapter 3

C6 rat glioma cells

C6 cell line derived from a rat glial tumour induced by N-nitrosomethylurea was cultured in nutrient mixture F-12 Ham dissolved in sterile-filtered water containing 2.5 g/L sodium bicarbonate (final pH = 7.4), 2.5% fetal bovine serum (FBS), 10% horse serum (HS) and 1% PenStrep (100 U/mL Penicillin + 100 µg/mL Streptomycin) in a humidified 5% carbon dioxide atmosphere at 37 °C. Cells were grown in T-75 (for NMR) culture flasks with filter-vented caps, seeded at approx. $1.0 \cdot 10^6$ cells per flask. Cells were passaged four times to obtain required sample size. The cells were trypsinized and washed twice with PBS. The harvested cells were frozen immediately in growth media + 5% DMSO and stored at -80 °C until use (for HRMAS NMR spectroscopy).

3T3-L1 mouse preadipocytes

The 3T3-L1 preadipocytes derived from a mouse embryo (ATCC, Manassas, Virginia, USA) were cultured in DMEM/GlutaMAX, supplemented with 10% of FBS, and 1% PenStrep (100 U/mL Penicillin + 100 µg/mL Streptomycin) in a humidified 5% carbon dioxide atmosphere at 37 °C. Cells were passaged four times to obtain required sample size. When cells reached confluence of 85-90%, they were washed three times with PBS and induced to differentiation with DMEM/F12 containing 10% FBS, 1% PenStrep, 0.2 mM IBMX, 10 µM rosiglitazone, 1 µM dexamethasone, 10 µg/mL insulin for 7 days. Cells were grown in T-75 (for NMR) culture flasks with filter-vented caps, seeded at approx. $1.0 \cdot 10^6$ cells per flask, respectively. The cells were trypsinized and washed twice with PBS. The harvested cells were frozen immediately in growth media + 5% DMSO and stored at -80 °C until use (for HRMAS NMR spectroscopy).

AML12 mouse hepatocytes

AML12 hepatocytes derived from a mouse transgenic for human TGF alpha (ATCC, Manassas, Virginia, USA) were cultured in DMEM/F12, supplemented with 10% of FBS, 1% PenStrep (100 U/mL Penicillin + 100 µg/mL Streptomycin), 10mL/L Insulin-Transferrin-

Selenium (Thermo Fisher Scientific, Waltham, MA, United States), and 40 ng/ml dexamethasone in a humidified 5% carbon dioxide atmosphere at 37 °C. Cells were grown in T-75 (for NMR) culture flasks with filter-vented caps, seeded at approx. $1.0 \cdot 10^6$ cells per flask. Cells were passaged four times to obtain required sample size. The cells were trypsinized and washed twice with PBS. The harvested cells were frozen immediately in growth media + 5% DMSO and stored at -80 °C until use (for HRMAS NMR spectroscopy).